Determination of the displacement demand for the out-of-plane seismic response of unreinforced masonry walls for the Groningen Case

Nikolaos Galanakis
February 2019

Master of Science Thesis
Delft University of Technology
Civil Engineering and Geosciences

Determination of the displacement demand for the out-of-plane seismic response of unreinforced masonry walls for the Groningen Case

By

Nikolaos Galanakis

in partial fulfilment of the requirements for the degree of

Master of Science

in Civil Engineering

at the Delft University of Technology

Thesis Committee:	Prof. Dr. Ir. J. G. Rots	TU Delft
	Dr. F. Messali	TU Delft
	Dr. Ir. G. J. P. Ravenshorst	TU Delft
	Ir. M. Spanenburg	BAM Advies en Engineering

An electroninc version of this thesis is available at http://repository.tudelft.nl/

Preface

This master thesis is submitted as a partial fulfilment of the requirements for the Master of Science degree in Structural Engineering, with a specialisation in Steel, Hybrid and Composite Structures at the Delft University of Technology. The theme is related to the out-of-plane seismic response of one-way vertically-spanning unreinforced masonry walls for the Groningen Case. The research was carried out under the supervision of the Delft University of Technology and BAM Advies en Engineering.

For the progression and finalisation of this research, the graduation commitee and my colleagues at BAM Advies en Engineering played a vital role with their significant guidance and advices. For that reason, I would like to express my sincere appreciation to them. Lastly, special thanks go to my family and beloved ones who supported me throughout this challenging period.

Nikolaos Galanakis
Maarssen, February 2019

Summary

This research describes the demand of a Displacement-based approach for the assessment of out-of-plane behaviour of one-way vertically-spanning unreinforced masonry (URM) walls of terraced and detached houses in the Groningen Province. One of the most vulnerable components of a typical Dutch unreinforced masonry building subjected to earthquake excitation is the face-loaded walls. As the Dutch masonry walls are quite slender, this matter is of significant importance.

Up to now, codes and standards evaluate the structural integrity of unreinforced masonry face-loaded walls with either force-based or displacement-based approaches. The latter present beneficial advantages, since the rocking mechanism of an out-of-plane wall is considered to be an instability problem. Particularly, for the definition of the demand (in terms of mid-height displacement for an out-of-plane unreinforced masonry wall) for the Groningen Case, it will be based on the design response outlined in New Zealand Society for Earthquake Engineering Standard (NZSEE) for the Seismic Assessment of Unreinforced Masonry Buildings. Nonetheless, a new rendition of the Shape Factor Coefficient $C_i(T_p)$ and Height Coefficient C_{Hi} is necessary, in order to relate the design response with the genuine characteristics of Groningen seismicity. The Shape Factor or Part Coefficient indicates the interaction between the seismic responses of the structural parts and the building, while the Height Coefficient indicates the amplification of the peak ground accelaration through the height of building.

The procedure towards the description of the out-of-plane seismic demand is analysed by **three parts**. In the **first part**, a series of **Nonlinear Time History (NLTH) analyses** are performed in **single degree of freedom (SDOF) systems**. In total, seven SDOF systems are modelled in Opensees. Each of them represents the equivalent SDOF system, according to Eurocode 8, of the considered structures for this research. The SDOF system characteristics as well as the ground motion records for five areas in the Groningen Province are provided from in-house studies of BAM Advies en Engineering. The ground motion records are related to the Draft NPR 9998:2017. Furthermore, two hysteresis rules for the structures are included in the Opensees Models. Hysteretic Rule 1 accounts for low-to-moderate energy dissipation, while Hysteretic Rule 2 for moderate energy dissipation. The hysteretic rules are in accordance with hysteretic behaviour of URM piers under in-plane loading. The geometry, loading conditions and mechanical properties of the piers are chosen to represent the piers in typical Dutch terraced and detached houses. These piers were tested at the Stevin Laboratory of the Delft University of Technology, which provided the data of the tests. Two specific in-plane wall specimens (COMP-2 and COMP-3) are used in this work. The Opensees parameters describing the aforementioned hysteretic rules, are calibrated according to the cyclic tests of these specimens. Next, the NLTH analyses are performed. The deliverables are the Floor Response Spectra (FRS) of each equivalent structure, per hysteretic rule, area and direction. Generally, a response spectrum is a plot that indicates the maximum response of linear oscillators with varying natural frequency or period. The oscillators are excited under the same vibration. Analogously, a FRS indicates the maximum seismic accelaration that the structural parts attract, if they are placed on the respective floor. Since a significant amount of FRS is provided from the NLTH analyses of the 1D Models, the production of Design Floor Accelaration Spectra per area is aimed. Design Floor Accelaration Spectra are "smooth" spectra that can be described by equations and act as an upper bound envelope for all the FRS produced per area. For their derivation, the Newmark-Hall method is applied to the mean Floor Response Spectra of all the structures per area. Consequently, a Design Spectrum per area is produced along with the equations that describe the Shape Factor Coefficient $C_i(T_p)$.

The Design Floor Accelaration Spectra efficiently describe the demand expressed in the response spectra of the 1D Models. Nevertheless, in some of the FRS, narrow high amplified spectra are observed with spectral values greater than the design plateau value. These cases are related to stiff structures that did not show proper plastic behaviour in direction X ("weak" direction of the structures governed by openings and rocking piers) and to all the structures in direction Y ("strong" direction of the structures governed by large shear walls), where they remain elastic, with the FRS to be bell shaped curves, highly amplified in a narrow period range around the fundamental period. This raises the necessity of examining if out-of-plane walls can potentially be subjected to these greater accelarations indicated by the narrow high amplified spectra. Therefore, the incorporation of a set of out-of-plane walls in the Opensees Models is decided, in order to compare their actual NLTH out-of-plane responses with their design responses Δ_{ph}. For the definition of the design response, the produced Shape Factor Coefficient $C_i(T_p)$ for the Groningen Case is used. Hence, the **second part** of this research deals with the **extended 1D Models**, which are described as **two degree of freedom mass-spring systems (2DOF systems)**. In the extended 1D Models, the nonlinear springs are in series and portray the hysteresis of the buildings and the out-of-plane walls. The hysteretic behaviour of the out-of-plane walls in the Opensees Models are calibrated to the experimental test of one-way spanning, double-clamped out-of-plane wall specimen COMP-7, performed at the Stevin Laboratory of the Delft University of Technology. Twelve wall configurations are considered, as a result of the 4 boundary conditions in the edges of one-way spanning walls presented in NZSEE Norm and 3 considered overburden loads (5 kN, 15 kN and 30 kN). The sensitivity studies in Opensees indicate that the design responses are larger than the NLTH responses for the non-failing walls and predict the failure when it is indicated in the NLTH responses. As a result, the Shape Factor Coefficient $C_i(T_p)$ satisfies also the cases in which the FRS present higher values than the design plateau value.

In the **third part** of the research, **NLTH analyses** are carried out in a **3D Model** that resembles four two-storey terraced houses with rigid diaphragms. The finite element method (FEM) software that is used for the NLTH analyses is ANSR-II and the **Macro-element based modelling approach** is adopted. ANSR-II allows the definition of nonlinear membrane elements to model the structural components. For shear walls and spandrels, specific in-plane backbone curves and hysteresis profiles are provided, being in agreement with the provisions of NZSEE Norm and Draft NPR 9998:2017. Regarding the in-plane rocking piers, no hysteresis is involved. However, the rocking capacity is in accordance with the Norms mentioned above. Triaxial excitations of the 3D Model with 11 sets of ground motions per area are performed in ANSR-II, following the requirements of Annex F of Draft NPR 9998:2017. From the NLTH analyses, the Floor Response Spectra are produced for each of the two floors of the 3D Model. These FRS are compared with the Design Floor Accelaration Spectra derived from the simplified 1D Models. A good predictabilty of the Response Spectra from the Design Spectra is found. Moreover, the Height Coefficient C_{Hi} is obtained as the ratio of the Peak Floor Accelaration (PFA) over the Peak Ground Accelaration (PGA). Linear regression analysis related to PFA/PGA ratios in the two floor levels of the structure is implemented per direction and area. The output is the linear equation describing the height effect as a function of height h. This equation has the same format with the one describing the Height Coefficient in NZSEE Norm, hence they are directly comparable.

Similar to the 1D Models and for analogous purposes, sensitivity studies of one-way vertically-spanning out-of-plane walls in ANSR-II are conducted. The variation of the walls is retained the same. The out-of-plane walls in the 3D Model are modelled as beam elements that can rock out of their plane. The behaviour of these beam elements under dynamic excitation in ANSR-II is described by elastic loading and unloading, so no hysteresis is introduced. That is a major difference compared with the Opensees Models. In spite of that, the behaviour of the out-of-plane beam elements in ANSR-II is based on the rigid bodies assumption and rocking mechanism of an out-of-plane wall according to Nonlinear Kinematic Analysis (NLKA). In fact, a good agreement is observed between the capacity curves of the considered out-of-plane walls in ANSR-II and the capacity curves derived from the NLKA method. The results of the sensitivity studies in ANSR-II lead to same conclusions as the ones derived from the sensitivity studies in Opensees Models. That enhances the ability of the Shape Factor Coefficient $C_i(T_p)$ and the Height Coefficient C_{Hi} to provide the appropriate design response.

As an overall conclusion, it is stated that the Shape Factor Coefficient $C_i(T_p)$ and the Height Coefficient C_{Hi} produced in this thesis, can be used for the definition of the displacement demand of one-way spanning out-of-plane walls for the Groningen Case, using the displacement-based methodology described in NZSEE Norm. The deliverables serve all the possible factors and parameters that distinguish the characteristics of the Dutch scenario. As the number of the Opensees Models is already satisfying, it is recommended to carry out NLTH analyses in more 3D Models. It is believed that this would further raise the consistency of the deliverables.

Contents

1 Introduction **1**
1.1 General . . . 1
1.2 Research objective and scope . . . 3
1.3 Methodology . . . 4

2 Literature review **5**
2.1 Unreinforced Masonry . . . 5
2.1.1 Masonry unit behaviour . . . 5
2.1.2 Composite behaviour . . . 6
2.2 Failure Mechanisms . . . 8
2.3 Hysteresis of structural components . . . 10
2.4 Strength and displacement verification approaches . . . 11
2.5 Out-of-plane behaviour of one-way vertically-spanning walls . . . 12
2.5.1 Post-cracked behaviour . . . 13
2.5.2 Nonlinear damping . . . 15
2.6 Analytical verifications of one-way vertically-spanning walls . . . 16
2.6.1 NZSEE method . . . 16
2.6.2 Draft NPR 9998:2017 method . . . 18
2.6.3 NTC method . . . 19
2.6.4 Remarks on the above methods . . . 20

3 1D Models **22**
3.1 Introduction . . . 22
3.2 Typologies . . . 23
3.3 SDOF Models . . . 27
3.3.1 Hysteretic Rules in Opensees . . . 27
3.3.2 Calibration of Hysteretic Rules . . . 30
3.3.3 In-plane hysteretic behaviour and Floor Response Spectra (FRS) . . . 32
3.3.4 Nonlinear viscous damping . . . 34
3.4 Nonlinear time history analyses (NLTHA) in Opensees . . . 36
3.4.1 Ground motion records . . . 36
3.4.2 Nonlinear Time History results . . . 36
3.5 Design Floor Accelaration Spectra . . . 38
3.5.1 Introduction . . . 38
3.5.2 Newmark - Hall method . . . 38
3.5.3 Design Spectra for the Groningen Case . . . 40
3.6 2DOF Models . . . 41
3.6.1 Incorporation of the OOP wall in the 1D model . . . 42
3.6.2 Nonlinear behaviour of OOP wall in Opensees . . . 42
3.6.3 Configurations of the OOP walls . . . 43
3.6.4 High amplified spectra . . . 44
3.6.5 Sensitivity studies of OOP walls in the 1D Models . . . 46
3.6.6 Sensitivity study of OOP walls - Direction X . . . 48

3.6.7 Sensitivity study of OOP walls - Direction Y . . . 53
3.7 Shape Factor Coefficient for the Groningen Case . . . 56

4 3D Model 59
4.1 Modelling in ANSR-II . . . 59
4.1.1 Modelling information . . . 60
4.1.2 Mesh definition . . . 60
4.1.3 Masses and weights . . . 64
4.1.4 Unreinforced masonry properties . . . 65
4.1.5 Unreinforced masonry shear walls . . . 65
4.1.6 Unreinforced masonry rocking piers . . . 66
4.1.7 Unreinforced masonry spandrels . . . 67
4.1.8 Rigid diaphragms . . . 68
4.1.9 Flexible diaphragms . . . 68
4.1.10 Out-of-plane walls in ANSR-II . . . 69
4.2 Nonlinear time history analyses (NLTHA) in ANSR-II . . . 71
4.2.1 Procedure . . . 71
4.2.2 Rayleigh damping . . . 71
4.2.3 Mean Floor Accelaration Spectra . . . 71
4.2.4 Normalised Floor Accelaration Spectra (FRS) . . . 72
4.2.5 Height Coefficient for the Groningen Case . . . 76
4.2.6 Sensitivity studies of OOP walls in the 3D Model . . . 79
4.2.7 Sensitivity study of OOP walls - Direction X . . . 79
4.2.8 Sensitivity study of OOP walls - Direction Y . . . 82

5 Conclusions and Recommendations 85
5.1 Conclusions . . . 85
5.2 Limitations of the research . . . 87
5.3 Recommendations for future research . . . 88

Appendix A 1D Models FRS Results 92
A.1 Appingedam . . . 92
A.2 Groningen . . . 96
A.3 Hoogezand . . . 100
A.4 Loppersum . . . 103
A.5 Overschild . . . 107

Appendix B Design Floor Accelaration Spectra Results 111
B.1 Appingedam . . . 111
B.2 Groningen . . . 112
B.3 Hoogezand . . . 113
B.4 Loppersum . . . 114
B.5 Overschild . . . 115

Appendix C OOP walls in ANSR-II and NLKA method 116

Appendix D Damage state of the 3D Model 119
D.1 Appingedam . . . 119
D.2 Groningen . . . 120
D.3 Hoogezand . . . 120
D.4 Loppersum . . . 121
D.5 Overschild . . . 121

Appendix E 3D Model FRS Results 122
E.1 Appingedam 122
E.2 Groningen 123
E.3 Hoogezand 123
E.4 Loppersum 124
E.5 Overschild 125

List of Figures

1.1 Number of events, magnitude per year and gas reduction (KNMI & NAM, 2017). 1
1.2 Distribution of epicentres (left) and Seismic hazard map for a return period of 475 years (right) in Groningen between January 2014 and January 2017 (KNMI, 2017). 2
1.3 Induced earthquakes (left) and tectonic earthquakes (right). 2
1.4 Typical Dutch detached house with OOP retrofitting. 2

2.1 Yield criterion (a) and typical stress-strain model (b) for a brick unit (Lotfi & Shing,1994). . . 5
2.2 Test setup for different specimens : (a) masonry prism, (b) triaxial state of stress at the interface of brick and mortar, (c) brick unit and (d) mortar cube [17]. 6
2.3 Typical failure modes of: (a) brick units, (b) mortar cubes and (c), (d) masonry prisms [17]. 6
2.4 Failure modes for different bed joint-load direction angles [30]. 6
2.5 Compressive stress-strain curves for masonry prisms [17]. 7
2.6 Comparison of stress-strain curves for brick units, mortar cubes and masonry specimens for (a) weak, (b) strong and (c) intermediate mortar [17]. 7
2.7 Shear stress-strain relationship [24]. 8
2.8 Biaxial compression projected onto $\sigma_1 - \sigma_2$ plane [30]. 8
2.9 Biaxial tension-compression projected onto $\sigma_1 - \sigma_2$ plane [30]. 8
2.10 In-plane failure modes of URM walls [13]. 9
2.11 Out-of-plane failure modes of URM walls (D'Ayala & Speranza, 2003). 9
2.12 Hysteresis loop example [19]. 10
2.13 Typical hysteretic loop for flexural response [35]. 10
2.14 Typical hysteretic loop for shear response [35]. 10
2.15 Hysteresis loop of specimen COMP-0b [22]. 11
2.16 Hysteresis loop of specimen COMP-7 [22]. 11
2.17 Secant stiffness K_e and maximum dispacement Δ_d [7]. 12
2.18 One-way bending of URM wall. Rigid bodies assumption [4]. 12
2.19 Real semi-rigid nonlinear capacity curve [10]. 13
2.20 Force-displacement relationship of deformable URM walls [11]. 14
2.21 Characterisation of a representative stiffness K_{eff} for the "substitute structure" [11]. 14
2.22 Experimental damping and Rayleigh damping - 50 mm Wall, No Overburden [10]. 15
2.23 Iterative process for the definition of equivalent damping [10]. 15
2.24 NLKA method scheme [28]. 16
2.25 Boundary conditions and eccentricities [28]. 16
2.26 Parts and Height effects. 17
2.27 Chart for deriving capacity seismic coefficient ξ_{SCC} [12]. 19

3.1 Equivalent single degree of freedom system. 22
3.2 Capacity curves in direction X. 23
3.3 Capacity curves in direction Y. 23
3.4 Drawing and capacity curves of Typology 1. 24
3.5 Drawing and capacity curves of Typology 2. 24
3.6 Drawing of Typologies 3 and 4 and capacity curves of Typology 4. 25
3.7 Drawing and capacity curves of Typology 5. 25

3.8 Drawing and capacity curves of Typology 6. 26
3.9 Drawing and capacity curves of Typology 7. 26
3.10 Hysteretic material model [46]. 28
3.11 Modified “thin” takeda model [45]. 28
3.12 Self-centering Material model in Opensees [21]. 28
3.13 Parallel Material model in Opensees [21]. 29
3.14 Self-centering material hysteretic response. 29
3.15 Parallel material hysteretic response. 29
3.16 Loading scheme for specimens COMP-2 and COMP-3 [22]. 30
3.17 COMP-2 Comparison of Hysteresis. 31
3.18 COMP-3 Comparison of Hysteresis. 31
3.19 COMP-2 Comparison of Energy per cycle. 31
3.20 COMP-3 Comparison of Energy per cycle. 31
3.21 Ground motion record for Groningen. 32
3.22 Capacity curve envelope of Typology 5. 32
3.23 Elastic-Plastic response of Typology 5. 32
3.24 Hysteretic Rule 1 of Typology 5. 33
3.25 Hysteretic Rule 2 of Typology 5. 33
3.26 Effect of hysteretic damping in FRS. 33
3.27 Effect of stiffness degrading systems in FRS. 33
3.28 Hysteretic behaviour - linear viscous damping. 35
3.29 Damping response - linear viscous damping. 35
3.30 Hysteretic behaviour - nonlinear viscous damping. 35
3.31 Damping response - nonlinear viscous damping. 35
3.32 Response of SDOF system considering nonlinear viscous damping and linear viscous damping. 36
3.33 Flow chart of the NLTH analyses in Opensees for direction X. 37
3.34 Flow chart of the NLTH analyses in Opensees for direction Y. 37
3.35 Newmark design spectra. 38
3.36 Definition of the mean + 2 std response. 40
3.37 Tripartite graph for the mean + 2 std response. 40
3.38 Design Floor Accelaration Spectrum and mean + 2 std response. 40
3.39 Design Floor Accelaration Spectrum and Typologies Mean FRS. 40
3.40 Resonance phenomenon due to the seismic interaction of the floor and the OOP wall. . . . 41
3.41 Representation of the extended 1D model. 42
3.42 Loading scheme for specimen COMP-7 [22]. 42
3.43 COMP-7 Comparison of Hysteresis. 43
3.44 Capacity curves - BC0. 44
3.45 Capacity curves - BC1. 44
3.46 Capacity curves - BC2. 44
3.47 Capacity curves - BC3. 44
3.48 High amplified spectra in Groningen for direction X. 45
3.49 High amplified spectra in Hoogezand for direction X. 45
3.50 High amplified spectra in Appingedam for direction Y. 45
3.51 High amplified spectra in Overschild for direction Y. 45
3.52 High amplified spectra in Loppersum for direction X. 45
3.53 High amplified spectra in Overschild for direction X. 45
3.54 Flow chart of the NLTH analyses regarding the extended 1D models in Opensees for direction X. 47
3.55 Flow chart of the NLTH analyses regarding the extended 1D models in Opensees for direction Y. 47
3.56 Appingedam - Typology 6: design and NLTH response of OOP walls. 48
3.57 Appingedam - Typology 7: design and NLTH response of OOP walls. 48

3.58 Groningen - Typology 4: design and NLTH response of OOP walls. 49
3.59 Groningen - Typology 6: design and NLTH response of OOP walls. 49
3.60 Groningen - Typology 7: design and NLTH response of OOP walls. 50
3.61 Hoogezand - Typology 6: design and NLTH response of OOP walls. 50
3.62 Hoogezand - Typology 7: design and NLTH response of OOP walls. 51
3.63 Loppersum - Typology 7: design and NLTH response of OOP walls. 51
3.64 Overschild - Typology 6: design and NLTH response of OOP walls. 52
3.65 Overschild - Typology 7: design and NLTH response of OOP walls. 52
3.66 Appingedam: design and NLTH response of OOP walls. 54
3.67 Groningen: design and NLTH response of OOP walls. 54
3.68 Hoogezand: design and NLTH response of OOP walls. 55
3.69 Loppersum: design and NLTH response of OOP walls. 55
3.70 Overschild: design and NLTH response of OOP walls. 56
3.71 Appingedam: with (left) and without (right) the high amplified spectra. 57
3.72 Groningen: with (left) and without (right) the high amplified spectra. 57
3.73 Hoogezand: with (left) and without (right) the high amplified spectra. 57
3.74 Loppersum: with (left) and without (right) the high amplified spectra. 58
3.75 Overschild: with (left) and without (right) the high amplified spectra. 58

4.1 Macro-element based Modelling (left) and Micro-Modelling (right) finite element arrangement [29]. 59
4.2 ANSR-II global axes [18]. 60
4.3 Plane stress element schematisation. 60
4.4 ANSR-II 3D Model. 61
4.5 Mesh of the wall panels of the 3D Model according to Macro-element based modelling methodology. 61
4.6 Mesh of the shear walls in direction Y. 61
4.7 Meshed piers in the 3D Model. 62
4.8 2 plane stress element meshed pier (left) and shear deformation profile (right). 62
4.9 4 plane stress element meshed pier (left) and shear deformation profiles of it (middle) and of the single element pier (right). 62
4.10 Capacity curves and hysteretic behaviours of a meshed pier consisted of 2 plane stress elements and the respective single element pier. 63
4.11 Capacity curves and hysteretic behaviours of a meshed pier consisted of 4 plane stress elements and the respective single element pier before the adjustment of the material properties. 63
4.12 Capacity curves and hysteretic behaviours of a meshed pier consisted of 4 plane stress elements and the respective single element pier after the adjustment of the material properties. 64
4.13 Bed Joint Sliding standardised backbone curve (left) and shear hysteresis for unreinforced masonry shear walls under cyclic loading in ANSR-II (right). 65
4.14 Rocking hysteresis for unreinforced masonry piers under cyclic loading in ANSR-II. 66
4.15 Standardised backbone curve (left) and shear hysteresis for unreinforced masonry spandrels under cyclic loading in ANSR-II (right). 67
4.16 Definition of the rigid diaphragm in ANSR-II. 68
4.17 Cyclic displacement pushover of the roof panel in ANSR-II. 68
4.18 OOP beam elements schematisation in ANSR-II. 69
4.19 Axial load and bending moment interaction (left) and resisting mechanism of rocking column element (right) [19]. 69
4.20 Agreement between the capacity curves derived from ANSR-II and NLKA method. 70
4.21 Behaviour of an OOP wall in ANSR-II under cyclic loading. 70
4.22 3D Model Mean Floors Response Spectra and Design Floor Spectrum in direction X for Appingedam. 72
4.23 3D Model Floor 2 Response Spectra and Design Floor Spectrum in direction X for Appingedam. 72

4.24 3D Model Mean Floors Response Spectra and Design Floor Spectrum in direction X for Groningen. 73
4.25 3D Model Floor 2 Response Spectra and Design Floor Spectrum in direction X for Groningen. 73
4.26 3D Model Mean Floors Response Spectra and Design Floor Spectrum in direction X for Hoogezand. 73
4.27 3D Model Floor 2 Response Spectra and Design Floor Spectrum in direction X for Hoogezand. 73
4.28 3D Model Mean Floors Response Spectra and Design Floor Spectrum in direction X for Loppersum. 73
4.29 3D Model Floor 2 Response Spectra and Design Floor Spectrum in direction X for Loppersum. 73
4.30 3D Model Mean Floors Response Spectra and Design Floor Spectrum in direction X for Overschild. 74
4.31 3D Model Floor 2 Response Spectra and Design Floor Spectrum in direction X for Overschild. 74
4.32 3D Model Mean Floors Response Spectra and Design Floor Spectrum in direction Y for Appingedam. 74
4.33 3D Model Floor 2 Response Spectra and Design Floor Spectrum in direction Y for Appingedam. 74
4.34 3D Model Mean Floors Response Spectra and Design Floor Spectrum in direction Y for Groningen. 75
4.35 3D Model Floor 2 Response Spectra and Design Floor Spectrum in direction Y for Groningen. 75
4.36 3D Model Mean Floors Response Spectra and Design Floor Spectrum in direction Y for Hoogezand. 75
4.37 3D Model Floor 2 Response Spectra and Design Floor Spectrum in direction Y for Hoogezand. 75
4.38 3D Model Mean Floors Response Spectra and Design Floor Spectrum in direction Y for Loppersum. 75
4.39 3D Model Floor 2 Response Spectra and Design Floor Spectrum in direction Y for Loppersum. 75
4.40 3D Model Mean Floors Response Spectra and Design Floor Spectrum in direction Y for Overschild. 76
4.41 3D Model Floor 2 Response Spectra and Design Floor Spectrum in direction Y for Overschild. 76
4.42 Height coefficient plot in Appingedam - Direction X. 77
4.43 Height coefficient plot in Appingedam - Direction Y. 77
4.44 Height coefficient plot in Groningen - Direction X. 77
4.45 Height coefficient plot in Groningen - Direction Y. 77
4.46 Height coefficient plot in Hoogezand - Direction X. 77
4.47 Height coefficient plot in Hoogezand - Direction Y. 77
4.48 Height coefficient plot in Loppersum - Direction X. 78
4.49 Height coefficient plot in Loppersum - Direction Y. 78
4.50 Height coefficient plot in Overschild - Direction X. 78
4.51 Height coefficient plot in Overschild - Direction Y. 78
4.52 Appingedam - Direction X: design and NLTH response of the 3D Model OOP walls. 79
4.53 Groningen - Direction X: design and NLTH response of the 3D Model OOP walls. 80
4.54 Hoogezand - Direction X: design and NLTH response of the 3D Model OOP walls. 80
4.55 Loppersum - Direction X: design and NLTH response of the 3D Model OOP walls. 81
4.56 Overschild - Direction X: design and NLTH response of the 3D Model OOP walls. 81
4.57 Appingedam - Direction Y: design and NLTH response of the 3D Model OOP walls. 82
4.58 Groningen - Direction Y: design and NLTH response of the 3D Model OOP walls. 83

4.59 Hoogezand - Direction Y: design and NLTH response of the 3D Model OOP walls. 83
4.60 Loppersum - Direction Y: design and NLTH response of the 3D Model OOP walls. 84
4.61 Overschild - Direction Y: design and NLTH response of the 3D Model OOP walls. 84

5.1 Loading and unloading path of an OOP wall in ANSR-II (left) and Opensees (right). 87

List of Tables

3.1 Information of SDOF systems for the direction X. 23
3.2 Information of SDOF systems for the direction Y. 23
3.3 Explanation of the Hysteretic Material command. 27
3.4 Explanation of the Self-Centering Material command. 28
3.5 Explanation of the Parallel Material command. 29
3.6 Hysteretic Rules parameters. 30
3.7 Energy dissipation in the experiment and in Opensees per cycle. 31
3.8 Spectrum amplification factors [26]. 39
3.9 OOP Hysteretic Rule parameters. 43
3.10 Information for the equivalent SDOF systems of OOP walls. 44
3.11 Typologies causing high amplified spectra per area. 46
3.12 Shape Factor Coefficient parameters per area. 58

4.1 Unreinforced masonry properties. 65
4.2 Eigenvalue analysis for the 3D Model. 71
4.3 PFA mean value and PFA mean value plus one standard deviation points per area and direction. 76
4.4 Parameter α for the definition of the Height Coefficient C_{Hi}. 78
4.5 Displacements (mm) of floor diaphragms in direction Y. 82

Acronyms

BC0	Boundary Condition 0
BC1	Boundary Condition 1
BC2	Boundary Condition 2
BC3	Boundary Condition 3
BPR	Basic Performance Ratio
CoM	Center of Mass
DDBD	Direct Displacement Based Design
DL	Damage Limitation
DOF	Degrees of Freedom
EC8	Eurocode 8
FE	Finite Element
FEM	Finite Element Method
FRS	Floor Response Spectra
HR1	Hysteretic Rule 1
HR2	Hysteretic Rule 2
KNMI	Koninklijk Nederlands Meteorologisch Instituut (Royal Netherlands Meteorological Institute)
NAM	Nederlandse Aardolie Maatschappij (Dutch Petroleum Company)
NBS	New Building Standard
NC	Near Collapse
NEN	Nederlandse Norm (Dutch Norm)
NLKA	Nonlinear Kinematic Analysis
NLTH	Nonlinear Time History
NLTHA	Nonlinear Time History Analysis
NPR	Nederlandse praktijkrichtlijn (Dutch Code of Practice)
NTC	Norme Tecniche Costruzioni
NZSEE	New Zealand Society for Earthquake Engineering
OOP	Out-of-plane
Opensees	Open System for Earthquake Engineering Simulation
PEER	Pacific Earthquake Engineering Research
PFA	Peak Floor Accelaration
PFD	Peak Floor Displacement
PFV	Peak Floor Velocity
PGA	Peak Ground Accelaration
PSA	Spectral Pseudo-Accelaration
PSD	Spectral Pseudo-Displacement
PSV	Spectral Pseudo-Velocity
SA	Spectral Accelaration
SD	Significant Damage
SD	Spectral Displacement
SDOF	Single Degree of Freedom
SLV	Salvaguardia della vita
std	Standard Deviation
SV	Spectral Velocity
tcl	Technical Program Language
URM	Unreinforced Masonry

Chapter 1

Introduction

1.1 General

In recent years seismic action has been observed in the northern part of the Netherlands. Gas extraction in the field of Groningen is identified as the source of the earthquakes. The gas exploitation started in 1963 and seismicity has been noticed since the early 1990s. From that point onward the number of seismic events rapidly increased, reaching the 30 seismic events in 2013 for earthquakes with a magnitude greater than 1.5 on the Richter scale. Moreover, the magnitude also increased with the highest value to be equal to 3.6 on the Richter scale in 2012. For that reason, the decrease in the gas production was decided, resulting to the decrease in the number of the seismic events from 2013 until present.

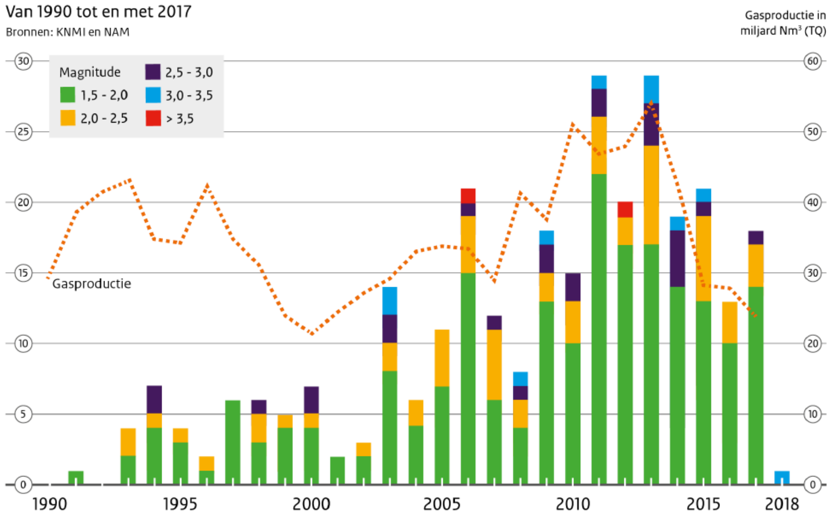

Figure 1.1: Number of events, magnitude per year and gas reduction (KNMI & NAM, 2017).

The epicentres of the earthquakes are located in the north-east part of the Netherlands. Due to the changes in the gas production in early 2014, the spatial distribution of the seismic actions and the hazard model for the definition of the peak ground accelarations (PGA) in the area altered, as the evaluation of the seismicity was based on the period 2014-2017. More specifically, for the updated hazard map, the maximum PGA value is 0.24 g or 2.4 m/s^2 and is located near Ten Boer and between Hoogezand and Hellum. The updated location of the epicentres and the PGA hazard map is indicated in figure 1.2.

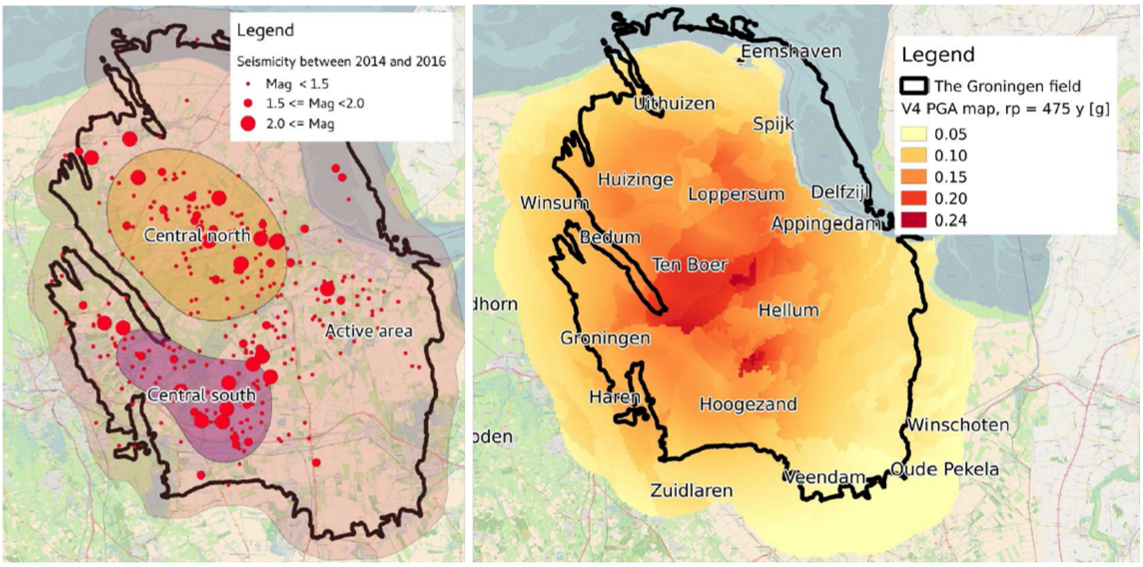
Legend
Seismicity between 2014 and 2016
Mag < 1.5
1.5 <= Mag <2.0
2.0 <= Mag
Central north
Active area
Central south
Legend
The Groningen field
V4 PGA map, rp = 475 y [g]
0.05
0.10
0.15
0.20
0.24
Eemshaven
Uithuizen
Spijk
Huizinge
Winsum
Loppersum
Delfzijl
Appingedam
Bedum
Ten Boer
Hellum
Groningen
Haren
Hoogezand
Winschoten
Veendam
Oude Pekela
Zuidlaren

Figure 1.2: Distribution of epicentres (left) and Seismic hazard map for a return period of 475 years (right) in Groningen between January 2014 and January 2017 (KNMI, 2017).

Groningen earthquakes can be characterised as induced ones. Induced seismicity is caused by human activities which lead to the variation of the geology conditions and eventually to seismic vibrations. The magnitudes for this type of earthquakes is usually low. On the contrary, tectonic earthquakes can be described as “natural” earthquakes, as they are resulting from the relative movement of the tectonic plates. Wide range of magnitudes is observed for tectonic earthquakes and usually they present higher values of magnitude compared to the induced ones.

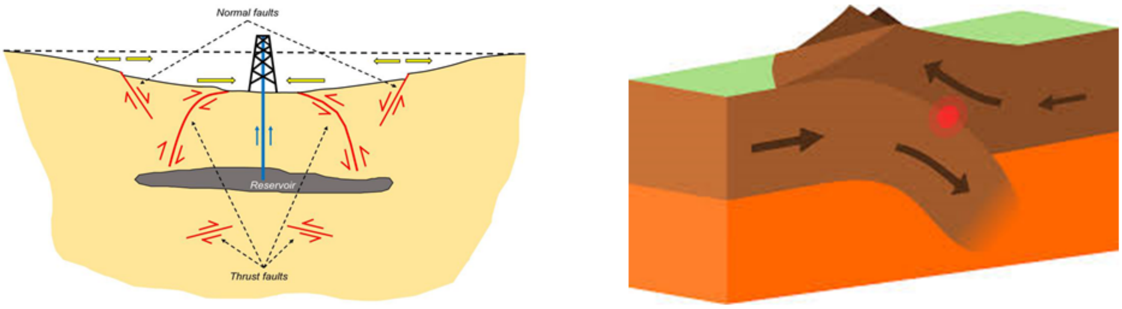
Normal faults
Reservoir
Thrust faults

Figure 1.3: Induced earthquakes (left) and tectonic earthquakes (right).

Regarding the residential buildings present in the province of Groningen, they are predominantly terraced and detached houses constructed of unreinforced masonry. The main load-bearing elements are the unreinforced masonry (URM) walls. These walls are rather slender and have low in-plane and out-of-plane (OOP) capacity. The diaphragms are constructed of concete (rigid diaphragms) or wood (flexible diaphragms). It is worth mentioning that typical Dutch houses were not designed according to any seismic Norm, so it can be concluded that they are prone to seismic actions. The statement above highlights the importance of the accurate assessment and retrofitting of the buildings in that area.

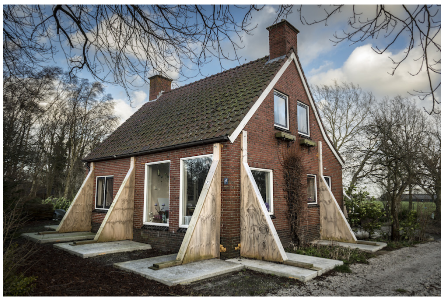

Figure 1.4: Typical Dutch detached house with OOP retrofitting.

1.2 Research objective and scope

Since the seismicity in the Netherlands is a relatively recent phenomenon, efforts have been made the last years for developing a Dutch Norm that will describe the procedure of the assessment and retrofitting of Dutch masonry houses. Other traditional seismic prone countries have already developed regulations that include seismic loads in the design of new structures and the retrofitting of existing ones. These regulations can be used as a significant basis for a newly created Norm, however the particularities of the case that this Norm will try to describe should be taken into account. Nowadays, Draft NPR 9998:2017 Norm [1] [12] is describing the assessment of the structural safety of Dutch masonry buildings for the Groningen Case. Most of the parts of this Draft Norm are well defined and adjusted to the induced earthquakes of the Netherlands, although there are aspects that should be investigated even further. Out-of-plane behaviour of masonry walls of typical Dutch houses subjected to induced seismicity belongs to this category.

The main objective of this thesis is to describe the demand of a displacement-based approach for assessing the out-of-plane behaviour of the masonry walls for the Groningen scenario. This will be performed by adjusting the foreign normative for the Dutch case in order to take into account the particularities of Dutch seismicity. The foreign normative selected is the NZSEE Norm [28]. Thus, the main research question is:

“Is it feasible to adjust the design seismic coefficient of the chosen foreign normative to the characteristics of the Dutch scenario?”

In detail, the design seismic coefficient defines the seismic demand for the structural part. Up to now, Draft NPR 9998:2017 [12] uses the design seismic coefficient referred to Eurocode 8 [25], which is irrelevant to the nature of induced earthquakes. The derivation of the design seismic coefficient will be based on the philosophy of NZSEE [28] Norm with the aim of defining the Parts or Shape Factor Coefficient and Height Coefficient, calibrated specifically for the Groningen seismic ground motions and typical buildings. The Shape Factor Coefficient indicates the amplification in the response of the structural part due to the seismic interaction between the part and the building, while the Height Coefficient indicates the amplification of the peak ground accelaration throughout the height of the building. To implement all the above, a series of NLTH analyses will be performed:

1. for typical Dutch houses.
2. with the assumption of one-way vertically-spanning walls.
3. for the induced earthquakes of the Groningen Province.

---

[1] A new version of NPR 9998 has been released on November 2018, but that does not contain significant differences with respect to the 2017 Draft NPR Norm for what concerns the out-of-plane behaviour.

1.3 Methodology

A certain methodology will be followed in order to answer the research question of this thesis. The required tasks for that and the respective chapters are described above.

Chapter 2: In this chapter the literature review is being held. Firstly, the material properties, mechanical behaviour, failure mechanisms and hysteresis profile of masonry are presented. In addition, the out-of-plane behaviour of URM walls is described. Eventually, general methods for the analytical verification of the OOP behaviour are explained and compared.

Chapter 3: This chapter will describe the procedure to be followed in order to perform NLTH analyses in simplified single degree of freedom (SDOF) mass-spring systems. These will resemble the equivalent SDOF systems of the structures that will be investigated. The main deliverable of these analyses will be the Shape Factor Coefficient $C_i(T_p)$. The 1D models will be also expanded to two degree of freedom (2DOF) systems with the integration of a set of OOP walls in the models. Sensitivity studies of these OOP walls will take place and will aim to the comparison between the actual NLTH responses and the design responses. The latter will be based on the Shape Factor Coefficient $C_i(T_p)$ described in this research.

Chapter 4: A series of NLTH analyses will be performed in a 3D Model of a typical Dutch house. The Shape Factor Coefficient $C_i(T_p)$ obtained from the 1D Models will be validated from the NLTH results of the 3D Model. Furthermore the Height Coefficient C_{Hi} will be derived. Last but not least, sensitivity studies of OOP walls will be implemented once more for the same purposes as in the 1D Models.

Chapter 5: This chapter will present the overall conclusions of the master thesis along with the limitations of the research. Moreover, recommendations for future studies will be provided.

Chapter 2

Literature review

2.1 Unreinforced Masonry

Masonry is a heterogeneous composite material consisted of bricks and mortar. Mortar is holding the bricks together by forming vertical joints (head joints) and horizontal joints (bed joints). The performance of masonry is highly dependent on the properties of its components and the interaction between them through the brick-mortar interface. As a material, it presents different behaviour in different directions, thus it is anisotropic. However, if the structure of units and mortar is considered, masonry can be characterised as an orthotropic material with the main withstanding direction to be the compression perpendicular to the bed joints. In the Netherlands, Unreinforced Masonry (URM) is traditionally used for construction purposes.

2.1.1 Masonry unit behaviour

Masonry units (bricks) present a quasi-brittle behaviour. When loaded in tension, the unit behaves linearly until the peak load and then a softening behaviour is observed, as the force gradually decreases to zero. This softening behaviour is the result of the development of micro-cracks into macro-cracks which eventually become open cracks [2]. On the other hand, masonry unit loaded in compression presents similar behaviour to concrete, as masonry can withstand greater compressive stresses than tensile stresses. After the reach of the peak load, softening is again observed until the residual stress is reached due to the crushing of the unit.

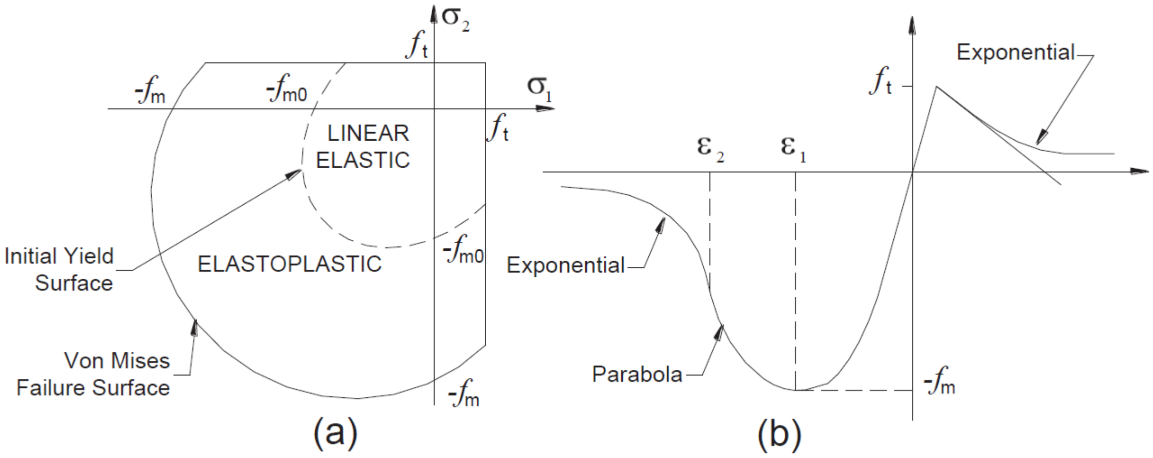

(a) (b)

Figure 2.1: Yield criterion (a) and typical stress-strain model (b) for a brick unit (Lotfi & Shing,1994).

2.1.2 Composite behaviour

It is difficult to predict the exact behaviour of masonry, as the interaction between its constituents is rather complex. The material properties can be defined from experimental tests on masonry specimens. Nevertheless, the variety of the properties of brick and mortar and the variation of loading orientation in masonry specimens creates a large number of test setups needed to define the constitutive relationships of masonry, thus it introduces scarcity to the results. In this section, the basic performance aspects of masonry will be presented based on several experiments.

Uniaxial compressive behaviour Figure 2.2 indicates a test setup for masonry specimens with relatively stiffer bricks and relatively softer mortar that were subjected to uniaxial compression perpendicular to the bed joint. Due to the deformation compatibility in the interface, mortar expanded laterally more compared to bricks. As a result, a bilateral tension coupled with axial compression appeared in bricks and a triaxial compression in mortar (Fig. 2.2b). This stress state led to the specimen failure owing to the vertical splitting cracks (Fig. 2.3c and d) in bricks (McNary and Abrams 1985, Atkinson and Noland 1983, Drysdale et al. 1994) [17]. Besides the uniaxial compression tests perpendicular to the bed joints, A. W. Page [30] also performed uniaxial compression tests where the bed-joint angle with respect to the load direction was different than 90°. In these tests, different failure modes were observed: the occurance of cracking and sliding in the bed and/or the head joints or even the combination of cracking in both brick and joint (figure 2.4).

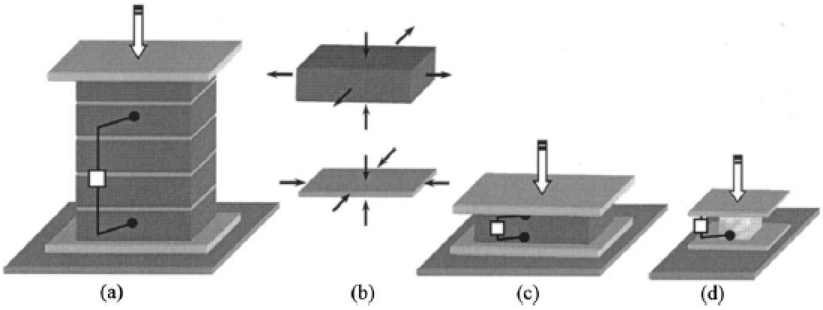

Figure 2.2: Test setup for different specimens : (a) masonry prism, (b) triaxial state of stress at the interface of brick and mortar, (c) brick unit and (d) mortar cube [17].

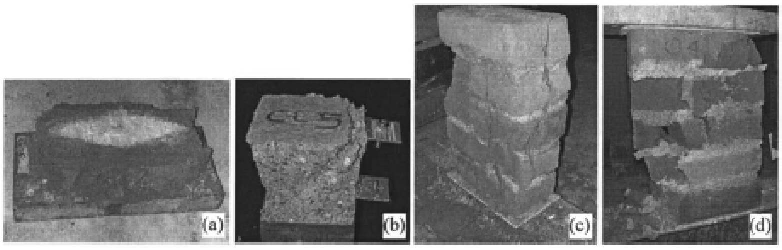

Figure 2.3: Typical failure modes of: (a) brick units, (b) mortar cubes and (c), (d) masonry prisms [17].

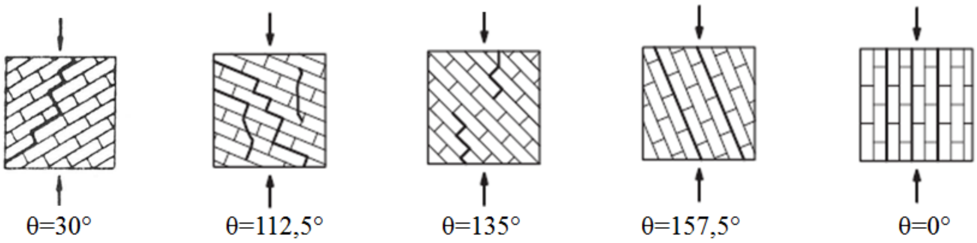

Figure 2.4: Failure modes for different bed joint-load direction angles [30].

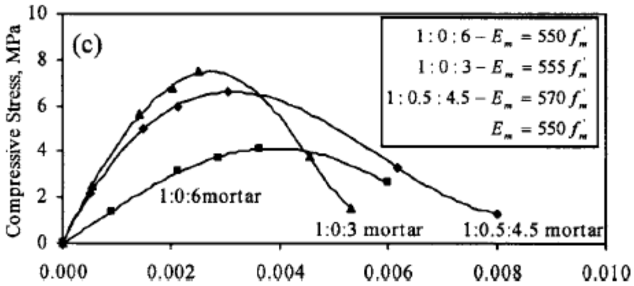

Figure 2.5: Compressive stress-strain curves for masonry prisms [17].

Furthermore, uniaxial compression experiments were performed for masonry prisms with three different grades of mortar (cement:lime:sand): weak (1:0:6) , intermediate (1:0.5:4.5) and strong (1:0:3) (figure 2.5). It was observed that masonry specimens with weak mortar were weaker than the ones with the intermediate and strong mortar. Additionally, the behaviour of masonry specimens with intermediate and strong mortar was similar in the linear range, while the prisms with intermediate mortars that contain lime presented larger ductility compared to the prisms with strong mortars. More specifically, in prisms with intermediate mortars, the compression stress f_m was 13% lower than the ones with strong mortars, however the ductility was about 50% more, resulting to an important improvement of the displacement capacity of masonry in compression without any significant reduction of the compressive strength. Hence the use of lime in mortars was judged beneficial.

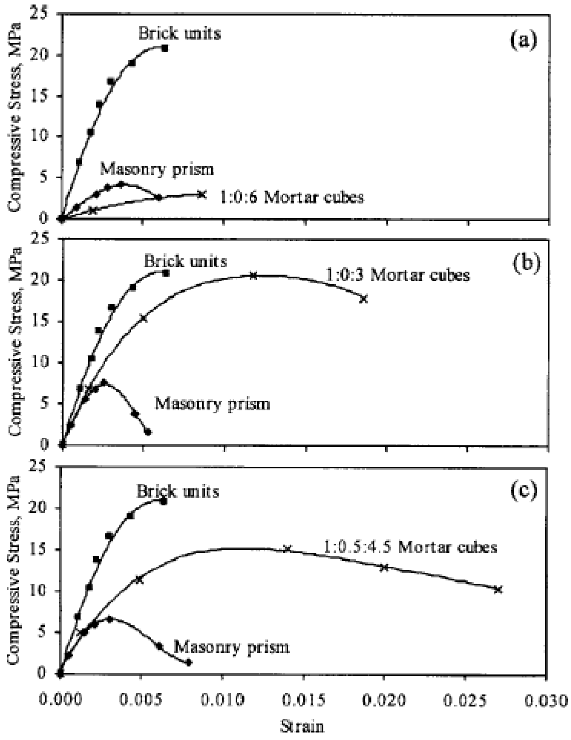

Figure 2.6: Comparison of stress-strain curves for brick units, mortar cubes and masonry specimens for (a) weak, (b) strong and (c) intermediate mortar [17].

Except from experimental tests in masonry specimens under uniaxial compression, tests were also implemented in mortar cubes and brick units (figures 2.2c,d and 2.3a,b). The stress-strain curves of masonry prisms with weak mortar fall in between of the stress-strain curves of brick units and weak mortar. On the contrary, for masonry with strong or intermediate mortar, the stress-strain curves are below the stress-strain curves of mortar cubes and brick units (figure 2.6). Therefore it should not be believed that the behaviour of masonry is in between the behaviours of its components. The last two experiments indicate the large scatter that different material properties of brick units and mortar can also produce in the experimental results and the difficulty to predict an exact behaviour for masonry.

Tensile behaviour To determine the tensile behaviour of masonry specimens, a series of uniaxial tension tests should be performed. Generally, the interface between a brick unit and a mortar joint is the weak link in masonry, when the specimen is subjected to pure tension. The tensile strength at the interface in this case will be determined by the chemical bond between mortar and brick units. This bond depends on the absorption rate of brick units. High absorption rate decreases the strength of the bond [24].

Shear behaviour Maximum shear resistance, like tensile resistance, was found highly dependent on the quality of the brick-mortar interface. This quality is defined by the mortar type, mortar water/cement ratio and workmanship (Atkinson et al, 1989) [24]. Moreover, Atkinson stated that shear resistance depends on normal stresses, as the result of shear with low normal stresses is the contraction and dilatation of the mortar, while in medium and high levels of normal stress, this effect is negligible. Plot of shear load with respect to shear strain from direct shear test experiments by Atkinson is presented below (figure 2.7). A sudden increase to peak stress, sudden decrease to residual stress and a secondary peak of the lateral load due to low normal stresses in the specimen are observed in the first load cycle. After the first cycle, the residual stress remained stable.

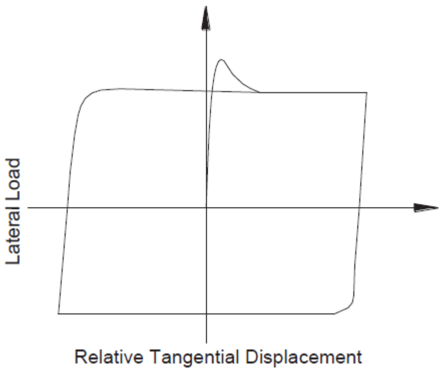

Figure 2.7: Shear stress-strain relationship [24].

Biaxial behaviour In reality, masonry is a material that exhibits biaxial stresses, when subjected to in-plane loading. Thus, in order to accurately define failure, one should investigate its biaxial behaviour. A.W. Page [30] examined the biaxial compression and biaxial compression-tension behaviour of masonry and his outcomes are presented below. Regarding the biaxial compression, the bed-joint direction had no impact on most of the principal stress ratios (figure 2.8). The failure mode for this stress state was splitting in a plane parallel to the free surface of the specimen (figure 2.3 c,d). On the contrary, for biaxial tension-compression, the bed joint direction played a vital role for all principal stress ratios, since the planes normal to the free surface of the specimen were always failing (figure 2.9).

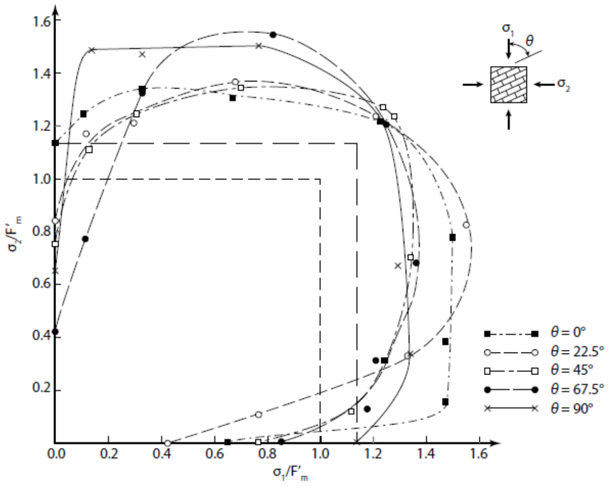

Figure 2.8: Biaxial compression projected onto $\sigma_1 - \sigma_2$ plane [30].

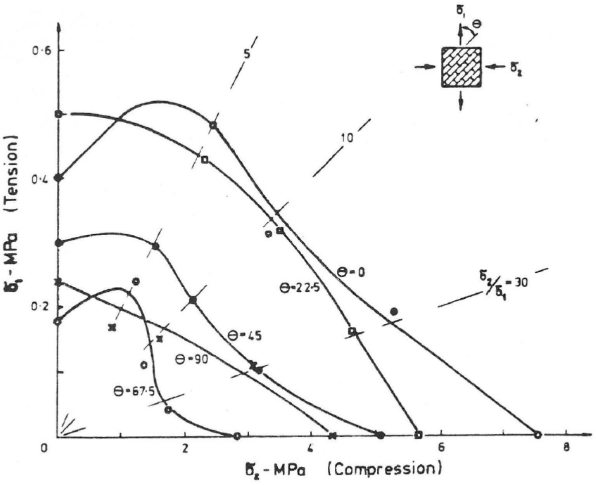

Figure 2.9: Biaxial tension-compression projected onto $\sigma_1 - \sigma_2$ plane [30].

2.2 Failure Mechanisms

Failure mechanisms observed in URM buildings are classified as local or global response mechanisms. In-plane failure mechanisms of URM walls along with failure or lack of anchorage between floors or roof and URM walls can be decisive for the overall stability of the structure, thus they are considered global mechanisms. Local failure mechanisms are connected with the verification of structural or non-structural parts. The out-of-plane failure mechanism of URM walls belongs to this category.

Generally, the common failure modes related to URM buildings are [6]:

- Lack of anchorage
- Anchor failure
- In-plane failure
- Out-of-plane failure
- Combined in-plane and out-of-plane effects
- Diaphragm-related failure

In-plane failure mechanisms are considered as global response mechanisms. Those are (a) Diagonal Tension failure, Bed Joint Sliding failure (b) and (c), Flexural or Rocking failure (d), and Toe Crushing (e) (figure 2.10). The failure mechanism with the most brittle behaviour is Diagonal Tension. It occurs when the shear strength of mortar is greater than the splitting strength of brick units and also when the axial stresses in the wall are significantly high. If the splitting strength of brick units is higher than the strength of mortar, Bed Joint Sliding failure is more likely to occur. This is a shear dominated failure with semi-brittle behaviour, providing larger deformation capacity compared to Diagonal Tension failure. Shear in-plane failure modes are more common for URM walls. On the other hand, Flexural or Rocking failure is a ductile failure mode providing significant deformation capacity compared to shear failure modes. It is observed in masonry piers with high aspect ratio (H/L).

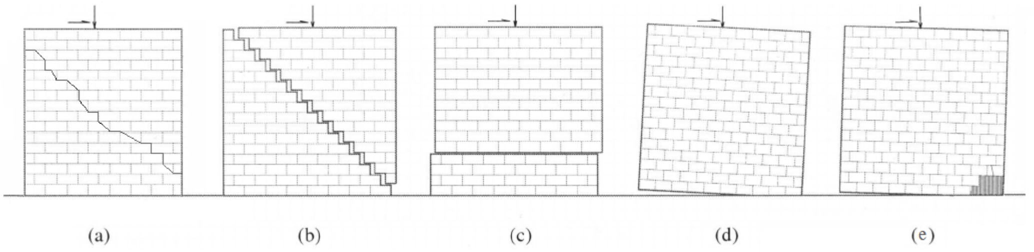

Figure 2.10: In-plane failure modes of URM walls [13].

Out-of-plane failure mechanisms are considered as local mechanisms. These failure modes describe masonry panels bending in the lateral direction, “out of their plane”. The failure forms in this case can be one-way bending, two way bending or even more complex forms, depending on the boundary conditions and the constraints along the edges of the masonry panels (figure 2.11). This thesis will be focused on the one-way bending URM walls. Extensive reference to the rocking mechanism of OOP behaviour will be impelmented in sections 2.5 and 2.6.

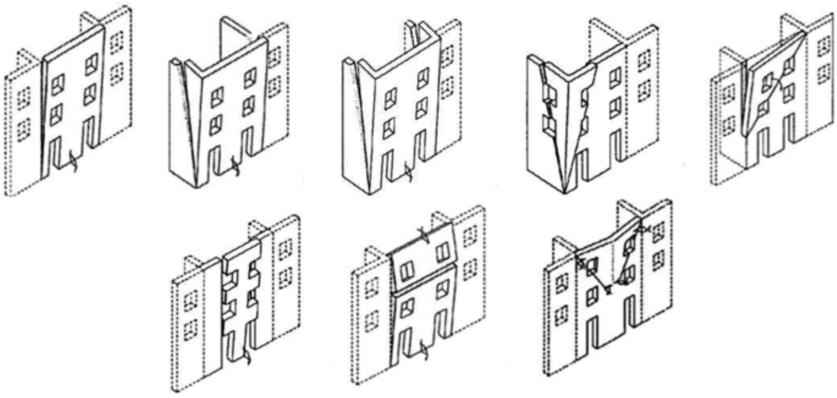

Figure 2.11: Out-of-plane failure modes of URM walls (D’Ayala & Speranza, 2003).

2.3 Hysteresis of structural components

The hysteresis profile of the structural components (i.e walls and piers) affect the behaviour of the structure as a whole under cyclic loading. Different experimental tests on masonry walls subjected to cyclic in-plane and out-of-plane loads indicated degradation of stiffness and strength due to cracking. As the load direction changes in a hysteresis loop, potential closing of cracks can lead to recovery of stiffness. However, this is not always the case, as permanent deformation may occur. Another important aspect of the hysteresis profile is the indication of the dissipated energy. The latter is expressed by the area inside the hysteretic loop.

In figure 2.12 a hysteresis loop of an element is presented. In the elastic phase the initial stiffness k_o is indicated. After the point of cracking, stiffness k_p describes the element. In the unloading phase, the unloading stiffness k_u will be smaller than the initial stiffness due to cracking. When loading in the opposite direction, recovery of the stiffness is expected because of the closure of the existing cracks. As a result, stiffness k_1 will be equal to the stiffness k_o. In contrast, stiffness k_1 will be less than the initial stiffness k_o, if plastic deformation occurs in the first half cycle. In the next cycles, degradation of strength and stiffness will be observed due to the damage of loading in both directions.

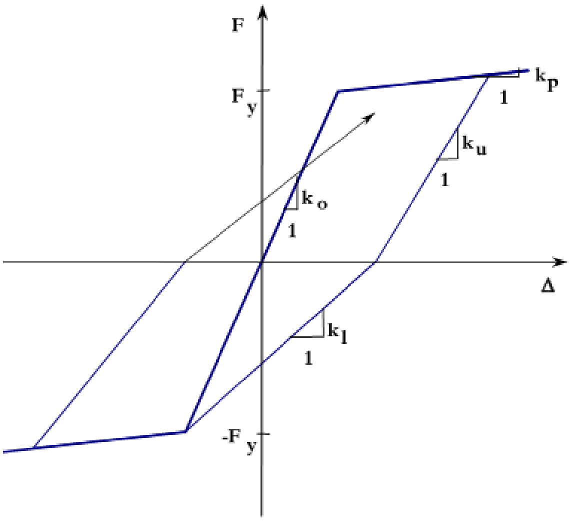

Figure 2.12: Hysteresis loop example [19].

Typical horizontal force-displacement loops for in-plane flexural and shear response of URM walls are presented in figures 2.13 and 2.14 respectively. According to Priestley M. J. N., Calvi G. M. and Kowalsky M. J. [35], large displacement capacity without significant stength degradation can be observed in the hysteresis loop for the flexural response, although with low energy dissipation. For the shear response, opposite observations hold, as it is described by smaller displacement capacity with significant strength and stiffness deterioration and higher energy dissipation.

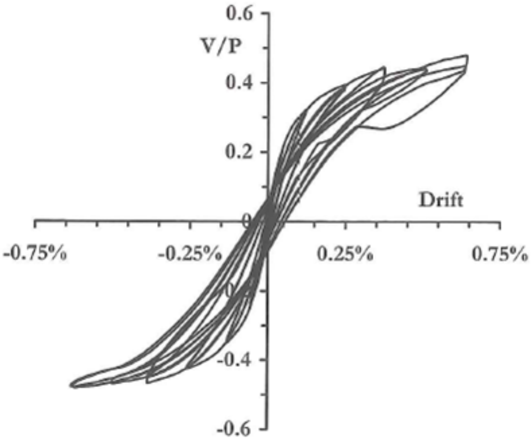

Figure 2.13: Typical hysteretic loop for flexural response [35].

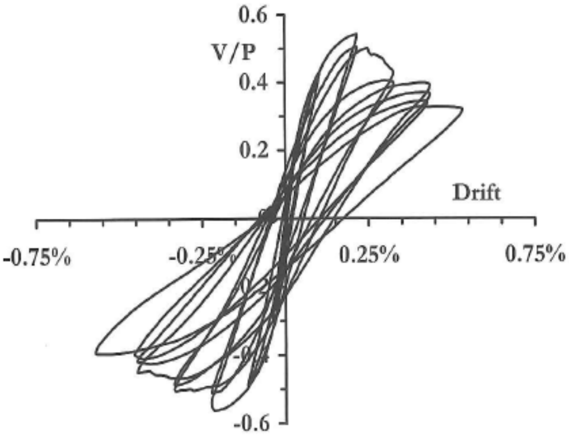

Figure 2.14: Typical hysteretic loop for shear response [35].

For the hysteresis response of one-way spanning URM walls acting out-of-plane, reference is made to the results of relevant experimental tests implemented at the Delft University of Technology [22]. Quasi-static cyclic tests were performed to two calcium-silicate wall specimens, COMP-0b (figure 2.15) and COMP-7 (figure 2.16). The dimensions of the walls were the same, however the support conditions on the wall boundaries were hinged for the former and clamped for the latter. In the elastic phase higher lateral resistance and stiffness was noticed in specimen COMP-7 due to the higher rotational stiffness of the supports. In the post-peak phase significant stiffness and strength reduction holds for both specimens. In addition, it is observed that the hysteretic cycles are narrow in both cases, thus the energy dissipation is rather low for the one-way spanning specimens.

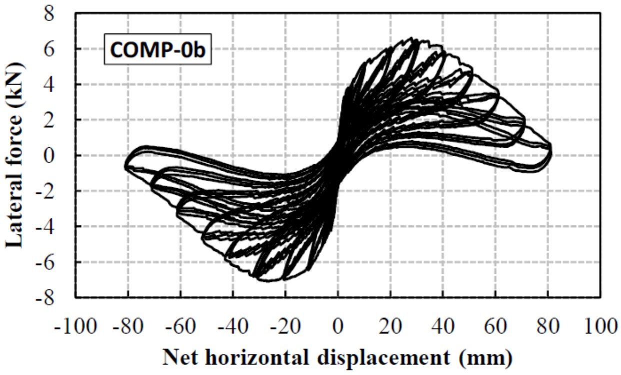

Figure 2.15: Hysteresis loop of specimen COMP-0b [22].

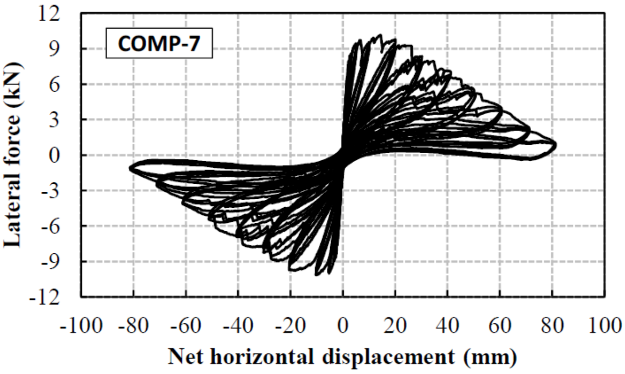

Figure 2.16: Hysteresis loop of specimen COMP-7 [22].

2.4 Strength and displacement verification approaches

For several years, the design and assessment of structures is performed with force-based approaches. The philosophy describing these procedures is based on the statement that the design forces acting on a structural element should not exceed its resistance capacity ($E_d \leqslant R_d$). In other words, implementing force-based approaches leads to elastic designs. The intial stiffness of the material is considered and the post-yielding behaviour of the element is not examined. This could be appropriate for materials with brittle behaviour, however this is not the case for materials that present ductility and energy dissipation. In order to integrate ductility to force-based procedures, reduction factors respective to different ductility levels are introduced to the elastic response suggesting to the reduction of the elastic forces.

Particularly in Earthquake Engineering, Eurocode 8 [25] proposes the use of the behaviour factor q to reduce the elastic response spectrum. The value of factor q depends on the type of the lateral system that is going to withstand the seismic forces and is derived from experiments. However, this methodology is not always accurate since ductility depends, besides on the structural type, also on the structural geometry and in many cases, iterations in the dimensioning of the lateral system are required to define the appropriate q factor for a certain ductility level. Since ductility is defined as the ratio of the maximum displacement or rotation over the yield displacement or rotation, it may be more suitable to consider checks based on displacement criteria in order to take into account the inelastic response.

The design and assessment of structures with the aim of satisfying a specific displacement performance limit can be executed using displacement-based approaches. Priestley (Priestley et al., 1993) introduced for the first time a displacement-based approach, the “Direct Displacement Based Design” or “DDBD”. This method replaces the structure with an equivalent linear system described by a secant stiffness K_e at a maximum displacement Δ_d (figure 2.17) and by an equivalent viscous damping which is equal to the summation of the elastic damping and the hysteretic energy dissipated during the inelastic response. The major advantage of this procedure is that it accounts for the inelastic behaviour of a structural element, thus for the inelastic displacement capacity of this element.

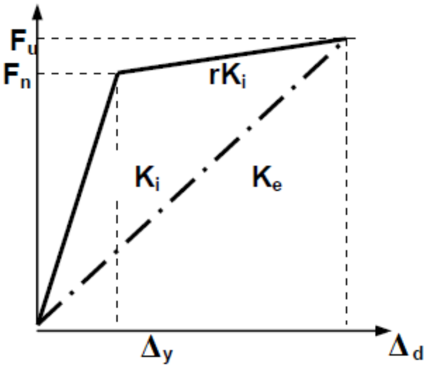

Figure 2.17: Secant stiffness K_e and maximum dispacement Δ_d [7].

2.5 Out-of-plane behaviour of one-way vertically-spanning walls

The most common method to investigate out-of-plane behaviour of one-way spanning URM walls is the “Nonlinear Kinematic Analysis” (NLKA). This is a displacement-based inelastic method that takes into account both the elastic and nonlinear behaviour of the face-loaded URM walls and actually regards OOP behaviour as a stability problem. According to this approach, two rigid bodies are considered bending out of their planes (figure 2.18) with the assumption that the major crack will appear in the mid-height of the wall. The assumption of the rigidity, meaning that no tensile strength and infinite compressive strength governs the material, is not always correct, although the errors introduced by the resulting approximations are not significant [28]. NLKA method is based on the principle of virtual work. The failure mechanism of the wall should be known beforehand and is dependent on the support conditions and the geometry of the wall. Combining the nonlinear geometric effects with the inherent nonlinear behaviour of unreinforced masonry as a material, one can state that out-of-plane behaviour of URM walls is a highly nonlinear phenomenon and thus complex to investigate.

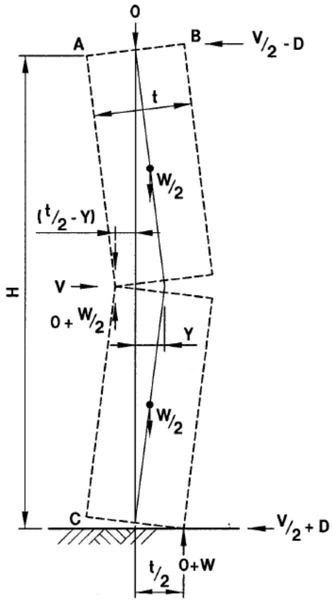

Figure 2.18: One-way bending of URM wall. Rigid bodies assumption [4].

2.5.1 Post-cracked behaviour

Doherty (2000) studied the post-cracked behaviour of face-loaded URM walls. After the formation of the hinges at the top, bottom and mid-height of the wall, which result to two rigid bodies acting out-of-plane, he stated that the behaviour of the wall depends on the interaction of gravity restoring moments, the movement of vertical reactions and the P-Δ overturning moments. When the P-Δ effects exceed the gravity restoring moments (figure 2.19, point of “Peak rigid resistance threshold” force), negative stiffness $K_e(1)$ governs the system. Instability occurs ($\Delta_{instability}$) when the vertical force above the mid-height crack moves outside of the wall thickness.

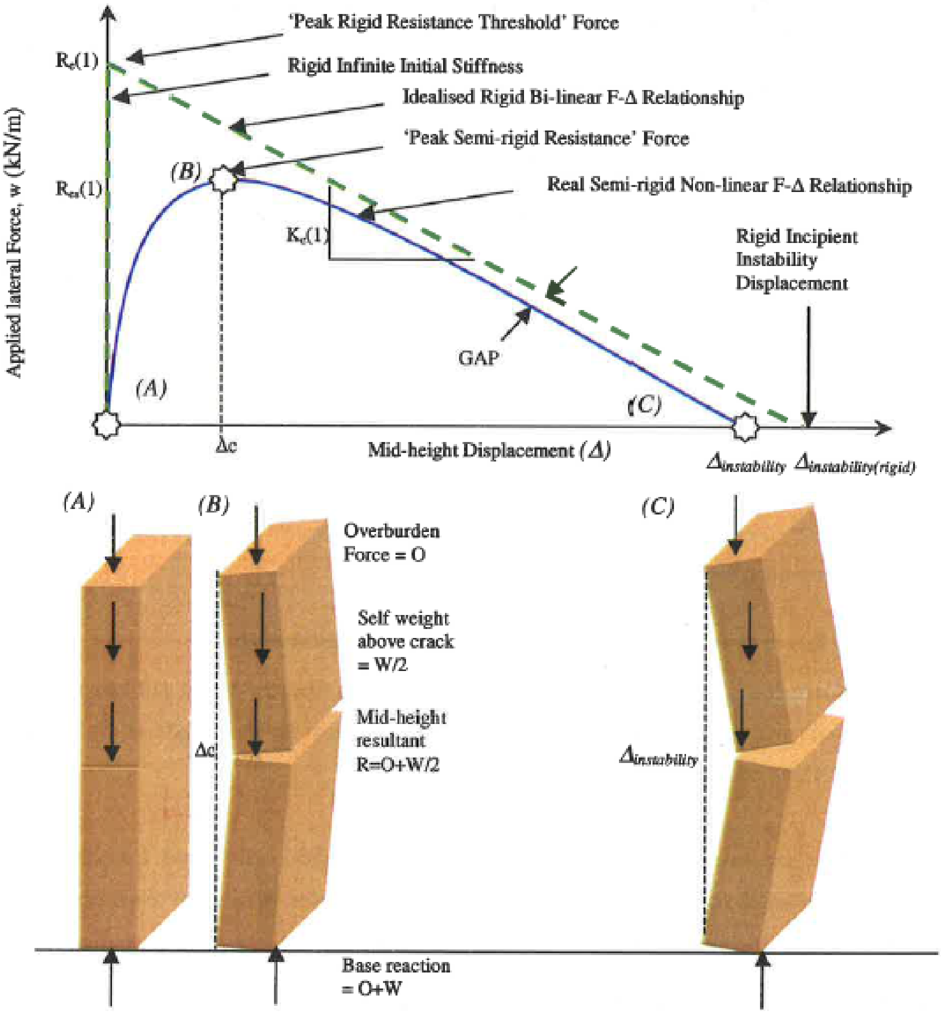
'Peak Rigid Resistance Threshold' Force
Rigid Infinite Initial Stiffness
Idealised Rigid Bi-linear F-Δ Relationship
'Peak Semi-rigid Resistance' Force
Real Semi-rigid Non-linear F-Δ Relationship
Rigid Incipient Instability Displacement
GAP
R_e(1)
R_es(1)
K_e(1)
Applied lateral Force, w (kN/m)
(A)
(B)
(C)
Δc
Mid-height Displacement (Δ)
Δinstability
Δinstability(rigid)
(A)
(B)
(C)
Overburden Force = O
Self weight above crack = W/2
Mid-height resultant R=O+W/2
Δc
Δinstability
Base reaction = O+W

Figure 2.19: Real semi-rigid nonlinear capacity curve [10].

In reality, URM walls are not characterised by the idealised rigid body theory, as the two free bodies do not behave as infinitely rigid ones. As a consequence, the bi-linear capacity curve of the URM wall is based on the simplified case. Basically, as the lateral displacement in the mid-height crack increases, the position of the vertical reaction forces move from the centerline of the wall to the extreme compressive faces, meaning that the gravitational restoring moments increase due to the increase of the level arm. At the point (B) of figure 2.19, which is respective to a displacement Δ_c, the effects of restoring moments and P-Δ cancel each other out and afterwards, as P-Δ effects take over, negative stiffness is observed. The real behaviour of the rocking mechanism matches then the behaviour of the bi-linear curve. Since the lateral stiffness of the rocking mechanism is a function of the displacement, the frequency-displacement relationship is also nonlinear.

Doherty also tried to investigate more in detail the semi-rigid behaviour of the rocking walls. He concluded that the threshold resistance in the bi-linear curve is reduced significantly to a “force plateau”, as it is shown in figure 2.20. The F-Δ curve deviates significantly from the bi-linear curve introduced for the rigid masonry blocks and it is basically a tri-linear curve. This is due to the nonlinear deformations that occur in the mortar joint at the pivot joints [11]. In the case of large displacements in the mid-height of the wall, there is little discrepancy from the bilinear curve. This tri-linear curve was found to describe effectively the experimental results of Doherty.

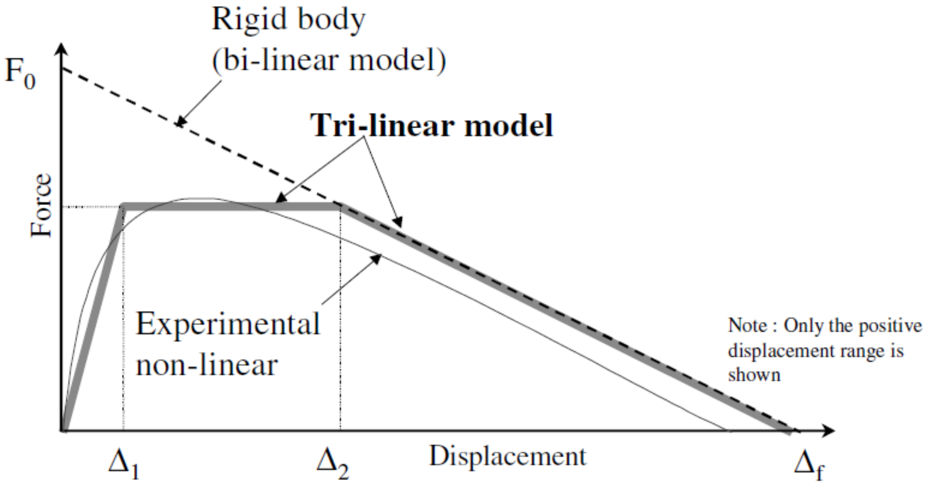

Figure 2.20: Force-displacement relationship of deformable URM walls [11].

Aiming to simplify the displacement-based analysis procedure for highly nonlinear systems, Doherty used the “substitute structure” methodology (Shibata & Sozen, 1976). According to this method, the real structure is substituted with a linear elastic SDOF system. The stiffness and damping properties of this system are determined in order the real structure and the equivalent one to reach the failure displacement under the same applied excitation. To test the effectiveness of the proposed analysis, a series of NLTH analyses were performed in different wall configurations and the results were compared with the respective ones from shaking table experiments [10]. The method was found consistent, as the effective secant stiffness K_{s-eff} described by Doherty for the substitute structure matched the values of K_{eff} derived from the NLTH analyses.

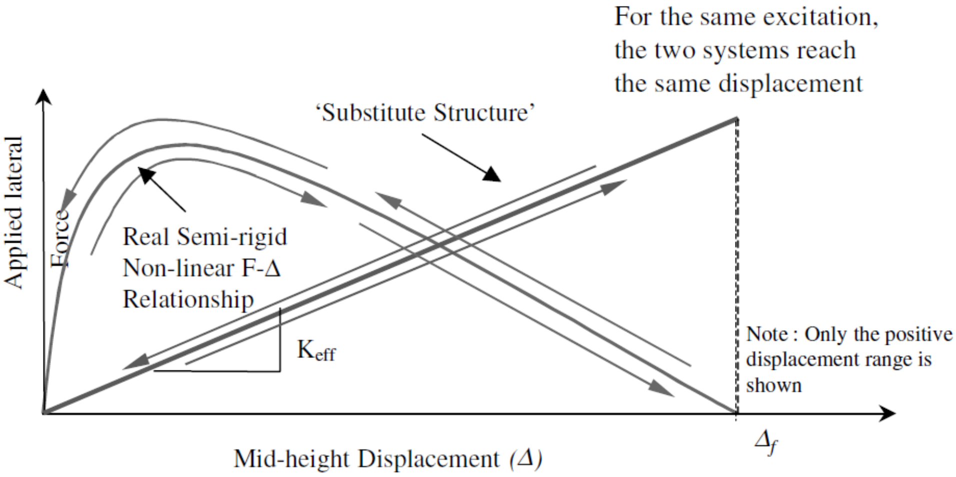

Figure 2.21: Characterisation of a representative stiffness K_{eff} for the “substitute structure” [11].

2.5.2 Nonlinear damping

Damping has an influence in the description of the rocking mechanism of the out-of-plane URM walls. In most of the physical problems, damping is characterised as an equivalent damping force with a similar decay rate under free vibration conditions due to its complex nature. Alternatively, it can be expressed by the Rayleigh damping, which is a linear combination of mass and stiffness proportional damping. Doherty compared the experimental results of his study with the Rayleigh damping and found that Rayleigh damping can describe the real nonlinear damping of the rocking mechanism of OOP walls [10]. Figure 2.22 indicates the Rayleigh damping as a reasonable lower boundary of the experimental equivalent viscous damping for masonry walls with thickness equal to 50 millimeters and with no applied overburden force.

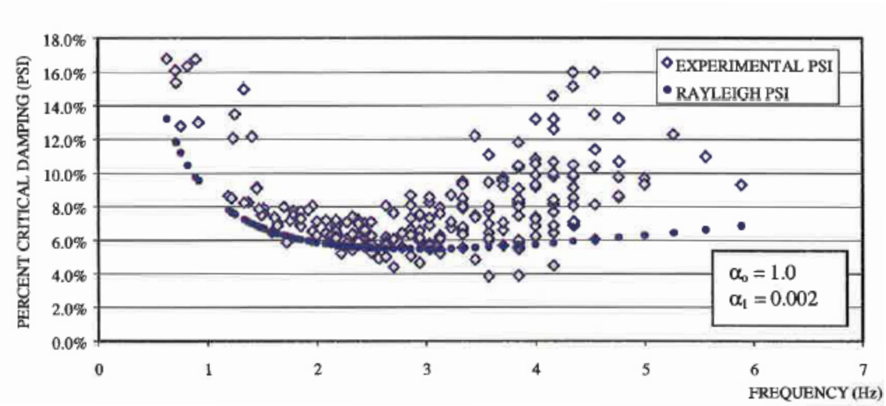

Figure 2.22: Experimental damping and Rayleigh damping - 50 mm Wall, No Overburden [10].

In a system with linear viscous damping, every hysteretic cycle provides the same viscous damping ratio. In reality, the equivalent viscous damping is frequency dependent (figure 2.22). Thus, an average or a lower bound proportional damping coefficient can be used as a simplified manner. For more precise calculations of the equivalent damping per hysteretic cycle, Doherty states that an iterative approach should be included in the NLTH analyses (figure 2.23) [10]. According to this method, the proportional damping is assumed for each half cycle of the response and the resulting proportional damping is calculated. If this does not match with the estimated value, new iteration should be implemented with the consideration of new initial condition. The only disadvantage of this method is the amount of time needed for the computations.

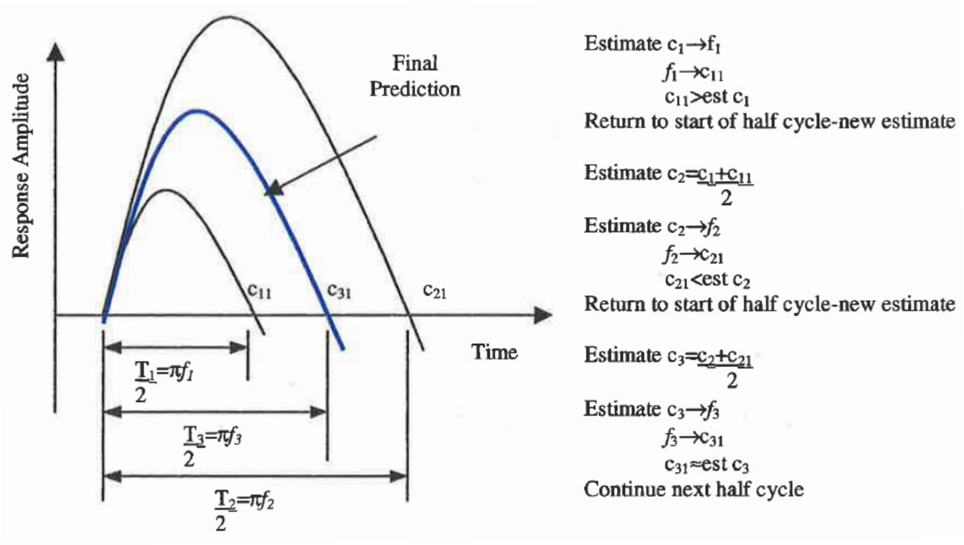
Response Amplitude
Final Prediction
c_{11}
c_{31}
c_{21}
Time
$\frac{T_1}{2}=\pi f_1$
$\frac{T_3}{2}=\pi f_3$
$\frac{T_2}{2}=\pi f_2$
Estimate $c_1 \rightarrow f_1$
$f_1 \rightarrow c_{11}$
$c_{11} > \text{est } c_1$
Return to start of half cycle-new estimate
Estimate $c_2 = \frac{c_1 + c_{11}}{2}$
Estimate $c_2 \rightarrow f_2$
$f_2 \rightarrow c_{21}$
$c_{21} < \text{est } c_2$
Return to start of half cycle-new estimate
Estimate $c_3 = \frac{c_2 + c_{21}}{2}$
Estimate $c_3 \rightarrow f_3$
$f_3 \rightarrow c_{31}$
$c_{31} \approx \text{est } c_3$
Continue next half cycle

Figure 2.23: Iterative process for the definition of equivalent damping [10].

2.6 Analytical verifications of one-way vertically-spanning walls

Three major Norms that are used for the verification of one-way spanning URM walls acting out of their plane are explained below. These are the New Zealand code for Earthquake Engineering [28], the Dutch Draft NPR 9998:2017 Norm [12] and the Italian Code NTC [27].

2.6.1 NZSEE method

This Norm uses an inelastic displacement-based analysis for walls spanning vertically between supports. The wall is divided in two rigid blocks, as described in section 2.5. The position of the hinges on the wall supports mainly depends on the rigidity of the diaphragms on the top and bottom of the wall and the connection between them (figure 2.24). More specifically, e_p shows the eccentricity of the force of the upper storeys from the mass centroid of the upper part of the wall and the eccentricities e_b and e_t relate the mass centroids of the upper and lower part with the hinges forming at the mid-height and bottom level of the wall respectively (figure 2.25).

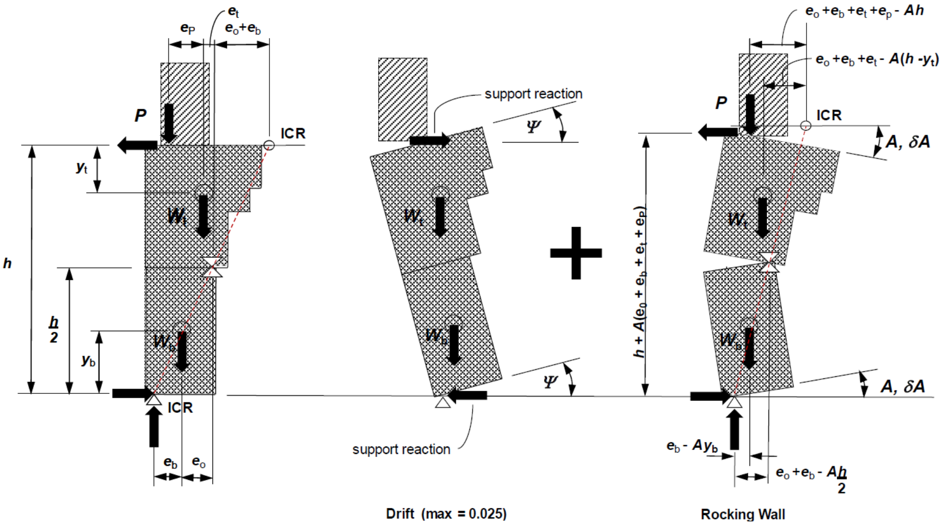

Figure 2.24: NLKA method scheme [28].

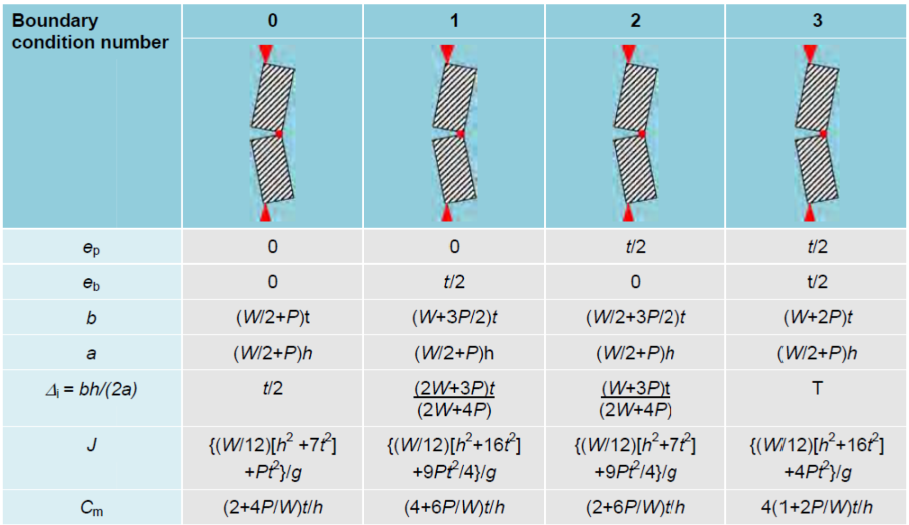

Boundary condition number	0	1	2	3
e_p	0	0	$t/2$	$t/2$
e_b	0	$t/2$	0	$t/2$
b	$(W/2+P)t$	$(W+3P/2)t$	$(W/2+3P/2)t$	$(W+2P)t$
a	$(W/2+P)h$	$(W/2+P)h$	$(W/2+P)h$	$(W/2+P)h$
$\Delta_i = bh/(2a)$	$t/2$	$\frac{(2W+3P)t}{(2W+4P)}$	$\frac{(W+3P)t}{(2W+4P)}$	T
J	$\{(W/12)[h^2+7t^2]+Pt^2\}/g$	$\{(W/12)[h^2+16t^2]+9Pt^2/4\}/g$	$\{(W/12)[h^2+7t^2]+9Pt^2/4\}/g$	$\{(W/12)[h^2+16t^2]+4Pt^2\}/g$
C_m	$(2+4P/W)t/h$	$(4+6P/W)t/h$	$(2+6P/W)t/h$	$4(1+2P/W)t/h$

Figure 2.25: Boundary conditions and eccentricities [28].

The instability mid-height deflection of the wall Δ_i is calculated by using the virtual work principle. The maximum deflection is then restricted to:

$$\Delta_m = 0.6 \cdot \Delta_i \tag{2.1}$$

Next step is the calculation of the effective period T_p of the wall corresponding to its “substitute structure” with secant stiffness K_{eff} (figure 2.21). Research indicates that the intersection point of the linearised curve of the “substitute structure” with the real semi-rigid curve is respective to a displacement:

$$\Delta_t = 0.6 \cdot \Delta_m = 0.36 \cdot \Delta_i \tag{2.2}$$

The effective period T_p is equal to:

$$T_p = 4.07 \cdot \sqrt{\frac{J}{\alpha}} \tag{2.3}$$

J is the rotational inertia of the masses related to the rigid bodies weights W_b and W_t of the out-of-plane wall and the overburden load P and is given in figure 2.25 for each boundary condition. Factor α can be found from the equation:

$$\alpha = W_b \cdot y_b + W_t \cdot (h - y_t) + P \cdot h \tag{2.4}$$

The displacement response Δ_{ph} is calculated as:

$$\Delta_{ph} = \gamma \cdot (T_p/2\pi)^2 \cdot C_p(T_p) \cdot R_p \cdot g \tag{2.5}$$

Participation factor γ represents the correlation of the displacements or forces between the “substitute structure” and the real out-of-plane rocking mechanism:

$$\gamma = \frac{(W_b \cdot y_b + W_t \cdot y_t) \cdot h}{2 \cdot J \cdot g} \tag{2.6}$$

Design seismic coefficient $C_p(T_p)$ specifies the accelaration demand for the rocking system and it is found as:

$$C_p(T_p) = C_i(T_p) \cdot C_{Hi} \cdot C_i(0) \tag{2.7}$$

Coefficient $C_i(0)$ is the Peak Ground Accelaration. Coefficient $C_i(T_p)$ is the “Parts Coefficient” and coefficient C_{Hi} is the “Height Coefficient”. As it was mentioned in section 1.2, the former indicates the interaction between the seismic responses of the structural parts and the building and the latter indicates how the peak ground accelaration amplifies through the height of the building (figure 2.26). These coefficients are also known as “filtering effects”. Last step is the displacement check between the seismic demand (Δ_{ph}) and the capacity of the wall (Δ_m):

$$\%NBS = 100 \cdot \Delta_m/\Delta_{ph} \tag{2.8}$$

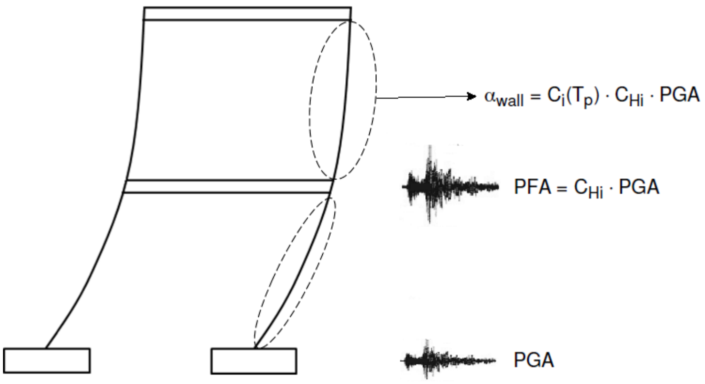

Figure 2.26: Parts and Height effects.

2.6.2 Draft NPR 9998:2017 method

Annex H of NPR Norm [12] provides a nonlinear kinematic analysis (NLKA) method for assessing face-loaded URM walls. It is stated that for the verification of local failure of face-loaded URM walls under seismic loads, a unity check should be performed:

$$\frac{S_{a;d}}{\xi_{SCC}} \leqslant 1 \tag{2.9}$$

where:

$S_{a;d}$	is the horizontal design seismic coefficient for the structural parts.
ξ_{SCC}	is the seismic capacity coefficient of the structural parts.

The design seismic coefficient is calculated as:

$$S_{a;d} = \alpha \cdot \frac{\gamma_a}{q_a} \cdot \left[\frac{3 \cdot \left(1 + \frac{z}{H}\right)}{1 + \left(1 - \frac{T_\alpha}{T_1}\right)^2} - 0.5 \right], \tag{2.10}$$

$$S_{a;d} \leqslant \alpha \cdot \frac{\gamma_a}{q_a} \tag{2.11}$$

where:

$T_a = \sqrt{\frac{0.28 \cdot h}{(1 + \frac{2 \cdot P}{W})}}$ for one-way spanning walls and gables and:

α	is the ratio of the design ground accelaration, $a_{g;d}$ to the accelaration gravity g.
γ_a	is the importance factor of the element and is equal to 1.
q_a	is the behaviour factor of the element and is equal to 1.
z	is the numeric value of the height of the centre of gravity of the wall.
H	is the numeric value of the height of the building above the foundation, in m.
h	is the numeric value of the height of the wall, in m.
T_a	is the numeric value of the fundamental period of the wall, in s.
T_1	is the numeric value of the fundamental period of the building using secant stiffness, in s.
t	is the numeric value of the thickness of the wall, in m.
P	is the numeric value of the total overburden acting on the top of the wall, in kN.
W	is the numeric value of the self-weight of the wall, in kN.

The derivation of the seismic capacity coefficient ξ_{SCC} is based on the NLKA method. For simpler calculation of the ξ_{SCC}, charts based on the respective charts of the NZSEE Norm are used. These charts essentially imprint the results of the NLKA method depending on the parameters: total overburden acting on the top of the wall P, self-weight of the wall W , height of the wall h, effective thickness of the wall t_{eff}, interstorey drift Ψ and eccentricities described in section 2.6.1. An example of this type of chart is presented in figure 2.27. The term BPR (Basic Performance Ratio) is the equivalent term of ξ_{SCC} in NZSEE Norm.

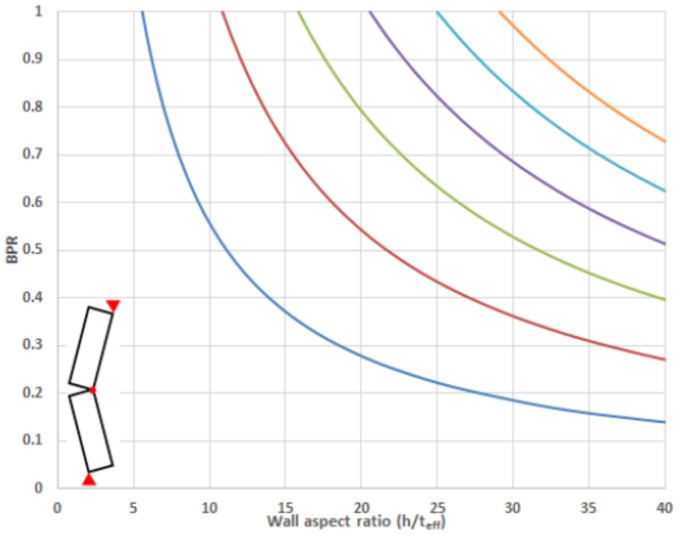

(d) $e_b=h_{eff}/2$; $e_p=-t_{eff}/2$

Figure 2.27: Chart for deriving capacity seismic coefficient ξ_{SCC} [12].

2.6.3 NTC method

Italian code NTC [27] uses the kinematic approach to describe the capacity of the face-loaded masonry walls. This capacity is characterised by the amplification parameter α, which is the ratio between the applied horizontal forces and the corresponding weights of the masses of the system and is represented as a function of the displacement d_k of a reference point (usually the mid-height of the wall). The capacity curve of the wall must be determined until instability occurs ($\alpha = 0$). This curve can be transformed into the capacity curve of an equivalent SDOF system. The displacement capacity of SDOF system will be compared with the displacement seismic demand. The NTC [27] procedure is summarised in the next steps:

1. Consideration of the structural part as a system of two rigid bodies using the NLKA method (see section 2.5). It is assumed zero tensile strength and infinite compressive strength for the masonry.
2. Evaluation of the horizontal multiplier of loads α_0, which initiates the rocking mechanism, by making use of the virtual work principle.
3. Evaluation of the horizontal multiplier of loads α as the displacement d_k of the control point increases.
4. Transformation of the capacity curve of the rocking mechanism in the capacity curve of the equivalent SDOF system.
5. Comparison of the displacement capacity of the SDOF system with the displacement demand.

The secant period of the equivalent SDOF system is determined as:

$$T_s = 2\pi\sqrt{\frac{d_s^*}{a_s^*}} \tag{2.12}$$

The instability displacement d_s^* is equal to the mininum value between the 40% of the ultimate displacement of the system and the displacements that are incompatible with the stability of local elements. Displacement d_s^* corresponds to “salvaguardia della vita” or SLV limit state according to NTC [27]. This limit state is respective to the “Significant Damage” (SD) limit state of Eurocode.

Step 5 of the procedure is described by the equation:

$$d_u^* \geq S_{De}(T_1) \cdot \psi(Z) \cdot \gamma \cdot \frac{\left(\frac{T_s}{T_1}\right)^2}{\sqrt{\left(1 - \frac{T_s}{T_1}\right)^2 + 0.02\frac{T_s}{T_1}}} \tag{2.13}$$

where:

S_{De}	is the elastic spectral displacement response of the structure in the first eigenmode, in m.
T_1	is the natural period of the structure, in s.
$\psi(Z)$	is the Height Coefficient.
γ	is the participation factor.
T_s	is the secant period of the part, in s.

2.6.4 Remarks on the above methods

NPR Norm presents similarities with the NZSEE Norm, as the latest version of the former is based on the latter. In addition, NTC Norm is characterised by similar procedures with NZSEE Norm. The similar characteristics of the three Norms are:

1. All Norms are based on the NLKA method. The wall consists of two rigid blocks and the formation of three hinges is considered.
2. All Norms consider the impact of the filtering effects on the respective design seismic coefficients. NZSEE implements that with the Parts Coefficient $C_i(T_p)$ and the Height Coefficient C_{Hi}, while NPR by considering the period of the structural part T_a and the ratio z/H. NTC Norm accounts for the filtering effects by considering the secant period of the part T_s and the Height Coefficient $\psi(Z)$.
3. The seismic capacity coefficient ξ_{SCC} of NPR is the equivalent term of Basic Performance Ratio (BPR) in the NZSEE Norm. The charts for the out-of-plane assessment of masonry walls in NPR are based on the methodology followed for the charts in NZSEE

However, discrepancies exist between the aforementioned methods. These are described below:

1. A basic difference lies in the validation checks that the Norms are using. NZSEE Norm, when the simplified charts of the BPR ratio are not used, and NTC Norm describe the equivalent SDOF system with a detailed procedure and the final check describes the comparison between the displacement capacity of this system and the displacement seismic demand. NPR Norm uses charts to derive the seismic demand ξ_{SCC} and the final check is between the design seismic coefficient and the seismic demand ξ_{SCC}.

2. In addition, NTC Norm validation is based on the SLV or Significant Damage limit state which is respective to a threshold displacement equal to 40% of the maximum displacement. The same holds for the NZSEE Norm. On the contrary, Draft NPR Norm validations are based on the Near Collapse limit state, which considers the threshold displacement as the 60% of the maximum displacement.

Regarding the respective design seismic coefficient, NZSEE Norm defined the filtering effects based on NLTH analyses in Steel and Concrete buildings with different typologies, taking into consideration the characteristics of the New Zealand's seismicity [39]. In contrast, NPR Norm uses the design seismic coefficient of Eurocode 8 (section 4.3.5.2 of NEN-EN 1998-1), which is related to force-based approaches and indicates the seismic demand for structural elements that are subjected to tectonic earthquakes. Consequently, it can not describe the nature of the induced earthquakes in the Groningen Province. Therefore, a similar procedure to the one performed for the NZSEE Norm is judged necessary for the NPR Norm, suggesting to the exact description of the design seismic coefficient for the Groningen Case.

Chapter 3

1D Models

3.1 Introduction

For the simplified 1D models, the examined structures are considered as equivalent mass-spring single degree of freedom (SDOF) systems. The transformation of a multi degree of freedom system into an equivalent single degree of freedom system is a standard procedure described in Eurocode 8 [25], as well as in Draft NPR 9998:2017 [12]. For the determination of the equivalent substitute structure, the mass m_i and the normalised displacement ϕ_i in the i^{th} level of the initial structure are taken into consideration. The forces or displacements Q of the structure are related to the forces or displacements Q^* of the equivalent SDOF system with the following equation:

$$Q = \Gamma \cdot Q^* \tag{3.1}$$

where:

Γ is the participation factor defined as:

$$\Gamma = \frac{m^*}{\Sigma m_i \cdot \phi_i} \tag{3.2}$$

m^* is the mass of the equivalent SDOF system and is obtained as:

$$m^* = m_i \cdot \phi_i \tag{3.3}$$

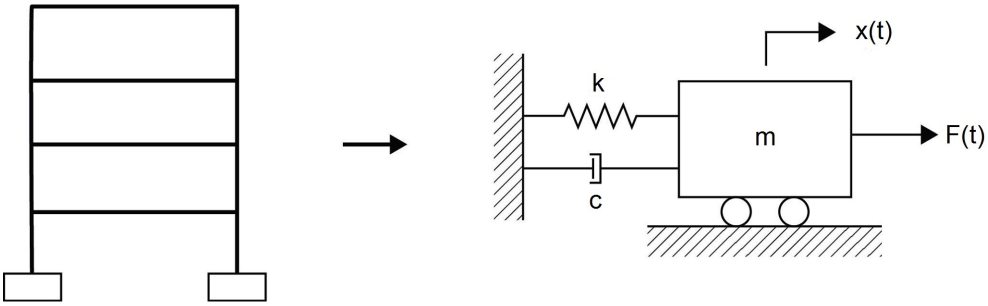

Figure 3.1: Equivalent single degree of freedom system.

In section 3.2, the considered typologies are presented and the characteristics of the equivalent SDOF systems are provided.

3.2 Typologies

Seven representative typologies are considered for the NLTH analyses. These cover the spectrum of the terraced and detached houses observed in the Groningen Province. The characteristics of each typology were provided from in-house studies of BAM Advies and Engineering. More specifically, the capacity curves of the respective equivalent SDOF systems were provided for the X and Y direction in terms of yield force F_y^*, yield displacement d_y^* and maximum displacement d_m^*. Furthermore, the SDOF characteristics were given. These are the elastic period T^*, the equivalent mass m^*, and the participation factor Γ. The information describing the equivalent SDOF systems are provided in the tables 3.1 and 3.2 together with the type of typology, the number of storeys and the type of floor.

Table 3.1: Information of SDOF systems for the direction X.

Direction X									
Typology No.	Typology Type	Storeys	Floor Type	T^* [sec]	m^* [kg]	F_y^* [kN]	d_y^* [mm]	d_m^* [mm]	Γ
1	terraced	2	concret slab	0.734	59776	44.5	10.2	29.4	1.24
2	terraced	2	“nehobo” floor	0.374	66144	35.4	1.9	37.7	1.1
3	detached	1	concrete slab	0.226	63018	62.7	1.3	18.2	1.19
4	detached	1	concrete slab	0.195	66597	73.6	1.1	19	1.07
5	terraced	2	timber diaphragm	0.548	49563	27.1	4.2	30.3	1.18
6	detached	1	timber diaphragm	0.142	104532	180.7	0.9	11.5	0.99
7	detached	1	timber diaphragm	0.112	75350	110.8	0.5	8.5	0.85

Table 3.2: Information of SDOF systems for the direction Y.

Direction Y									
Typology No.	Typology Type	Storeys	Floor Type	T^* [sec]	m* [kg]	F_y^* [kN]	d_y^* [mm]	d_m^* [mm]	Γ
1	terraced	2	concret slab	0.123	62392	260.6	1.6	13	1.18
2	terraced	2	“nehobo” floor	0.111	58782	334.3	1.8	8.8	1.06
3	detached	1	concrete slab	0.085	74597	429.9	1.1	10	0.94
4	detached	1	concrete slab	0.099	74585	284.3	0.9	10.5	1
5	terraced	2	timber diaphragm	0.088	42893	231	1.1	7.5	1.11
6	detached	1	timber diaphragm	0.088	104532	406.2	0.8	11.9	0.96
7	detached	1	timber diaphragm	0.118	75350	342.2	1.6	21.9	0.83

Direction X is the weak direction for all the typologies. A combination of piers, spandrels and wide openings are existing in that direction and determine a rather flexible in-plane response with large drifts and nonlinear behaviour of the structure. Direction Y is significantly stiffer owing to the large shear walls. This direction is characterised by small drifts, high shear capacity and a rather elastic behaviour throughout a seismic excitation. Comparative graphs for the capacity curves of all the typologies per direction are depicted in figures 3.2 and 3.3. Moreover, drawings of the typologies along with the capacity curves in both directions are provided in figures 3.4 to 3.9.

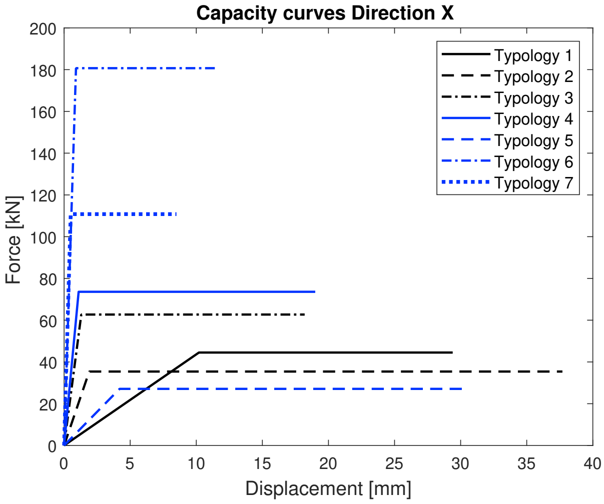

Figure 3.2: Capacity curves in direction X.

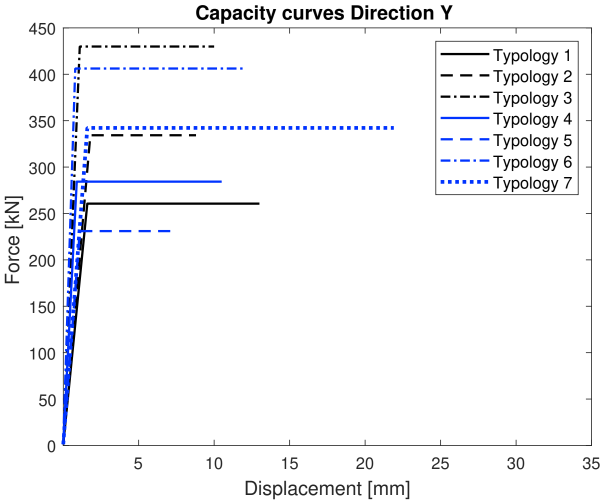

Figure 3.3: Capacity curves in direction Y.

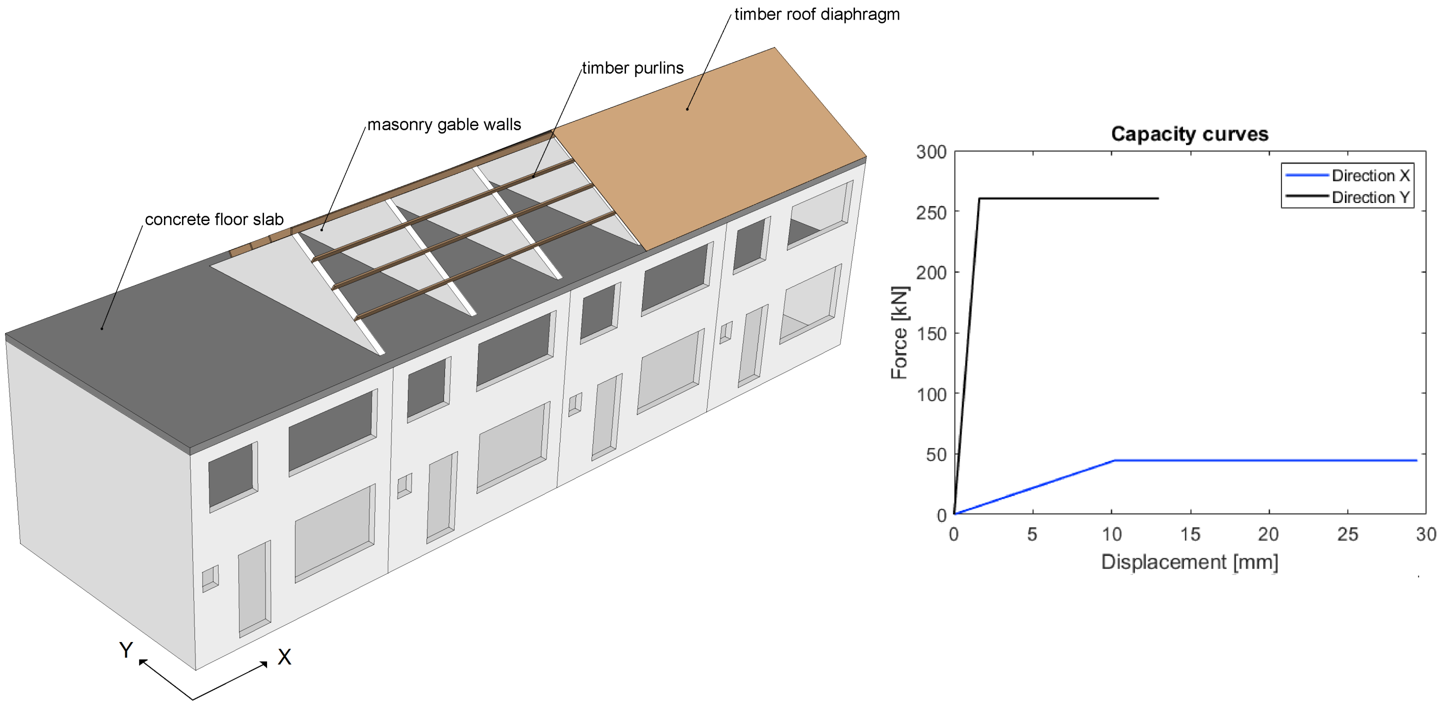
timber roof diaphragm
timber purlins
masonry gable walls
concrete floor slab
Y
X
Capacity curves
Direction X
Direction Y
Force [kN]
300
250
200
150
100
50
0
0
5
10
15
20
25
30
Displacement [mm]

Figure 3.4: Drawing and capacity curves of Typology 1.

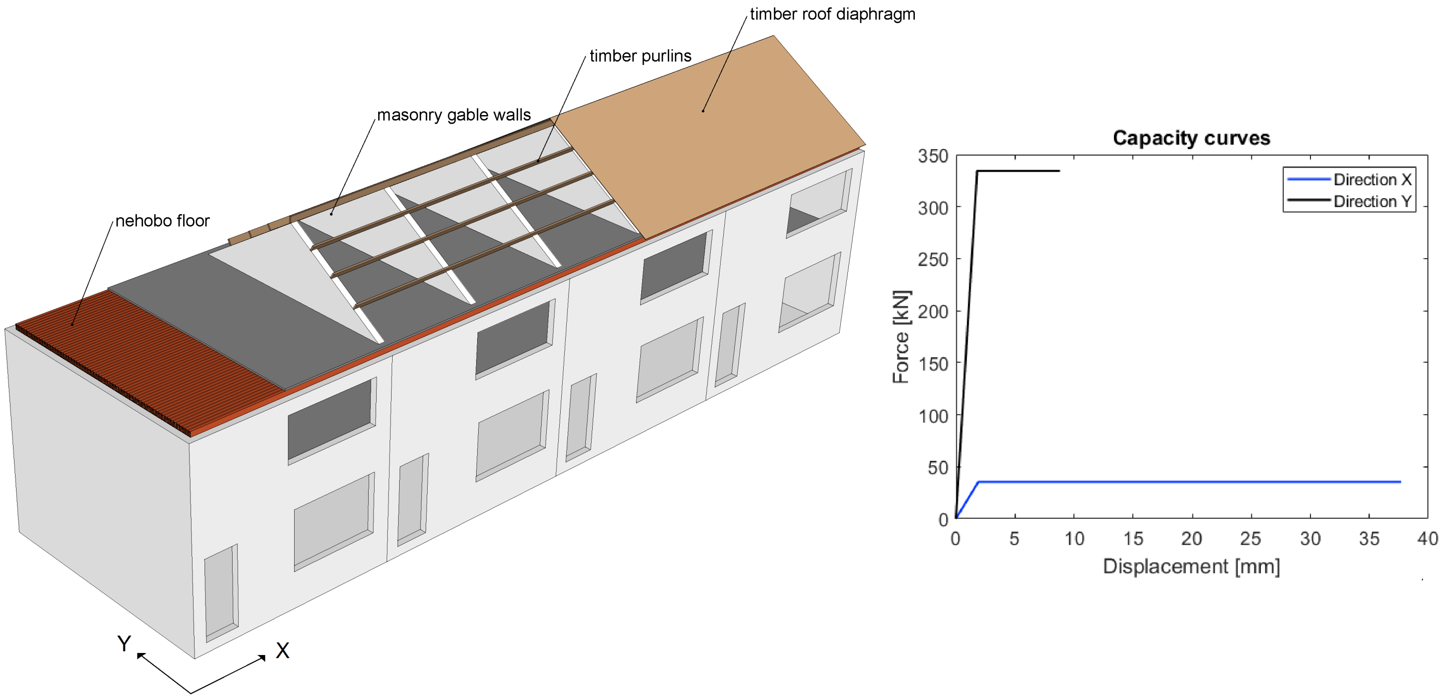
timber roof diaphragm
timber purlins
masonry gable walls
nehobo floor
Y
X
Capacity curves
Direction X
Direction Y
Force [kN]
350
300
250
200
150
100
50
0
0
5
10
15
20
25
30
35
40
Displacement [mm]

Figure 3.5: Drawing and capacity curves of Typology 2.

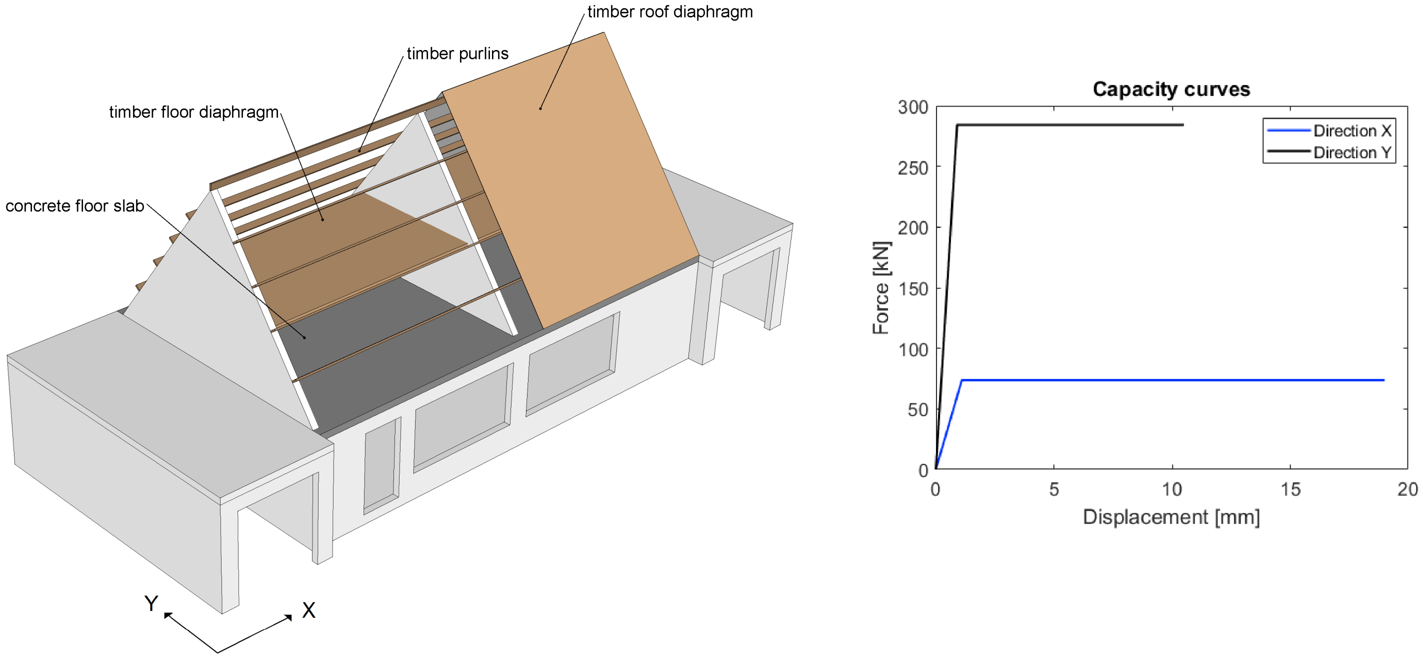
timber roof diaphragm
timber purlins
timber floor diaphragm
concrete floor slab
Y
X
Capacity curves
Direction X
Direction Y
Force [kN]
300
250
200
150
100
50
0
0
5
10
15
20
Displacement [mm]

Figure 3.6: Drawing of Typologies 3 and 4 and capacity curves of Typology 4.

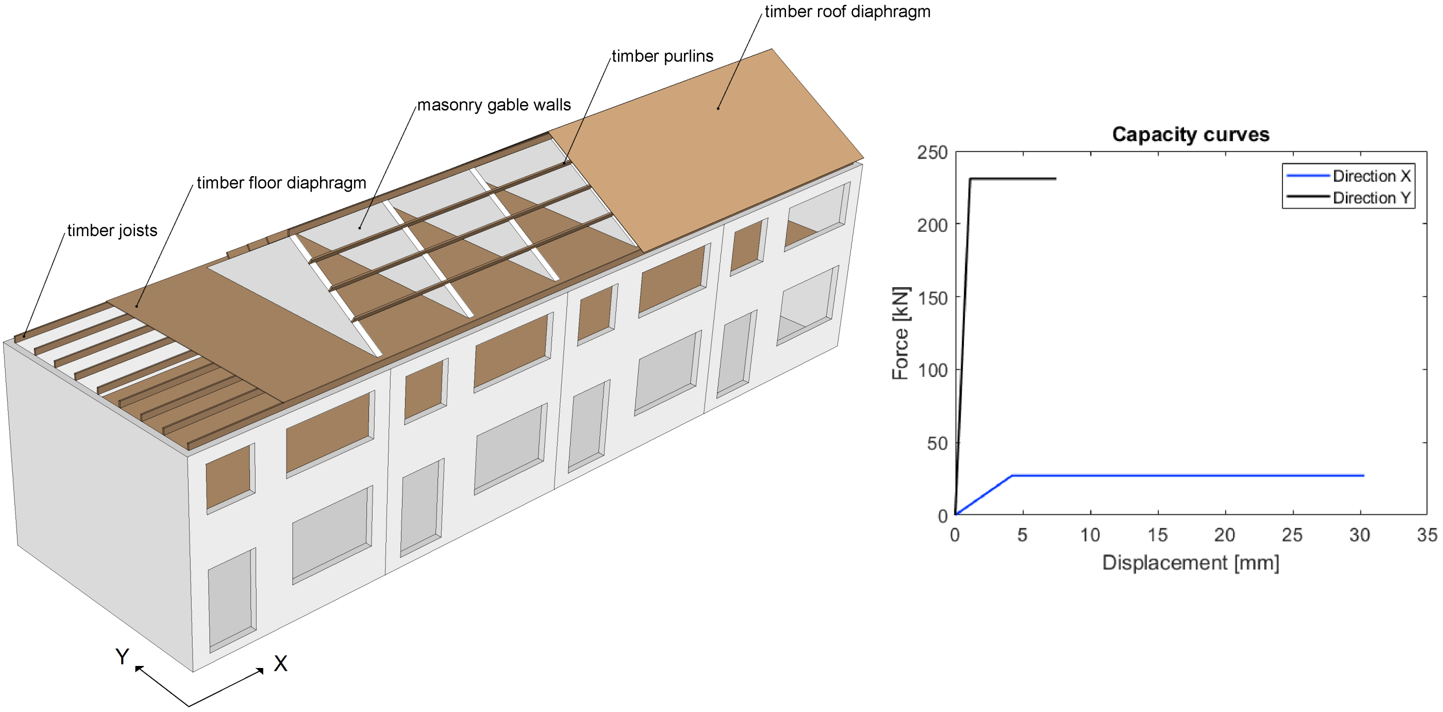
timber roof diaphragm
timber purlins
masonry gable walls
timber floor diaphragm
timber joists
Y
X
Capacity curves
Direction X
Direction Y
Force [kN]
250
200
150
100
50
0
0
5
10
15
20
25
30
35
Displacement [mm]

Figure 3.7: Drawing and capacity curves of Typology 5.

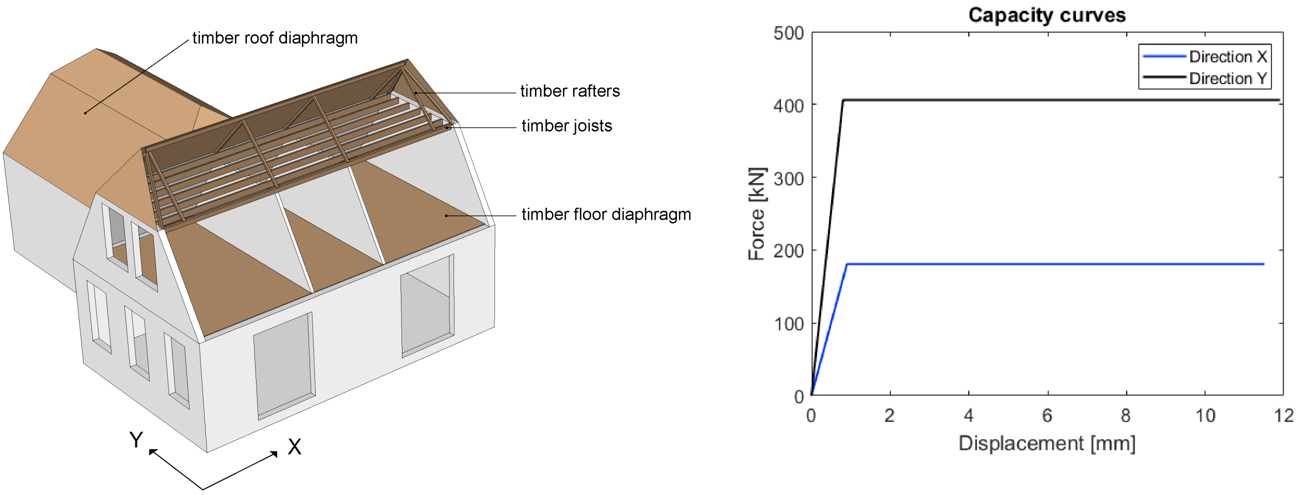

Figure 3.8: Drawing and capacity curves of Typology 6.

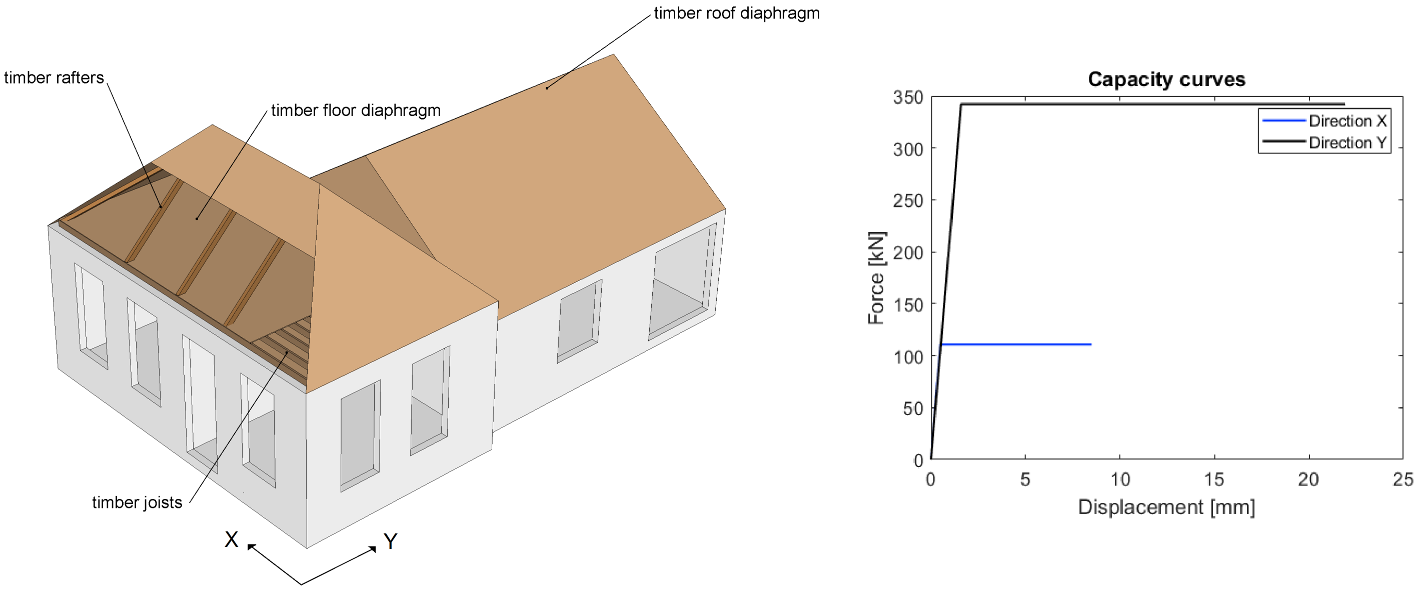

Figure 3.9: Drawing and capacity curves of Typology 7.

3.3 SDOF Models

The nonlinear time history analyses of the 1D single degree of freedom (SDOF) models are implemented in Opensees (Open System for Earthquake Engineering Simulation). Opensees is a finite element method (FEM) software, developed at the University of California, Berkeley Pacific Earthquake Engineering Research Center (PEER). The programming language of Opensees is the technical program language (tcl). The main reason of selecting Opensees for the NLTH analyses in the 1D models is the flexibility of describing and applying hysteretic models.

3.3.1 Hysteretic Rules in Opensees

When a structure is subjected to a seismic excitation, its components present nonlinear behaviour. Thus, the intention of this research is to incorporate the appropriate hysteresis in the considered structures. For this purpose, Opensees provides an adequate number of hysteretic materials. Two of them are chosen for the NLTH analyses, the Hysteretic Material and the Self-Centering Material. These Opensees material laws are considered as the most suitable to calibrate the desired hysteresis, as it is described in section 3.3.2.

3.3.1.1 Hysteretic Material

This command is describing a uniaxial bilinear hysteretic material with pinching of force and deformation, damage due to ductility and energy and degraded unloading stiffness based on ductility. The Opensees command for the hysteretic material is given below:

```
uniaxialMaterial Hysteretic $matTag $s1p $e1p $s2p $e2p $s3p $e3p $s1n $e1n $s2n $e2n
$s3n $e3n $pinchX $pinchY $damage1 $damage2 $beta
```

Table 3.3: Explanation of the Hysteretic Material command.

uniaxialMaterial Hysteretic	Description
matTag	Tag of the material
sip eip	stresses/forces and strains/deformations of the envelope points in the positive direction
sin ein	stresses/forces and strains/deformations of the envelope points in the negative direction
pinchX	pinching factor for strain/deformation during reloading
pinchY	pinching factor for stress/force during reloading
damage1	Adjusting damage due to ductility
damage2	Adjusting damage due to energy
beta	Adjusting the unloading stiffness

Priestley M. J. N., Calvi G. M. and Kowalsky M. J. [35] state that the modified “thin” takeda model (figure 3.11) is proposed to describe the hysteretic profile of concrete frame structures and masonry structures. According to this model the unloading stiffness is determined as:

$$k_u = k_o \cdot \mu^{-\alpha} \tag{3.4}$$

where:

k_o	is the stiffness in the previous loading phase.
μ	is the ductility.

In figure 3.10 the equation that defines the unloading stiffness of the hysteretic material in Opensees is displayed. The unloading stiffness is equal to $mu^{-beta} \cdot K_0$, which is equivalent to equation 3.4. Hence, hysteretic material is the most appropriate to simulate modified “thin” takeda hysteresis profiles.

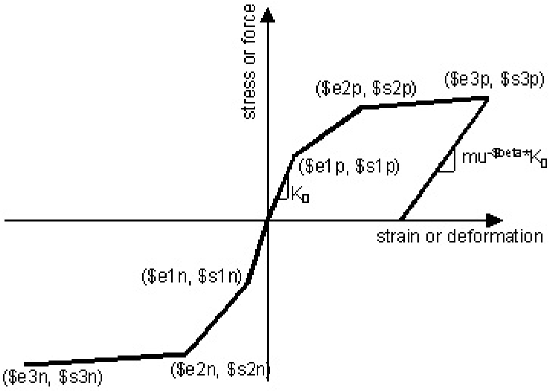
stress or force
strain or deformation
($e1p, $s1p)
($e2p, $s2p)
($e3p, $s3p)
($e1n, $s1n)
($e2n, $s2n)
($e3n, $s3n)
K0
mu^-$beta*K0

Figure 3.10: Hysteretic material model [46].

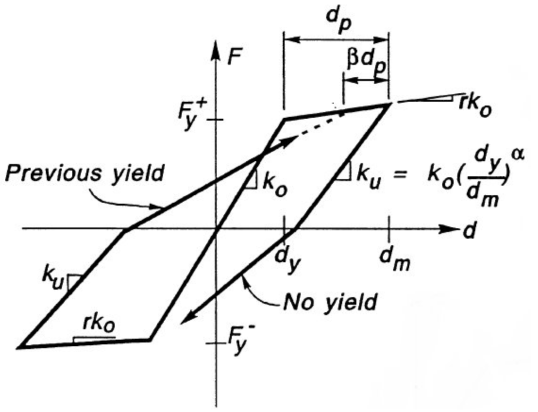
F
d
d_p
βd_p
F_y^+
F_y^-
rk_o
k_o
$k_u = k_o(\frac{d_y}{d_m})^\alpha$
Previous yield
d_y
d_m
No yield
k_u
rk_o

Figure 3.11: Modified "thin" takeda model [45].

3.3.1.2 Self-Centering Material

This command is used to construct a uniaxial self-centering or flag-shaped material with optional non-recoverable slip and an optional stiffness increase when high strains occurs. The Opensees command is described below:

```
uniaxialMaterial SelfCentering $matTag $k1 $k2 $sigAct $beta $epsSlip $epsBear
rBear
```

Table 3.4: Explanation of the Self-Centering Material command.

uniaxialMaterial Self-Centering	Description
matTag	Tag of the material
k1	Initial tifness
k2	Post-activation stiffness
sigAct	Activation stress/force (transition k1 to k2)
beta	height of the flag
epsSlip	Slip strain/deformation
epsBear	Bearing strain/deformation
rBear	Ratio of bearing stiffness to k1

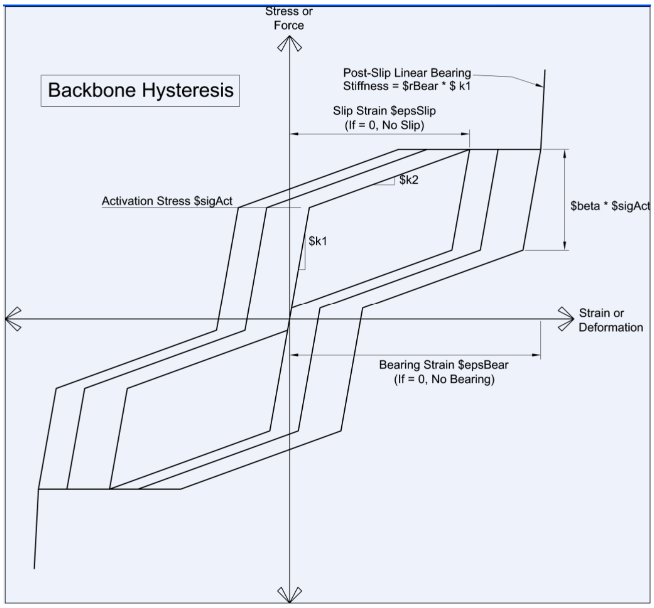
Stress or Force
Backbone Hysteresis
Post-Slip Linear Bearing Stiffness = $rBear * $ k1
Slip Strain $epsSlip (If = 0, No Slip)
$k2
Activation Stress $sigAct
$beta * $sigAct
$k1
Strain or Deformation
Bearing Strain $epsBear (If = 0, No Bearing)

Figure 3.12: Self-centering Material model in Opensees [21].

Self-centering material is recommended for simulating the hysteretic response of rocking wall systems.

3.3.1.3 Parallel Material

The performance of the self-centering material for the in-plane hysteretic profiles of the 1D models, that are calibrated based on in-plane rocking hysteretic profiles (section 3.3.2), is proved to be unsatisfactory. The material provides a good fit to the rocking hysteretic curves of the considered experiment specimens, however it does not indicate stiffness degradation. Therefore, it is decided to combine in parallel the self-centering material with the hysteretic material, which provides stiffness degradation through cyclic loading. Opensees allows this option with the command:

```
uniaxialMaterial Parallel $matTag $tag1 $tag2
```

Table 3.5: Explanation of the Parallel Material command.

uniaxialMaterial Parallel	Description
matTag	Tag of the material
tagi	Material tags of the materials wanted to be combined

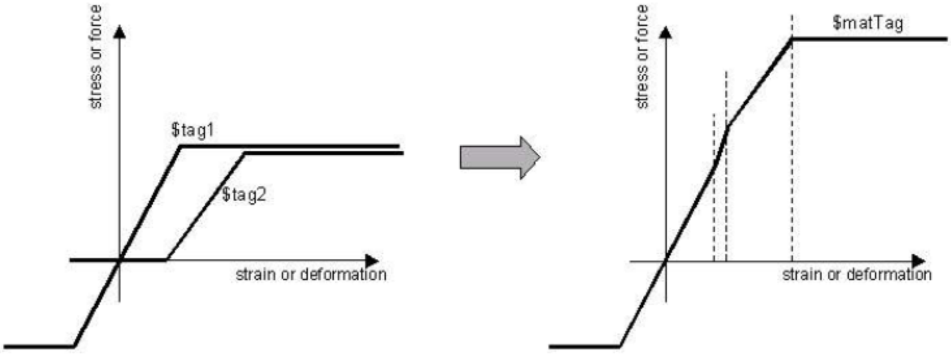

Figure 3.13: Parallel Material model in Opensees [21].

It is reminded that in a parallel model, strains are equal, while stresses and stiffnesses are additive. Towards a better understanding, in figures 3.14 and 3.15 the hysteretic responses of a system are displayed under cyclic loading with the use of the self-centering material and the parallel material respectively. The same capacity envelope curve and hysteretic energy is indicated in both figures. Nevertheless, the self-centering material is governed from elastic unloading with no stiffness degradation.

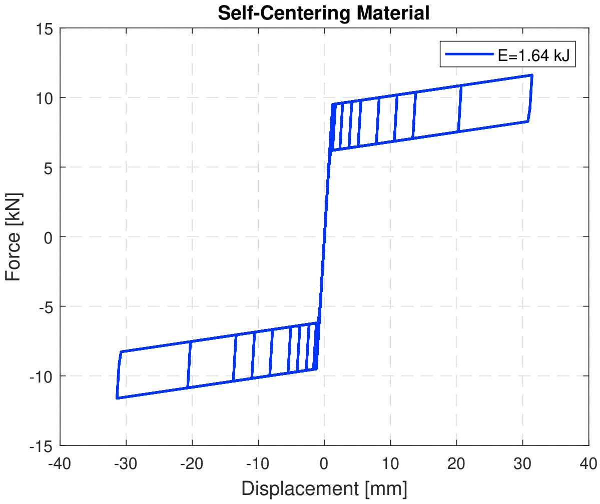

Figure 3.14: Self-centering material hysteretic response.

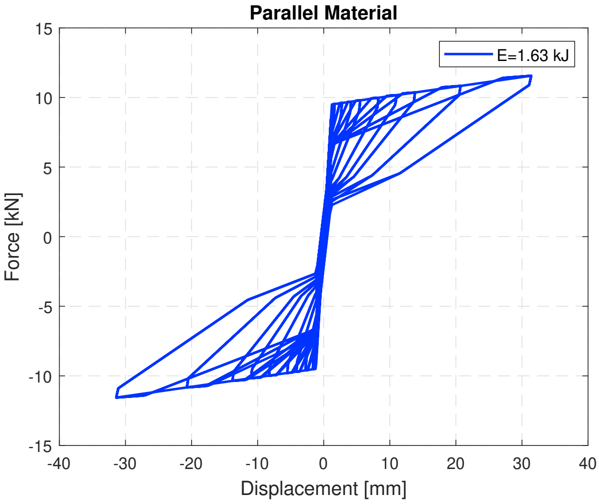

Figure 3.15: Parallel material hysteretic response.

3.3.2 Calibration of Hysteretic Rules

In this section, the parameters affecting the hysteresis of the uniaxial materials used in Opensees models are calibrated according to cyclic tests of in-plane rocking masonry wall specimens, performed at the Delft University of Technology [22] (table 3.6). More specifically, a match of the total energy as well as the energy in every cycle of the Opensees models with the respective energies of the experiments is attempted (table 3.7 and figures 3.19 and 3.20). The selected specimens are COMP-2 and COMP-3. The former is a clamped in-plane rocking specimen simulating low-to-moderate energy dissipation. The latter is a double-clamped in-plane rocking specimen simulating moderate energy dissipation. As a result, two hysteretic rules are created for each typology. The loading scheme for the experiment is indicated in figure 3.16.

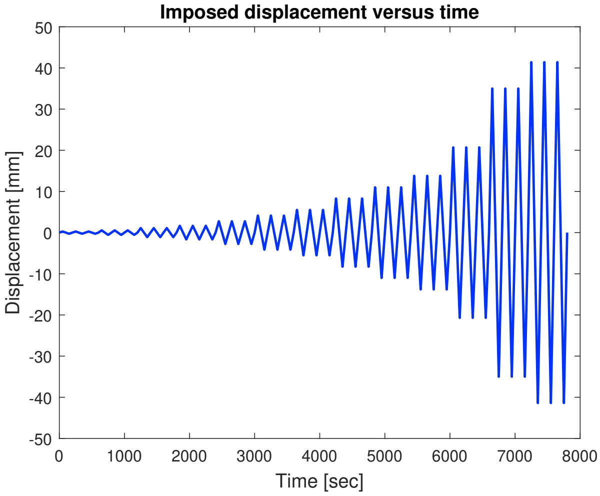

Figure 3.16: Loading scheme for specimens COMP-2 and COMP-3 [22].

3.3.2.1 Hysteretic Rule 1 - COMP-2

For the Hysteretic Rule 1 (HR1), the hysteretic material and the self-centering material are parallel combined. The response of the Opensees specimen under the cycling loading scheme is indicated in figure 3.17, superposed with the experiment hysteresis. The energy in Opensees matches the energy of the experiment (1.339 kJ versus 1.341 kJ).

3.3.2.2 Hysteretic Rule 2 - COMP-3

For the Hysteretic Rule 2 (HR2), the hysteretic material is employed. The response of the Opensees specimen is indicated in figure 3.18, superposed with the experiment hysteresis. The energy in Opensees matches the energy of the experiment (2.807 kJ versus 2.816 kJ).

Table 3.6: Hysteretic Rules parameters.

Parameters	Hysteretic Rule 1	Hysteretic Rule 2
k1	3850	-
k2	1e-07	-
sigAct	4.75	-
beta1	0.1	-
s1p/s1n	4.75/-4.75	14.4/-14.4
e1p/e1n	0.00123/-0.00123	0.000643/-0.000643
s2p/s2n	4.75/-4.75	14.4/-14.4
e2p/e2n	0.04343/-0.04343	0.035/-0.035
pinchX/pinchY	0.9/1	1/1
damage1/damage2	0/0	0/0
beta2	0.9	0.902

The parameters that are adopted for the SDOF systems are beta1, beta2, pinchX and pinchY. These parameters determine the hysteresis profile derived from the calibration of the experiments.

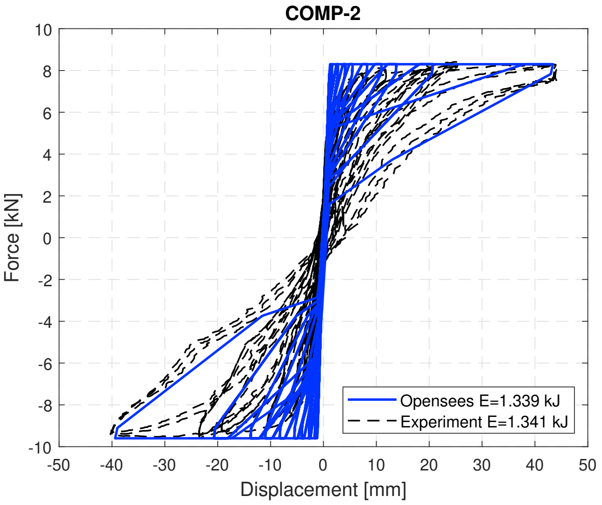

Figure 3.17: COMP-2 Comparison of Hysteresis.

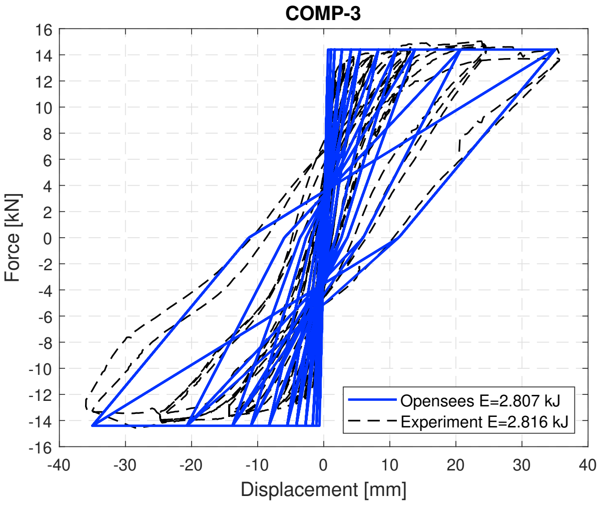

Figure 3.18: COMP-3 Comparison of Hysteresis.

Table 3.7: Energy dissipation in the experiment and in Opensees per cycle.

energy (kJ)				
cycle	test COMP-2	Opensees COMP-2	test COMP-3	Opensees COMP-3
1	0.000627962	5.80E-20	0.000324362	1.31E-20
2	0.003231428	3.02E-08	0.001282412	1.48E-07
3	0.00597674	5.29E-19	0.003382931	5.99E-07
4	0.008653772	0.0055844	0.014194654	0.014371135
5	0.01573882	0.0187727	0.022622301	0.039056944
6	0.02287639	0.0336129	0.055134166	0.069619672
7	0.04460206	0.048229	0.085256245	0.100242016
8	0.06419899	0.0850661	0.160226652	0.186189437
9	0.1217265	0.1180891	0.28393154	0.259765496
10	0.2534365	0.154094	0.30376353	0.342051184
11	0.3049716	0.2619364	0.846659632	0.60671191
12	0.4949064	0.6139397	1.039389668	1.182606714
total	1.34094716	1.3393	2.816168093	2.807283933

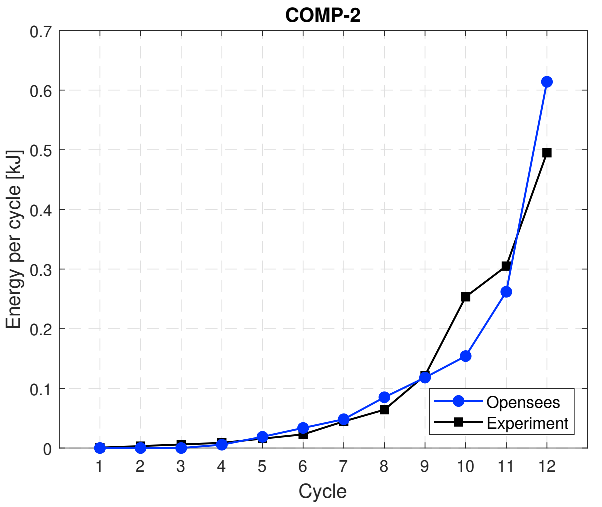

Figure 3.19: COMP-2 Comparison of Energy per cycle.

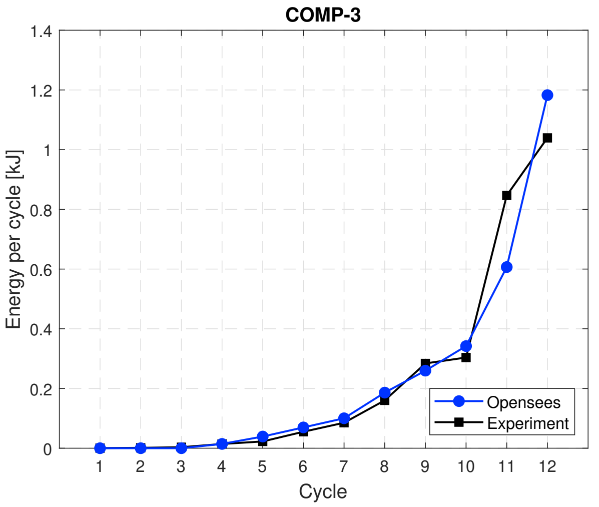

Figure 3.20: COMP-3 Comparison of Energy per cycle.

3.3.3 In-plane hysteretic behaviour and Floor Response Spectra (FRS)

The influence of modelling the in-plane hysteretic behaviour of a structure in the production of Floor Response Spectra (FRS) is discussed in this section. For this purpose, Typology 5 is considered with three different hysteretic responses:

1. Elastic-Plastic loading and Elastic unloading.
2. Hysteretic Rule 1.
3. Hysteretic Rule 2.

Elastic-Plastic loading and Elastic unloading response symbolises the scenario of zero hysteretic energy dissipation. Hysteretic Rule 1 symbolises the scenario of low-to-moderate hysteretic energy dissipation, while Hysteretic Rule 2 symbolises the scenario of moderate hysteretic energy dissipation. A ground motion record from Groningen is selected for the excitation of the model (figure 3.21). The capacity curve envelope of Typology 5 in direction X is indicated in the figure 3.22. This envelope also describes the behaviour of the structure for the case of no hysteretic energy dissipation (figure 3.23).

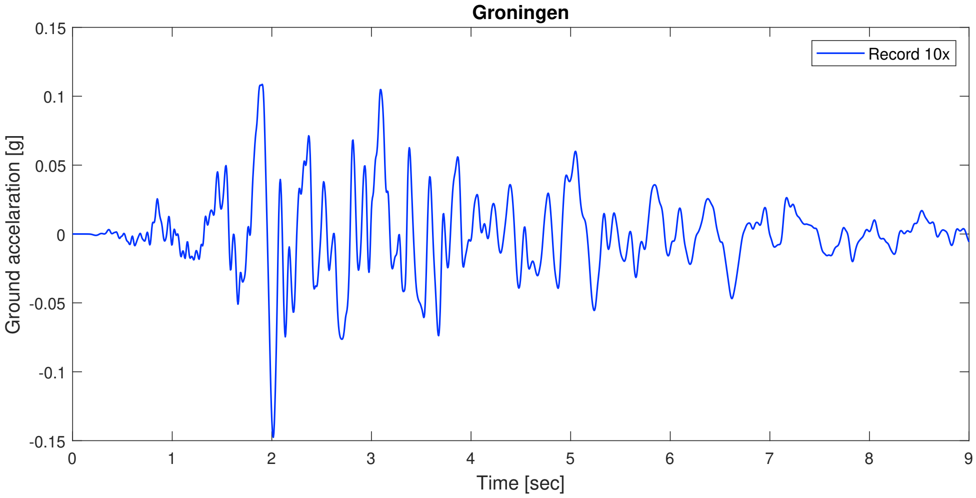

Figure 3.21: Ground motion record for Groningen.

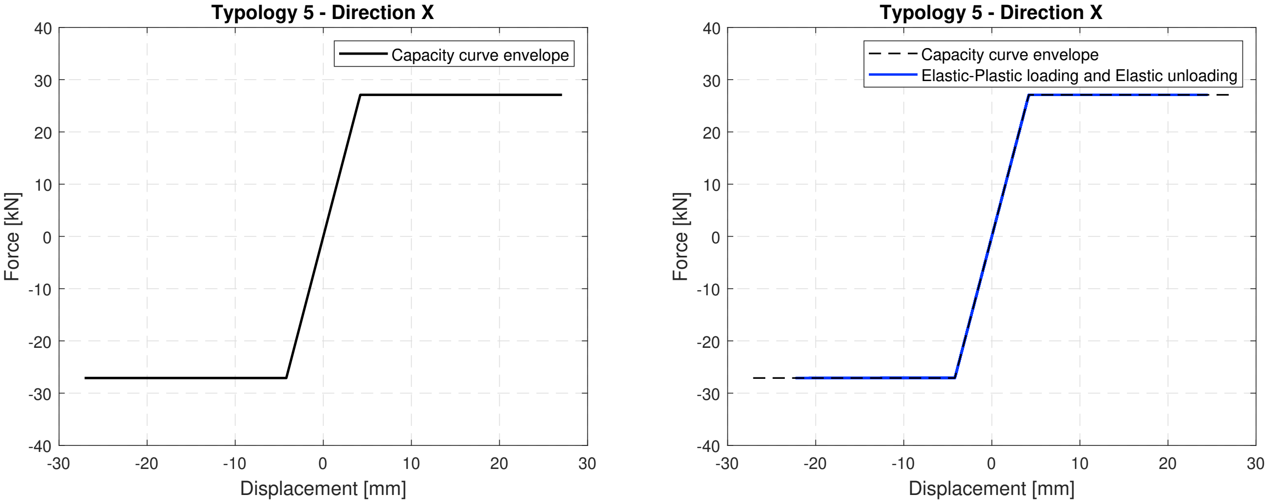

Figure 3.22: Capacity curve envelope of Typology 5.

Figure 3.23: Elastic-Plastic response of Typology 5.

The hysteretic curves of the equivalent SDOF system of Typology 5 for the Hysteretic Rule 1 and 2 are depicted in figures 3.24 and 3.25 respectively.

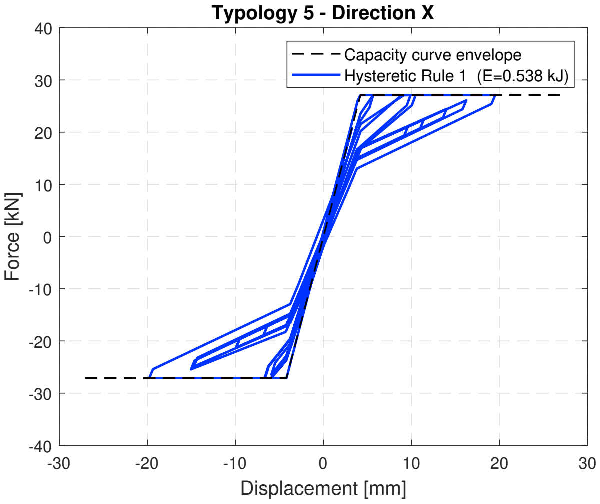

Figure 3.24: Hysteretic Rule 1 of Typology 5.

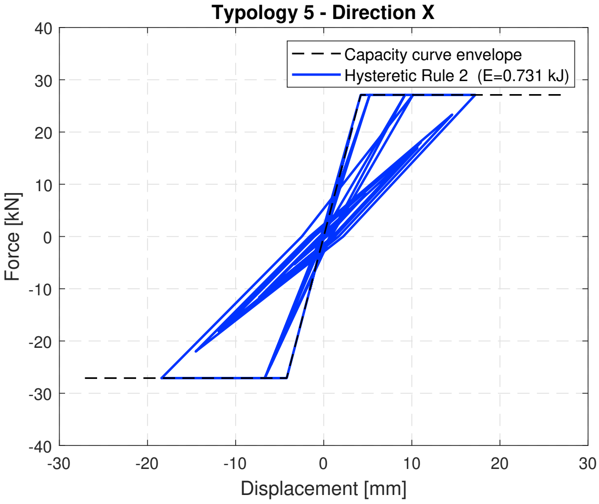

Figure 3.25: Hysteretic Rule 2 of Typology 5.

The Floor Response Spectra for each of the 3 hysteretic behaviours are plotted in the same graph (figure 3.26).

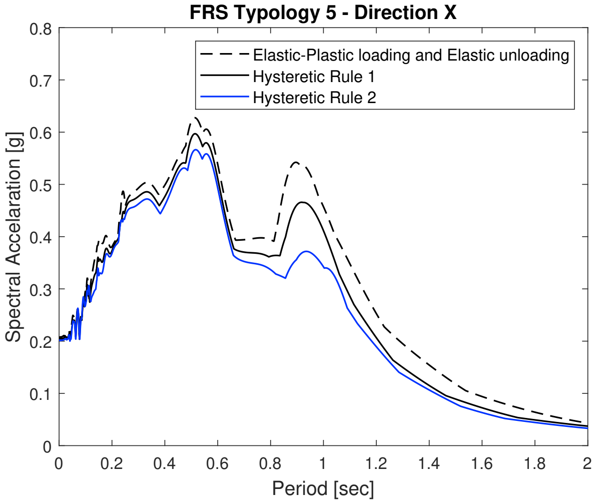

Figure 3.26: Effect of hysteretic damping in FRS.

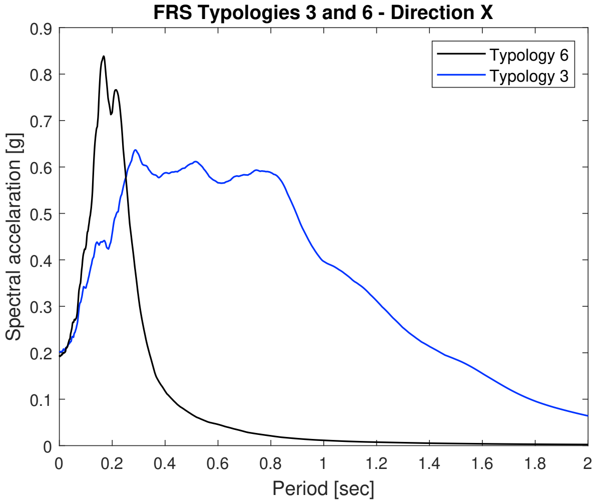

Figure 3.27: Effect of stiffness degrading systems in FRS.

It is observed in figure 3.26 that the response spectrum related to Hysteretic Rule 2 presents lower values of spectral accelaration than the response spectrum corresponding to Hysteretic Rule 1. The highest values of spectral accelaration are noticed in the response spectrum derived from the Elastic-Plastic loading and Elastic unloading case. As it is expected, Floor Response Spectrum shows lower spectral accelaration values when hysteretic damping increases in a system.

Figure 3.27 indicates another important effect of the in-plane behaviour regarding the derivation of Floor Response Spectra. Typologies 3 and 6 are considered. Typology 3 is rather flexible in direction X, while Typology 6 is significantly stiff. Both typologies are excited by the same ground motion record of Groningen. It is observed that Typology 3 presents a highly nonlinear behaviour compared to Typology 6, which remains mainly elastic. It can be concluded that peak values of Floor Accelaration Spectra are shifted away towards higher periods in systems with degrading stiffness [44]. As a result, lower peak spectral values and wider spectra are noticed.

3.3.4 Nonlinear viscous damping

For linear SDOF systems, the linear viscous damping is described by the damping coefficient c:

$$c = 2 \cdot m \cdot \omega_n \cdot \zeta \tag{3.5}$$

where:

m	is the mass of the SDOF system.
ω_n	is the natural frequency of the SDOF system.
ζ	is the damping ratio.

Linear viscous damping represents damping in the initial phase of the response, before hysteretic damping takes place. Calvi [35] underlined that using linear viscous damping throughout the whole excitation of hysteretic SDOF systems leads to unrealistic high damping forces and non-conservative response results. Hence, damping should be related to the tangent stiffness of the system, suggesting that the damping coefficient is updated whenever the stiffness changes.

In this research, nonlinear viscous damping of SDOF systems is described as:

$$c_i = 2 \cdot m \cdot \omega_i \cdot \zeta \tag{3.6}$$

where ω_i is related to tangent stiffness k_i. In order to integrate nonlinear viscous damping in Opensees, rayleigh command is used:

```
rayleigh $alphaM $betaK $betaKinit $betaKcomm
```

The damping matrix C (a single value for a SDOF system) is specified as:

$$[C] = \text{alphaM} \cdot [M] + \text{betaK} \cdot [\text{Kcurrent}] + \text{betaKinit} \cdot [\text{Kinit}] + \text{betaKcomm} \cdot [\text{KlastCommit}] \tag{3.7}$$

Setting alphaM=0, betaKinit=0, betaKcomm=0, it is derived $c = \text{betaK} \cdot \text{Kcurrent} = \text{betaK} \cdot \omega_i^2 \cdot m$.

The damping ratio is defined as $\zeta = \frac{\text{alphaM}}{2} \cdot \frac{1}{\omega_i} + \frac{\text{betaK}}{2} \cdot \omega_i = \frac{\text{betaK}}{2} \cdot \omega_i$

and substituting $\omega_i = \frac{2 \cdot \zeta}{\text{betaK}}$ in the equation describing the damping coefficient c, results to:

$c = \text{betaK} \cdot \omega_i \cdot \frac{2 \cdot \zeta}{\text{betaK}} \cdot m = 2 \cdot m \cdot \omega_i \cdot \zeta$, which is essentially equation 3.6.

To understand the importance of defining nonlinear viscous damping as the damping in the initial phase of the excitation of a system, Typology 5 is again considered to be excited with the same ground motion record. The hysteretic rule of modified “thin” takeda is considered for the SDOF system. Regarding the definition of damping, two NLTH analyses are implemented. In the first analysis, linear viscous damping is adopted, while in the second analysis, nonlinear viscous damping is adopted. The hysteretic curves are plotted for these two cases (figures 3.28 and 3.30). Moreover, the damping force versus the displacement graphs are plotted for each case (figures 3.29 and 3.31). The areas inside the loops indicate the relative energy dissipation. For the hysteretic curves, this energy is called hysteretic damping energy, while for the damping force versus displacement graphs, this energy is called initial or elastic damping energy.

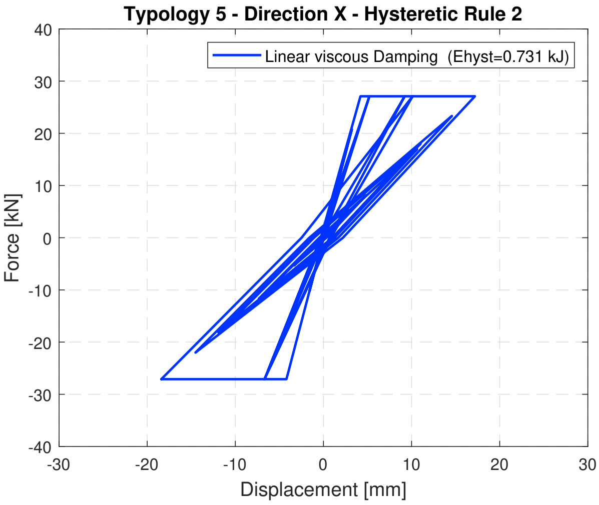

Figure 3.28: Hysteretic behaviour - linear viscous damping.

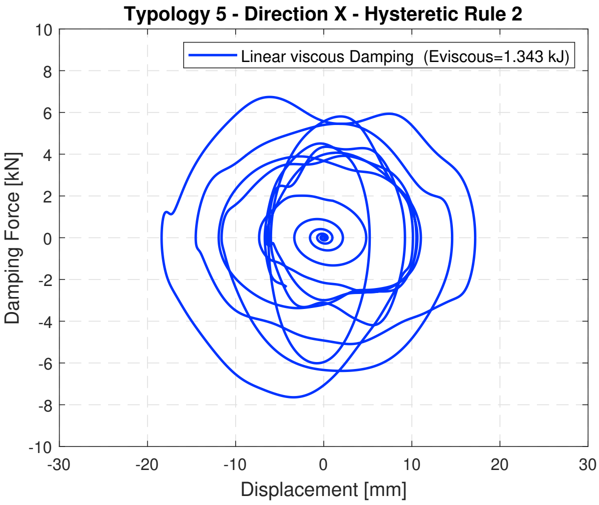

Figure 3.29: Damping response - linear viscous damping.

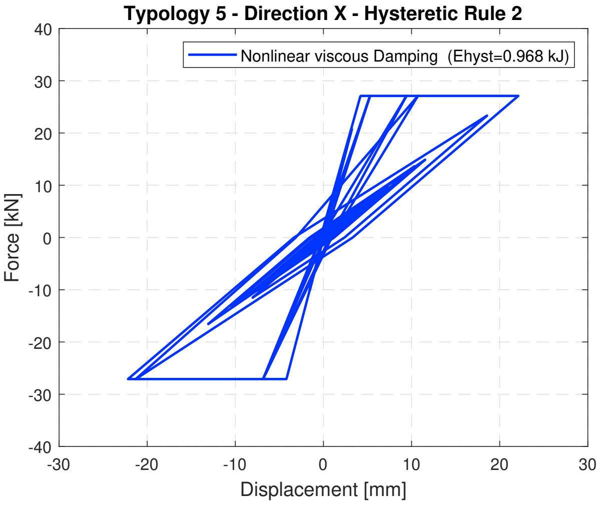

Figure 3.30: Hysteretic behaviour - nonlinear viscous damping.

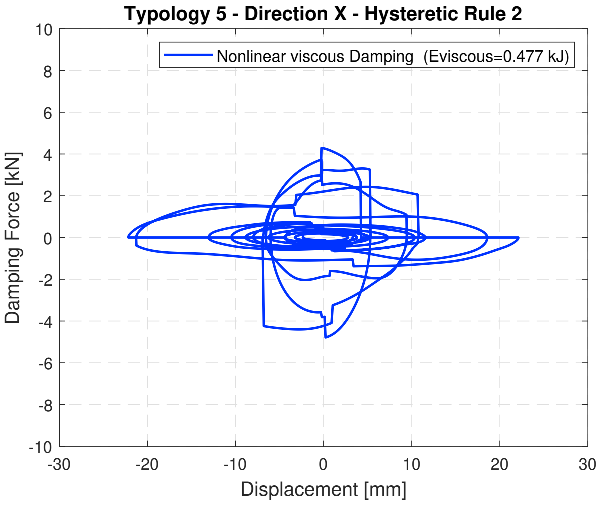

Figure 3.31: Damping response - nonlinear viscous damping.

The total energy dissipated considering linear viscous damping is equal to 2.074 kJ. The ratio of the initial damping energy over the total damping energy reaches the percentage of 65%, which means that the ratio of the hysteretic damping energy over the total damping energy is just 35 %. This is quite unusual, if it is considered that the structure presents high ductility level and inelastic behaviour, suggesting that the response should be governed from the hysteretic energy. This unrealistic result is due to the selection of the initial stiffness for the definition of the damping coefficient c.

When the damping coefficient is related to tangent stiffness, the initial damping energy is significantly reduced. The ratio of the initial damping energy over the total energy dissipation is then equal to 33 % , while the ratio of the hysteretic energy absorption over the total energy is equal to 67 %. In addition, a change of the damping force is noticed in figure 3.31, when the stiffness is altered. Especially when the response of the structure reaches the capacity envelope plateau, the damping force is equal to 0 and a significant drop to this value is observed.

Another impact of this issue is adressed in figure 3.32. The response of the SDOF system is depicted by considering nonlinear viscous damping and linear viscous damping. In the latter case the maximum displacement is underestimated by 21 % when compared to the maximum displacement of the former case. The difference between these two cases in the way that the structure damps out after the seismic excitation is also pronounced.

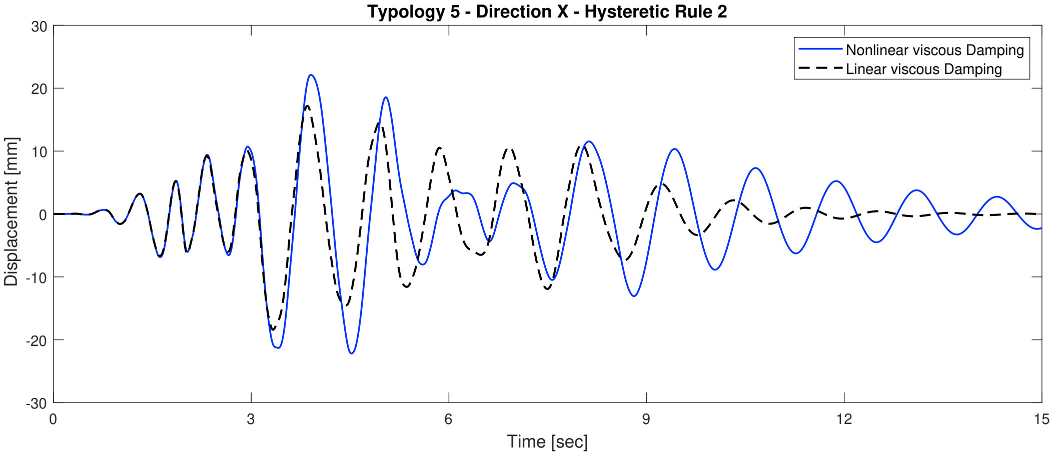

Figure 3.32: Response of SDOF system considering nonlinear viscous damping and linear viscous damping.

3.4 Nonlinear time history analyses (NLTHA) in Opensees

3.4.1 Ground motion records

Five areas are selected for this research. These are Appingedam, Groningen, Hoogezand, Loppersum and Overschild. For each area, 22 ground motion records are provided from in-house studies of BAM Advies and Engineering (11 in each direction). The records are related to Draft NPR 9998:2017 [12] and are compatible with the frequency characteristics, magnitude, epicenter depth, strong motion duration, soil condition and soil nonlinearity (soil damping) of the earthquakes in the abovementioned areas.

Draft NPR 9998:2017 [12] states that 11 ground motion records should be used for the assessment of the Near Collapse (NC) limit state. More specifically, for the indirect check of NC limit state via deformation criteria, the mean response of the structure excited in 11 ground motions can be used for the verification of non-exceedance of the seismic limit state criteria.

3.4.2 Nonlinear Time History results

The results derived from the analyses are the Floor Accelaration Spectra for each typology, in each area and direction. The procedure followed for the derivation of FRS for each typology, in each area, considering each Hysteretic Rule per model, for the direction X is:

1. Excitation of the model using 11 ground motion records in direction X.
2. Derivation of 11 responses of the model in terms of accelaration versus time.
3. Derivation of 11 elastic response spectra ($\zeta = 5\%$) from the respective accelaration responses. These are the Floor Accelaration Spectra.
4. Determination of the mean Floor Response Spectrum.

The same procedure holds for direction Y. The total number of mean FRS produced for direction X is 70 (5 areas x 7 typologies x 2 hysteretic rules). Concerning the mean FRS for direction Y, the total number is 35. This is due to the fact that the structures in that direction remain elastic, so the impact of the hysteretic rules in the response proved to be irrelevant. The mean FRS graphs are concentrated in Appendix A and are categorised per area.

Aiming to a greater understanding regarding the implementation of the NLTH analyses in Opensees and the derivation of the mean FRS, flow charts of the procedure for direction X and Y in one area are provided below. Judging by the figures 3.33 and 3.34, it is easy to be concluded that a significant amount of output is created from the Opensees analyses. Post-processing of these results, but also of all the analyses performed in this thesis is executed from MATLAB scripts.

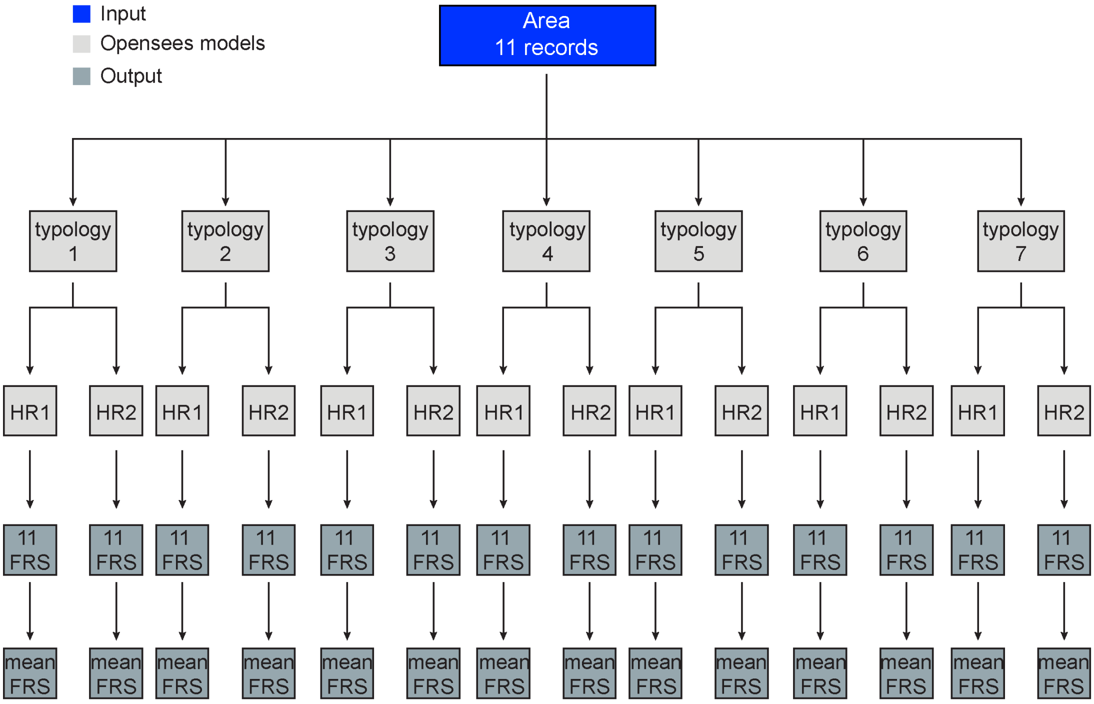
Input
Opensees models
Output
Area
11 records
typology 1
typology 2
typology 3
typology 4
typology 5
typology 6
typology 7
HR1
HR2
11 FRS
mean FRS

Figure 3.33: Flow chart of the NLTH analyses in Opensees for direction X.

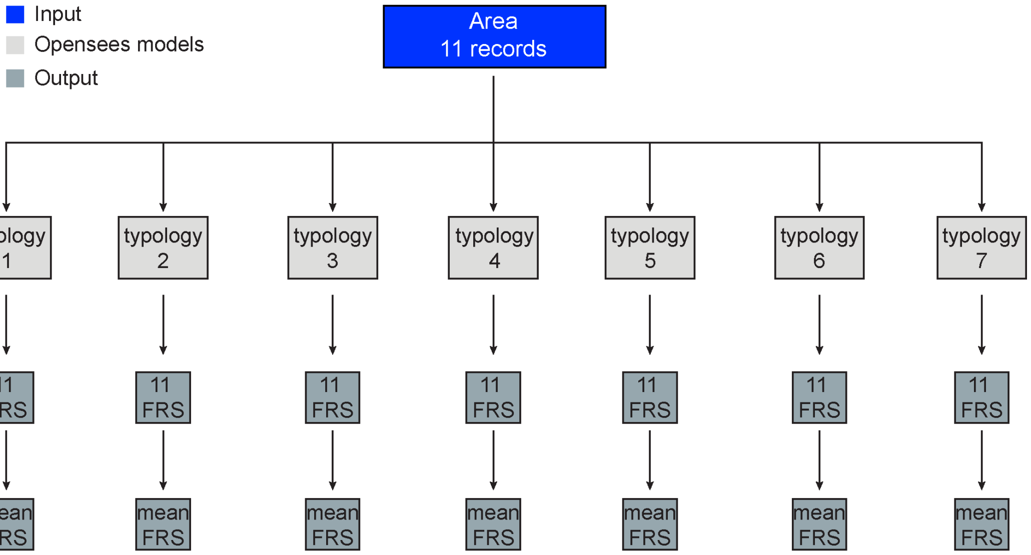
Input
Opensees models
Output
Area
11 records
typology 1
typology 2
typology 3
typology 4
typology 5
typology 6
typology 7
11 FRS
mean FRS

Figure 3.34: Flow chart of the NLTH analyses in Opensees for direction Y.

3.5 Design Floor Accelaration Spectra

3.5.1 Introduction

Design Floor Accelaration Spectra are determined in order to define the Shape Factor Coefficient $C_i(T_p)$ for the Groningen Case. Observing the mean FRS graphs produced from NLTHA in Opensees, irregularities are noticed owing to:

1. Ground motion records (Areas).
2. Typologies characteristics.
3. Hysteretic Rules.
4. Direction of the seismic activity.

Especially for direction X, where the structures present nonlinear behaviour, it is rather difficult to find a pattern that will cover the majority of the mean FRS produced. In direction Y, the elastic bell-shaped FRS is recognised as a pattern for all the cases considered. However the natural period, where the peak spectral accelaration is observed, differs from case to case.

A procedure is described in section 3.5.2 in order to produce the Design Floor Accelaration Spectra for the governing direction X. Concerning direction Y, the validation of the produced Design Floor Accelaration Spectra in direction X will be implemented for the mean FRS in direction Y, since it is appropriate to have common Design Floor Accelaration Spectra in both directions.

3.5.2 Newmark - Hall method

The method employed for producing the Design Floor Accelaration Spectra, is the Newmark - Hall method [26]. Newmark - Hall method [26] is based on the illustration of a response spectrum in a tripartite graph (figure 3.35). Since the response spectrum in terms of spectral accelarations is known, the pseudo-velocity (PSV) and pseudo-displacement (PSD) response spectra can be derived by applying the following equations:

$$SV = \omega \cdot SD = PSV \tag{3.8}$$

$$SD = \frac{SA}{\omega^2} = PSD \tag{3.9}$$

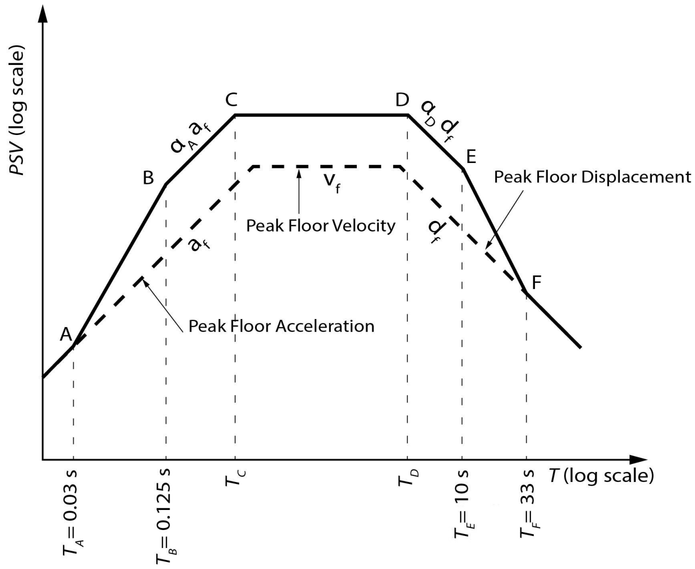

Figure 3.35: Newmark design spectra.

The logarithmic expressions of SA and SD can now be plotted together, in the graph of PSV versus period. The axes of this graph are in logarithmic scale. Axes in angle of 45^o are related to spectral pseudo-displacements PSD, while axes in angle of 135^o are related to spectral accelarations SA. The methodology followed for the derivation of the tripartite response spectrum is explained in the following steps:

1. Design of the lines related to the peak floor accelaration a_f, peak floor velocity v_f and peak floor displacement d_f (dashed lines in figure 3.35).
2. Definition of the vertical lines related to periods: T_A = 0.03 sec, T_B = 0.125 sec, T_E = 10 sec, T_F = 33 sec.
3. Design of the line parallel to the peak floor accelaration line, related to the value $\alpha_A \cdot a_f$, where α_A is the spectrum amplification factor of the accelaration (table 3.8). The line of constant spectral accelaration starts at period T_B.
4. Design of the line parallel to the peak floor velocity line, related to the value $\alpha_V \cdot v_f$, where α_V is the spectrum amplification factor of the velocity (table 3.8). The intersection point C of this line with the line of constant spectral accelaration defines corner period T_C.
5. Design of the line parallel to the peak floor displacement line, related to the value $\alpha_D \cdot d_f$, where α_D is the spectrum amplification factor of the displacement (table 3.8). The intersection point D of this line with the line of constant spectral velocity defines period T_D.
6. For $T < T_A$ the spectral accelaration is considered equal to the floor accelaration.
7. For $T > T_F$ the spectral displacement is considered equal to the floor displacement.

The amplification factors α_A, α_V and α_D represent the ratios of the response spectra to the peak ground motions for acceleration, velocity and displacement respectively. The equations that Newmark derived for these amplification factors are based on statistical analysis of 28 ground motion records from California Earthquakes. For each groud motion, a value of the α_A, α_V and α_D was found for a specific damping ratio ζ%. Two sets of equations for the amplfication factors were then provided from Newmark [26] (table 3.8). The first set refers to the mean value and the second set to the mean plus one standard deviation value of the amplification factors. In the same manner, the period ranges of the amplifications of the PGA, PGV and PGD, which are defined by the periods T_A, T_B, T_E and T_F, are also related to the statistical analysis of the 28 ground motion records in Newmark's study. A sufficient description of the procedure used by Newmark for the determination of the amplification factors can be found at the PhD Thesis of Bo Li, page 34 [5]. In addition, this method is generally used for the derivation of Design Ground Accelaration Spectra. However, in this research is used to produce the Design Floor Accelaration Spectra in an analogous way.

Table 3.8: Spectrum amplification factors [26].

amplification factor	Mean (50%)	Mean + 1 std (84.1%)
α_A	$3.21 - 0.68 \cdot \ln\zeta$	$4.38 - 1.04 \cdot \ln\zeta$
α_V	$2.31 - 0.41 \cdot \ln\zeta$	$3.38 - 0.67 \cdot \ln\zeta$
α_D	$1.82 - 0.27 \cdot \ln\zeta$	$2.73 - 0.45 \cdot \ln\zeta$

For the derivation of the Design Spectra for the Groningen Case, the second set (Mean + 1 std) of amplification factors is selected. The derived response spectra of this research are elastic so ζ is equal to 5%.

3.5.3 Design Spectra for the Groningen Case

The procedure discussed in section 3.5.1 is implemented for the investigated areas. Starting with Appingedam, the normalised (Saf/PFA) mean FRS of all the considered typologies and hysteretic rules, are gathered in one plot. The purpose of the Design Spectrum is to provide an upper bound estimate for the spectral values determined at all of the mean FRS. In other words, Design Spectrum aims to be the envelope of the mean responses of all the typologies and hysteretic rules per area. For this reason, the response of the mean value plus two standard deviation of the mean FRS is defined (97.7% [1] of the typologies and hysteretic rules investigated per area, figure 3.36) and provided as an input for the Newmark-Hall method. Next, the tripartite graph is constructed (figure 3.37) in order to produce the design spectrum in logarithmic scale axes. By transposing the design spectrum from logarithmic scale to linear scale, the normalised Design Floor Accelaration Spectrum is obtained (figure 3.39).

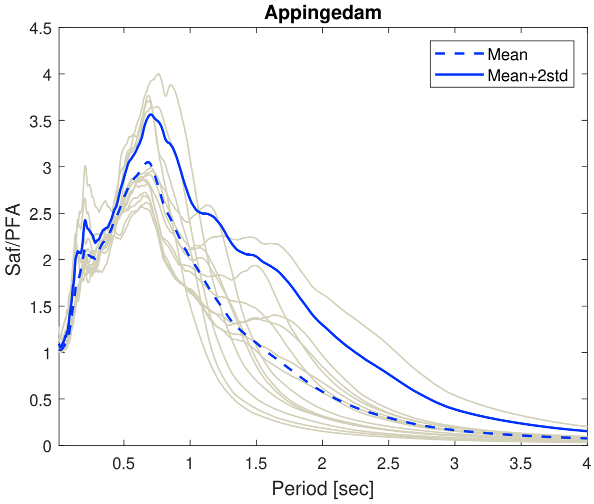

Figure 3.36: Definition of the mean + 2 std response.

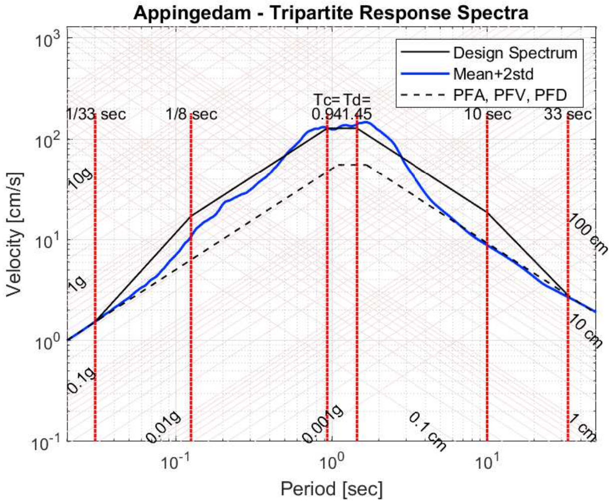

Figure 3.37: Tripartite graph for the mean + 2 std response.

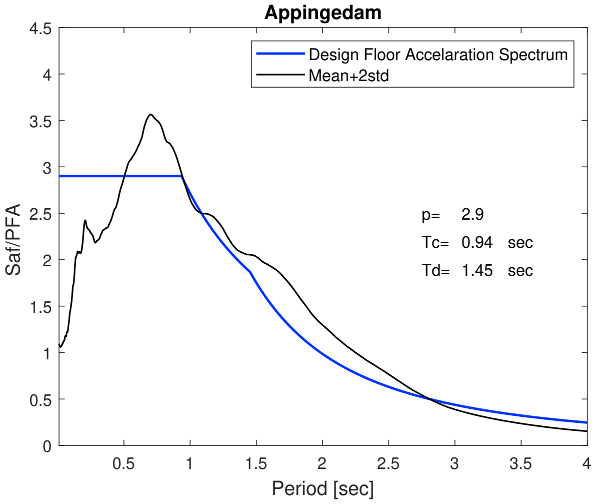

Figure 3.38: Design Floor Accelaration Spectrum and mean + 2 std response.

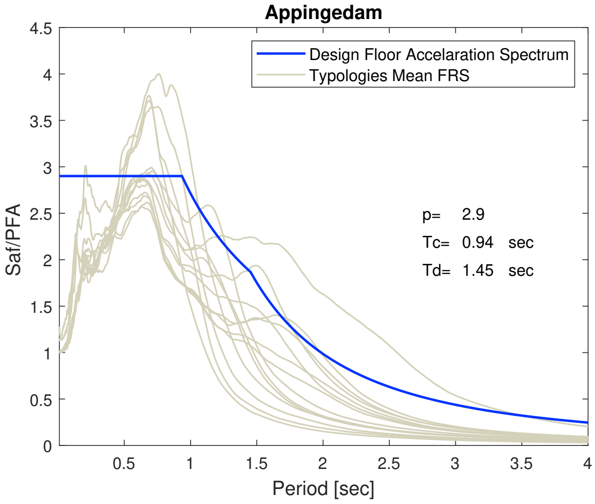

Figure 3.39: Design Floor Accelaration Spectrum and Typologies Mean FRS.

The same procedure is followed for the areas Groningen, Hoogezand, Loppersum and Overschild. The respective graphs can be found at Appendix B.

---

[1] The cumulative probability 84.1% of non-exceedance for the considered amplification factors should not be confused with the 97.7% response of the mean FRS.

3.6 2DOF Models

Design Floor Accelaration Spectra are an envelope of the mean FRS per area in direction X. Nonetheless, high amplified spectra presenting greater spectral values than the design plateau value are observed (see Appendix B). These spectra are the mean FRS responses of typologies 6 and 7, which are characterised by significant in-plane stiffness and minor inelastic behaviour. In direction Y, all the typologies present narrow high amplified spectra with higher spectral accelaration values than the design plateau value. The reason is the elastic behaviour of all the typologies in this direction.

In detail, a response spectrum is a plot indicating the maximum response of linear oscillators with varying natural frequency or period being excited by the same vibration. Thus, if the elastic period of the wall coincides with the period range of the high amplified spectra, resonance will occur due to the seismic interaction of the OOP wall and the floor. Consequently, the wall will be subjected to significant accelarations (figure 3.40). These spectral accelarations are larger compared to the ones indicated by the Design Floor Accelaration Spectra. Hence, it is important to investigate the ability of the derived Design Floor Accelaration Spectra to include the actual NLTH response of the OOP walls for the typologies creating high amplified spectra. To implement this, the following procedure is carried out:

1. Incorporation of the OOP wall in the 1D model.
2. Description of the nonlinear behaviour of the OOP wall in Opensees.
3. Sensitivity study of different configurations of OOP walls resulted from different boundary conditions and overburden loads. This requires the:
    - 3.1. Excitation of the models for the typologies that create the high amplified spectra in each area.
    - 3.2. Comparison of the NLTH displacement response of the OOP walls with the design displacement Δ_{ph} that is defined in NZSEE method. For the calculation of Δ_{ph}, instead of using the Shape Factor coefficient that New Zealand Norm describes, the one obtained in this research is employed. Consequently, the ability of the Shape Factor Coefficient $C_i(T_p)$ to act as upper bound value of the actual response and predict the failure of OOP wall is determined.

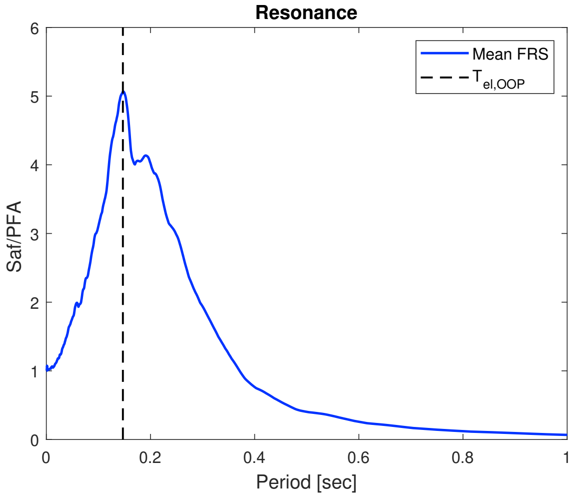

Figure 3.40: Resonance phenomenon due to the seismic interaction of the floor and the OOP wall.

3.6.1 Incorporation of the OOP wall in the 1D model

The extended 1D model is described as a two degree of freedom (2DOF) system. The nonlinear springs of the building and the OOP wall are in series. With this model, the OOP dynamic behaviour of a wall subjected to a ground motion record, filtered by the hysteretic behaviour of the structure, can be studied. Additionally, the resonance phenomenon between the equivalent systems of the building and the OOP wall is captured.

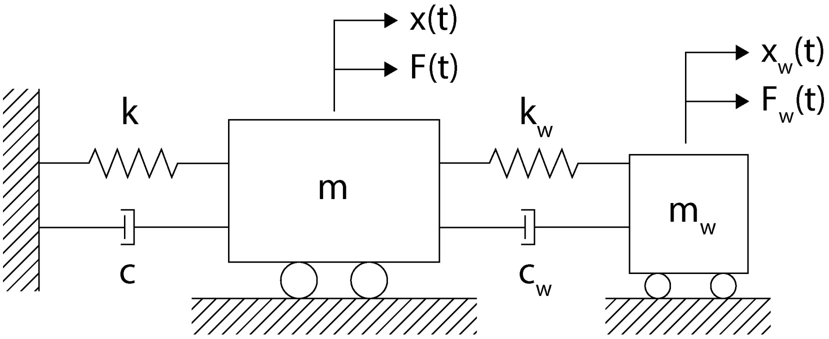

Figure 3.41: Representation of the extended 1D model.

3.6.2 Nonlinear behaviour of OOP wall in Opensees

The description of the nonlinear spring of the mass that resembles the OOP wall, is addressed in the same manner as in section 3.3.2. The calibration of the parameters defining the hysteretic profile in Opensees is based on the specimen COMP-7 [22]. The type of test applied in specimen COMP-7 is one-way out-of-plane test. The out-of-plane rotational stiffness of the supports for the sample COMP-7 is significant. Thus, the boundary conditions at the top and bottom of the wall are clamped. The loading scheme of the experiment, in terms of displacement, is indicated in figure 3.42.

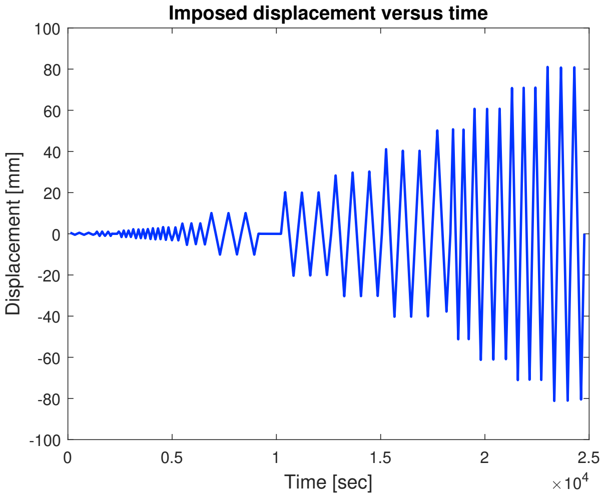

Figure 3.42: Loading scheme for specimen COMP-7 [22].

The hysteretic material and the self-centering material is used for the definition of the hysteretic profile of the OOP wall and calibrated accordingly to the specimen COMP-7. The extracted paremeters are indicated in table 3.9. The parameters that define the hysteresis are sigAct, beta1, pinchX, pinchY and beta2. The hysteretic response of the Opensees mass compared to the experiment is depicted in figure 3.43.

Table 3.9: OOP Hysteretic Rule parameters.

Parameters	OOP Hysteretic Rule
k1	575
k2	-11.0978
sigAct	1.725
beta1	0.3
s1p/s1n	9.775/-9.775
e1p/e1n	0.003/-0.003
s2p/s2n	1e-06/-1e-06
e2p/e2n	0.08/-0.08
pinchX/pinchY	1/1
daamage1/damage2	0/0
beta2	1.15

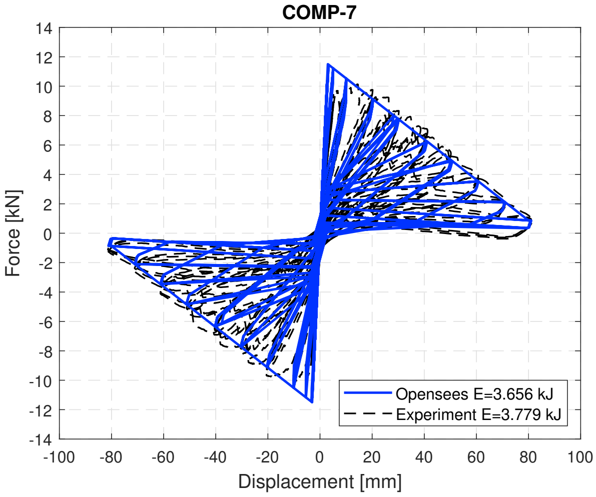

Figure 3.43: COMP-7 Comparison of Hysteresis.

3.6.3 Configurations of the OOP walls

For the sensitivity study of the OOP walls, 12 configurations of walls are investigated. These are the outcome of considering 4 boundary conditions (BC0, BC1, BC2 and BC3) in accordance with Draft NPR 9998:2017 [12] and NZSEE Norm [28] and 3 overburden loads (5 kN, 15 kN and 30 kN). The walls have a length of 1 meter, a height of 2.76 meters and a thickness of 0.102 meters.

For each case, the capacity curves are derived using FEM software ANSR-II. Then, the capacity curves of the equivalent SDOF systems of the OOP walls are obtained. This is achieved by dividing the forces and displacements of the initial capacity curves with the participation factor γ of the out-of-plane rocking mechanism for each case. The participation factor γ is described in the NZSEE Norm [28]. The mass of the equivalent SDOF system of the OOP wall m* is defined as 3/4 of the total mass m.

The defined capacity curves of the equivalent SDOF systems of the OOP walls are introduced in Opensees. These are illustrated in figures 3.44 to 3.47.

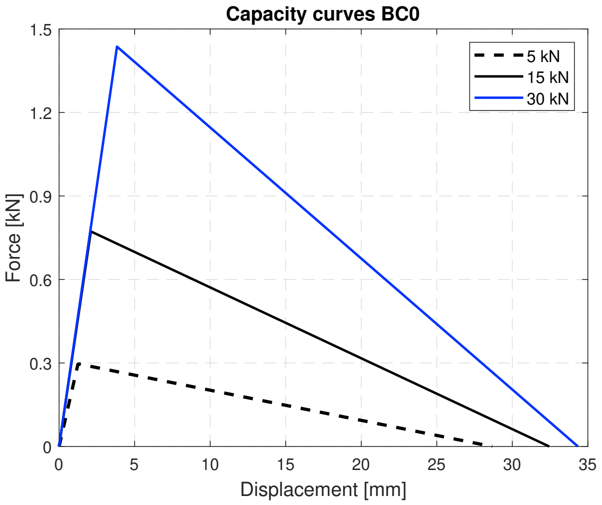

Figure 3.44: Capacity curves - BC0.

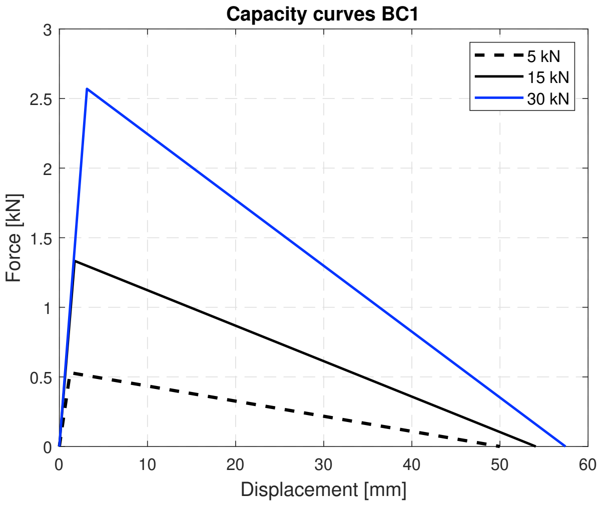

Figure 3.45: Capacity curves - BC1.

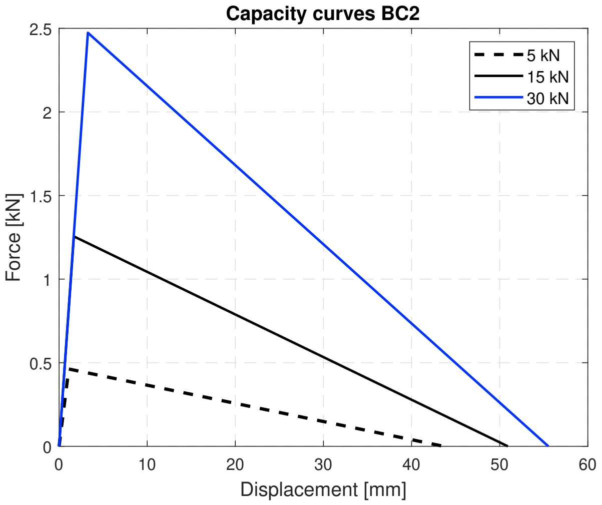

Figure 3.46: Capacity curves - BC2.

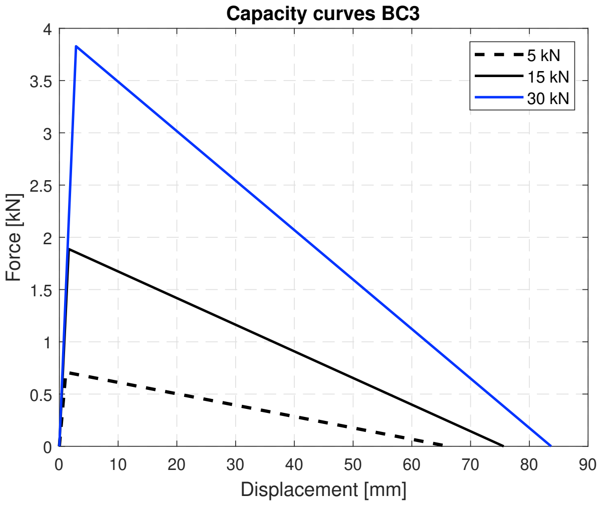

Figure 3.47: Capacity curves - BC3.

Table 3.10: Information for the equivalent SDOF systems of OOP walls.

BCs	BC0			BC1			BC2			BC3		
Overburden	5 kN	15 kN	30 kN	5 kN	15 kN	30 kN	5 kN	15 kN	30 kN	5 kN	15 kN	30 kN
F_{y*} [kN]	0.30	0.77	1.44	0.53	1.33	2.57	0.46	1.26	2.47	0.71	1.89	3.83
d_{y*} [mm]	1.25	2.10	3.83	1.22	1.73	3.13	1.10	1.68	3.27	1.10	1.60	2.84
d_{m*} [mm]	28.67	32.45	34.35	49.98	54.07	57.43	43.64	50.93	55.52	66.18	75.64	83.71
γ	1.47	1.43	1.40	1.42	1.35	1.29	1.44	1.37	1.30	1.39	1.27	1.17
T_p [sec]	0.52	0.34	0.25	0.52	0.35	0.26	0.52	0.35	0.26	0.53	0.36	0.28
$T_{el,OOP}$ [sec]	0.25	0.20	0.20	0.19	0.14	0.14	0.19	0.14	0.14	0.15	0.11	0.11

3.6.4 High amplified spectra

The elastic period range of the equivalent systems of the OOP walls can be defined and compared with the period range of the high amplified spectra. This will demonstrate whether resonance is likely to occur. In Groningen (figure 3.48) and Hoogezand (figure 3.49), for direction X, the period range of the narrow high amplified spectra matches the elastic period range of the OOP walls. In these cases the response of the OOP walls will be amplified because of resonance phenomena. Furthermore, in direction Y, all the typologies present high amplified bell-shaped spectra. The elastic periods of the considered OOP walls may coincide with the period range of the narrow high amplified FRS (figures 3.50 and 3.51). Hence, resonance effects are possible in direction Y, as well.

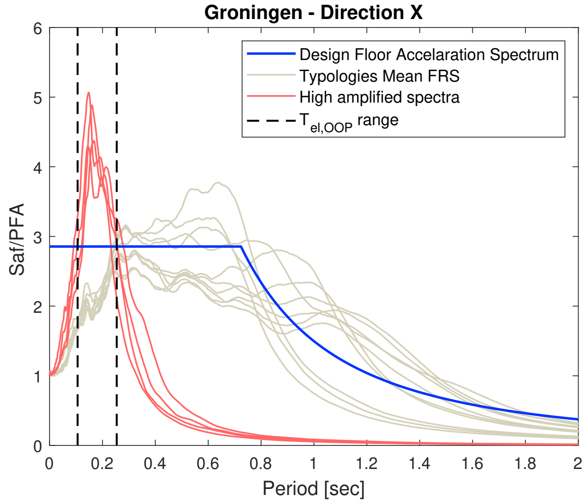

Figure 3.48: High amplified spectra in Groningen for direction X.

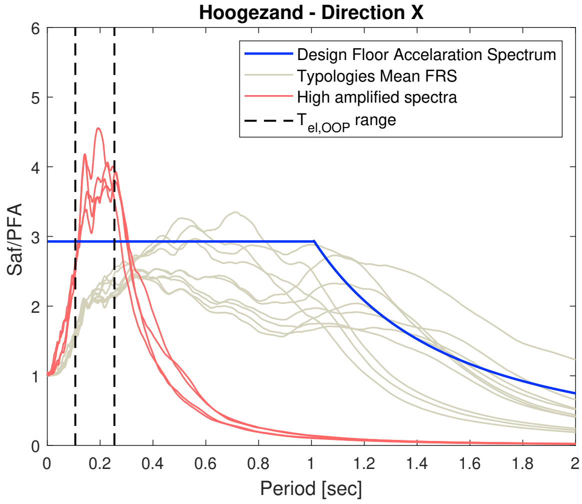

Figure 3.49: High amplified spectra in Hoogezand for direction X.

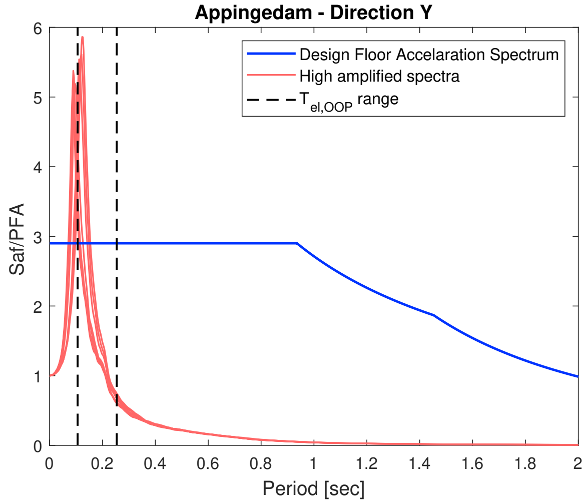

Figure 3.50: High amplified spectra in Appingedam for direction Y.

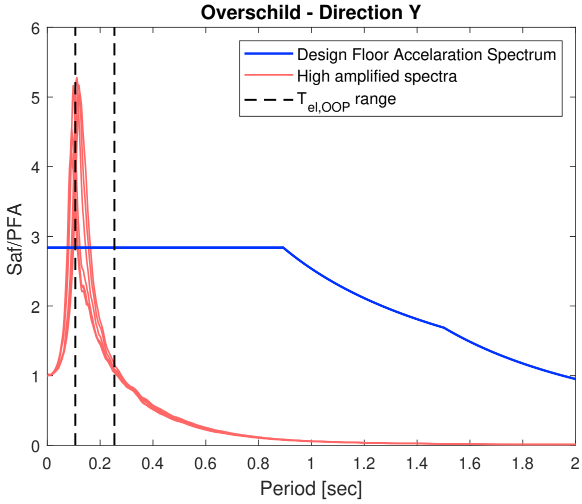

Figure 3.51: High amplified spectra in Overschild for direction Y.

In Appingedam (figure 3.39), Loppersum (figure 3.52) and Overschild (figure 3.53), for direction X, the resonance range is related to higher periods, because the typologies creating high amplified spectra present greater hysteretic behaviour. Nevertheless, the sensitivity studies are also implemented for these cases.

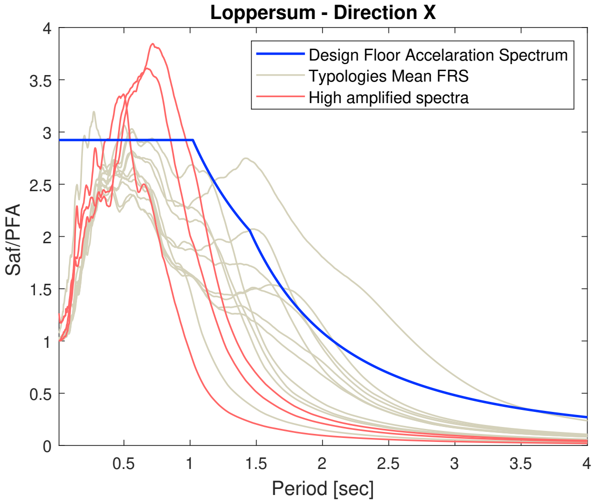

Figure 3.52: High amplified spectra in Loppersum for direction X.

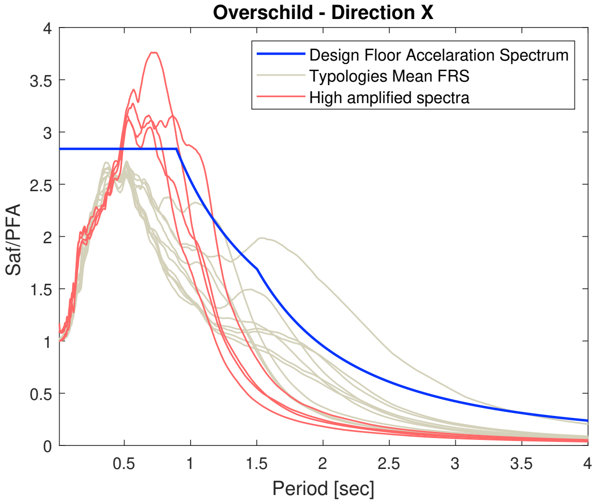

Figure 3.53: High amplified spectra in Overschild for direction X.

3.6.5 Sensitivity studies of OOP walls in the 1D Models

As already mentioned above, only the typologies that their mean FRS have spectral values greater than the design plateau value, are accounted for the sensitivity studies. These typologies per area are listed in table 3.11.

Table 3.11: Typologies causing high amplified spectra per area.

Areas	Appingedam	Groningen	Hoogezand	Loppersum	Overschild
Typologies	6, 7	4, 6, 7	6, 7	7	6, 7

For each OOP wall, area and typology considered (including both Hysteretic Rules HR1 and HR2), 11 OOP wall responses are recorded in terms of displacements, since 11 accelerographs are being used per area. These responses are relative to the displacements of the equivalent structure. The maximum values are found for each of these 11 responses. The mean of the maximum wall responses is then derived and compared to the mean of the 11 design displacement responses Δ_{ph} according to NZSEE [28]. This procedure is illustrated in figures 3.54 and 3.55 for direction X and direction Y respectively. The reason for having 11 design responses Δ_{ph} is the height coefficient C_{Hi}, which is found as the ratio of the Peak Floor Accelaration (PFA) over the Peak Ground Accelaration (PGA). This coefficient is different per ground motion, since the response of the equivalent mass of the structure and thus its PFA differs per ground motion. The PGAs of the ground motions of an area slightly differ from each other, because they attempt to indicate the same PGA value in the elastic ground spectrum of that area. For the design displacement responses according to NZSEE [28], the Shape Factor Coefficient $C_{\mathrm{i}}(T_{\mathrm{p}})$ derived from this research is used. The displacement response Δ_{ph} per ground motion is given from the equation:

$$\Delta_{\mathrm{ph}} = C_{\mathrm{i}}(T_{\mathrm{p}}) \cdot C_{\mathrm{Hi}} \cdot C_{\mathrm{i}}(0) \cdot \gamma \cdot (T_{\mathrm{p}}/2\pi)^2 \tag{3.10}$$

where:

$C_{\mathrm{i}}(T_{\mathrm{p}})$	is the Shape Factor Coefficient.
C_{Hi}	is the Height Coefficient, which is found as $\frac{\mathrm{PFA}}{\mathrm{PGA}}$ per ground motion.
$C_{\mathrm{i}}(0)$	is the PGA in m/s^2 per ground motion.
γ	is the participation factor of the out-of-plane rocking mechanism.
T_{p}	is the effective period of the OOP wall.

At this point, it is argued that the Height Coefficient in the simplified 1D model of a structure is related to an “equivalent floor level” of that building. By preserving the definition of the Height Coefficient C_{Hi}, the ratio PFA/PGA is used for the equation 3.10. However, the exact derivation of the Height Coefficient C_{Hi} is implemented in the 3D Model NLTH analyses. This is explained by the ability to monitor the ratios PFA/PGA in each floor level of the 3D Model and derive the Height Coefficient profile through its height.

The results of the analyses are gathered in one plot for each area, typology and direction. In that plot, the mean of the 11 maximum NLTH displacement responses is indicated for each wall. Furthermore, the mean of the 11 design values Δ_{ph} of the response is depicted along with the maximum usable displacement Δ_{m}. Above this threshold, the OOP wall is assumed to fail.

The criteria that should be met for the majority of the walls in order to disregard the impact of the high amplified spectra in the Design Floor Accelaration Spectra are:

1. The ability of the design values to be an upper bound of the actual NLTH responses ($\Delta_{\mathrm{ph}} > \Delta_{\mathrm{NLTH}}$).
2. As secondary criterion, the prediction of the OOP failure from the design response ($\Delta_{\mathrm{ph}} > \Delta_{\mathrm{m}}$), when this failure is resulted from the NLTH response.

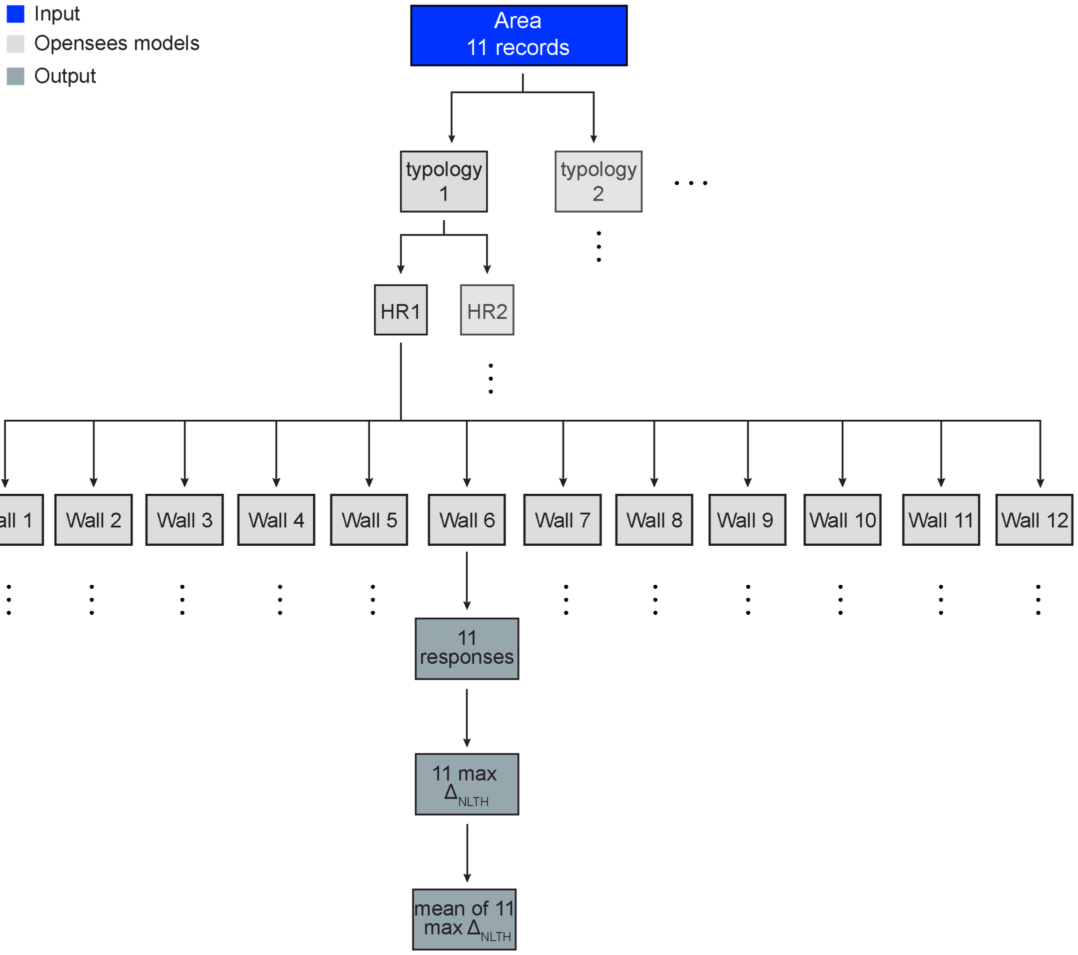
Input
Opensees models
Output
Area
11 records
typology
1
typology
2
. . .
HR1
HR2
Wall 1
Wall 2
Wall 3
Wall 4
Wall 5
Wall 6
Wall 7
Wall 8
Wall 9
Wall 10
Wall 11
Wall 12
11
responses
11 max
Δ NLTH
mean of 11
max Δ NLTH

Figure 3.54: Flow chart of the NLTH analyses regarding the extended 1D models in Opensees for direction X.

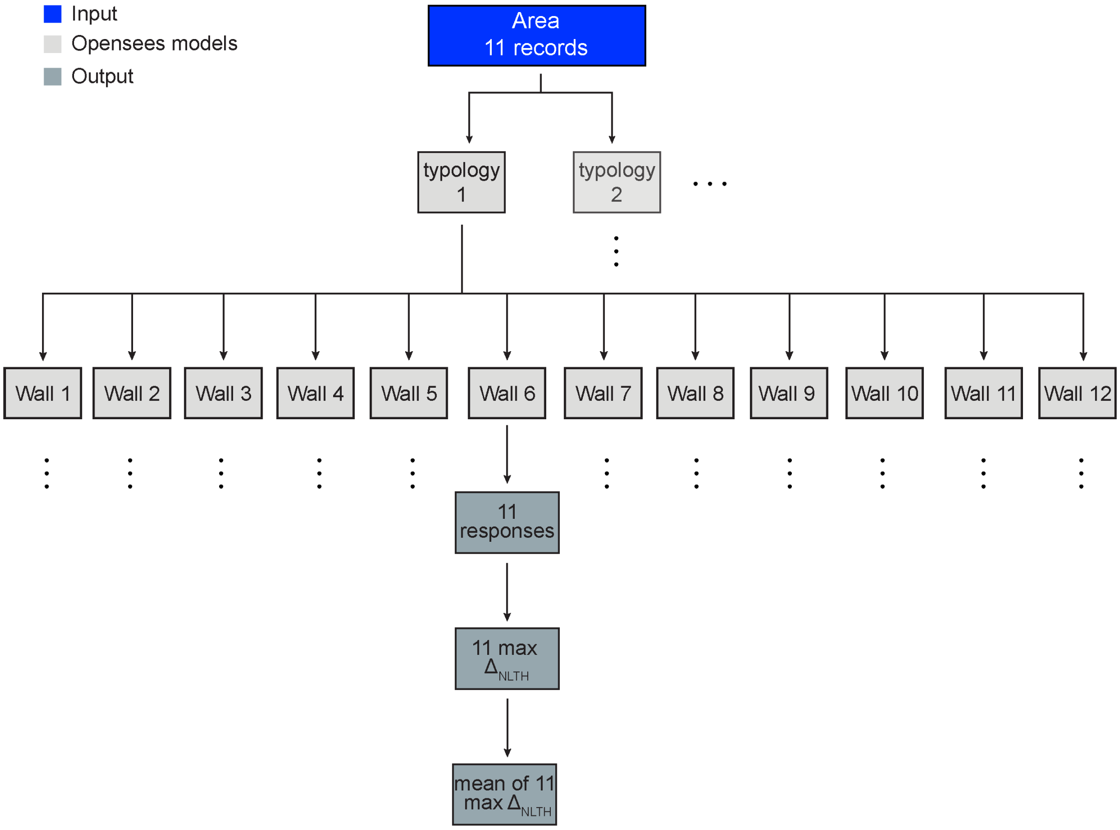
Input
Opensees models
Output
Area
11 records
typology
1
typology
2
. . .
Wall 1
Wall 2
Wall 3
Wall 4
Wall 5
Wall 6
Wall 7
Wall 8
Wall 9
Wall 10
Wall 11
Wall 12
11
responses
11 max
Δ NLTH
mean of 11
max Δ NLTH

Figure 3.55: Flow chart of the NLTH analyses regarding the extended 1D models in Opensees for direction Y.

3.6.6 Sensitivity study of OOP walls - Direction X

3.6.6.1 Appingedam

The prediction of the design response of OOP walls compared to the NLTH response is satisfactory for Appingedam. In detail, the design response Δ_{ph} is greater than the NLTH response for the walls BC1 30kN, BC2 30 kN, BC3 5kN, BC3 15kN, BC3 30kN for both typologies. Additionally, the failure is predicted in walls BC0 5kN, BC0 15kN, BC1 5kN and BC2 5 kN for both typologies. Nevertheless, the NLTH response related to HR1 for the wall BC0 30 kN in typology 6 is slightly greater than the design response. Moreover, the wall is failing for the HR2 according to the NLTH analyses. This is not indicated from the design response. The specific wall has low maximum usable displacement Δ_m. It is reminded that an OOP wall becomes quickly instable and prone to collapse, when its displacement overcomes the displacement of $0.6 \cdot \Delta_m$. That is because the response of the wall is highly dependent on the ground motion characteristics after that point. The same conclusion can be adressed for walls BC1 15kN and BC2 15kN in Typology 6, where failure is indicated from the NLTH response corresponding to HR2, but not from the design response.

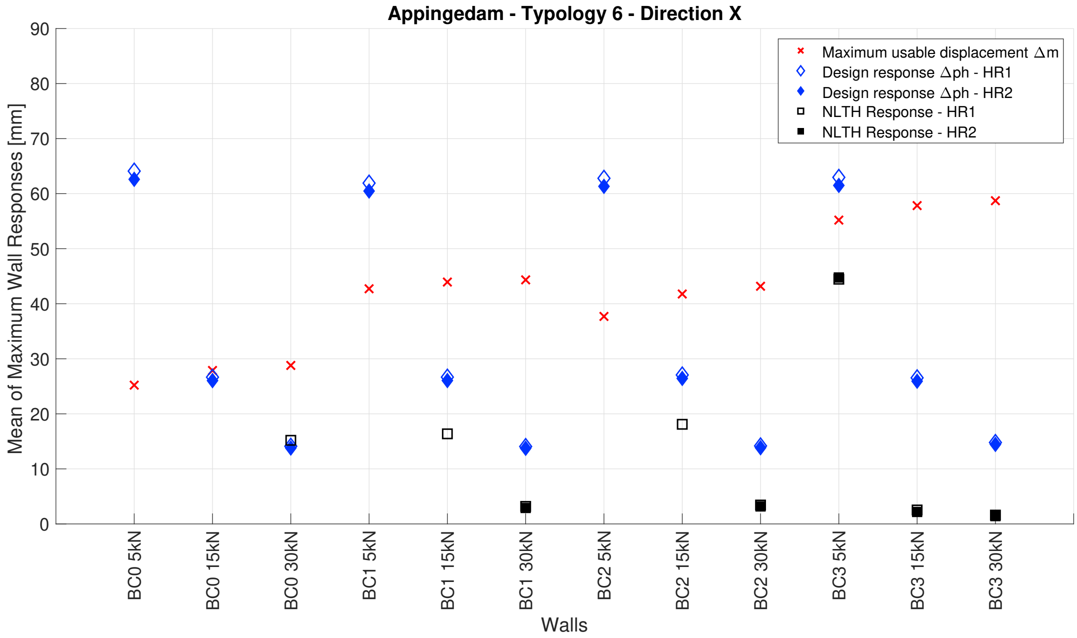

Figure 3.56: Appingedam - Typology 6: design and NLTH response of OOP walls.

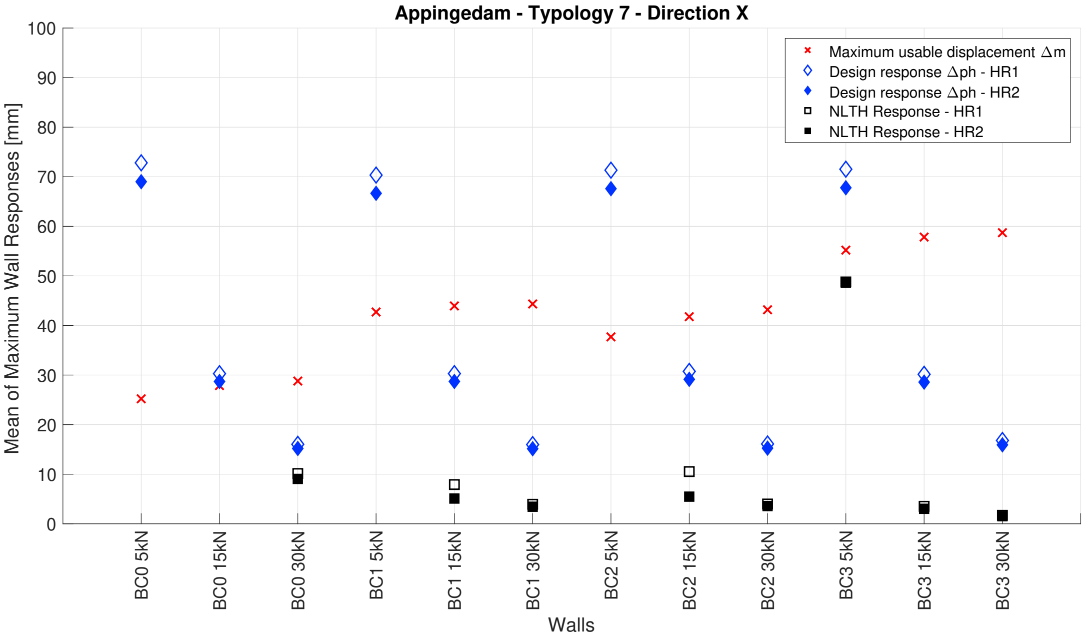

Figure 3.57: Appingedam - Typology 7: design and NLTH response of OOP walls.

3.6.6.2 Groningen

For Groningen Typologies 6 and 7, the design responses Δ_{ph} are greater than the NLTH responses in all the wall configurations. It should be noted, though, that failure is predicted for walls BC0 5kN, BC1 5kN, BC2 5kN for typology 6 and BC0 5kN, BC2 5kN for typology 7 according to the design response, while this is not indicated in the NLTH response. Regarding Typology 4, the design response Δ_{ph} is higher or close to NLTH responses for the majority of the walls. The failure of BC0 5kN is indicated both in the design response and the NLTH response. However, the design response indicates failure for walls BC1 5kN and BC2 5kN, while the NLTH response does not.

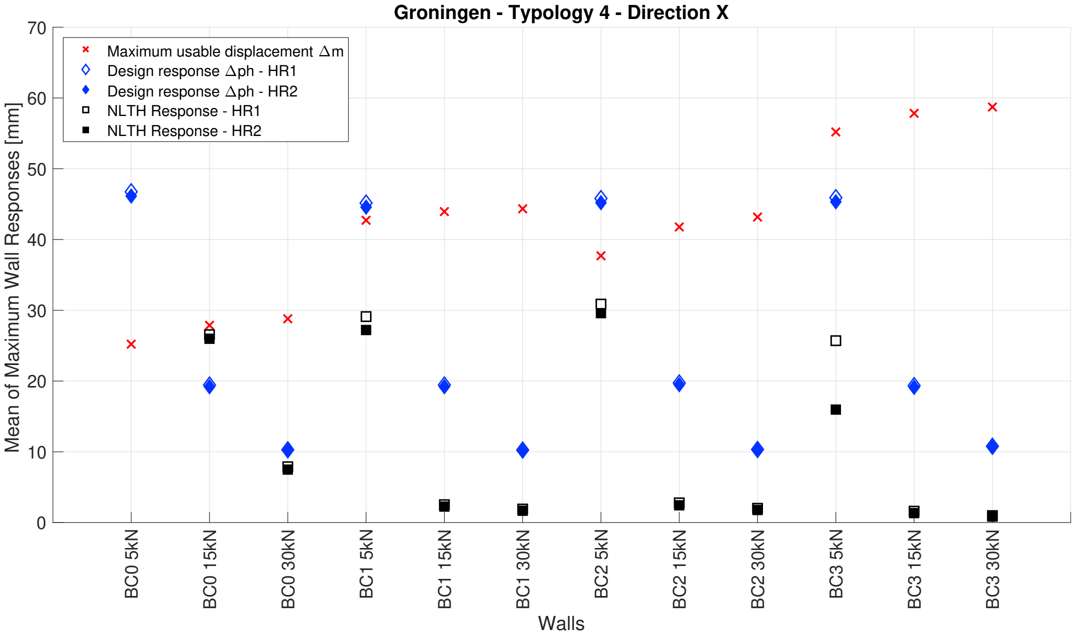

Figure 3.58: Groningen - Typology 4: design and NLTH response of OOP walls.

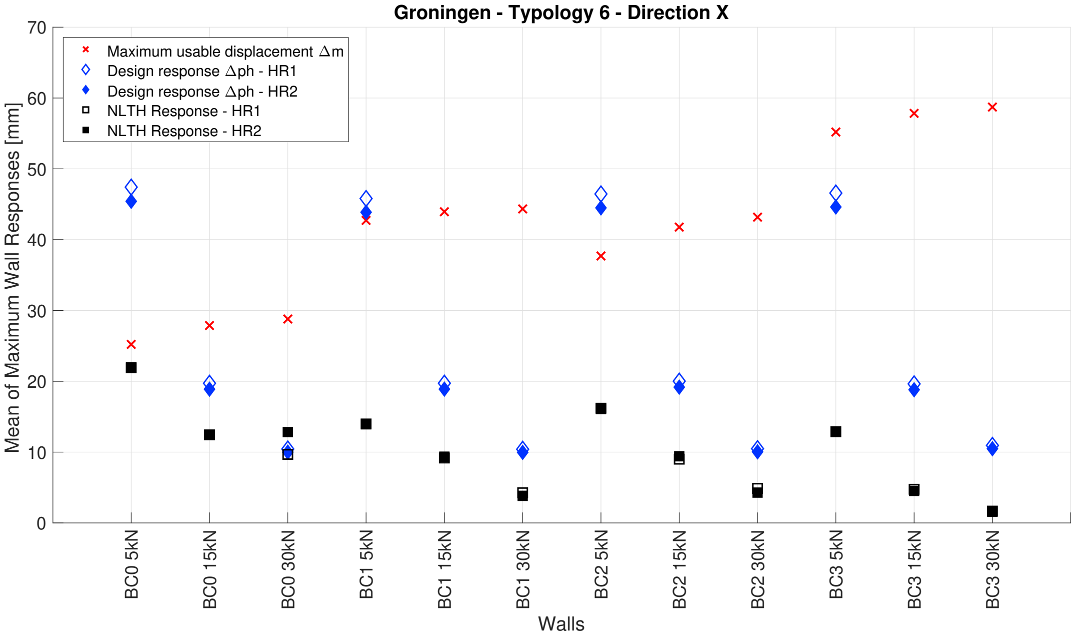

Figure 3.59: Groningen - Typology 6: design and NLTH response of OOP walls.

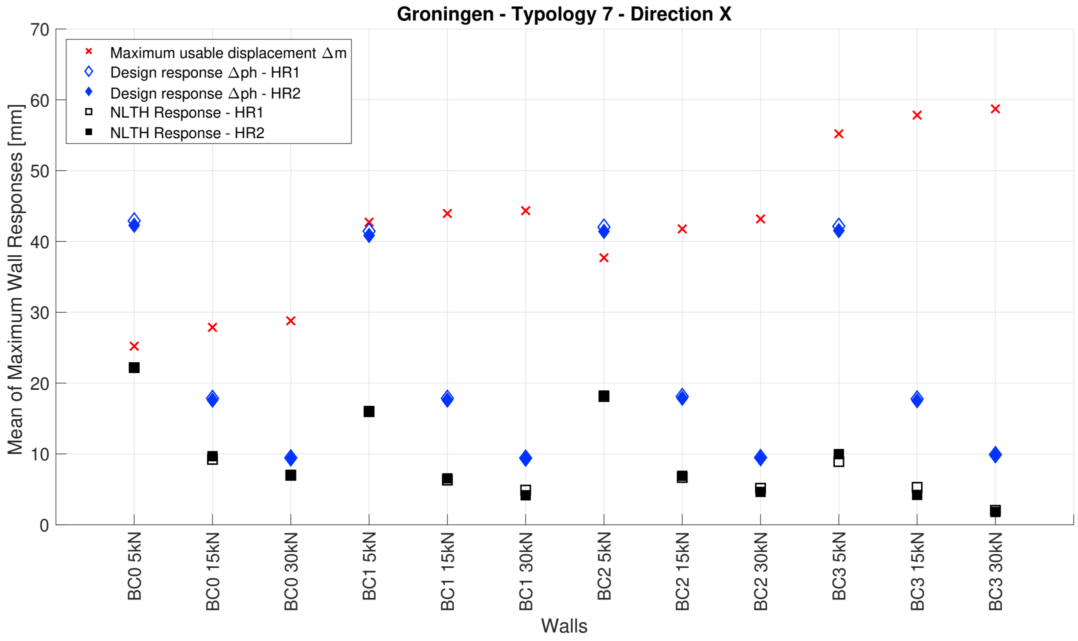

Figure 3.60: Groningen - Typology 7: design and NLTH response of OOP walls.

3.6.6.3 Hoogezand

Regarding Hoogezand area, Typologies 6 and 7 give similar results. The design response act as an upper bound value for the NLTH response in all the wall configurations. Failure of the wall BC0 5kN is indicated from the NLTH analyses and this is predicted from the design response. Nevertheless, the design response indicates failure in walls BC1 5kN and BC2 5kN for both typologies, which is not found in the NLTH responses.

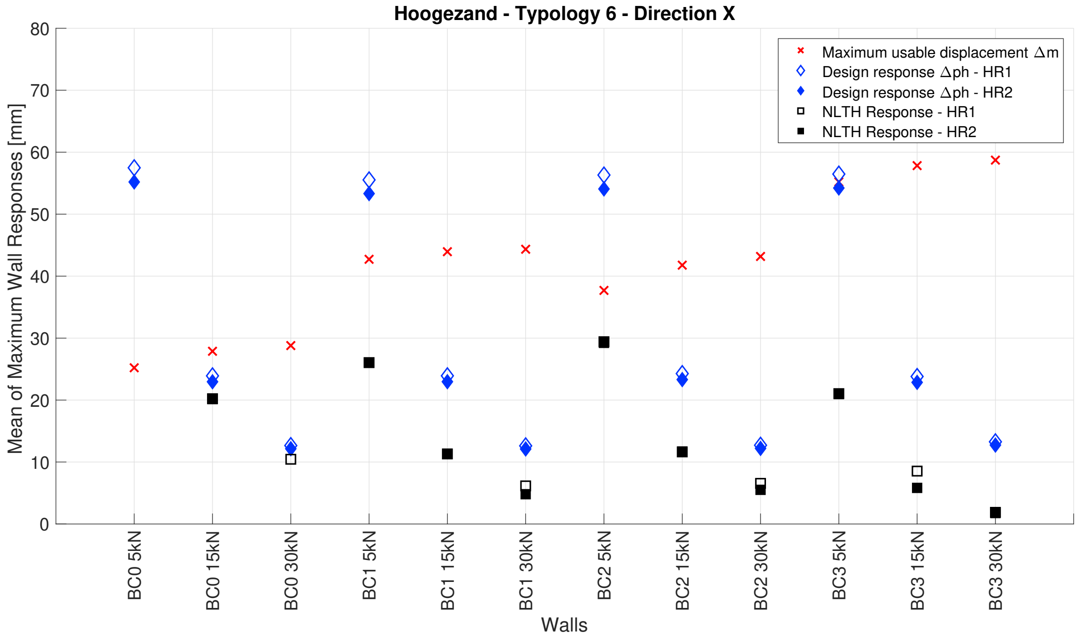

Figure 3.61: Hoogezand - Typology 6: design and NLTH response of OOP walls.

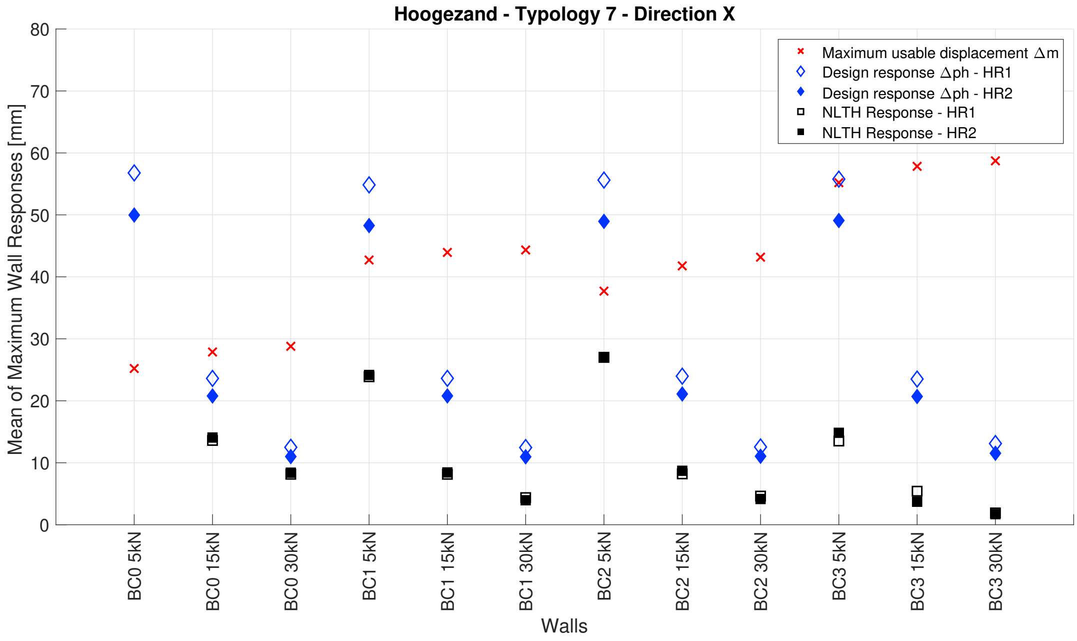

Figure 3.62: Hoogezand - Typology 7: design and NLTH response of OOP walls.

3.6.6.4 Loppersum

In Loppersum, only Typology 7 results to high amplified spectra in direction X. The criterion $\Delta_{ph} > \Delta_{NLTH}$ is met for the walls BC0 30kN, BC1 5kN, BC1 15kN, BC1 30kN, BC2 15kN, BC2 30kN, BC3 5kN, BC3 15kN and BC3 30kN. Nevertheless, while the NLTH response is less than the design response in the cases of walls BC1 5kN and BC3 5kN, design response indicates OOP failure for these walls. Eventually, failure is indicated from both the design and NLTH response in the cases of BC0 5kN, BC0 15kN and BC2 5kN.

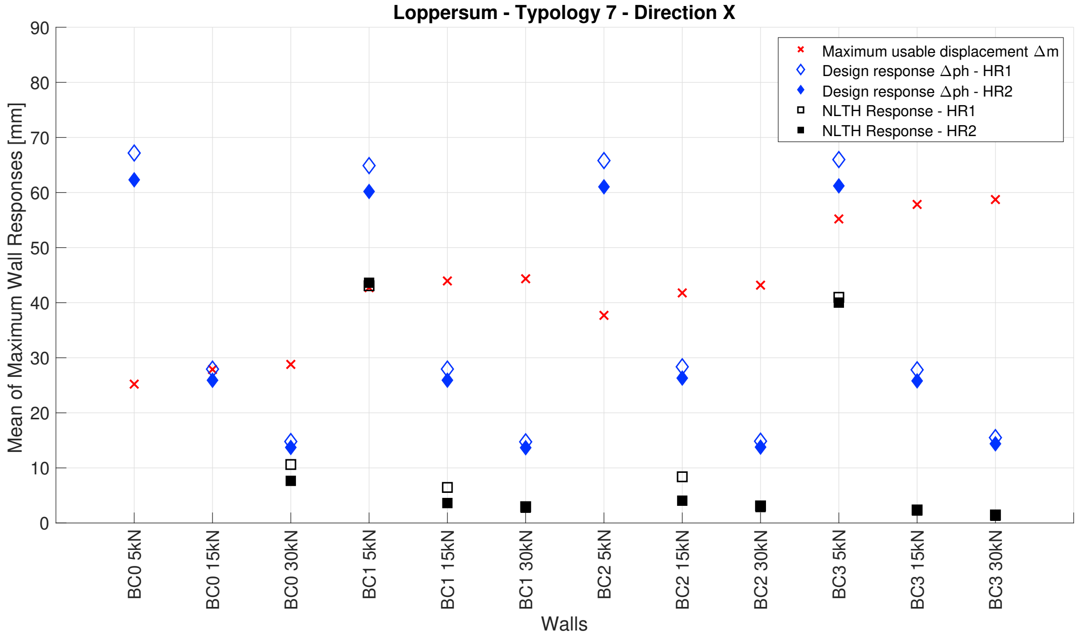

Figure 3.63: Loppersum - Typology 7: design and NLTH response of OOP walls.

3.6.6.5 Overschild

In Overschild, for both typologies, the failure indicated in NLTH response is predicted from the design response for the walls BC0 5kN, BC0 15kN, BC1 5kN, and BC2 5kN. This is also the case for walls BC1

15kN and BC2 15kN in Typology 6. Moreover, the design response is the upper bound of the NLTH response for the walls BC1 30kN, BC2 30kN, BC3 5kN, BC3 15kN and BC3 30kN in Typology 6. The same holds in Typology 7 for the walls BC1 15kN, BC1 30kN, BC2 15kN, BC2 30kN, BC3 5kN, BC3 15kN and BC3 30kN. As far as the wall BC3 5kN is concerned, even though the design response is greater than the NLTH response for both typologies, the NLTH responses overpass or are slightly close to the maximum usable displacement. In that case, the design response indicates failure while NLTH response does not show instability of the OOP wall. The result could be again justified by the fact that an OOP wall is highly sensitive to the ground motion characteristics at these displacement levels. This could lead to a quick instable phase and collapse (similar to the case of the wall BC0 30kN, where failure is obtained from NLTH response but not from the design response) or to a non-collapse event allowing the wall to deform beyond the maximum usable displacement Δm, which is equal to 60 % of its displacement capacity.

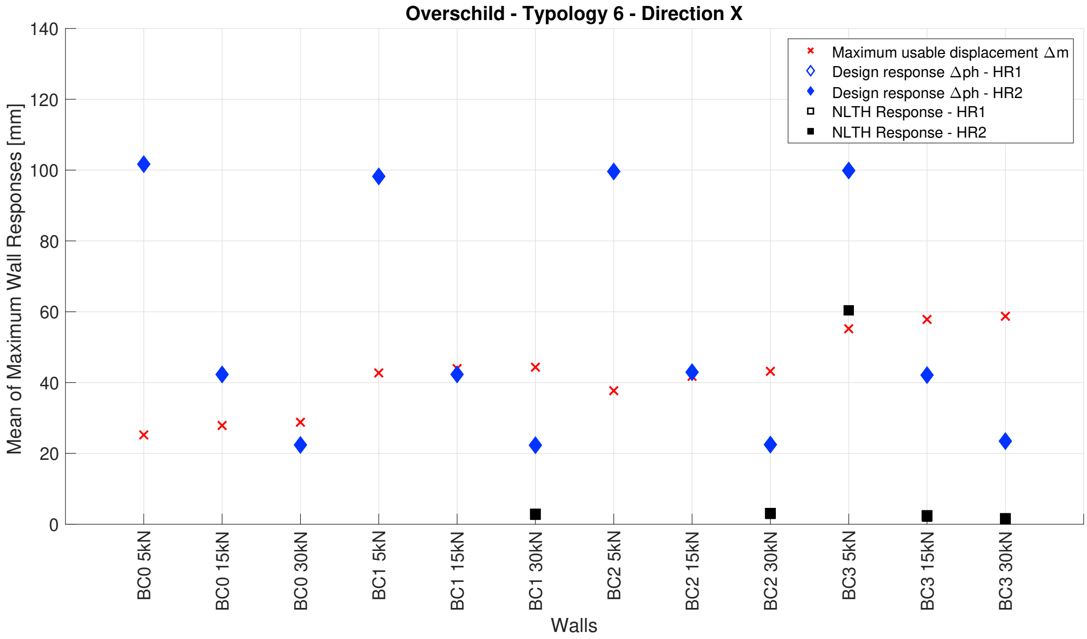

Figure 3.64: Overschild - Typology 6: design and NLTH response of OOP walls.

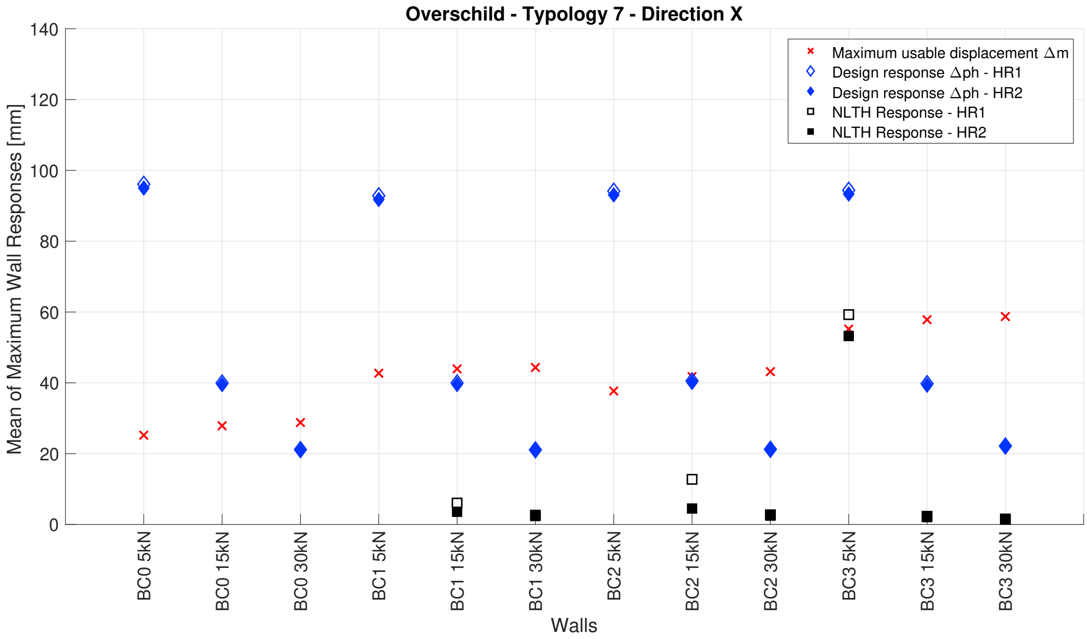

Figure 3.65: Overschild - Typology 7: design and NLTH response of OOP walls.

An overall conclusion for direction X is that the Design Floor Accelaration Spectra act as the upper bound envelope of the out-of-plane responses for the typologies that create high amplified spectra with peak values above the design plateau value. This is justified by the fact that design response Δ_{ph} is greater than the NLTH responses for the non-failing walls and predicts the failure of the walls that failed in the NLTH analyses (failure determined by the NLTH analyses). Nevertheless, when failure is judged by the design response as $\Delta_{ph} > \Delta_{m}$, it is not always indicated in the NLTH analyses.

3.6.7 Sensitivity study of OOP walls - Direction Y

The same procedure is carried out for direction Y of the buildings. The structures remain elastic in direction Y, so all the typologies produce narrow high amplified bell-shaped Floor Response Spectra. The maximum spectral accelarations in the FRS are beyond the plateau value of the derived Design Floor Accelaration Spectra, but only for a small range of periods around the natural periods of the buildings in direction Y. The ability of the design response Δ_{ph} to include the NLTH response will be investigated once more. However in direction Y, since a clearer pattern is observed in the sensitivity study of the OOP walls, their responses from all the typologies per area will be adressed in the same graph.

Similar conclusions are obtained for the direction Y. The design response Δ_{ph} is larger than the NLTH response for all the non-failing walls. Additionally, for all the cases that NLTH response indicates failure, the design response also predicts the failure. Nevertheless, there are specific cases that should be adressed per area.

In Appingedam, for the case of wall BC1 5kN, both NLTH response and design response pass the maximum usable displacement Δ_{m}. Design response indicates failure under these circumstances. However, in the NLTH analyses, the OOP wall does not fail. Moreover, regarding the wall BC3 5kN in Appingedam, the design response exceeds the Δ_{m} displacement which results in failure, whereas the NLTH analyses do not indicate failure. The same scenario is met in:

-Groningen for walls BC0 5kN, BC1 5kN, BC2 5kN

-Hoogezand for walls BC1 5kN, BC2 5kN

-Loppersum for wall BC1 5kN

-Overschild for wall BC3 5kN

These two correlations of the NLTH and design response are already explained in the section of the sensitivity study of OOP walls in direction X. The explanation is based on the significant sesitivity of the OOP wall in the ground motion characteristics after the out-of-plane displacement of $0.36 \cdot \Delta_{instability}$.

The only cases that failure of OOP walls is indicated by NLTH analyses and is not predicted from the design response in direction Y, are wall BC0 15kN in Loppersum and wall BC0 30kN in Overschild. For wall BC0 15kN the design response is rather close to displacement Δ_{m}, however for wall BC0 30kN the difference between the design response and Δ_{m} is not negligible.

3.6.7.1 Appingedam

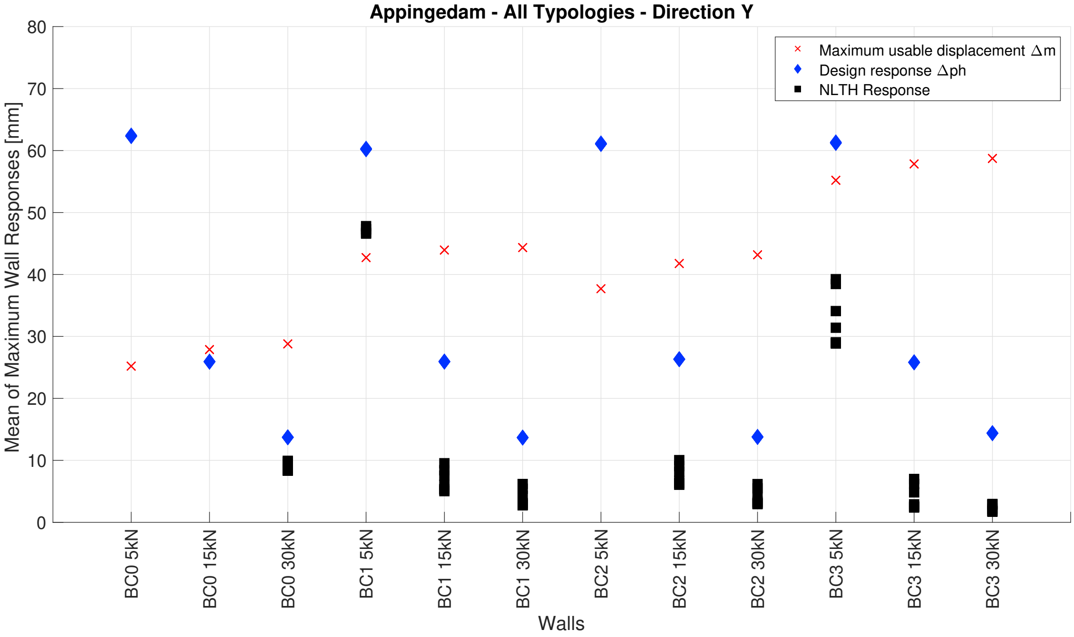

Figure 3.66: Appingedam: design and NLTH response of OOP walls.

3.6.7.2 Groningen

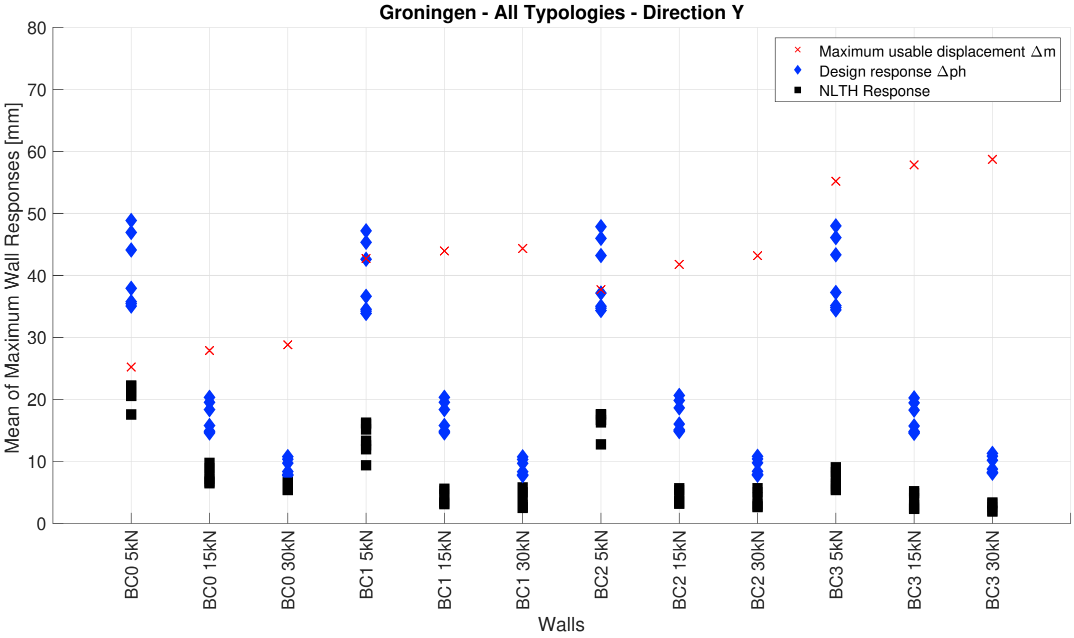

Figure 3.67: Groningen: design and NLTH response of OOP walls.

3.6.7.3 Hoogezand

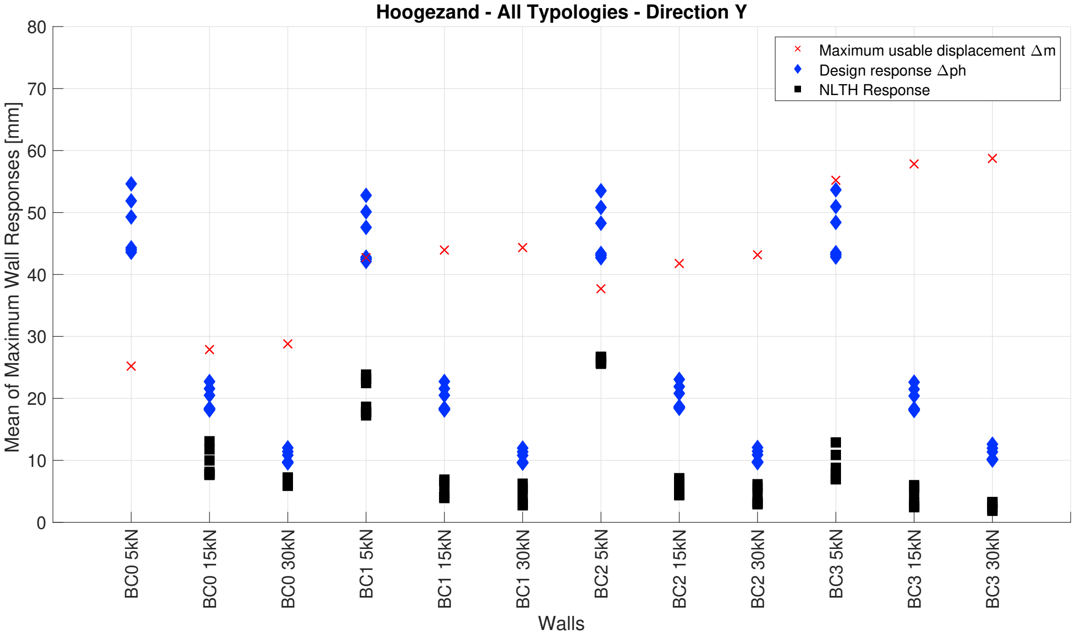

Figure 3.68: Hoogezand: design and NLTH response of OOP walls.

3.6.7.4 Loppersum

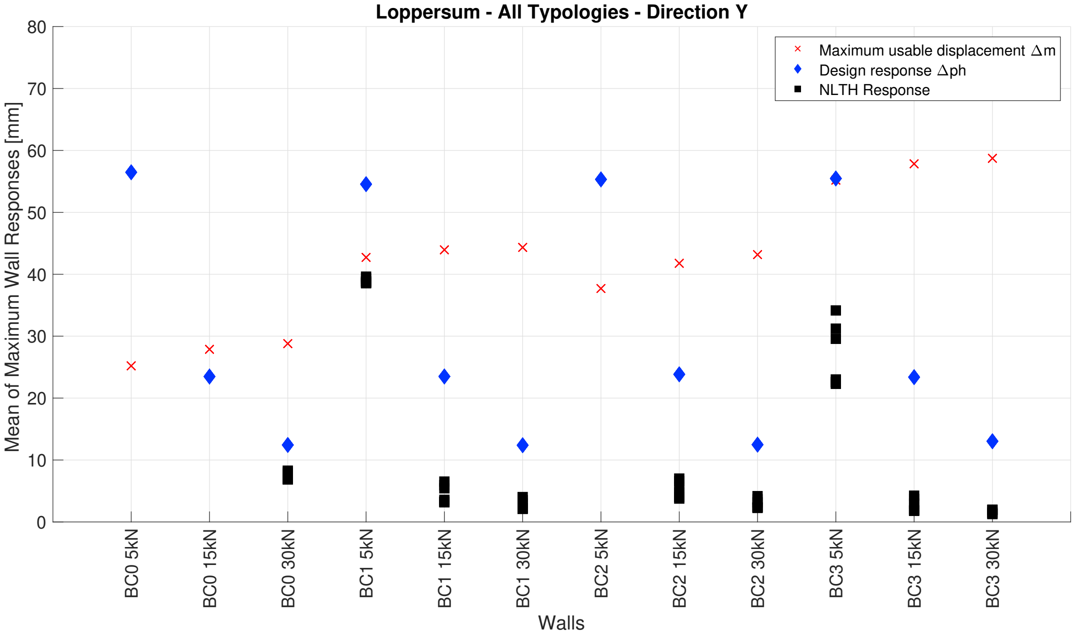

Figure 3.69: Loppersum: design and NLTH response of OOP walls.

3.6.7.5 Overschild

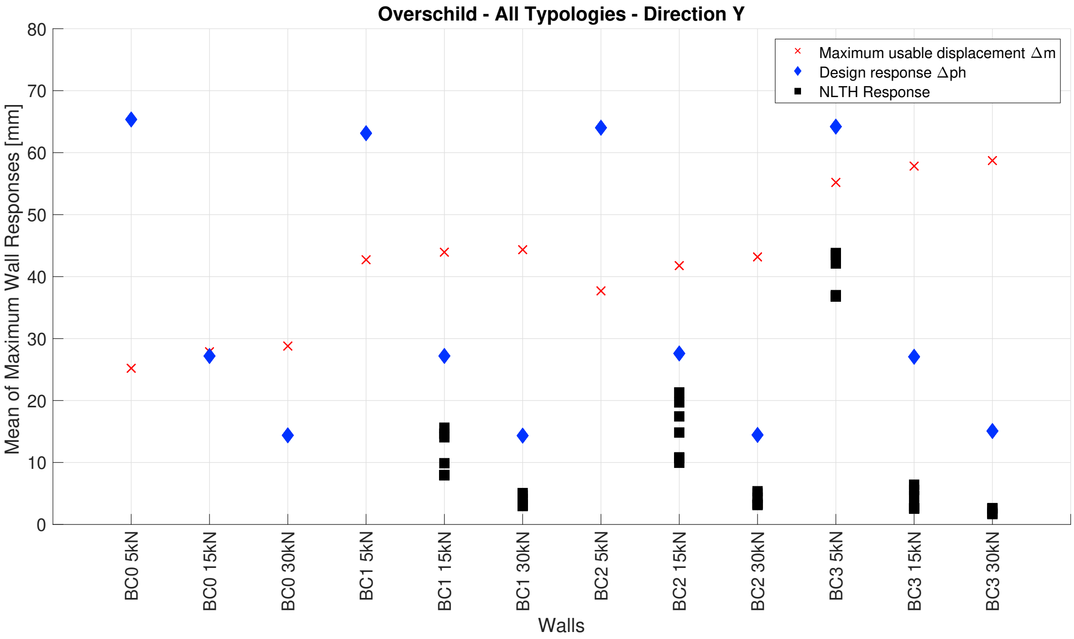

Figure 3.70: Overschild: design and NLTH response of OOP walls.

3.7 Shape Factor Coefficient for the Groningen Case

The Design Spectra produced for the Groningen Case cover the shape of the mean FRS of Typologies 1 to 5 for all the areas, while Typologies 6 and 7 resulted to high amplified spectra with peak spectral accelaration values above the design plateau level. Consequently, sensitivity studies of OOP walls in direction X and Y for these typologies were performed aiming to compare the design response with the NLTH actual response.

The sensitivity studies led to the following conclusions:

1. Design response Δ_{ph} is an upper bound value of the NLTH response for all the cases of the non-failing OOP walls.

2. When NLTH response indicates failure, design response predicts this failure.

3. When design response indicates failure (design displacement Δ_{ph} is larger than the maximum usable displacement Δ_{m}), it is not always indicated by the NLTH response. However, the design response is still greater than the NLTH response (Δ_{ph}>Δ_{NLTH}).

In the figures below, the normalised Design Floor Accelaration Spectra are depicted with and without the high amplified spectra. The mean FRS shapes are in agreement with the normalised Design Floor Accelaration Spectrum per area.

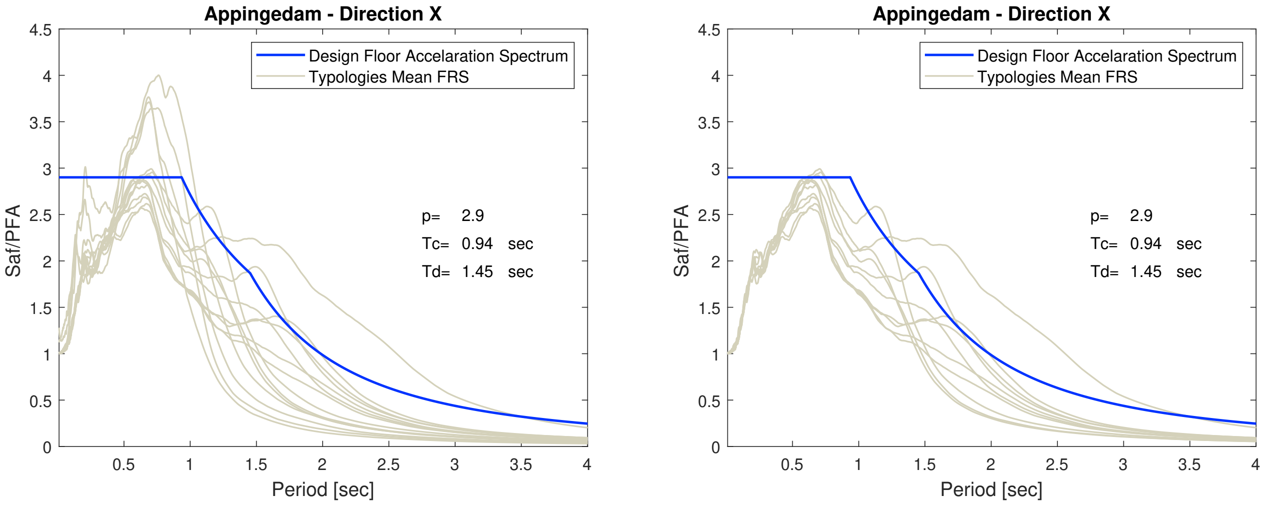

Figure 3.71: Appingedam: with (left) and without (right) the high amplified spectra.

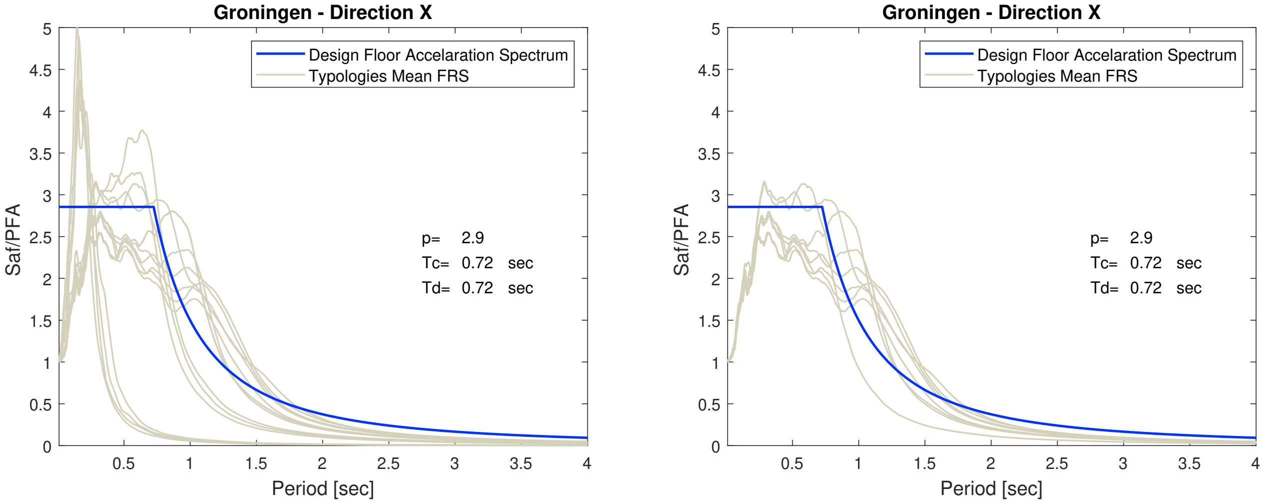

Figure 3.72: Groningen: with (left) and without (right) the high amplified spectra.

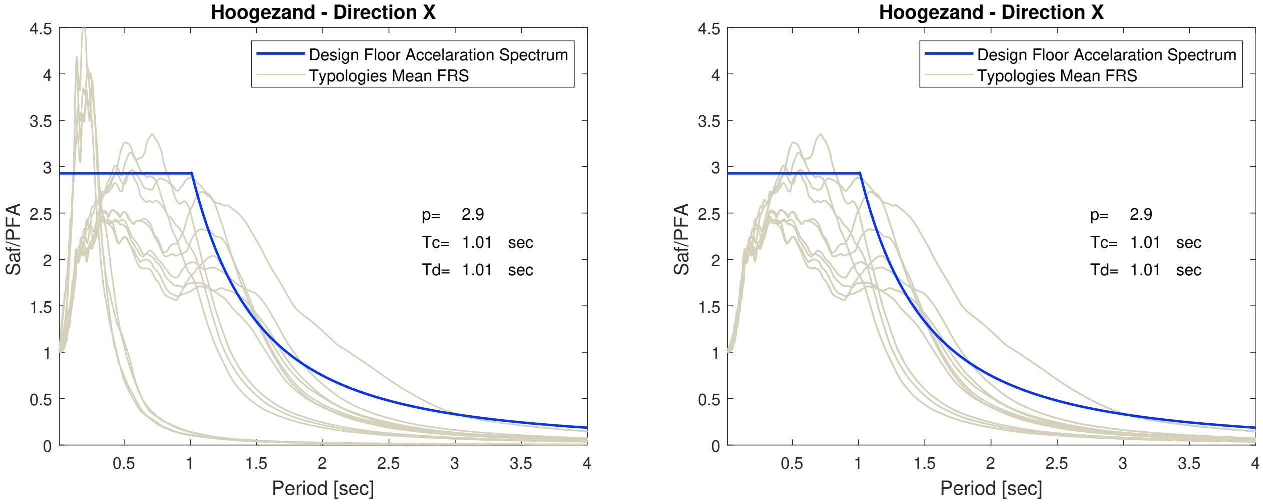

Figure 3.73: Hoogezand: with (left) and without (right) the high amplified spectra.

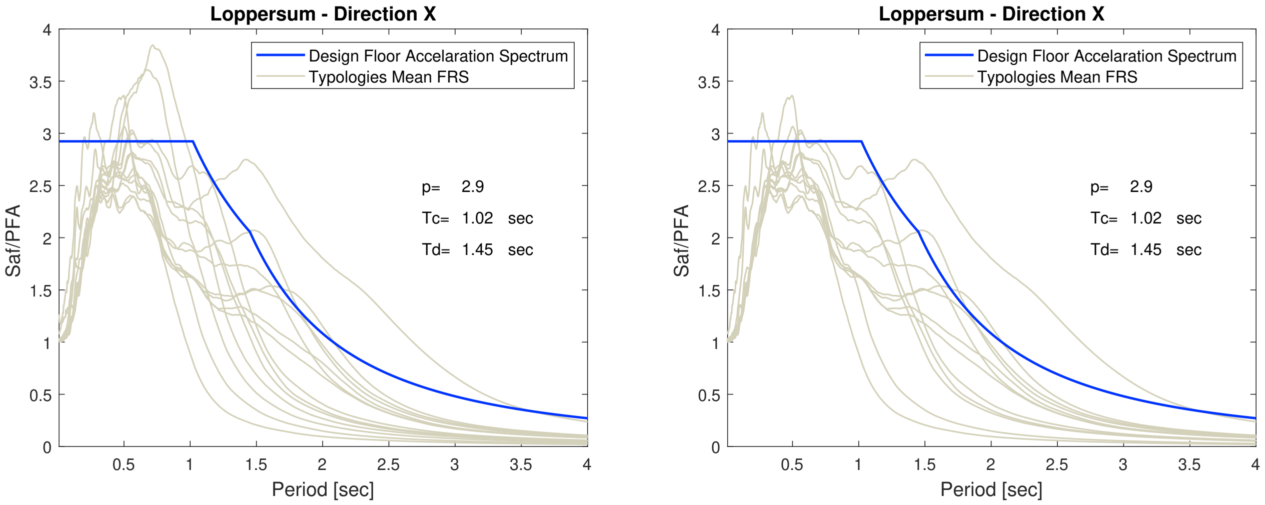

Figure 3.74: Loppersum: with (left) and without (right) the high amplified spectra.

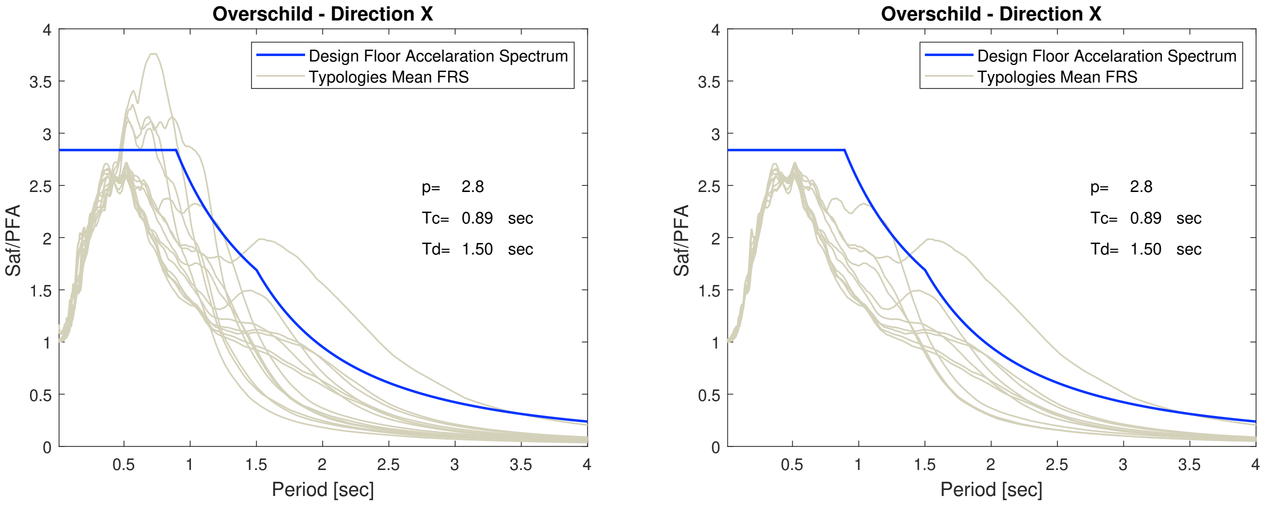

Figure 3.75: Overschild: with (left) and without (right) the high amplified spectra.

The ratio between the peak ground accelaration and the plateau value of the elastic response spectrum p, the corner period T_C and the period that indicates the start of the constant displacement response of the spectrum T_D, were obtained from the Newmark - Hall method per area. The values of these parameters are presented in table 3.12. The Shape Factor Coefficient $C_i(T_p)$ is defined as:

$$C_i(T_p) = p \qquad 0 \le T_p \le T_C \tag{3.11}$$

$$C_i(T_p) = p \cdot \frac{T_C}{T_p} \qquad T_C \le T_p \le T_D \tag{3.12}$$

$$C_i(T_p) = p \cdot \frac{T_C \cdot T_D}{T_p^2} \qquad T_p \le 4 \tag{3.13}$$

Table 3.12: Shape Factor Coefficient parameters per area.

	Appingedam	Groningen	Hoogezand	Loppersum	Overschild
p	2.9	2.9	2.9	2.9	2.8
T_C	0.94	0.72	1.01	1.02	0.89
T_D	1.45	0.72	1.01	1.45	1.5

Chapter 4

3D Model

In this chapter the Shape Factor Coefficient obtained from the simplified 1D Models is compared with the results of the NLTH analyses of a 3D Model. Moreover, the description of the Height Coefficient C_{Hi} is issued. Only one building typology (Typology 1) is considered for the 3D analyses. The 3D Model is related to the complete structure of the typology, consisted of four identical terraced houses. The respective 1D Model was considered as the submodel of the structure (one terraced house) in the in-house studies that provided the SDOF characteristics. The software employed for the implementation of the NLTH analyses is ANSR-II. It is a finite element method (FEM) software, developed at the University of California, Berkeley in the 1970's.

4.1 Modelling in ANSR-II

ANSR-II uses the Macro-element based modelling approach. According to this approach, each finite element represents a component of the structure (i.e. a wall panel). FEM softwares using this method often provide a set of hysteretic rules and backbone relationships that describe the element hysteretic behaviour and plasticity. These are in agreement with experimental test data, standards and guidelines. Furthermore, the mortar joints are not modelled in the Macro-element based approach, in contrast to more detailed FEM approaches (Micro-Modelling and Macro-modelling). In addition, the capture of local failure mechanisms (i.e. toe crushing of a rocking pier) or the interaction of flexure and shear in masonry walls is not possible with this method. These abilities are provided only by Micro-Modelling approaches. However, it presents advantages against to more detailed methods. These are the computational time efficiency and the numerical stability.

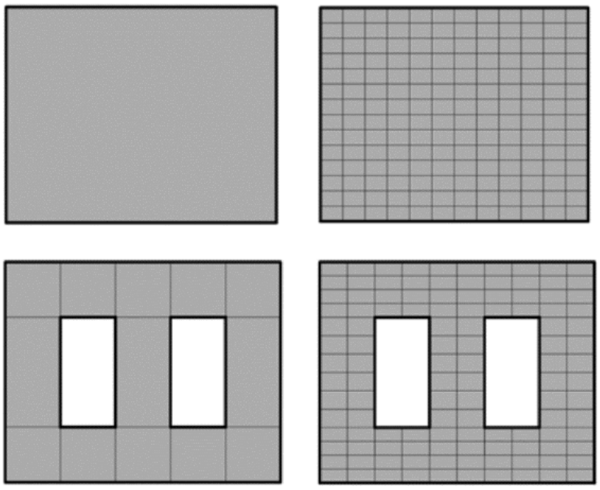

Figure 4.1: Macro-element based Modelling (left) and Micro-Modelling (right) finite element arrangement [29].

4.1.1 Modelling information

Grid definition is the basis for creating a finite element model in ANSR-II. The grid is defined in two horizontal directions (X and Z) and one vertical direction (Y). The global coordinate system of the software is depicted in figure 4.2. Column lines in the plan view and elevations that define the horizontal levels are used for the definition of the geometry of the structure. Nodes are created from the intersection of the column lines and the elevations. Each node has six degrees of freedom (DOFs): three translational (DOF X, DOF Y, DOF Z) and three rotational (DOF XX, DOF YY and DOF ZZ).

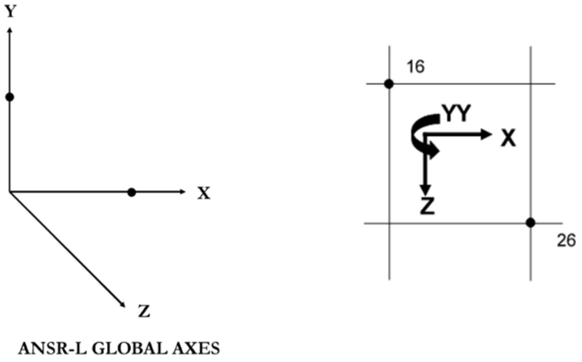

Figure 4.2: ANSR-II global axes [18].

Structural wall elements in ANSR-II are modelled as plane stress or membrane elements. Plane stress elements are 4 node stress elements with in-plane stiffness only and they are intended to model shear deformations. The constitutive equation that describes the shear stress - shear strain relationship depends on the capacity curve envelope for shear walls found at NZSEE Norm [28]. The capacity curve envelope and the nonlinear behaviour of these elements is described in section 4.1.5.

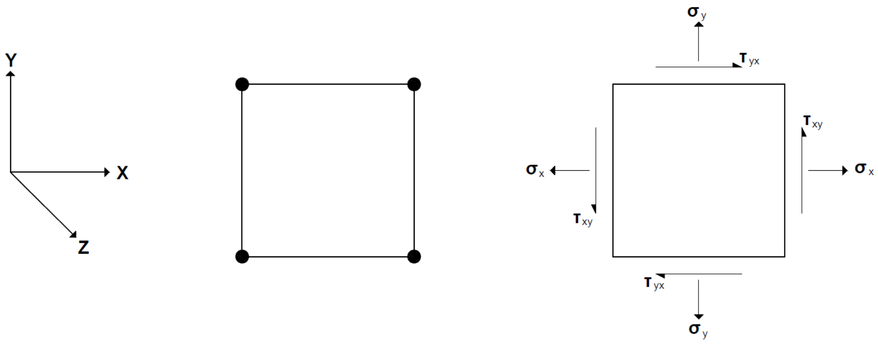

Figure 4.3: Plane stress element schematisation.

4.1.2 Mesh definition

The mesh of the wall panels is highly dependent on the continuity of the load path. The grid of the plane elements is selected so as corners of adjacent elements meet at a common node to form a continuous structure. Incompatibilities in adjacent elements can lead to the wrong generation of stresses and deformations.

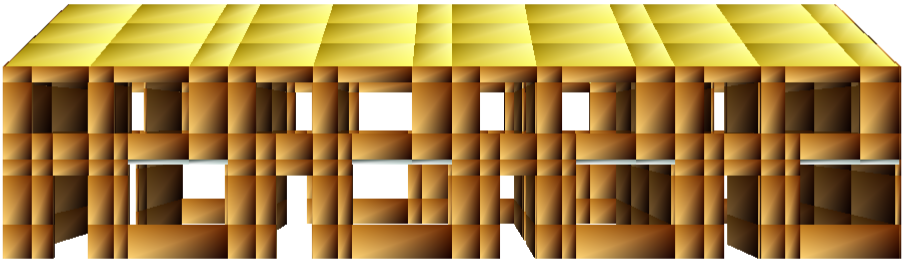

Figure 4.4: ANSR-II 3D Model.

In figure 4.5 the mesh of the side view of the structure is illustrated. The grey panels surrounded by the green lines are the plane stress elements that resemble the wall piers and spandrels. Furthermore, the gap elements and massless beam elements (“dummy” beams) are depicted in the figure. The necessity of these elements is described on sections 4.1.3 and 4.1.6. The grid ensures the continuity of the load path in a static as well as in a dynamic situation. For instance, if a pier is prone to rock, the vertical force is transferred from its toe to the intermediate node of the spandrel below, which is then delivered to the intermediate node of a pier or spandrel in the lower levels. In figure 4.6 the mesh of the shear walls in the strong direction of the structure is presented. The length of the membrane elements are correlated to the flanges effective length.

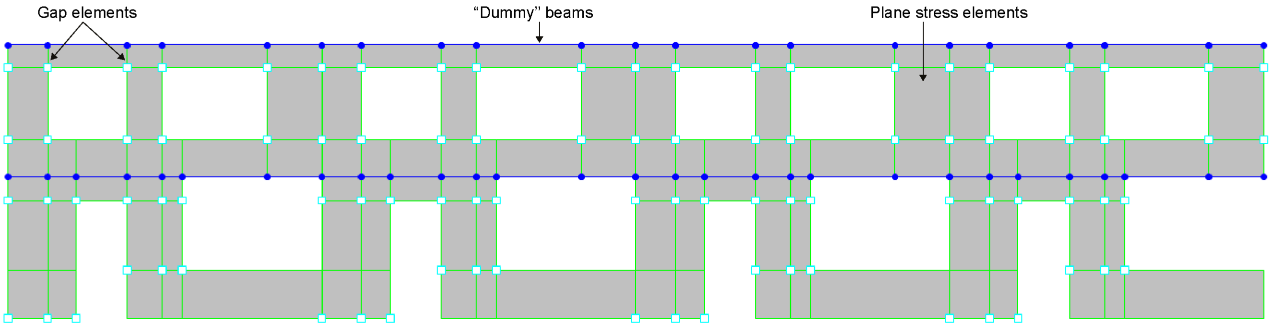

Figure 4.5: Mesh of the wall panels of the 3D Model according to Macro-element based modelling methodology.

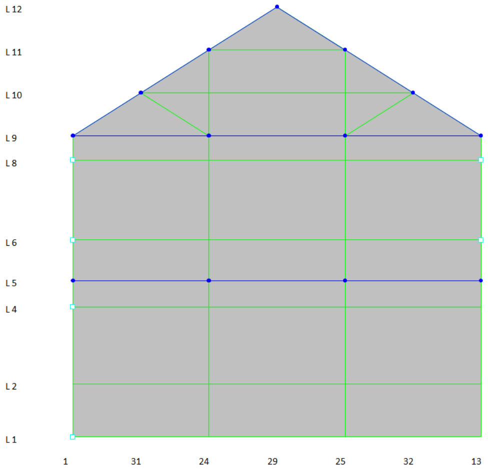

Figure 4.6: Mesh of the shear walls in direction Y.

The mesh continuity is a significant aspect in order to capture the right load path. Nevertheless, it might lead to piers consisting of two or more plane stress elements. As it is explained later, a plane-stress element in ANSR-II is described by a nonlinear hysteretic behaviour and a standardised backbone curve for shear failure mechanisms. Consequently, the material properties of a meshed pier need to be adjusted in order to match the behaviour of the respective single membrane element pier.

The majority of the meshed piers in the 3D Model consist of 2 plane stress elements (right side of figure 4.7). Only exception is one meshed pier in the ground floor, which is discretised to 4 plane stress elements (left side of figure 4.7). The shear deformations of the meshed piers with 2 and 4 plane stress elements are indicated in figures 4.8 and 4.9 respectively. In addition, in figure 4.9 the expected deformed shape of the single element pier is illustrated in the right side.

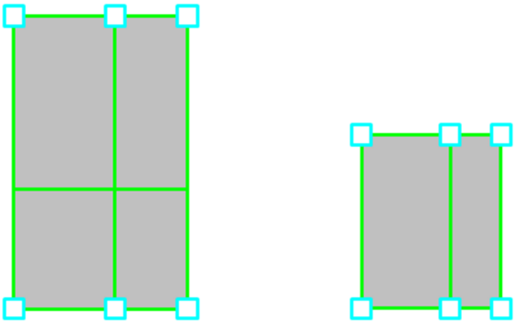

Figure 4.7: Meshed piers in the 3D Model.

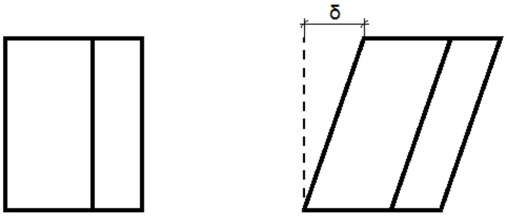

Figure 4.8: 2 plane stress element meshed pier (left) and shear deformation profile (right).

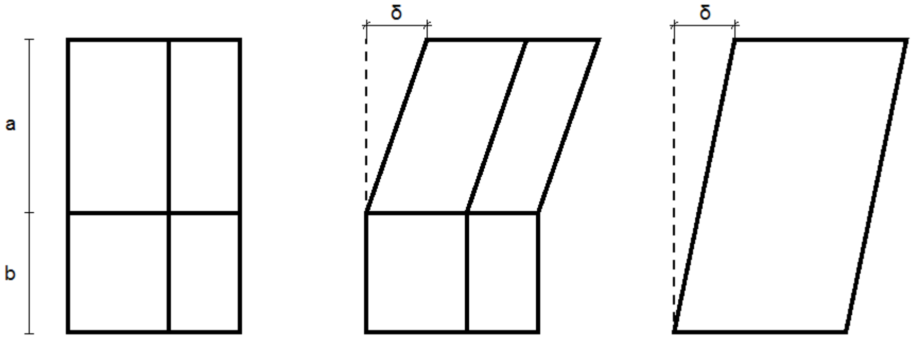

Figure 4.9: 4 plane stress element meshed pier (left) and shear deformation profiles of it (middle) and of the single element pier (right).

Submodels with the meshed and entire piers are created and displacement pushover analyses are implemented for both cases. The results of the submodels for the meshed piers with the 2 plane stress elements indicate a good agreement in terms of capacity curves and hysteretic behaviours with the results of the respective single element piers (figure 4.10). No adjustment of the material properties is needed.

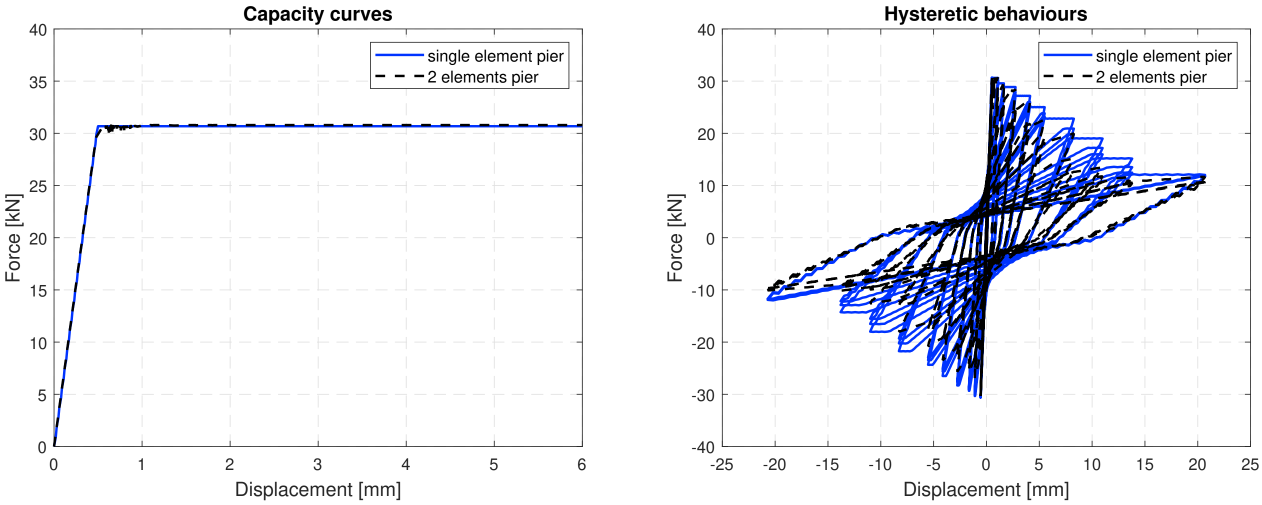

Figure 4.10: Capacity curves and hysteretic behaviours of a meshed pier consisted of 2 plane stress elements and the respective single element pier.

This is not the case for the meshed pier depicted in figure 4.9. In a cyclic pushover in ANSR-II, the shear deformation profile is the one depicted in the middle, while for the single plane stress element pier is the one in the right of the aforementioned figure. With no adjustment in the material properties, the capacity curves and hysteretic behaviours of the two submodels are indicating in figure 4.11. It is observed that the initial capacity is the same for the two piers, however the meshed pier presents lower stiffness. Comparing the cyclic behaviours, the residual capacity of the two piers are different (lower for the meshed pier).

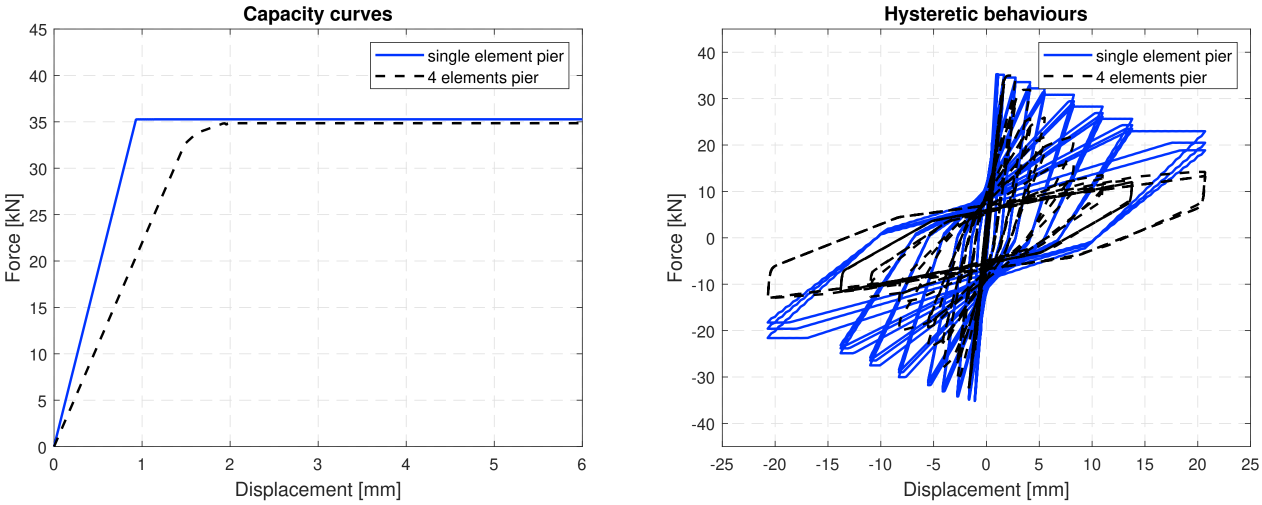

Figure 4.11: Capacity curves and hysteretic behaviours of a meshed pier consisted of 4 plane stress elements and the respective single element pier before the adjustment of the material properties.

In order to equate the stiffness of the meshed pier with the one of the single element pier, the Young's and Shear Modulus are adjusted so as the ratio of the moduli between the meshed and the single element pier equals the ratio of their heights (equations 4.1 and 4.2).

$$E_{meshed} = \frac{a+b}{a} \cdot E_{single} \tag{4.1}$$

$$G_{meshed} = \frac{a+b}{a} \cdot G_{single} \tag{4.2}$$

The dimensions a and b are depicted in figure 4.9. For the adjustment of the residual capacity of the meshed pier, the cohesion c is reduced and the friction coefficient μ is increased, in order to match the initial capacity and the cyclic behaviour of the single element pier (figure 4.12).

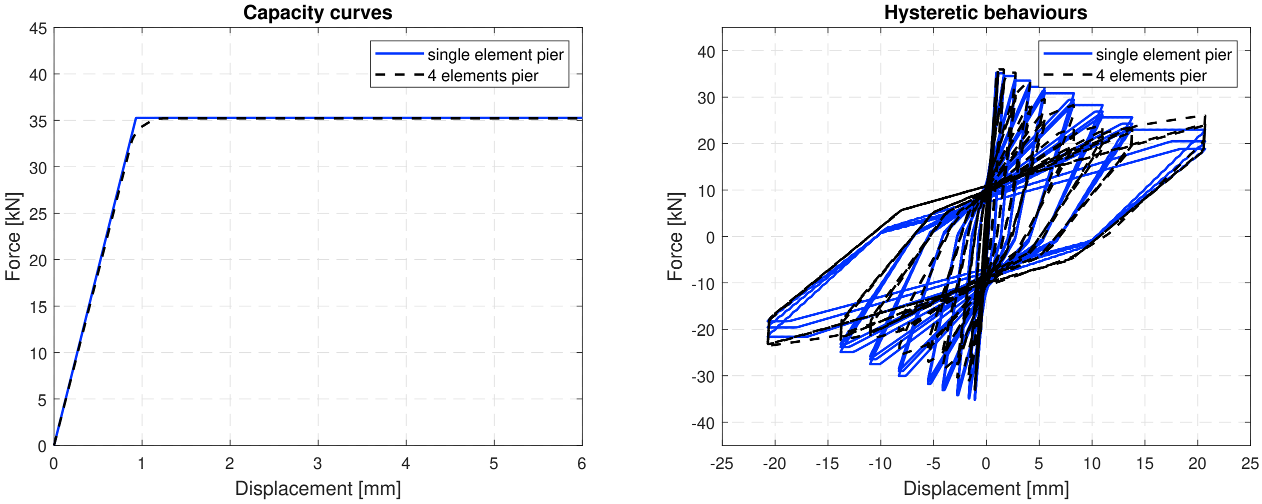

Figure 4.12: Capacity curves and hysteretic behaviours of a meshed pier consisted of 4 plane stress elements and the respective single element pier after the adjustment of the material properties.

Regarding the rocking behaviour of meshed piers, no adjustment is necessary, because the plane stress elements do not yield and no hysteresis is incorporated in the in-plane rocking mechanism. When a meshed pier rocks in a cyclic displacement pushover in ANSR-II, it behaves exactly as the respective single membrane element pier.

4.1.3 Masses and weights

ANSR-II assigns mass at any of the six degrees of freedom per node. If a degree of freedom is fixed, the mass assigned to it will be ignored. The software assembles the mass from:

1. Diaphragm mass and mass moments of inertia.
2. Mass assigned from element self-weight and/or distributed loads on beam elements.
3. User specified translational or rotational mass at specific nodes.

The mass of a plane stress element is assigned equally to its nodes and applied as a nodal translational mass in each of the three directions. However, since the plane stress element has no out-of-plane stiffness, the translational DOF corresponding to the out-of-plane direction is fixed and the mass is ignored. In order to recover the mass in the out-of-plane direction, ANSR-II provides an option called “Assign Missing Mass Vertically”. This command will assign the missing mass to the nearest node, which has the respective degree of freedom free. Masses are cumulative to masses already specified at a node. A mass density should be specified for the materials, otherwise no mass will be generated. Regarding the 3D Model related to this research, it is chosen the plane stress element weights to be generated by using the material weight density and the element area or thickness. The element weight is distributed equally to each node of the element, analogously with the mass distribution.

In general, the generation of the element and diaphragm masses and weights in ANSR-II can be related, but it can be defined independently, as well. Hence, a mass can be determined without being translated to weight and vice-versa. As far as the weight of the rigid diaphragm is concerned, there is the choice of generating the weight from its mass. However this is not used in this modelling process. ANSR-II allows the definition of the diaphragm translational and rotational masses at the center of its mass (CoM), while the weight can be assigned independently either as a distributed load in massless beam elements (“dummy” beams) above the wall panels and spandrels or beam elements that resemble concrete beams (lintels). Regarding the flexible diaphragms, these are modelled as plane stress elements. Consequently, masses and weights are generated similarly to the masonry panels.

4.1.4 Unreinforced masonry properties

The unreinforced masonry material properties are in agreement with the Draft NPR Norm [12]. These are presented in the table below:

Table 4.1: Unreinforced masonry properties.

Compression Strength f_m (MPa)	7
Young's Modulus E_m (MPa)	4000
Shear Modulus G_m (MPa)	1650
Bed-joint Cohesion c (kPa)	250
Coefficient of Friction μ_f	0.6

4.1.5 Unreinforced masonry shear walls

Unreinforced masonry (URM) walls that are prone to shear failure mechanisms are modelled as nonlinear membrane elements. These elements in ANSR-II include cyclic stiffness and strength degradation rules to describe the hysteresis profile of a shear URM wall through a seismic excitation. For the shear walls of the 3D Model, the so called "NZSEE MASONRY URM 2016 Bed Joint Sliding Only" element type is used. This element is described by the Bed Joint Sliding standardised backbone curve and Takeda hysteresis rule, as depicted in figure 4.13. The considered material properties ensure that Bed Joint Sliding failure mechanism governs and not Diagonal Tension. As it is expected, this element type predicts the exact shear bed joint sliding capacity given from NZSEE [28] and Annex G of Draft NPR 9998:2017 Norm [12]:

$$V_s = 0.7 \cdot (t_{nom} \cdot L_w \cdot c + \mu_f \cdot (P + P_w)) \tag{4.3}$$

where:

t_{nom}	is the thickness of the wall, in mm.
L_w	is the length of the wall, in mm.
c	is the masonry bed-joint cohesion, in kN/mm^2.
μ_f	is the masonry coefficient of friction.
P	is the superimposed and dead load at the top of the wall/pier, in kN.
P_w	is the self-weight of the wall/pier above the sliding plane being considered, in kN.

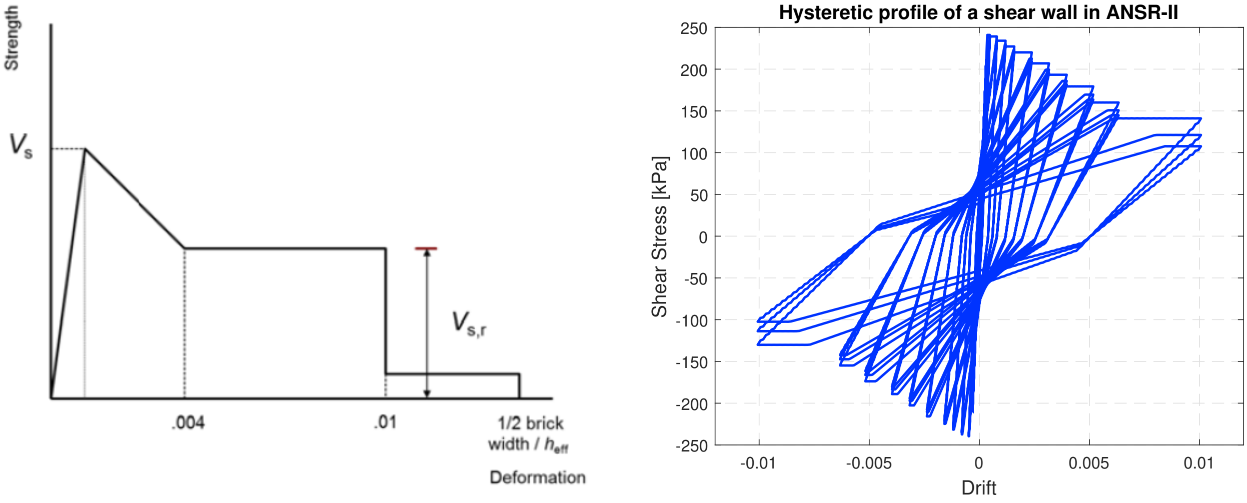

Figure 4.13: Bed Joint Sliding standardised backbone curve (left) and shear hysteresis for unreinforced masonry shear walls under cyclic loading in ANSR-II (right).

4.1.6 Unreinforced masonry rocking piers

The plane stress elements in ANSR-II are designed to model only shear deformations. The accuracy of this type of elements is low when the deformations are dominated by flexure. Thus, the in-plane rocking failure mechanism of masonry piers should be modelled with a different technique. For this purpose, ANSR-II provides gap elements that can be introduced in the corners of the membrane elements. The gap elements are defined as elastic compression zero tension spring elements which allow the uplift to occur when the uplift force exceeds the gravity force. The prediction of the rocking capacity is precise when gap elements are being used and in accordance with NZSEE [28] and Draft NPR 9998:2017 [12] Norms:

$$V_r = 0.9 \cdot (\alpha \cdot P + 0.5 \cdot P_w) \cdot \frac{L_w}{h_{eff}} \tag{4.4}$$

where:

t_{nom}	is the thickness of the wall, in mm.
α	is equal to 0.5 for fixed-free cantilever wall and 1 for fixed-fixed pier.
L_w	is the length of the pier, in mm.
h_{eff}	is the effective height of the pier.
P	is the superimposed and dead load at the top of the wall/pier, in kN.
P_w	is the self-weight of the wall/pier above the sliding plane being considered, in kN.

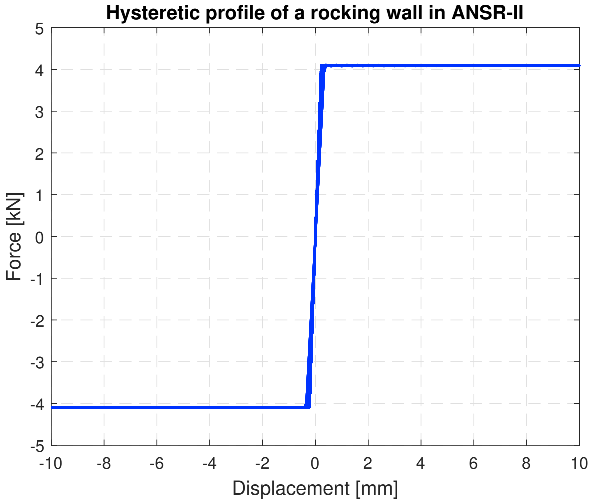

Figure 4.14: Rocking hysteresis for unreinforced masonry piers under cyclic loading in ANSR-II.

Since the gap element is elastic in compression, it can not indicate energy dissipation due to toe crushing. The hysteretic profile in rocking piers is elastic-plastic loading elastic unloading. An efford to introduce hysteresis to rocking piers in ANSR-II was performed. Briefly, truss elements were used, along with the gap elements, that would yield under tension and dissipate energy. That worked in component level. However, the truss elements were introducing forces in the corners of the membrane elements, thus rocking capacity. In order to reduce the rocking capacity, a part of the overburden (usually half or more of the overburden) should be removed from the pier. In structure level that meant that this gravity force should be restored below the pier as a fixed uniformly distributed load above the spandrel. Consequently, during the NLTH analysis the alternation of the vertical stresses and forces was restricted. This could lead to the wrong generation of the dynamic loads to spandrels and piers in the lower levels and to a different dynamic behaviour of the structure as a whole. The lack of hysteresis of rocking piers due to toe crushing is a limitation owing to the application of the Macro-element based modelling method.

4.1.7 Unreinforced masonry spandrels

Spandrels are modelled in ANSR-II using nonlinear membrane elements. The type of these elements is called “NZSEE MASONRY URM 2016 Spandrel Weak Mortar”. The software calculates the flexural and shear capacity of the spandrels according to NZSEE Norm [28]:

-Flexural capacity (peak flexural strength and residual flexural strength)

$$V_{fl} = (f_t + p_{sp}) \cdot \frac{h_{sp}^2 \cdot b_{sp}}{3 \cdot l_{sp}} \tag{4.5}$$

$$V_{fl,r} = \frac{p_{sp} \cdot h_{sp}^2 \cdot b_{sp}}{l_{sp}} \cdot (1 - p_{sp} \cdot f_m/0.425) \tag{4.6}$$

-Shear capacity (peak shear strength for weak mortar and residual shear strength)

$$V_s = \frac{2}{3} \cdot (c + \mu_f \cdot p_{sp}) \cdot h_{sp} \cdot b_{sp} \tag{4.7}$$

$$V_{s,r} = \frac{11}{16} \cdot p_{sp} \frac{h_{sp}^2 \cdot b_{sp}}{l_{sp}} \tag{4.8}$$

where:

f_t	is the equivalent tensile strength of masonry spandrel.
p_{sp}	is the axial stress in the spandrel.
h_{sp}	is the height of the spandrel.
b_{sp}	is the width of the spandrel.
l_{sp}	is the clear length of spandrel between adjacent wall piers.

In-plane strength of unreinforced masonry spandrels is taken as the lower of flexural and shear strength. Furthermore, the standardised backbone curve according to NZSEE [28] and Draft NPR 9998:2017 Norm [12] as well as the hysteresis profile of an unreinforced masonry spandrel in ANSR-II is depicted in figure 4.15.

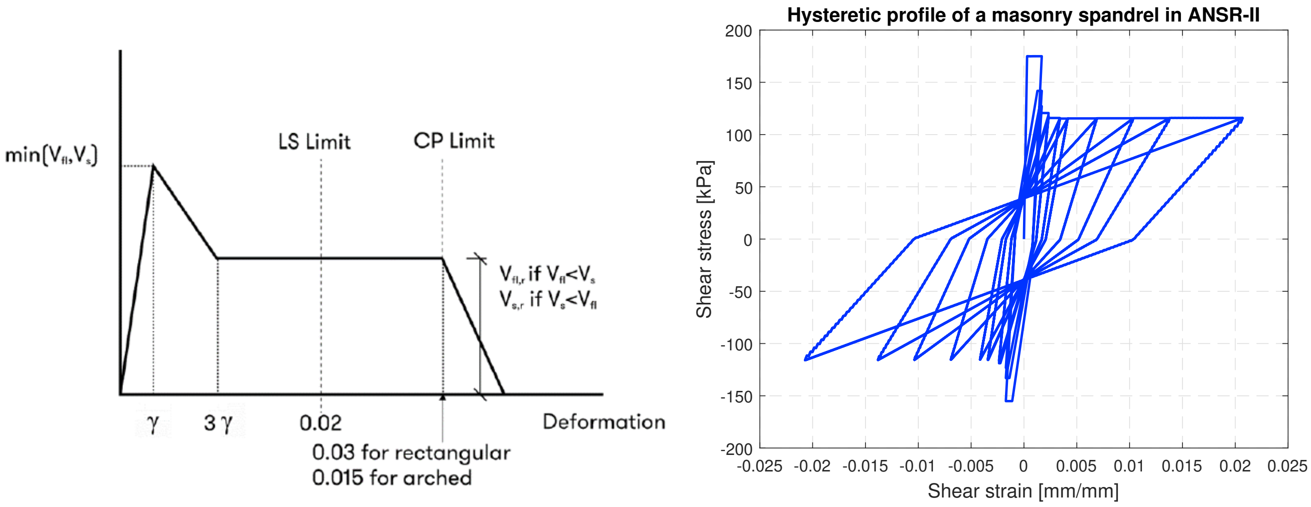

Figure 4.15: Standardised backbone curve (left) and shear hysteresis for unreinforced masonry spandrels under cyclic loading in ANSR-II (right).

4.1.8 Rigid diaphragms

Rigid diaphragms in ANSR-II are modelled by a combination of slaving of degrees of freedom and rigid links. Only beam elements can be slaved to the diaphragm, suggesting that their degrees of freedom X and Z are slaved to the master node. Nodes of other element types (i.e. wall panels) at the reference level of the diaphragm, are connected to the master node via rigid links. It is reminded that nodes with fixed (slaved) degrees of freedom have their respective masses ignored. Therefore, in the case of beam elements the mass is ignored and added to the respective mass of the master node. In contrast, the nodes attached to the wall panels will retain the masses assigned to them, since the X and Z degrees of freedom are free.

The input for describing the properties of rigid diaphragms in ANSR-II allows the user to define the center of mass coordinates at the reference level and the translational mass m_x and m_z of the diaphragm. The rotational mass is then calculated automatically. In figure 4.16 the definition of the concrete diaphragm of the 3D model is presented. The lines represent the rigid links between the master node and the nodes of the membrane elements.

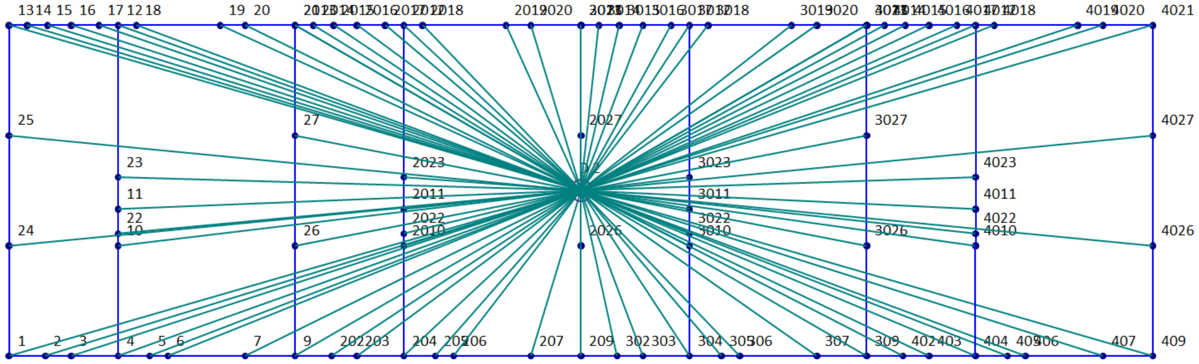
13 14 15 16 17 12 18
19 20
2019 2020
3019 3020
4019 4020 4021
25
27
2027
3027
4027
23
2023
3023
4023
11
2011
3011
4011
22
2022
3022
4022
24
10
26
2010
2026
3010
3026
4010
4026
1 2 3 4 5 6 7 9
202 203 204 205 206 207 209
302 303 304 305 306 307 309
402 403 404 405 406 407 409

Figure 4.16: Definition of the rigid diaphragm in ANSR-II.

4.1.9 Flexible diaphragms

Timber roof panels of the 3D Model are characterised as flexible diaphragms and they are modelled as plane stress elements. A shear stiffness of G_d = 33 kN/m is selected for the timber roof panels in this model. This value complies with the results of a cyclic test of a roof diaphragm performed at the Delft University of Technology for a detached house in Groningen [36]. The cyclic behaviour of the roof diaphragm is rather elastic with minor hysteresis according to the test. A submodel of the roof plane stress elements with the exact mesh produced in the 3D Model is created in ANSR-II and a cyclic displacement pushover is performed until the displacement of 60 millimeters. The behaviour of the roof membrane elements (figure 4.17) is in agreement with the one found from the experiment.

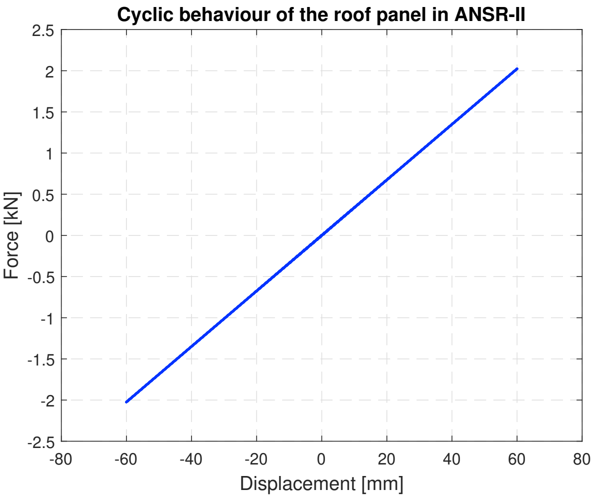

Figure 4.17: Cyclic displacement pushover of the roof panel in ANSR-II.

4.1.10 Out-of-plane walls in ANSR-II

Out-of-plane rocking mechanism of unreinforced masonry walls is implemented in ANSR-II with the so called “rocking column element”. This type of element is consisted of two beam elements, as depicted in figure 4.18. The depth D and the thickness B of the column can be defined. The depth (length) studied for one-way vertically-spanning OOP unreinforced masonry walls is considered to be 1 meter.

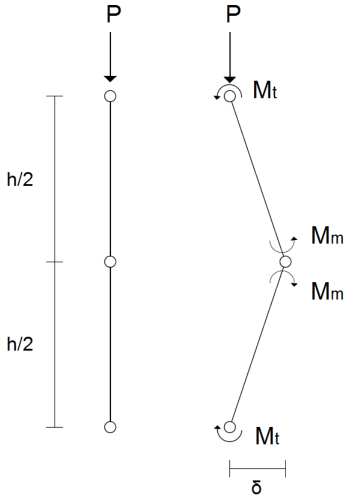

Figure 4.18: OOP beam elements schematisation in ANSR-II.

The moment capacity of an unreiforced masonry section is only provided by the axial load. ANSR-II calculates the moment resistance by considering the normal force N - bending moment M interaction diagram illustrated in the left side of figure 4.19. According to this diagram, the moment resistance increases until a certain value of the normal force (balance point). After this value, the moment resistance decreases with the increase of the normal force. To calculate the moment resistance, the equilibrium of moments around the centerline of the column can be considered (right side of figure 4.19). The resisting moment can be calculated as $M_R = (P/2) \cdot (D - c)$. The balance point is reached when c is equal to D/2. The resisting moment will then be equal to $M_R = 0.25 \cdot P \cdot D$ and the balance point will be equal to $P = 0.5 \cdot B \cdot D \cdot f_m$. The moment resistance can now be rewritten as : $M_R = (B \cdot D^2 \cdot f_m)/8$.

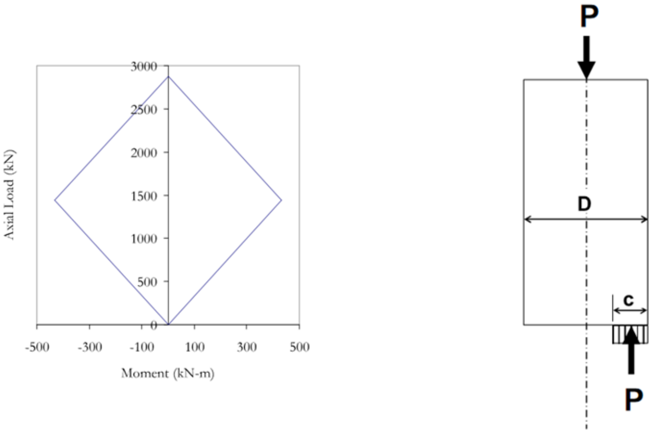

Figure 4.19: Axial load and bending moment interaction (left) and resisting mechanism of rocking column element (right) [19].

Nonlinear Kinematic Analysis (NLKA), described in NZSEE [28] and Draft NPR 9998:2017 [12], defines the capacity curve envelope of one-way bending OOP walls by calculating the maximum horizontal force H and maximum displacement δ in the mid-height level of the wall:

$$H = 2 \cdot \left(P + \frac{W}{2}\right) \cdot \frac{2 \cdot \delta}{h} \tag{4.9}$$

$$\delta = \frac{P \cdot e_p + 2 \cdot \left(P + \frac{W}{2}\right) \cdot e_0 + (P + W) \cdot e_b}{2 \cdot \left(P + \frac{W}{2}\right)} \tag{4.10}$$

where:

P	is the overburden load.
W	is the self-weight of the OOP wall.
e_p	is the eccentricity of the overburden load.
e_0	is the eccentricity within a crack in the wall.
e_b	is the eccentricity of the bottom support of the wall.

Considering the same variation in boundary conditions and in overburden loads as in the sensitivity studies of the OOP walls in the 1D models, a set of displacement pushover analyses are performed in ANSR-II. The OOP walls are modelled as “rocking column elements” and the different boundary conditions are implemented by restraining or releasing the rotational DOF ZZ of the edge nodes of the beam elements. The resisting bending moment of the nodes with restrained rotational DOF ZZ is calculated from the software as described above. As soon as the bending moment capacity is exceeded in the nodes, the rotational DOF ZZ is released, creating a hinge.

In Appendix C the capacity curves of the OOP walls resulted from ANSR-II displacement pushover analyses are plotted along with the respective capacity curve envelopes of the NLKA method. It is concluded that there is a good agreement among the results. A comparison between the capacity curve in ANSR-II and the capacity curve envelope derived from the NLKA method for the wall configuration BC3 30kN is depicted in figure 4.20.

The behaviour of the “rocking column element” under cyclic and potentially seismic loads is described by elastic unloading (figure 4.21). Therefore, no dissipation of energy occurs in the element during a seismic excitation, in contrast to the hysteretic behaviour of OOP wall in Opensees.

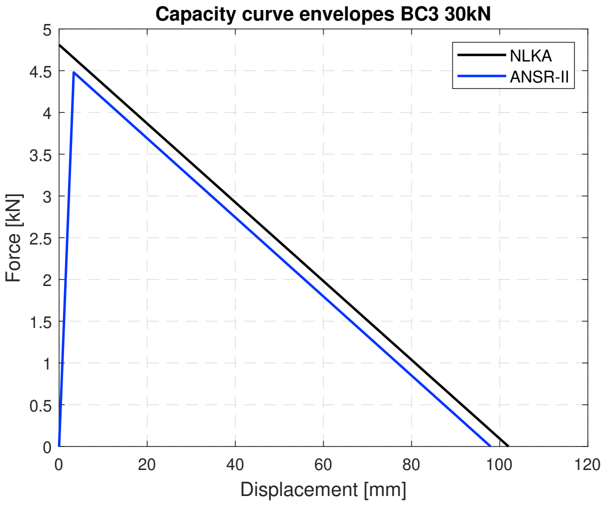

Figure 4.20: Agreement between the capacity curves derived from ANSR-II and NLKA method.

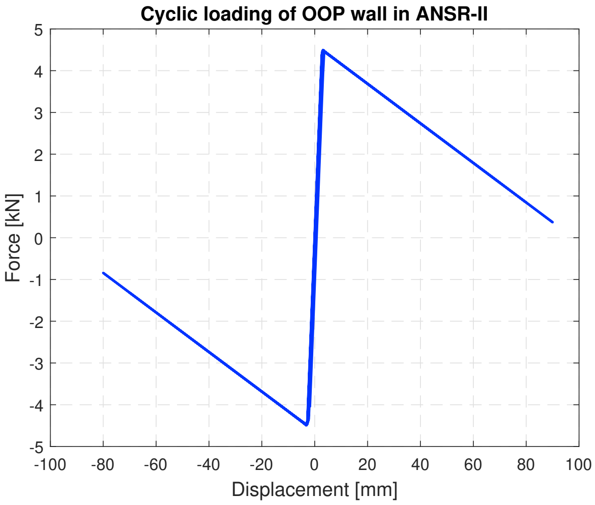

Figure 4.21: Behaviour of an OOP wall in ANSR-II under cyclic loading.

4.2 Nonlinear time history analyses (NLTHA) in ANSR-II

4.2.1 Procedure

Nonlinear time history analyses of the 3D Model are conducted in ANSR-II. The objectives are the comparison of the Design Floor Accelaration Spectra obtained from the simplified 1D Models with the response Floor Accelaration Spectra of the 3D Model and the derivation of the Height Coefficient C_{Hi}. Similarly to the 1D Models, the areas of interest are Appingedam, Groningen, Hoogezand, Loppersum and Overschild.

Annex F of Draft NPR 9998:2017 [12] states that the simultaneous interaction of tri-axial ground motion records should be accounted for the verification of the structural performance of FEM Models with nonlinear time history methods. In ANSR-II a set of 11 tri-directional ground motions per area is used for the seismic excitation of the 3D Model. In contrast, this was not the case for the one-dimensional simplified models, since these were excited seperately from 11 records per area in direction X and 11 records per area in direction Y.

4.2.2 Rayleigh damping

Damping plays a vital role in nonlinear time history analyses, since the results in terms of displacements and accelarations are highly sensitive to the amount of damping considered. ANSR-II adopts Rayleigh damping model for the NLTH analyses. To determine Rayleigh damping, two eigenmodes i and j of the structure should be known. Chopra [9] proposes that the selection of modes i and j with specified damping ratios (usually ζ = 5%) should be chosen to ensure damping ratios lower than the specified value ζ for all the modes with significant contribution to the seismic response. For this purpose, eigenvalue analysis of the 3D Model is performed in ANSR-II. The range of the eigenperiods is calculated from the highest contributing period until the period where the 90% of cumulative mass is reached for each direction. This period range per direction is presented in table 4.2. The range of eigenperiods defined in ANSR-II for the calculation of Rayleigh damping is 1.367 - 0.05 seconds. The reason for choosing the value of 0.05 seconds and not 0.024 seconds is because damping periods less than 0.05 seconds cause numerical problems during the analysis.

Table 4.2: Eigenvalue analysis for the 3D Model.

range	Direction X	Direction Y
Eigenperiods [sec]	1.367 - 0.053	0.150 - 0.024
cumulative mass	2.34% - 93.13%	1.02% - 95.17%
dominant eigenperiod [sec]	0.146	0.075
mass participation respective to dominant eigenperiod	83.71%	59.81%

Stiffness proportional part of Rayleigh damping in ANSR-II is related to the initial stiffness of the structure. This is due to the non-convergence issues which lead to an early termination of the analyses, when tangent stiffness is being used. This concludes the main difference in the definition of damping with the 1D Models, where the stiffness proportional damping was related to the tangent stiffness of the system.

4.2.3 Mean Floor Accelaration Spectra

Mean Floor Accelaration Spectra of the 3D Model are produced from the NLTH analyses. Each mean FRS is plotted along with the 11 FRS in one graph and it is produced per area, floor and direction. 20 FRS graphs are gathered in Appendix E, categorised per area.

Torsional effects due to the potential irregular location of the nodal masses in the 3D Model are taken into consideration for the NLTH analyses. Accelarations and displacements are recorded in the center of mass and in the corners of each rigid diaphragm. The column lines that are relative to the corners of the diaphragms in the 3D Model are C1, C13, C4021 and C409 (see figure 4.16). In Appendix E and the sections below, the mean FRS, the normalised FRS and the Height Coefficient plots corespond to the node of the diaphragm where the maximum ratio PFA/PGA is found.

4.2.4 Normalised Floor Accelaration Spectra (FRS)

In this section the normalised FRS of the second floor of the 3D Model and the mean normalised FRS of the first and second floor are plotted together with the Design Floor Accelaration Spectrum derived from the 1D Models per area and direction. In Appendix D, the damage state of the mesh in the weak direction of the structure is reported for one record per area. This will help the interpretation of the results.

4.2.4.1 Direction X

In direction X, for the areas with the most significant PGAs (Appingedam, Loppersum and Overschild), a good prediction of the highest mean floor spectral accelaration is observed from figures 4.22, 4.28 and 4.30. In addition, judging by the figures 4.23, 4.29 and 4.31, where the 11 responses of the floor 2 are depicted for each of these areas, the plateau period range of the Design Floor Accelaration Spectra matches the period range relative to the maximum values of the response spectra.

For the areas that present the lowest PGAs (Groningen and Hoogezand), the structure remains mainly elastic and, as a result, narrow high amplified spectra are derived in figures 4.25 and 4.27 for the responses of the Floor 2. Nevertheless, the maximum values of the mean spectral floor accelaration for Groningen and Hoogezand seems to be in agreement with the respective design plateau values. It should be stated that the submodel of Typology 1 in the NLTH analyses of the 1D Models presented high nonlinear behaviour in Groningen and Hoogezand (see Appendix A). An explanation for this discrepancy is that, in the in-house studies that provided the SDOF characteristics, the spandrels of the submodel were not modelled. In contrast, the spandrels in the 3D Model in ANSR-II are modelled, hence a stiffer behaviour is observed. The comparison between the elastic period of the 1D Model and the dominant eigen period of the 3D Model in direction X validates that, as well. The former is 0.734 seconds and the latter is 0.146 seconds with a mass participation of 83.71%.

It is concluded that the Design Floor Accelaration Spectra produced from the 1D Models are able to predict the mean FRS related to this 3D Model for the direction X. Regarding the FRS that overcome the design plateau value, sensitivity studies by incorporating the OOP walls in the 3D Model are conducted later on, similarly to the simplified models, in order to check the predictability of the Shape Factor Coefficient in more depth.

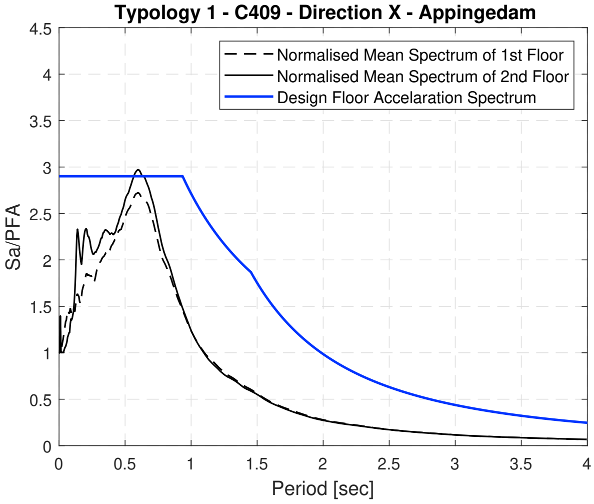

Figure 4.22: 3D Model Mean Floors Response Spectra and Design Floor Spectrum in direction X for Appingedam.

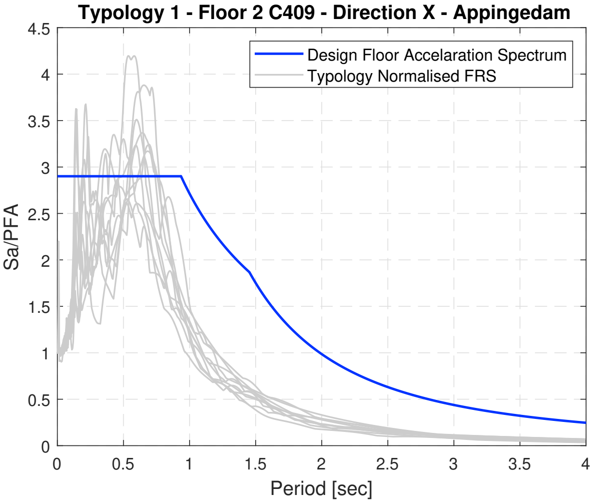

Figure 4.23: 3D Model Floor 2 Response Spectra and Design Floor Spectrum in direction X for Appingedam.

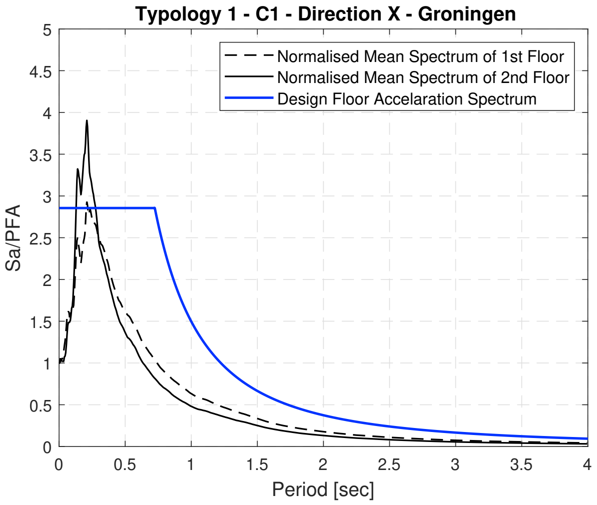

Figure 4.24: 3D Model Mean Floors Response Spectra and Design Floor Spectrum in direction X for Groningen.

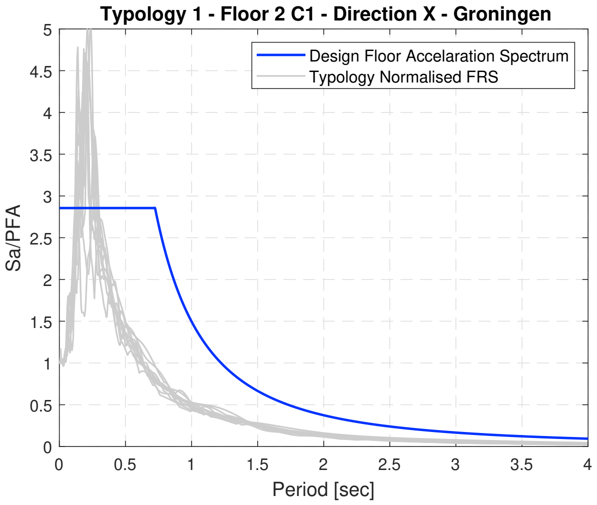

Figure 4.25: 3D Model Floor 2 Response Spectra and Design Floor Spectrum in direction X for Groningen.

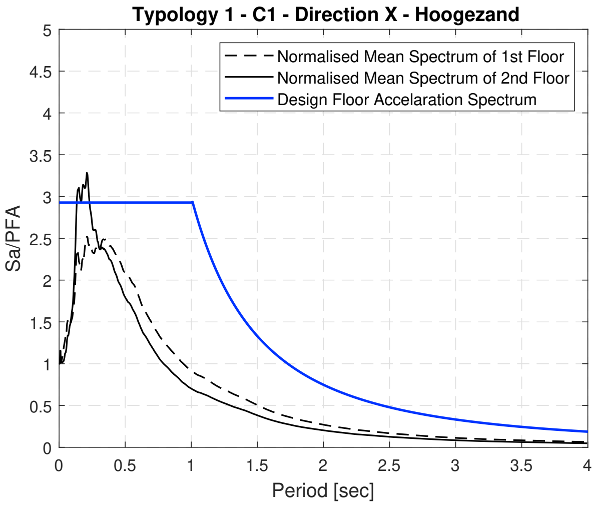

Figure 4.26: 3D Model Mean Floors Response Spectra and Design Floor Spectrum in direction X for Hoogezand.

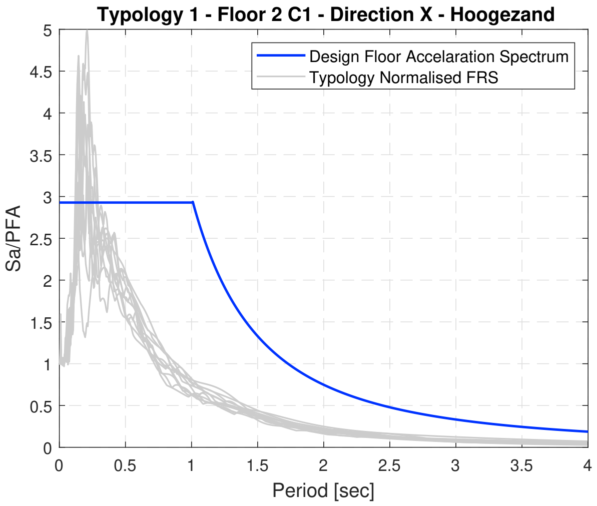

Figure 4.27: 3D Model Floor 2 Response Spectra and Design Floor Spectrum in direction X for Hoogezand.

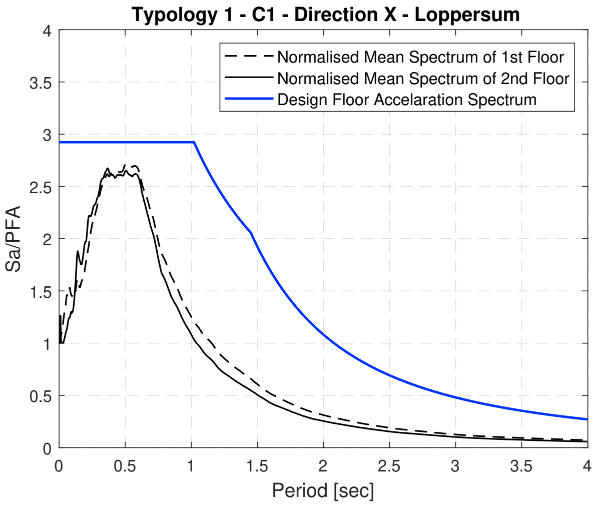

Figure 4.28: 3D Model Mean Floors Response Spectra and Design Floor Spectrum in direction X for Loppersum.

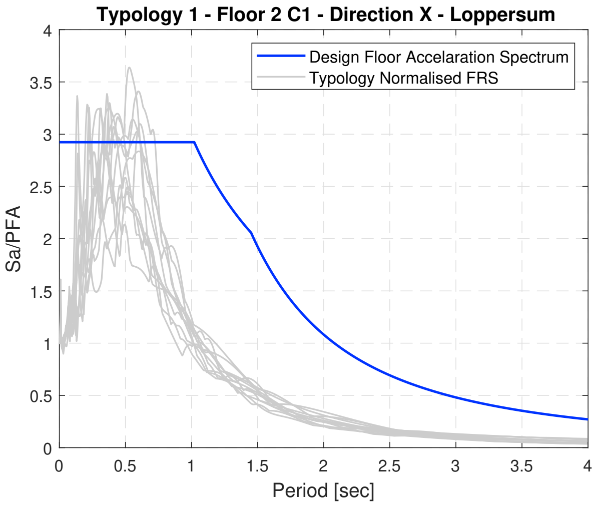

Figure 4.29: 3D Model Floor 2 Response Spectra and Design Floor Spectrum in direction X for Loppersum.

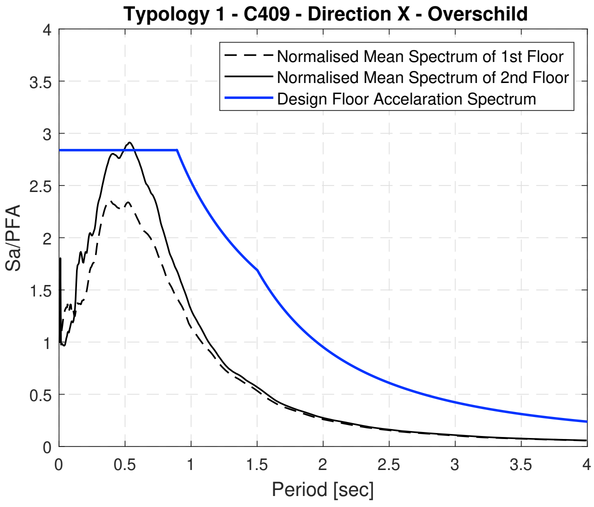

Figure 4.30: 3D Model Mean Floors Response Spectra and Design Floor Spectrum in direction X for Overschild.

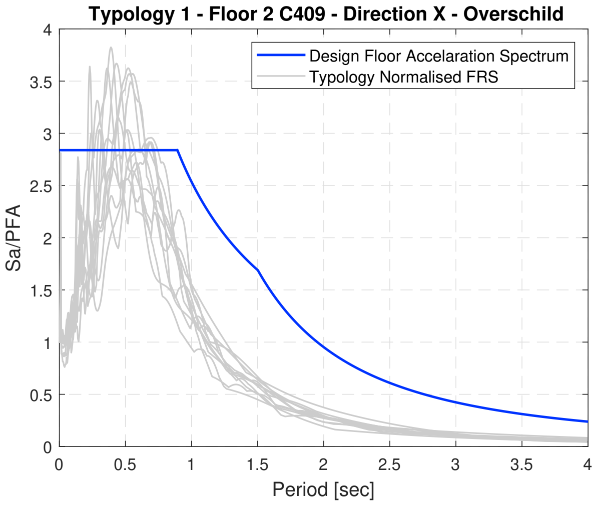

Figure 4.31: 3D Model Floor 2 Response Spectra and Design Floor Spectrum in direction X for Overschild.

4.2.4.2 Direction Y

Figures 4.32 to 4.41 clearly show that the Design Floor Accelaration Spectra are an upper bound envelope also for the Floor Response Spectra of the structure in direction Y. However, a great discrepancy between the Floor Response Spectra of the 3D Model and the ones derived from the NLTH analyses in the 1D Models is the lack of the bell-shaped curves, at which significant values of spectral accelaration are observed at the natural period of the SDOF systems (see Appendix A). The fact that the 3D Model remains elastic in direction Y for all the NLTH analyses performed, enhances this discrepancy even more. Nevertheless, a SDOF system is described by only one natural period with all the seismic mass related to this period. Furthermore the response spectrum for linear SDOF systems will indicate the highest spectral amplitudes in a narrow range around the natural period. In contrast, an eigenvalue analysis in a 3D Model indicates more than one dominant mode. More specifically, for this 3D Model the dominant eigenperiod in direction Y is equal to 0.075 seconds with a mass participation of 59.81 %. The rest 40.19 % is spread to other periods or modes.

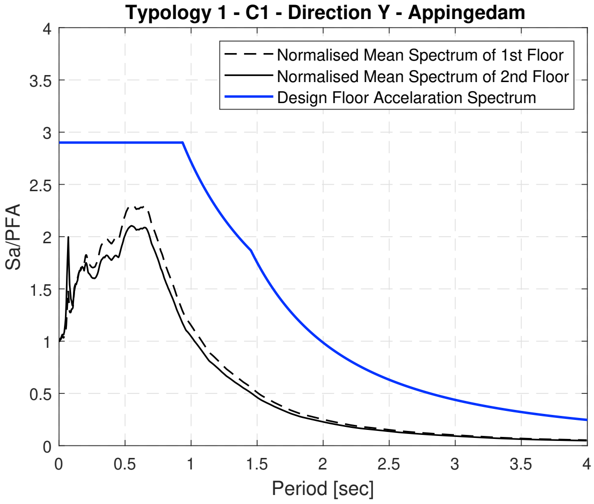

Figure 4.32: 3D Model Mean Floors Response Spectra and Design Floor Spectrum in direction Y for Appingedam.

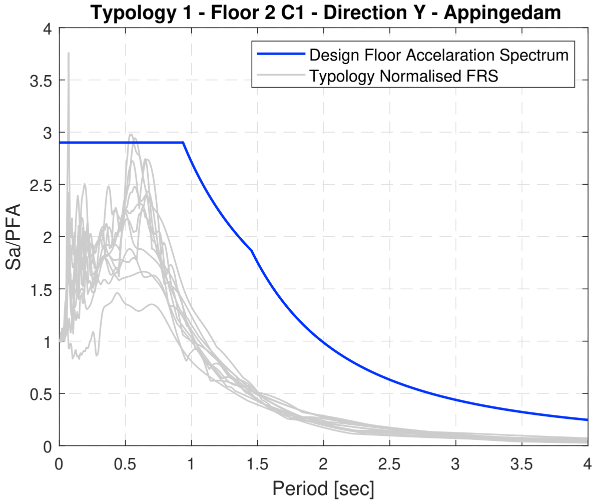

Figure 4.33: 3D Model Floor 2 Response Spectra and Design Floor Spectrum in direction Y for Appingedam.

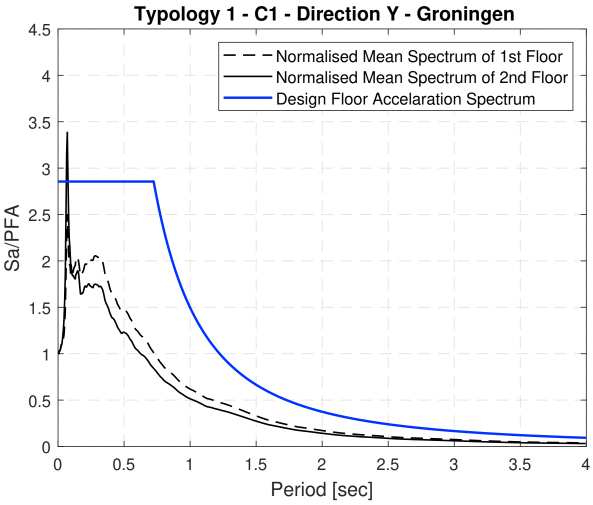

Figure 4.34: 3D Model Mean Floors Response Spectra and Design Floor Spectrum in direction Y for Groningen.

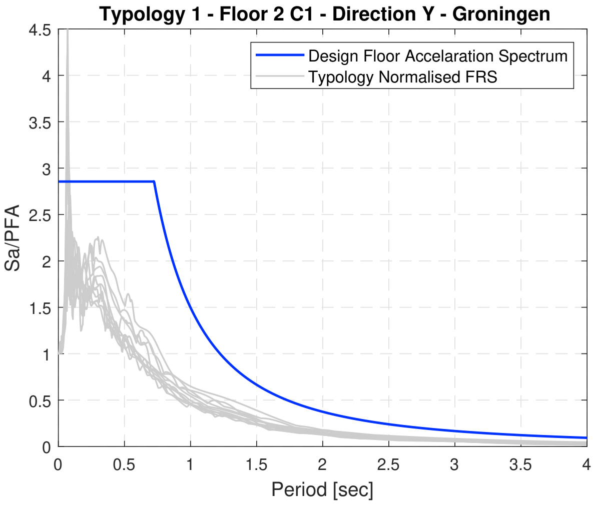

Figure 4.35: 3D Model Floor 2 Response Spectra and Design Floor Spectrum in direction Y for Groningen.

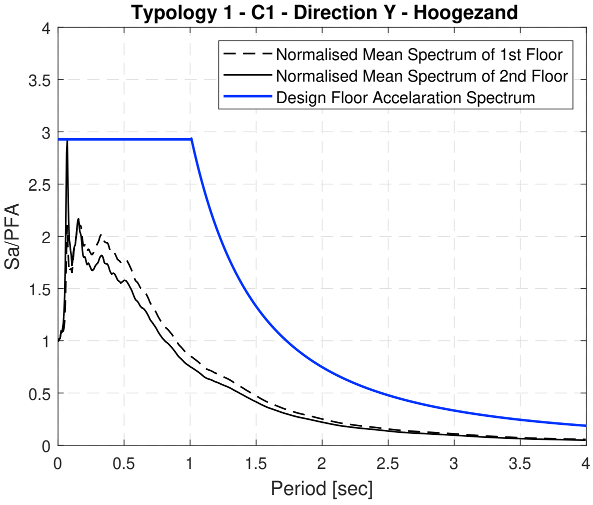

Figure 4.36: 3D Model Mean Floors Response Spectra and Design Floor Spectrum in direction Y for Hoogezand.

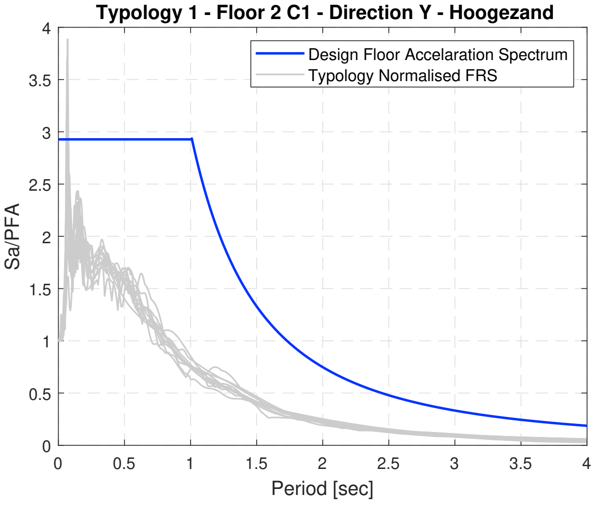

Figure 4.37: 3D Model Floor 2 Response Spectra and Design Floor Spectrum in direction Y for Hoogezand.

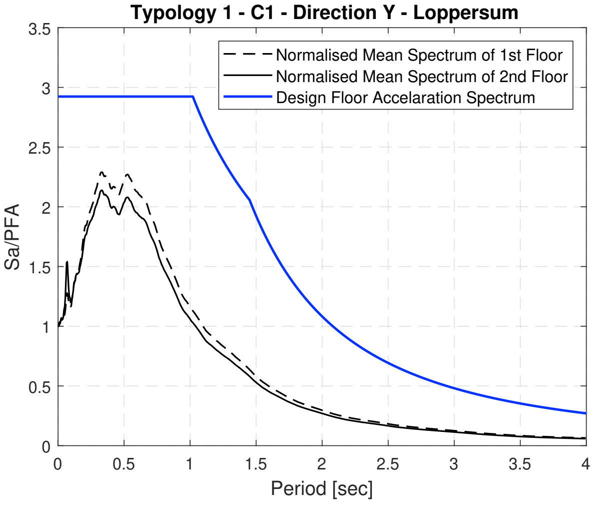

Figure 4.38: 3D Model Mean Floors Response Spectra and Design Floor Spectrum in direction Y for Loppersum.

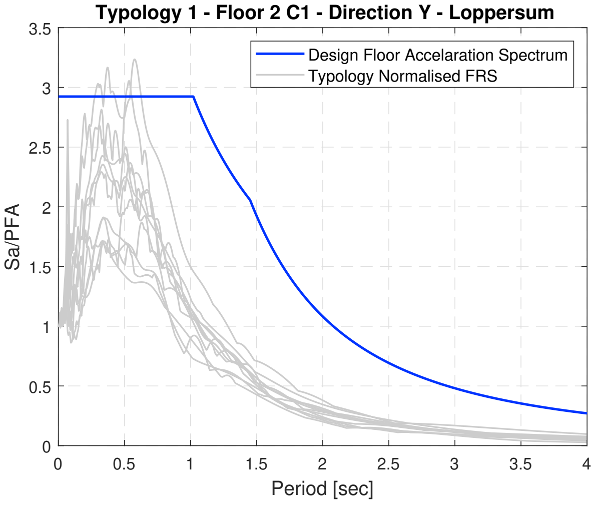

Figure 4.39: 3D Model Floor 2 Response Spectra and Design Floor Spectrum in direction Y for Loppersum.

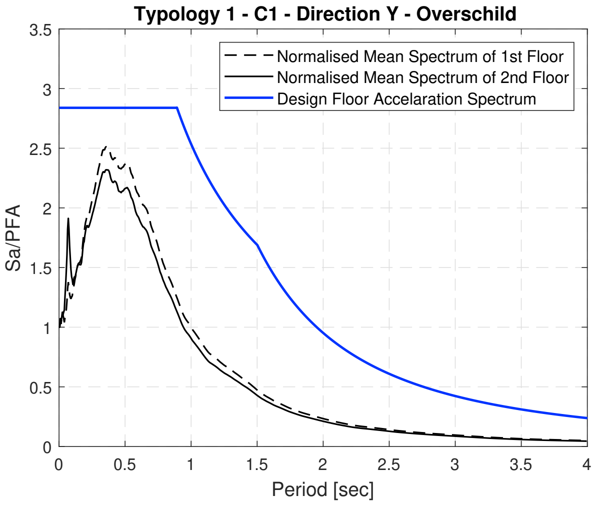

Figure 4.40: 3D Model Mean Floors Response Spectra and Design Floor Spectrum in direction Y for Overschild.

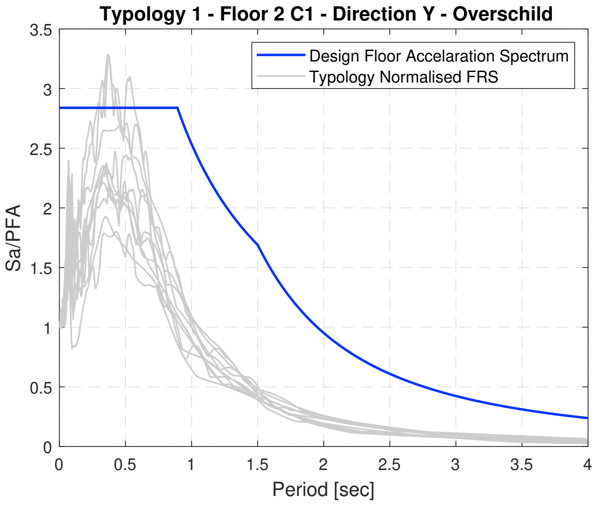

Figure 4.41: 3D Model Floor 2 Response Spectra and Design Floor Spectrum in direction Y for Overschild.

4.2.5 Height Coefficient for the Groningen Case

The Height Coefficient is determined as the function of the ratio of the Peak Floor Accelaration (PFA) over the Peak Ground Accelaration (PGA) through the height of a structure. Concerning the Height Coefficient C_{Hi} for the Groningen Case, the maximum floor accelarations per area and direction are extracted from the NLTH analyses in ANSR-II. These accelarations are normalised to the PGA and then plotted against the floor heights (figures 4.42 to 4.51). In order to define a linear function [1] describing the most unfavourable floor accelaration profile through the height of the structure, a linear regression analysis is implemented. This analysis focuses on the points of the mean peak floor accelaration plus one standard deviation per floor and the starting point (1,0). Consequently, the Height Coefficient C_{Hi} is aimed to satisfy 84.1% of all the PFA responses per floor level. Table 4.3 gathers the points with respect to the PFA mean values and PFA mean plus one standard deviation values per area and direction.

Table 4.3: PFA mean value and PFA mean value plus one standard deviation points per area and direction.

		Direction X		Direction Y	
Areas	Floor	mean	mean+1std	mean	mean+1std
Appingedam	1	1.1349	1.3383	1.1376	1.4594
	2	1.2800	1.4435	1.2557	1.6186
Groningen	1	1.2340	1.4253	1.1882	1.3556
	2	1.7084	1.9482	1.4346	1.6484
Hoogezand	1	1.1830	1.3088	1.1515	1.2889
	2	1.5100	1.7671	1.3132	1.4752
Loppersum	1	1.1023	1.2825	1.1032	1.3562
	2	1.4274	1.6434	1.2140	1.5038
Overschild	1	1.1439	1.2873	1.0905	1.3264
	2	1.2284	1.3470	1.2093	1.5132

---

[1] A linear function is considered for the description of the Height Coefficient C_{Hi} in order to be in agreement with the format of the Height Coefficient equation found at NZSEE Norm [28] for structural heights less than 12 meters. Nonetheless, a better match can be achieved with polynomial functions.

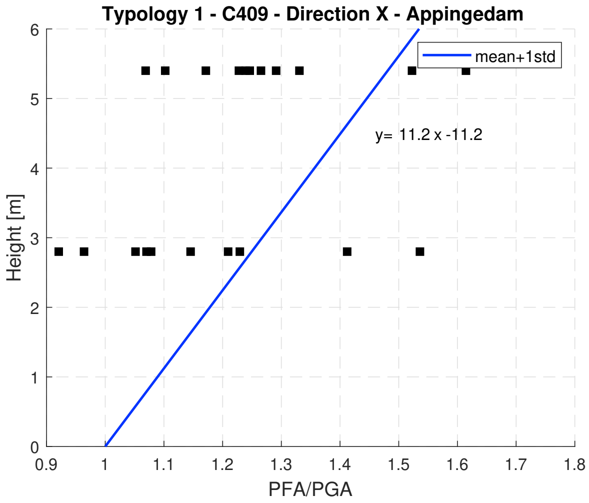

Figure 4.42: Height coefficient plot in Appingedam - Direction X.

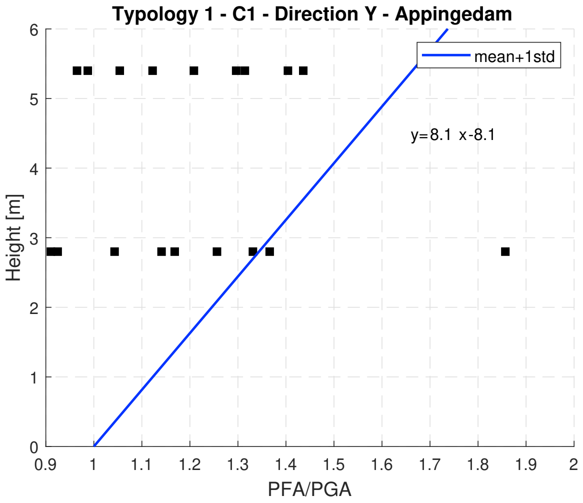

Figure 4.43: Height coefficient plot in Appingedam - Direction Y.

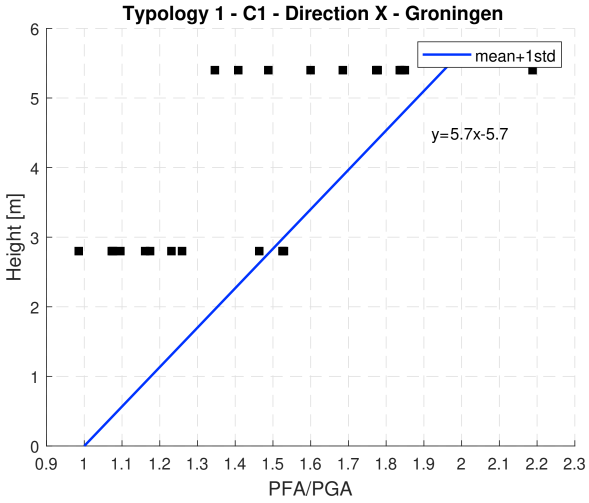

Figure 4.44: Height coefficient plot in Groningen - Direction X.

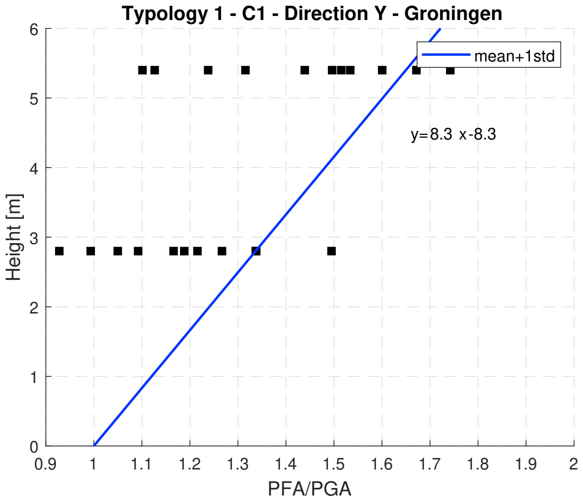

Figure 4.45: Height coefficient plot in Groningen - Direction Y.

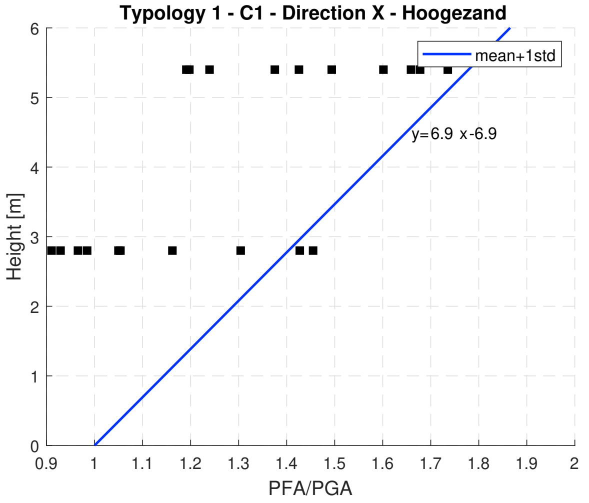

Figure 4.46: Height coefficient plot in Hoogezand - Direction X.

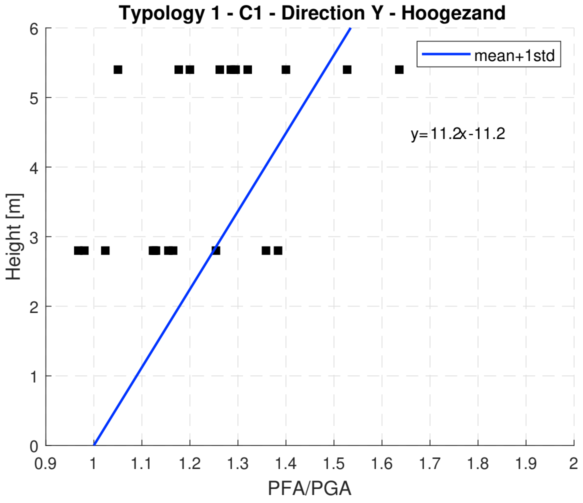

Figure 4.47: Height coefficient plot in Hoogezand - Direction Y.

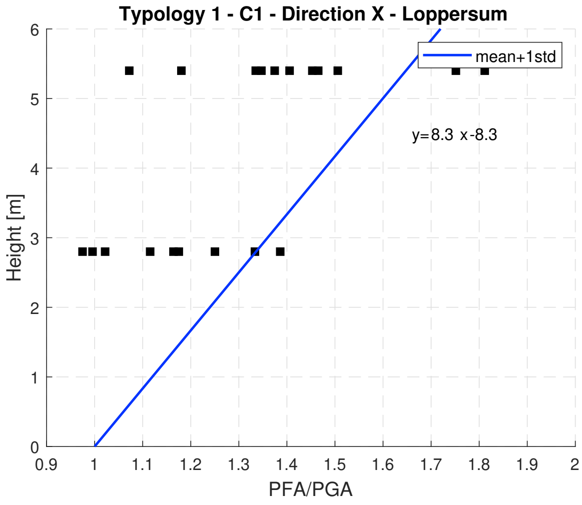

Figure 4.48: Height coefficient plot in Loppersum - Direction X.

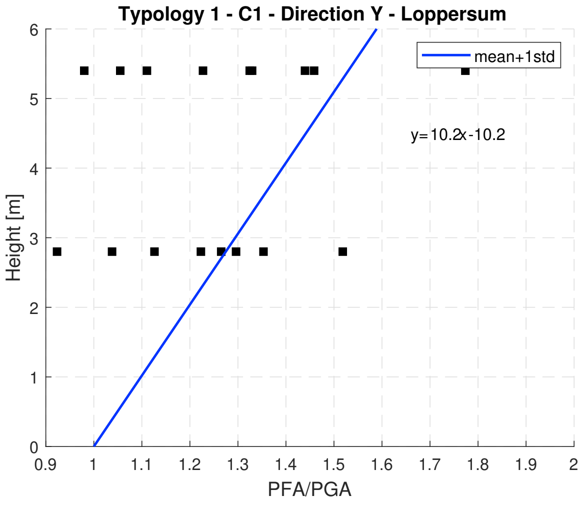

Figure 4.49: Height coefficient plot in Loppersum - Direction Y.

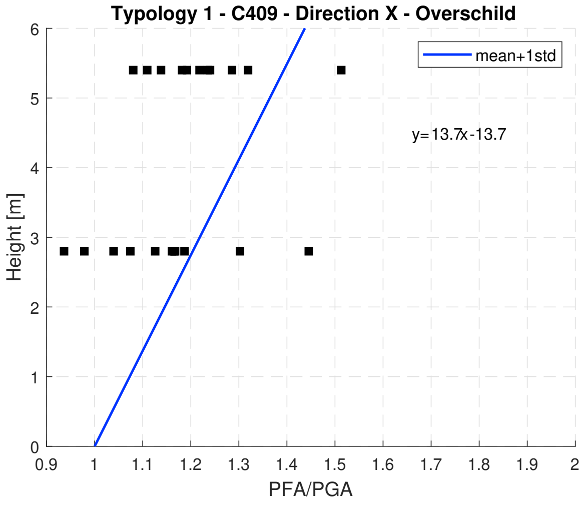

Figure 4.50: Height coefficient plot in Overschild - Direction X.

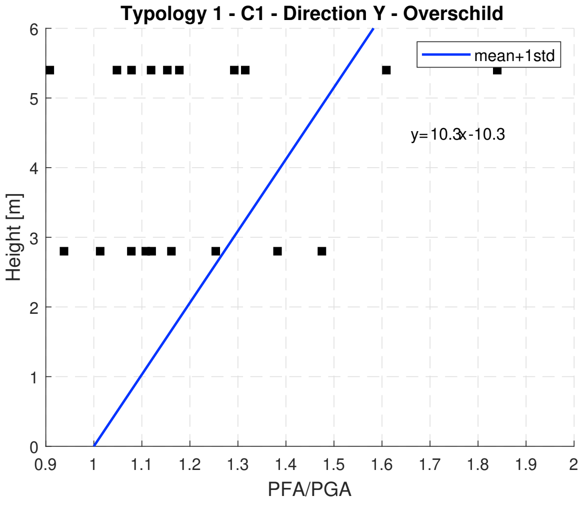

Figure 4.51: Height coefficient plot in Overschild - Direction Y.

In each of the plots above, the function $y = \alpha \cdot x - x$ of the line describing the Height Coefficient is presented. This function is equivalent to the mathematical expression:

$$C_{Hi} = \frac{h}{\alpha} + 1 \tag{4.11}$$

Parameter α depends on the area and direction. The values of α extracted from the linear regression analyses are summarised in table 4.4. The format of the Height Coefficient C_{Hi} for the Groningen Case is analogous and thus directly comparable to the one from NZSEE Norm [28] for structural heights below 12 meters.

Table 4.4: Parameter α for the definition of the Height Coefficient C_{Hi}.

Areas	Direction X	Direction Y
Appingedam	11	8
Groningen	6	8
Hoogezand	7	11
Loppersum	8	10
Overschild	14	10

4.2.6 Sensitivity studies of OOP walls in the 3D Model

Sensitivity studies of OOP walls are carried out in the 3D Model. The reason is to evaluate the ability of the Shape Factor Coefficient $C_i(T_p)$ and the Height Coefficient C_{Hi} to satisfy the actual NLTH response of OOP walls in ANSR-II or to predict failure. The criteria to be met are the ones mentioned for the 1D Models (see section 3.6.5). Identical to the 1D Models are also the configurations of the OOP walls. The graphs presented in this section are analogous to the graphs of the sensitivity studies in the previous chapter. Nevertheless, there is a minor difference. In the figures below, the NLTH out-of-plane response at the mid-height level of the walls placed on the ground floor (Level 1) and first floor (Level 2) of the structure is depicted. On the contrary, the NLTH response of the SDOF system was illustrated for the Hysteretic Rules HR1 and HR2 in the sensitivity studies in Opensees.

4.2.7 Sensitivity study of OOP walls - Direction X

4.2.7.1 Appingedam

In Appingedam for direction X, the design response is greater than the NLTH response for the non-failing walls and predicts the failure when it is indicated by the NLTH analyses.

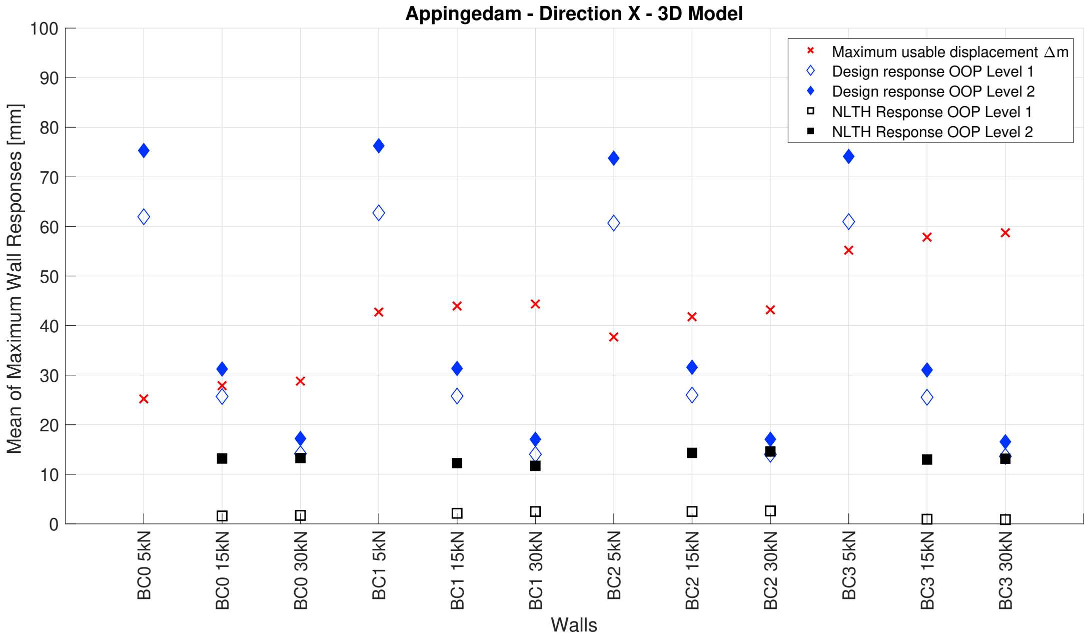

Figure 4.52: Appingedam - Direction X: design and NLTH response of the 3D Model OOP walls.

4.2.7.2 Groningen

Regarding Groningen, the design response is an upper bound value of the NLTH response for all the non-failing walls. Furthermore, it predicts the failure of wall BC0 5kN. Nevertheless, the design responses of the walls BC1 5kN and BC2 5kN indicate failure, if they are placed on Floor 1 (mid-height Level 2). This failure is not pointed out by the respective NLTH responses. These discrepancies are already explained in the Opensees sensitivity studies of OOP walls.

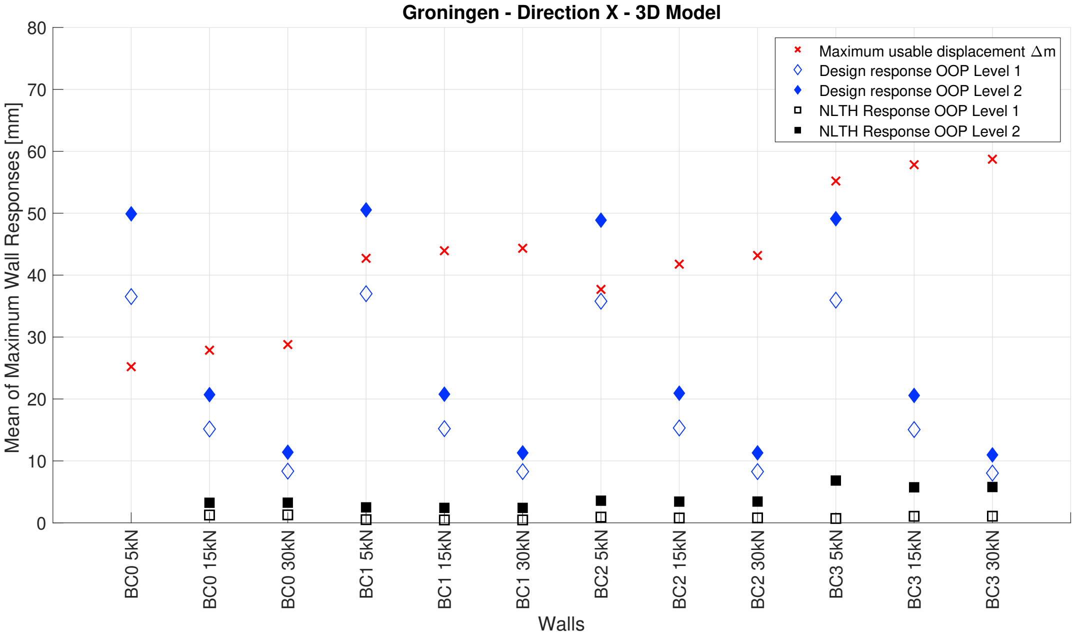

Figure 4.53: Groningen - Direction X: design and NLTH response of the 3D Model OOP walls.

4.2.7.3 Hoogezand

In Hoogezand, the design response satisfy all the NLTH responses of the non-failing walls. In addition, it predicts the failure of wall BC0 5kN. However, the design response indicates failure for the walls BC1 5kN and BC2 5kN at both mid-height levels and for wall BC3 5kN at mid-height Level 2. These failures are not in agreement with the respective NLTH responses.

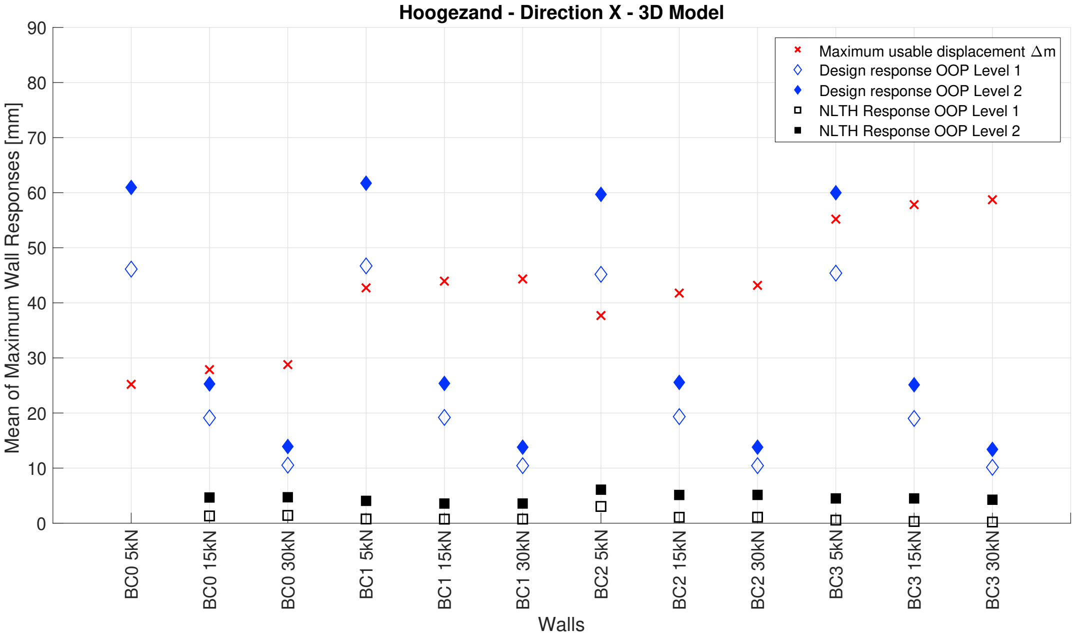

Figure 4.54: Hoogezand - Direction X: design and NLTH response of the 3D Model OOP walls.

4.2.7.4 Loppersum

Similar conclusions are drawn in Loppersum for the non-failing walls. The design response acts as an upper boundary of the NLTH response. When failure is indicated by the nonlinear time history analyses for walls BC0 5kN and BC2 5kN, it is predicted by the design response. Exceptions are the walls BC1 5kN and BC3 5kN, which according to the design response, failure is met at both OOP levels. This is not found in the NLTH analyses.

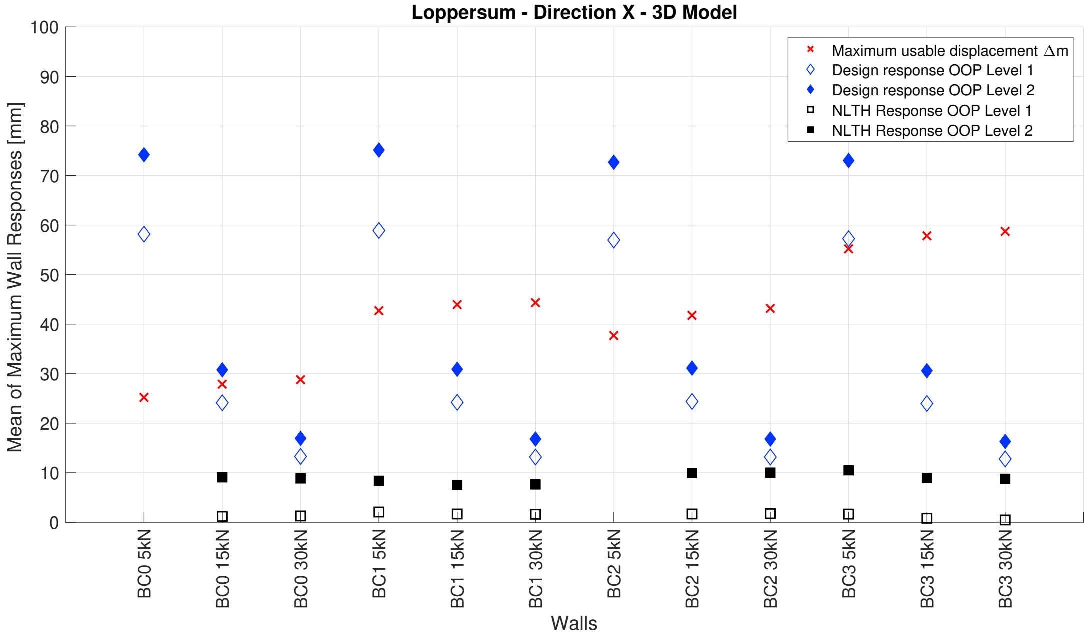

Figure 4.55: Loppersum - Direction X: design and NLTH response of the 3D Model OOP walls.

4.2.7.5 Overschild

In Overschild, the area with the highest PGA, the performance of the design response Δ_{ph} against the NLTH response is judged satisfactory. The design response is larger than the NLTH response of the walls BC0 30kN, BC1 15kN, BC1 30kN and BC2 30kN, BC3 15kN and BC3 30 kN at both OOP levels. Furthermore, it predicts the failure of the NLTH responses for the walls BC0 5kN, BC0 15kN, BC1 5kN, BC2 5kN and BC3 5kN at the mid-height Levels 1 and 2. Nonetheless, NLTH analyses indicate failure of the wall BC2 15kN at both levels, while this is not predicted by the design response.

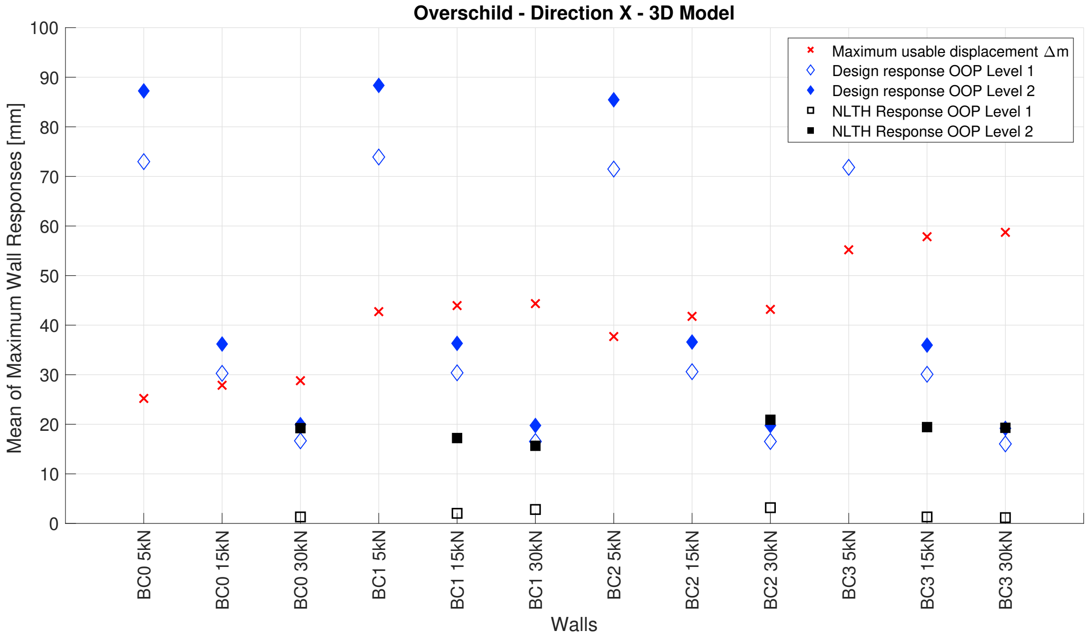

Figure 4.56: Overschild - Direction X: design and NLTH response of the 3D Model OOP walls.

4.2.8 Sensitivity study of OOP walls - Direction Y

The results from the sensitivity study of OOP walls in ANSR-II for the direction Y of the 3D Model are illustrated below. In all the areas, the OOP walls develop minor displacements. This can be explained by the maximum displacements of the rigid floor diaphragms during the NLTH analyses in direction Y (table 4.5). The maximum displacement observed in the first and second floor was 0.31 mm and 0.60 mm respectively. The amplification of the mid-height displacement of the OOP walls compared to the displacement of the diaphragms is significant, but the resulted mid-height displacements are still small (close to 2 millimeters for the majority of the walls). The sensitivity study of OOP walls of the 1D Models in direction Y indicated higher mid-height displacements. However, due to the aforementioned singular natural period of the SDOF systems and the participation of the total equivalent seismic mass to that period, the Floor Response Spectra of the elastic SDOF systems in direction Y present high spectral amplitudes only in a narrow period range around the natural period. Consequently, the simplified 1D models present more pronounced resonance effects and thus higher displacements in the OOP walls. This is more noticeable when the elastic period of the wall coincides with the fundamental period of the equivalent stucture. In contrast, the 59% of the mass participates in the dominant eigen mode of the 3D Model, which leads to lower spectral amplitudes and milder resonance effects between the floors and the OOP walls.

A way to increase the mass participation percentage in the governing eigen mode in direction Y is to introduce soil springs in the 3D Model. Generally, in fixed-base models, the mass corresponding to the relatively undeformed parts of the structure is not accounted in the total mass activated in the dominant eigen mode during a dynamic excitation. The 3D Model presents high stiffness in direction Y and the walls have high rocking and shear capacity. In realistic conditions, the soil will govern the displacements in this direction due to soil-structure interaction, especially if the soil condition in the Netherlands is considered. Soil springs incorporate this phenomenon in the 3D Model and lead to higher displacements at the levels of the rigid diaphragms and thus at the mid-height level of the OOP walls.

Table 4.5: Displacements (mm) of floor diaphragms in direction Y.

	Appingedam	Groningen	Hoogezand	Loppersum	Overschild
Floor 2	0.50	0.37	0.39	0.46	0.60
Floor 1	0.26	0.18	0.20	0.24	0.31

4.2.8.1 Appingedam

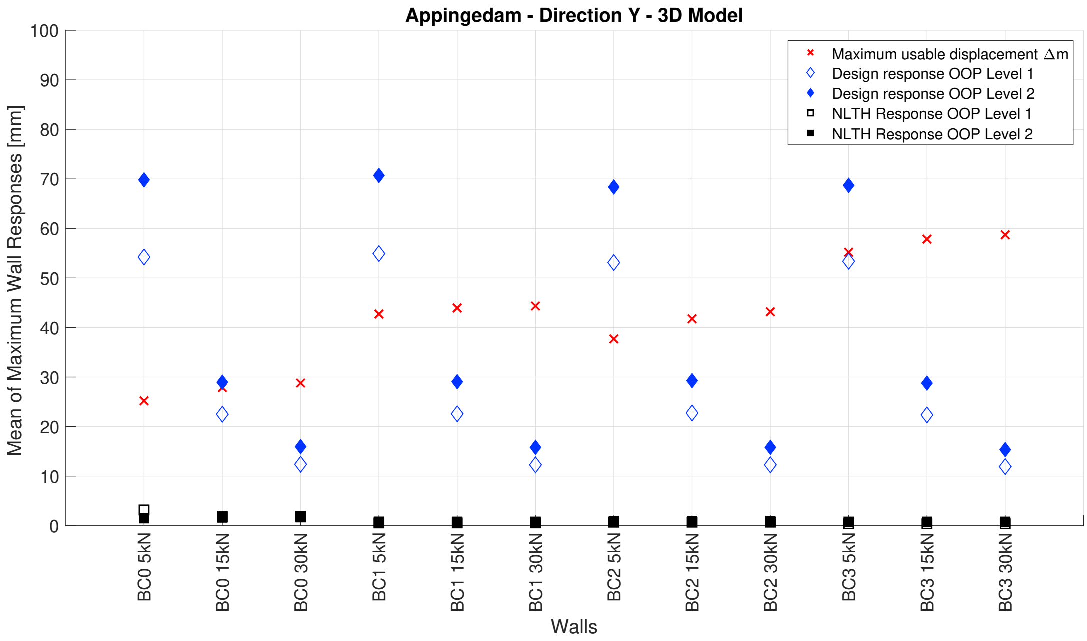

Figure 4.57: Appingedam - Direction Y: design and NLTH response of the 3D Model OOP walls.

4.2.8.2 Groningen

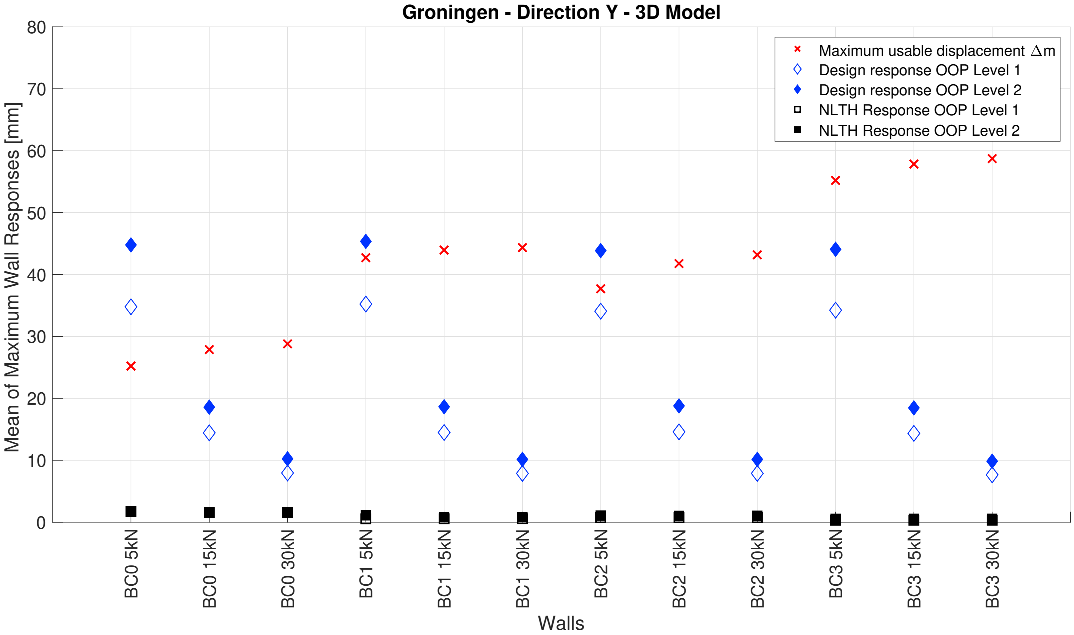

Figure 4.58: Groningen - Direction Y: design and NLTH response of the 3D Model OOP walls.

4.2.8.3 Hoogezand

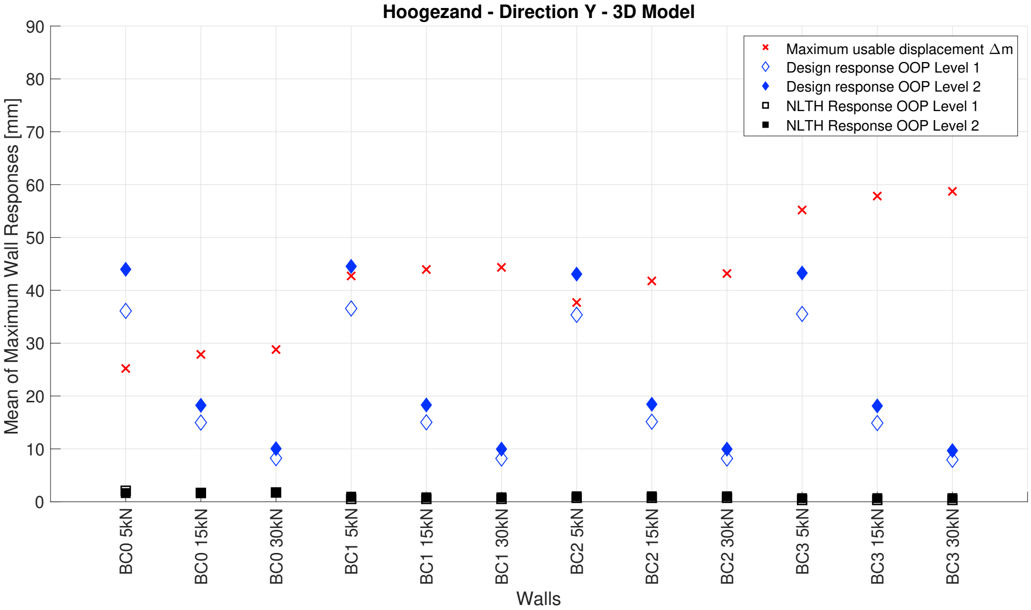

Figure 4.59: Hoogezand - Direction Y: design and NLTH response of the 3D Model OOP walls.

4.2.8.4 Loppersum

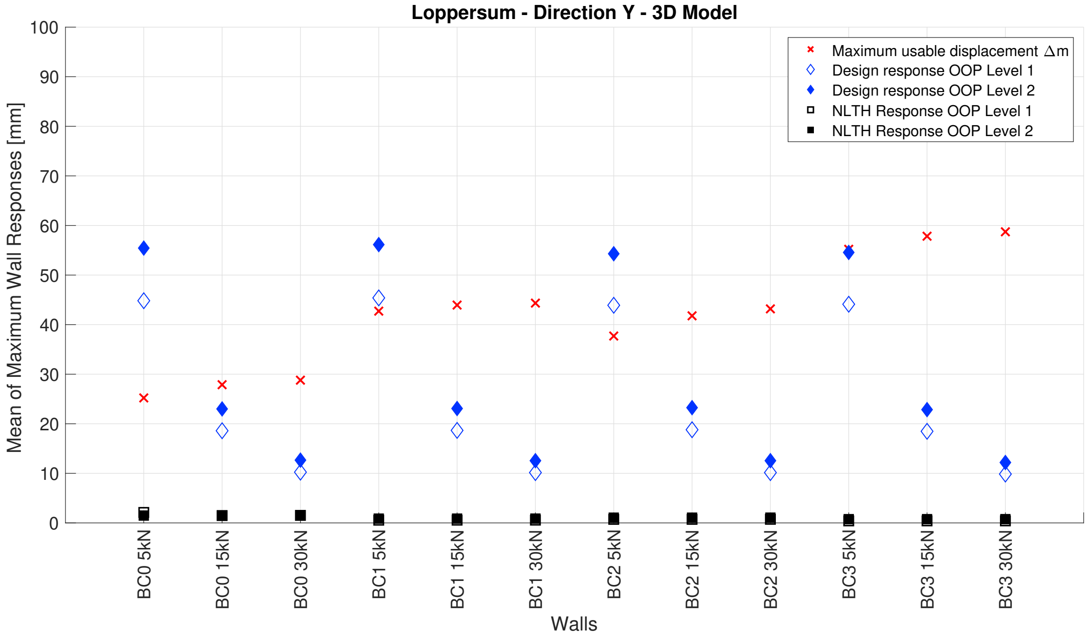

Figure 4.60: Loppersum - Direction Y: design and NLTH response of the 3D Model OOP walls.

4.2.8.5 Overschild

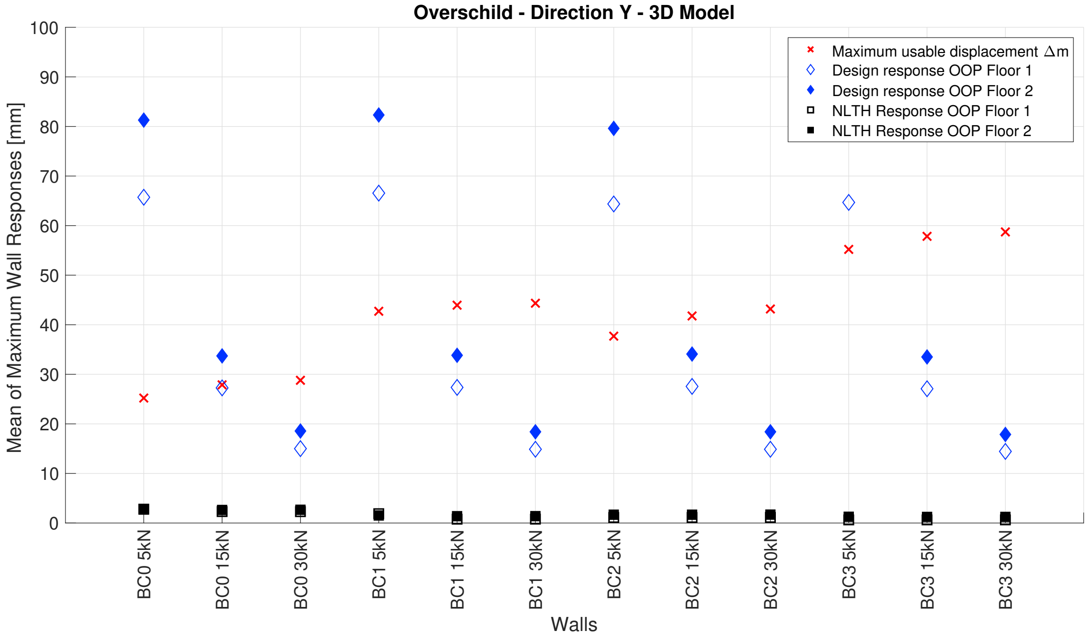

Figure 4.61: Overschild - Direction Y: design and NLTH response of the 3D Model OOP walls.

Chapter 5

Conclusions and Recommendations

5.1 Conclusions

The main goal of this thesis is to predict the displacement demand that should be used to assess the out-of-plane behaviour of one-way bending unreinforced masonry walls in terraced and detached houses built in the Groningen Province. This project derives a solid methodology to attain this target.

In detail, this methodology is based on the NZSEE Norm [28], which employs a displacement-based approach for the assessment of the one-way vertically spanning out-of-plane walls. However, NZSEE approach takes into account the New Zealand's seismic characteristics. Thus, the adjustment of the foreign normative to the particularities of the Dutch scenario is necessary. For this reason, a number of typologies representing typical Dutch terraced and detached houses were considered and two modelling approaches (1D and 3D modelling) were adopted. In addition, the hysteretic behaviour of the models was based on experimental tests on single structural components (i.e. piers) for both in-plane and out-of-plane loading performed at the Stevin Laboratory of the Delft University of Technology. Furthermore, the ground motion records employed in the NLTH analyses are analogous to the induced seismicity found in the Groningen Province and more specifically in the areas of Appingedam, Groningen, Hoogezand, Loppersum and Overschild. Via elaboration of the outputs of the performed analyses, the Shape Factor Coefficient $C_i(T_p)$ and Height Coefficient C_{Hi} for the Groningen Case were defined. Consequently, this work allows the beneficial use of the NZSEE Norm [28] displacement-based approach with the pertinent coefficients that characterise the houses in the Groningen Province.

Particularly for the derivation of the Shape Factor Coefficient $C_i(T_p)$, 1D NLTH analyses were performed in Opensees. Seven representantive typologies were modelled as equivalent SDOF systems and in total 110 ground motion records were used. The wide set of data produced (mainly in terms of Floor Response Spectra) created a comprehensive basis for the description of the Design Floor Accelaration Spectra. Subsequently, the equations that define the Shape Factor Coefficient $C_i(T_p)$ as a function of the effective period T_p of the OOP wall were derived by using the Newmark-Hall Method.

Moreover, the Floor Response Spectra were also investigated for one specific typology by means of a 3D Model in ANSR-II. The outputs of the NLTH analyses in the 3D Model strengthened the intergrity of the Design Floor Accelaration Spectra produced by the simplified 1D Models. Especially for the areas with the highest PGAs (Appingedam, Loppersum and Overschild) the highest mean floor spectral accelaration can be accurately predicted for the “weak” in-plane direction of the typology (direction X). In addition, the plateau period range of the Design Floor Accelaration Spectra matches the period range related to the maximum values of the response spectra of Floor 2 of the 3D Model in direction X. Concerning the areas with the lowest PGAs (Groningen and Hoogezand), the 3D Model remained elastic in direction X, presenting narrow high amplified Floor Response Spectra. Similar FRS were observed also in the simplified 1D models that remained elastic in direction X (typologies 6 and 7) for these areas (figures 3.48 and 3.49).

Regarding the response of the 3D Model in the “strong” in-plane direction of the typology (direction Y), the demand of the Floor Response Spectra is satisfied by the Design Floor Accelaration Spectra. The 3D Model behaved elastically in direction Y for all the NLTH analyses, similarly to the behaviour of the 1D Models in this direction. Nonetheless, a major discrepancy is identified between the response of the 3D Model and the 1D models in direction Y. This is the absence of the narrow high amplified bell-shaped curves that were observed in the response spectra of the 1D Models. Commonly, an eigenvalue analysis of a 3D Model results to more than one eigen mode. The dominant eigen mode, related to the dominant eigen period, concentrates the majority of the mass that participates in the dynamic response in a specific direction of the model. On the contrary, in a mass-spring system, the mass participating to the dynamic excitation is the total mass of the equivalent structure and it is assigned only to one period, the fundamental period of the system. Hence, the spectral amplitudes in the simplified models are significant in the fundamental periods, while in the 3D Model the spectral amplitudes are lower in the dominant eigen period, since it is related to 59% of the total mass. The rest of the mass is assigned to other modes.

Another important output from the 3D Model analyses, is the Height Coefficient C_{Hi}. The Height Coefficient C_{Hi} is obtained as the ratio of the Peak Floor Accelaration (PFA) over the Peak Ground Accelaration (PGA) and described as a linear function of the height of the structure. In addition, parameter α was added in the equation as the denominator of the height. Parameter α describes the dependency of the Height Coefficient C_{Hi} on the area and direction of the structure. The equation derived for the Height Coefficient C_{Hi} has the same format with the respective equation in the NZSEE Norm [28]. Therefore, comparisons can be made for their impact in the design response. In detail, NZSEE Norm [28] uses a value of 6 for the parameter α, while this value is the lower boundary for the α values described for the Groningen Case. Thus, NZSEE Norm [28] overestimates the Height Coefficient C_{Hi} for the Dutch scenario regarding this specific model.

Besides the derivation of the Shape Factor Coefficient and Height Coefficient, sensitivity studies of OOP walls in the 1D Models, but also in the 3D Model, were performed. Twelve configurations were considered depending on the boundary conditions and the overburden loads of the walls. From these studies, certain patterns and differences of the general behaviour of OOP walls per area and direction were concluded. For direction X, the mean of the maximum wall responses for the non-failing walls of the 3D Model were comparable with the respective results of the 1D Models. For direction Y, the mean of the maximum wall responses for the non-failing walls in the 3D Model were significantly lower than the respective displacements in the 1D Models. An average displacement of all the non-failing OOP walls for the 1D Models in direction Y for all the areas can be estimated to be just below 10 millimeters, while this value for the 3D Model is 2 millimeters. This can be justified from the fact that the 3D Model in direction Y is very stiff with negligible displacements at the floor levels (below 1 millimeter). The amplification of the mid-height displacement of the OOP wall compared to the displacement of the diaphragms is significant but the resulted mid-height displacement is small. Moreover, the resonance effects in 1D Models are more pronounced. The spectral amplitudes are considerably high in the fundamental period of the linear SDOF systems. For this reason, the OOP wall (especially when its elastic period coincides with the elastic periods of the 1D Models in direction Y) attracts higher accelarations compared to the OOP wall in the 3D Model.

Eventually, from the aforementioned sensitivity studies, conclusions can be drawn for the general performance of the design response Δ_{ph} (based on the Shape Factor Coefficient $C_i(T_p)$ and Height Coefficient C_{Hi} obtained from this research) compared to the NLTH response. These are:

1. Design response is an upper bound value of the NLTH response for all the cases of the non-failing OOP walls.
2. When NLTH response indicates failure, design response predicts this failure.
3. When design response indicates failure (design displacement Δ_{ph} is larger than the maximum usable displacement Δ_m), it is not always indicated by the NLTH response. However, the design response is still greater than the NLTH response ($\Delta_{ph}>\Delta_{NLTH}$).

5.2 Limitations of the research

Although a thorough investigation has been conducted to address the problem of this thesis, some inherent limitations still exist, especially regarding the 3D Model.

First of all, the mass-spring systems in Opensees were modelled very accurately in order to capture the right dynamic behaviour of their equivalent structures. Nevertheless, a limitation of these models is the description of the hysteretic profile of the equivalent structures based on the hysteresis of rocking URM piers. Although the transition for the description of the hysteresis profile from component to structure level and the use of generalised hysteretic rules (i.e. Takeda) is rather a common practice for researches related to the dynamic excitation of SDOF systems, it should be pointed out as a limitation of this research.

As far as the 3D Model is concerned, the major limitation is the absence of hysteresis in the dynamic behaviour of OOP walls. ANSR-II is able to capture the geometrical nonlinearity due to the rocking mechanism of OOP walls. However, it can not indicate hysteresis owing to material deterioration (strength and stiffness degradation). Thus, if an out-of-plane wall in ANSR-II returns to the location where the $P-\Delta$ overturning moments are less than the gravitational restoring moments, it will regain all of its initial stiffness and strength. Due to the peculiarity of the loading and unloading path of the OOP walls in ANSR-II, they will either develop relatively small mid-height displacements or fail. In Opensees Models, where strength and stiffness degradation occurs based on the calibrated hysteresis of the double-clamped one-way bending test specimen COMP-7, the non-failing OOP walls are able to present larger mid-height displacements in some cases of the sensitivity studies.

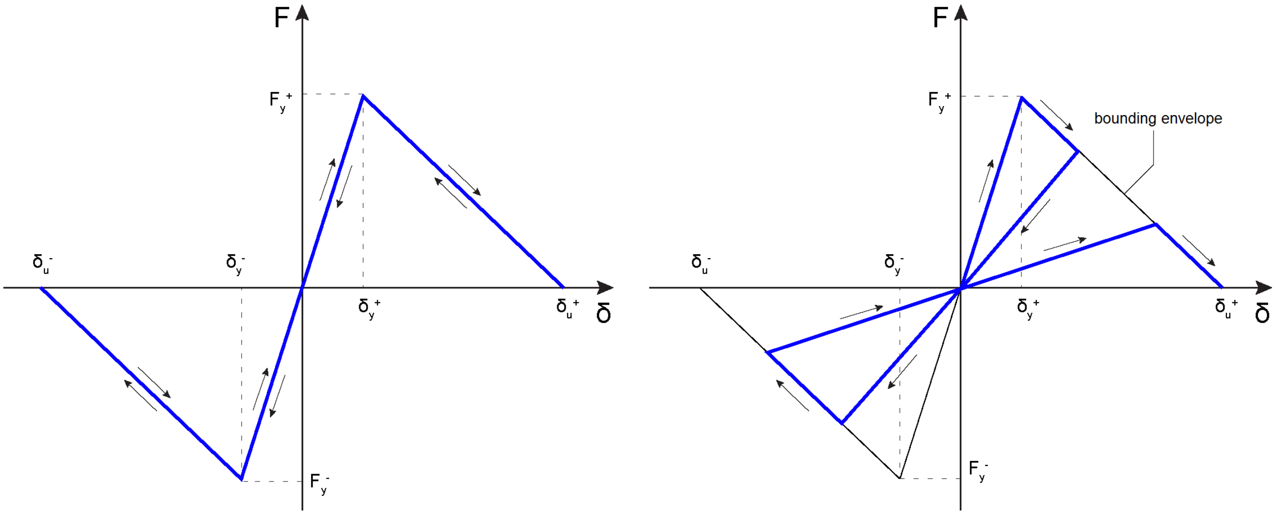

Figure 5.1: Loading and unloading path of an OOP wall in ANSR-II (left) and Opensees (right).

Additionally, another limitation found in the 3D Model is the inability to model hysteresis for rocking piers. ANSR-II incorporates nonlinear hysteresis behaviour only for the plane stress elements dominated by shear deformation. Nonetheless, rocking piers present rather low energy dissipation due to toe crushing. Only Micro-Modelling can model toe crushing, thus energy dissipation for URM rocking piers, with the appropriate definition of constitutive models and hysteretic rules. Consequently, the limitation of introducing no hysteresis in rocking piers is a limitation of the Macro-element based modelling approach.

Finally, fixed-base model assumption limits the response of the structure in direction Y, because it does not capture the structure-soil interaction. The rocking and shear capacity of the walls in direction Y is significant and owing to the soil condition in the Netherlands, subsidence due to soil compaction will occur. Additive displacements to the floor levels in direction Y of the structure can then be found. In direction X the opposite conclusions are reached, since the behaviour of the structure is weaker and it will govern the displacements. Hence, for direction X, the fixed-base approach is efficient.

5.3 Recommendations for future research

This thesis established a comprehensive derivation of the Shape Factor Coefficient $C_i(T_p)$ and Height Coefficient C_{Hi} concerning the correct implementation of the NZSEE [28] displacement-based approach for the Groningen Case. Nevertheless, there is still work to be done that could raise the reliability of the deliverables, especially of the Height Coefficient C_{Hi}.

To begin with, the same procedure described in this report, should be performed for an adequate number of 3D Models with rigid and flexible diaphragms. The respective results from the NLTH analyses should then be compared with the Design Floor Accelaration Spectra and Height Coefficient C_{Hi} derived in this research.

A further recommendation is the incorporation of soil springs in the 3D Models. The soil springs should be able to reflect the soil conditions typically found in the investigated seismic areas of the Netherlands.

A final proposition is related to the sensitivity studies on the response of OOP walls. A crucial task would be the incorporation of two-way bending out-of-plane walls in a 3D Model that resembles a typical Dutch house. Micro-Modelling approach should be adopted for such purposes. However, challenges will be probably met on the definition of the boundary conditions, yield or cracking pattern of the wall, constitutive laws and hysteresis rules for the OOP wall. In addition, major difficulties regarding computational time and convergence criteria might rise. All of these demanding issues would probably result to “fixed” models of the walls. However, this potential study could reveal the benefits of two-way spanning in comparison to one-way spanning assumption.

References

[1] Abbasi M., Moustafa M. A., *Effect of Viscous Damping Modeling Characteristics on Seismic Response of Bridges*, Conference Paper, Dept. of Civil and Enviromental Engineering, University of Nevada, Reno, USA. August 2017.

[2] Bakeer T., *Collapse Analysis of Masonry Structures under Earthquake Actions* Chair of Structural Design, TU Dresden, 8 edition, 2009. ISBN 9783867801300.

[3] Barandun A., *Seismic Behavior of Unreinforced Masonry Walls with Soft-Layer Strip Bearings* Technical Report, Master Thesis SS, ETH Zurich, 2013.

[4] Blaikie E. L., Davey R. A., *Seismic behaviour of faced loaded unreinforced masonry walls*, 12th World Conference on Earthquake Engineering, Auckland, New Zealand, 2000.

[5] Bo Li, *Response Spectra for Seismic Analysis and Design*, University of Waterloo, Ontario, Canada, 2015.

[6] Bruneau M., *State-of-the-art Report on Seismic Performance of Unreinforced Masonry Buildings*, Journal of Structural Engineering, 120(1):230-251, 1994.

[7] Calvi G. M., Priestley M. J. N., Kowalsky M. J., *Displacement-Based Seismic Design of Structures*, 3rd Panhellenic Conference on Earthquake, Mechanical and Technical Seismology, 2008.

[8] Chiou S. B., Chang Y. W., Jean W. Y., Chai J. F., *A Study on the Spectrum Shape for Performance Based Design of Tapei Basin*, 14th World Conference on Earthquake Engineering, Beijing, China, 2008.

[9] Chopra Anil K., *Dynamics of Structures, Theory and Applications to Earthquake Engineering*, Fourth Edition, Pearson Education Inc., 2012. ISBN 13: 978-0-13-285803-8.

[10] Doherty K. T., *An investigation of the weak links in the seismic load path of unreinforced masonry buildings*, PhD Thesis, The university of Adelaide, Australia, 2000.

[11] Doherty K. T., Griffith M. C., Lam N., Wilson J., *Displacement-based seismic analysis for out-of-plane bending of unreinforced masonry walls*, Earthquake Engineering and Structural Dynamics, Earthquake Engng Struct. Dyn. 2002; 31:833-850, John Wiley & Sons, Ltd.

[12] Draft NPR 9998, Practical Guideline, *Assessment of structural safety of buildings in case of erection, reconstruction and disapproval - Basic rules for seismic actions: induced earthquakes*, 2017.

[13] ElGawady M., Lestuzzi P., Badoux M., M.ASCE, *Static Cyclic Response of Masonry Walls Retrofitted with Fiber-Reinforced Polymers*, Journal of Composites for Construction, 2007.

[14] Esposito R., Terwel K., Ravenshorst G., Schipper R., Messali F., Rots J.G., *Cyclic Pushover Test on an Unreinforced Masonry Structure reseambling a Typical Dutch Terraced House*, 16^{th} World Conference on Earthquake Engineering: Santiago, Chile, 2016.

[15] Finley A. C., *Unintended Consequences of Modeling Damping in Structures*, Journal of Structural Engineering, ASCE, April 2008. DOI: 10.1061/(ASCE)0733-9445(2008)134:4(581).

[16] Ghodrati Amiri G., Manouchehri Dana F., Sedighi S., *Determination of Design Acceleration Spectra for Different Site Conditions, Magnitudes, Safety Levels and Damping Ratios in Iran*, International Journal of Civil Engineering, Vol.6, No. 3, September 2008.

[17] Hemant B., Kaushik, Durgesh C. Rai, Sudhir K. Jain, M. ASCE, *Stress-Strain Characteristics of Clay Brick Masonry under Uniaxial Compression*, Journal of Materials in Civil Engineering ASCE, 2007.

[18] Kelly E. T., *Performance Based Evaluation of Buildings, Reference Manual Volume 3: Evaluation of Performance*, Holmes Consulting Group Ltd, 2014.

[19] Kelly E. T., *Performance Based Evaluation of Buildings, Reference Manual Volume 4: Reference Material, Nonlinear Pushover and Time History Analysis*, Holmes Consulting Group Ltd, 2014.

[20] Malhotra Praveen K., *Normalized Response Spectrum of Ground Motion*, The Bridge and Structural Engineer, Volume 45, Number 1, March 2015.

[21] Mazzoni S., McKenna F., Scott M. H., Fenves G. L., et al. *OpenSees Command Language Manual*, Open System for Earthquake Engineering Simulation, July 2016.

[22] Messali F., Ravenshorst G., Esposito R., Rots J., *Large-scale testing program for the seismic characterization of Dutch masonry walls*, Final published version, Delft University of Technology, Delft, the Netherlands, 2017.

[23] Messali F., Rots J.G., *In-plane Drift Capacity at Near Collapse of Rocking Unreinforced Calcium Silicate and Clay Masonry Piers*, Engineering Structures 164 (2018) 183-194.

[24] Mosalam K., Glascoe L., Bernier J., *Mechanical Properties of Unreinforced Brick Masonry, Section 1*. Lawrence Livermore National Laboratory, 2009.

[25] NEN-EN 1998-1, *Eurocode 8 - Ontwerp en berekening van aardbevingsbestendige constructies - Deel 1: Algemene regels, seismische belastingen en regels voor gebouwen*, 2005.

[26] Newmark N. M., Hall W. J., *Development of Criteria for Seismic Review of Selected Nuclear Power Plants*,U.S. Nuclear Regulatory Commission, Office of Nuclear Reactor Regulation, 1978. Under Contract No. AT(49-24)-0116.

[27] NTC, *Istruzioni per l’applicazione delle “Norme tecniche per le costruzioni”*, Consiglio Superiore dei Lavori Pubblici, 2008.

[28] NZSEE, New Zealand Society of Earthquake Engineering, *Assessment and Improvement of the Structural Performance of Buildings in Earthquakes*, Section 10 Revision, 2015.

[29] Oliver S., McKenzie H., Makan K., *Performance-based Design and Assessment of the Wellington Town Hall*, 16th European Conference on Earthquake Engineering, Thessaloniki, June 2018.

[30] Page A. W., *An Experimental Investigation of the Biaxial Strength of Brick Masonry*, 1982.

[31] Pant D. R., Wijeyewickrema A. C., *On Modeling Viscous Damping in Nonlinear Dynamic Analysis of Base-Isolated Reinforced Concrete Buildings*, 15th World Conference on Earthquake Engineering, Lisboa 2012.

[32] Paolo Martino Calvi (2014), *Relative Displacement Floor Spectra for Seismic Design of Non Structural Elements*, Journal of Earthquake Engineering, 18:7, 1037-1059, DOI: 10.1080/13632469.2014.923795.

[33] Penner O., Elwood K., *Out-of-Plane Dynamic Stability of Unreinforced Masonry Walls: Parametric Study and Assesment Guidelines*, Dept. of Civil and Enviromental Engineering, University of Auckland, New Zealand, 2015.

[34] Penner O., Elwood K., *Out-of-Plane Dynamic Stability of Unreinforced Masonry Walls: Shake Table Testing*, Dept. of Civil and Enviromental Engineering, University of Auckland, New Zealand, 2015.

[35] Priestley M. J. N., Calvi G. M., Kowalsky M. J., *Displacement-Based Seismic Design of Structures*, IUSS Press, Instituto Universitario di Studi Superiori di Pavia, 2007. ISBN 978-88-6198-000-6.

[36] Ravenshorst G. J. P., Mirra M. (2017). *Quasi-static cyclic tests on timber diaphragms representing a detached house.* Delft University of Technology. Report number C31B67WP4-7, version 1, 11 November 2017.

[37] Saatcioglu M., Shooshtari M., Naumoski N., Foo S., *Development of Floor Design Spectra for Operational and Functional Components of Concrete Buildings in Canada*, 14th World Conference on Earthquake Engineering, Beijing, China, 2008.

[38] Schott C., Schwarz J., *Reliability of Eurocode 8 Spectra and the problems of their application to central european earthquake regions*, 13th World Conference on Earthquake Engineering, August 2004. Paper No. 3403.

[39] Shelton R. H., Study report No. 124, *Seismic response of building parts and non-structural components*, BRANZ 2004. ISSN: 0113-3675.

[40] Takeda T., Sozen M. A., Nielsen N. N., *Reinforced Concrete Response to Simulated Earthquakes*, Ohbayashi-Gumi Technical Research Report No. 5, 1971.

[41] Tsoukalas A., Ditmar P., *Lecture Notes: Structural Response to Earthquakes (CIE5260)*, Delft University of Technology, Faculty of Civil Engineering and Geosciences, 2017.

[42] Vaculik J., Griffith M., *Time-History Analysis for Unreinforced Masonry Walls in Two-way Bending*, The 14th World Conference on Earthquake Engineering, Beijing, China, October 2008.

[43] Vaculik J., Lumantarna E., Griffith M., Lam N., Wilson J., *Dynamic Response Behaviour of Unreinforced Masonry Walls Subjected to Out of Plane Loading*, Australian Earthquake Engineering Society Conference 2007, Wollongong, NSW, January 2007.

[44] Vukobratovic V., Fajfar P., *A Method for Direct Generation of Floor Accelaration Spectra for Inelastic Structures*, 22nd Conference on Structural Mechanics in Reactor Technology, San Francisco, California, USA, August 2013. Division V.

[45] Welch D. P.,Sullivan T.J., *Influence of Structural and Fragility Modelling Decisions in the Loss Assessment of RC Buildings*, International Conference on Computational Methods in Structural Dynamics and Earthquake Engineering, June 2013. DOI: 10.7712/120113.4523.C1476.

[46] Hysteretic Material - OpenSees - UC Berkeley [Online]. Available: http://opensees.berkeley.edu/wiki/index.php/Hysteretic_Material

Appendix A

1D Models FRS Results

A.1 Appingedam

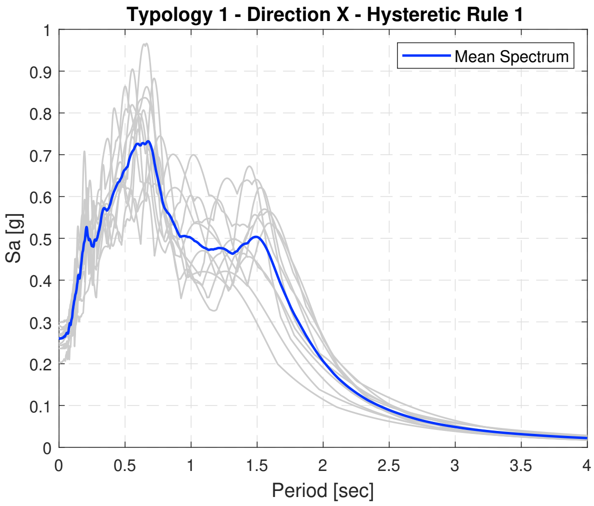
Typology 1 - Direction X - Hysteretic Rule 1

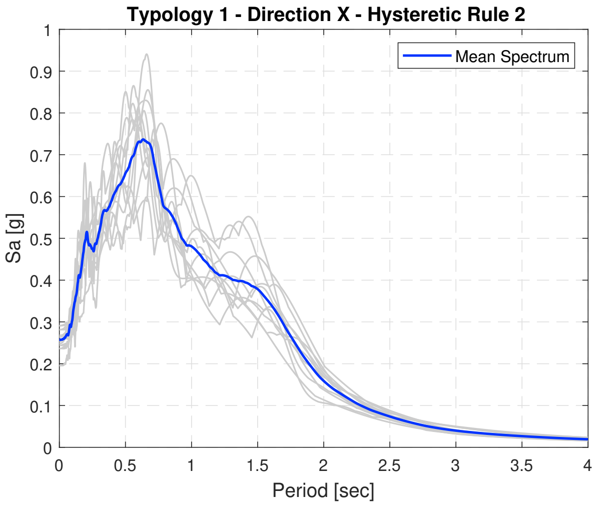
Typology 1 - Direction X - Hysteretic Rule 2

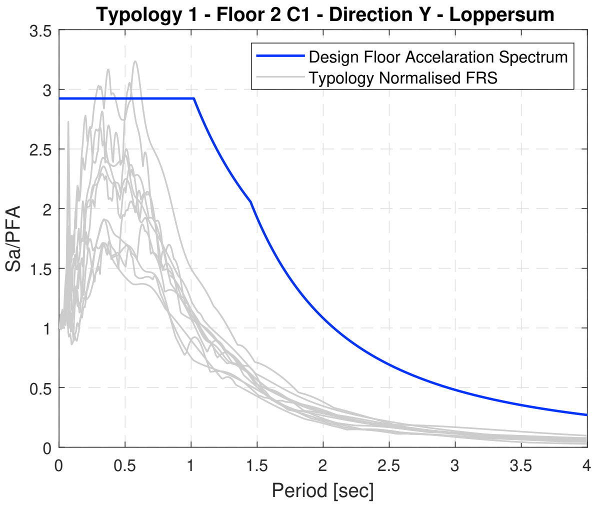
Typology 1 - Floor 2 C1 - Direction Y - Loppersum

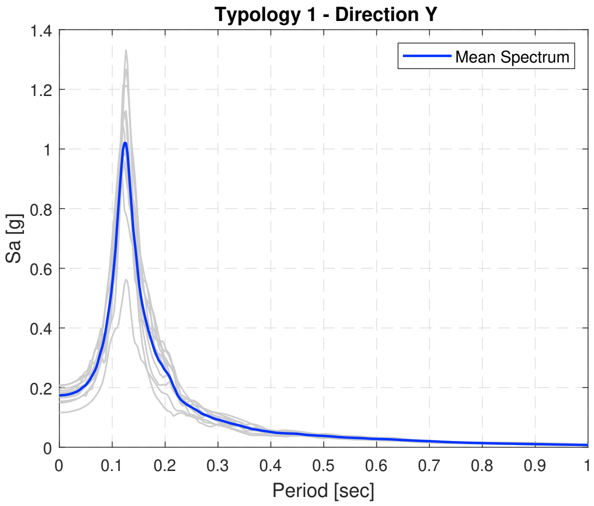
Typology 1 - Direction Y

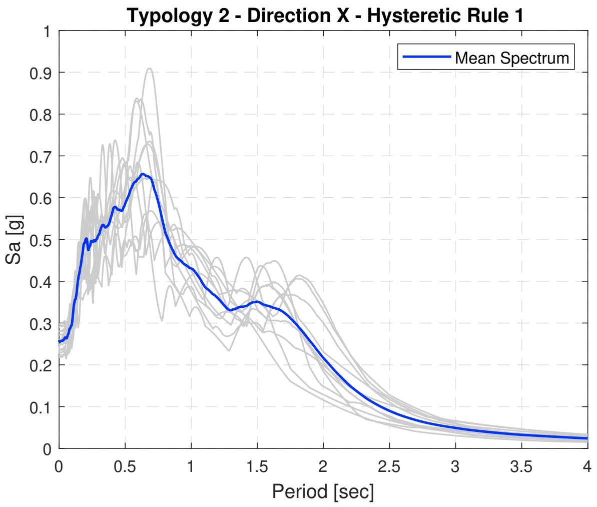
Typology 2 - Direction X - Hysteretic Rule 1

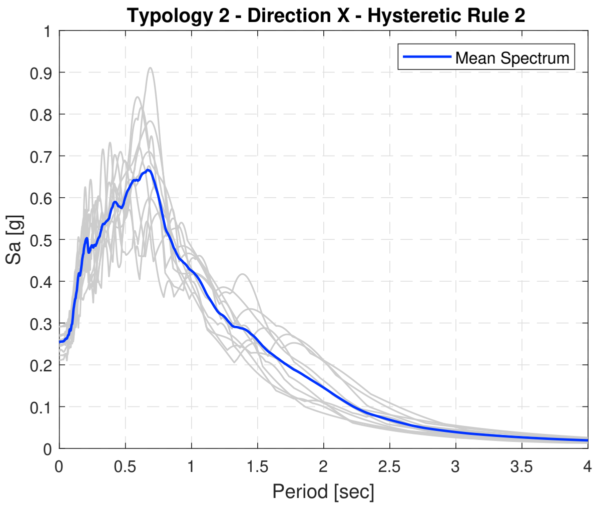
Typology 2 - Direction X - Hysteretic Rule 2

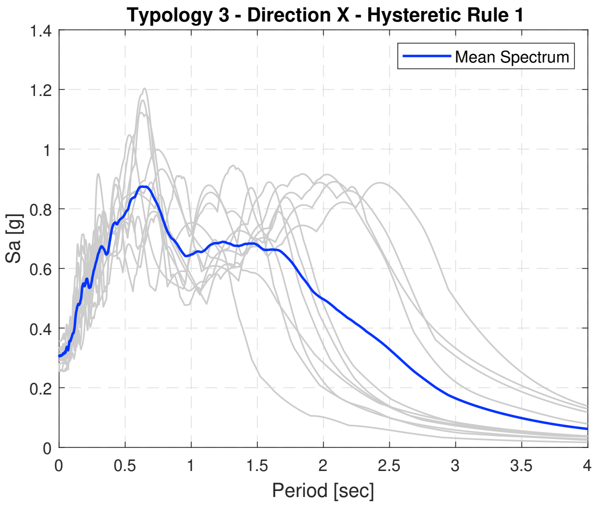
Typology 3 - Direction X - Hysteretic Rule 1

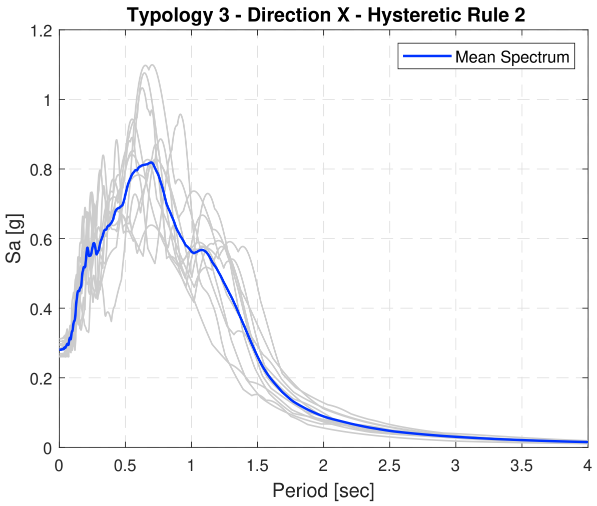
Typology 3 - Direction X - Hysteretic Rule 2

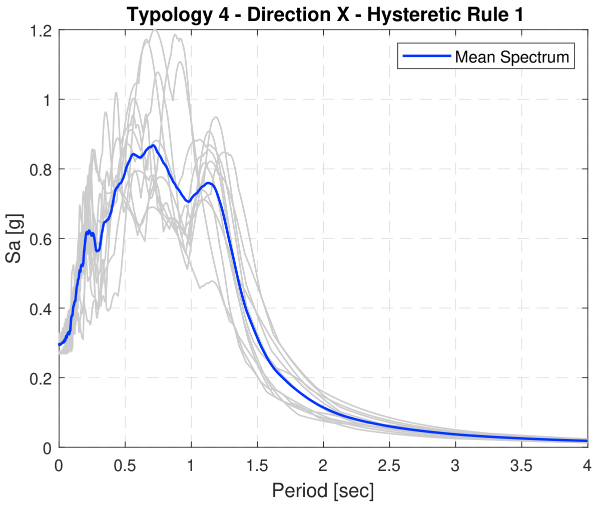
Typology 4 - Direction X - Hysteretic Rule 1

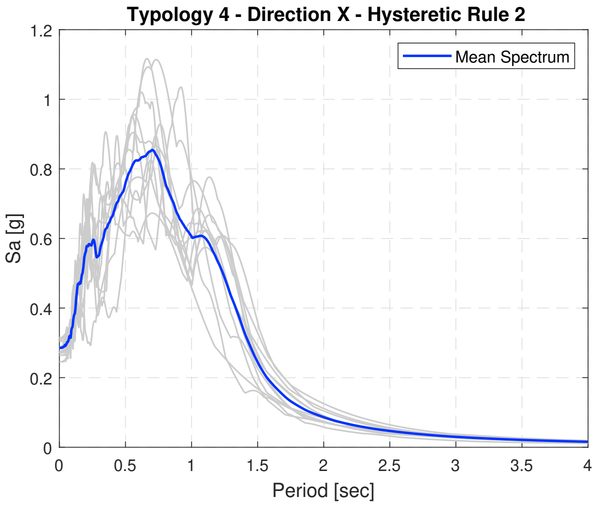
Typology 4 - Direction X - Hysteretic Rule 2

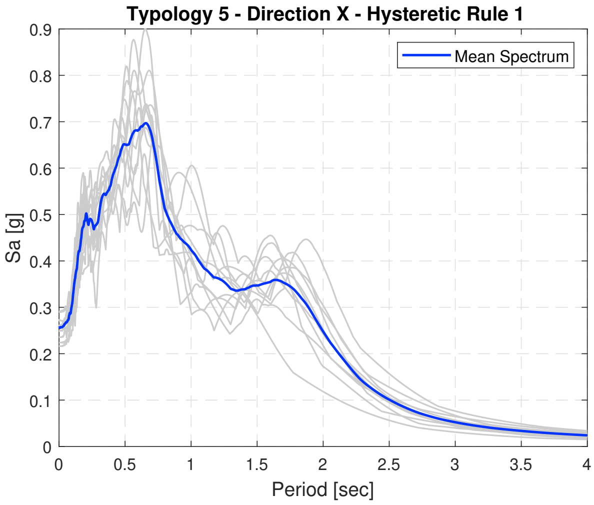
Typology 5 - Direction X - Hysteretic Rule 1

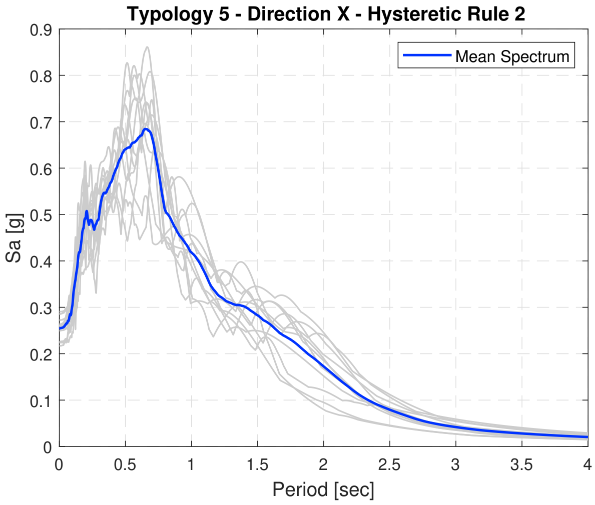
Typology 5 - Direction X - Hysteretic Rule 2

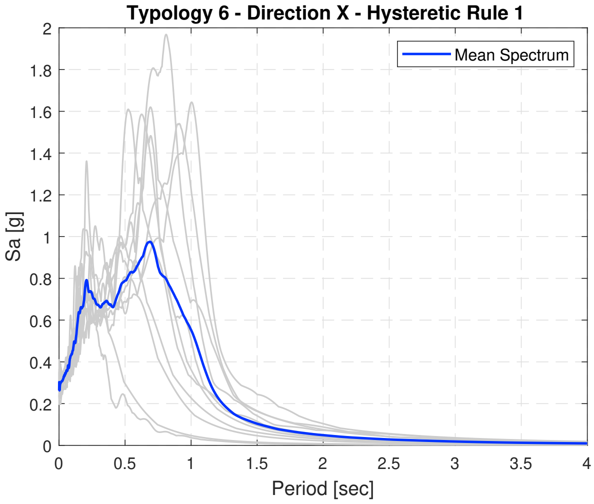
Typology 6 - Direction X - Hysteretic Rule 1

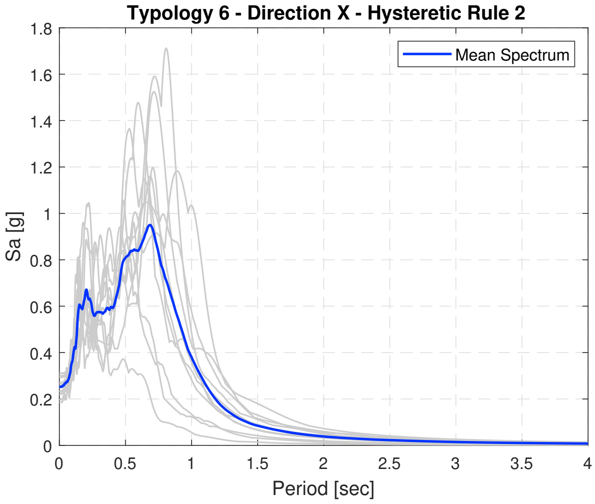
Typology 6 - Direction X - Hysteretic Rule 2

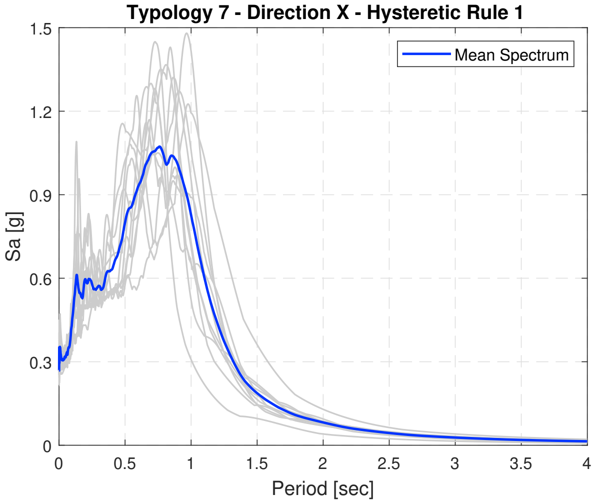
Typology 7 - Direction X - Hysteretic Rule 1

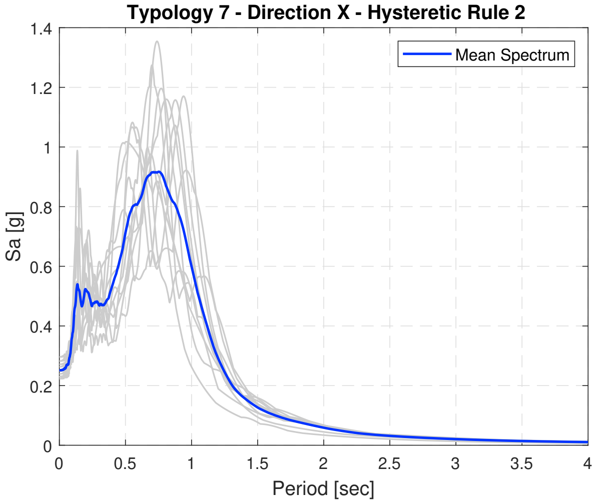
Typology 7 - Direction X - Hysteretic Rule 2

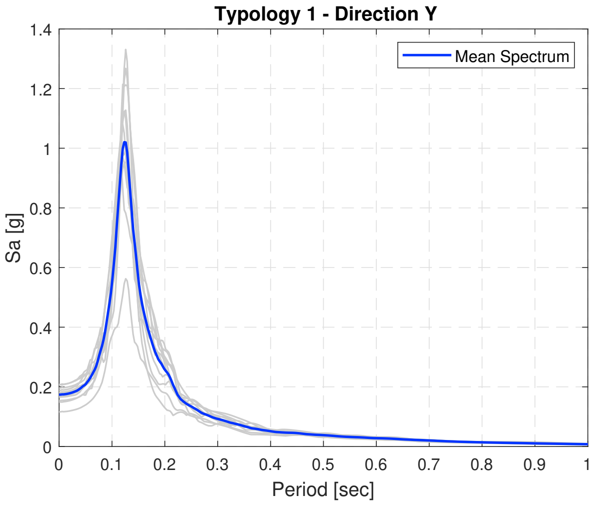
Typology 1 - Direction Y

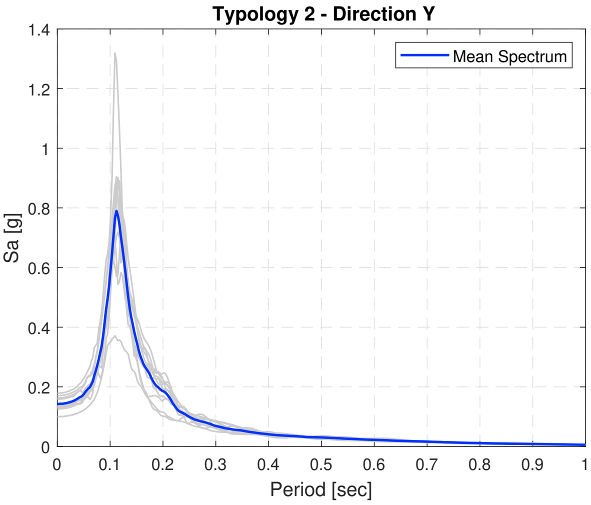
Typology 2 - Direction Y

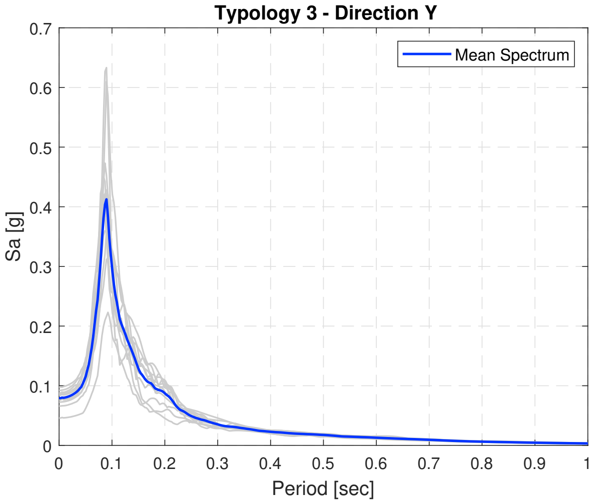
Typology 3 - Direction Y

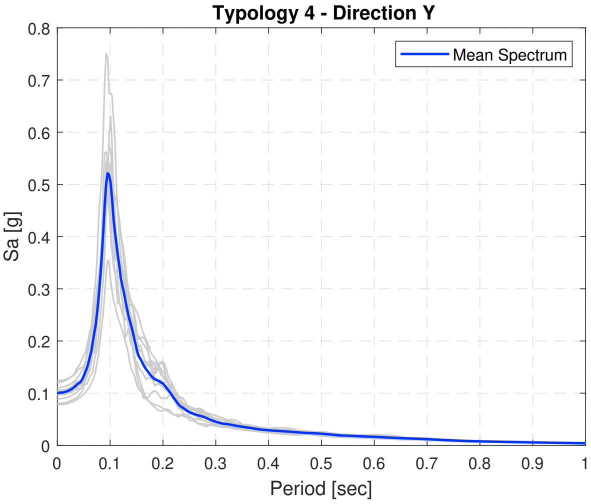
Typology 4 - Direction Y

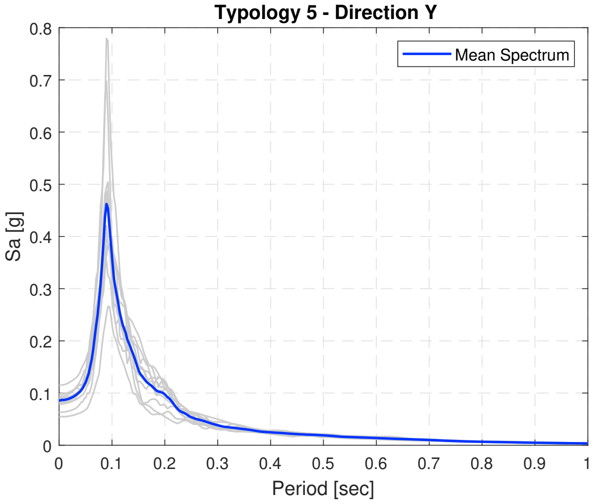
Typology 5 - Direction Y

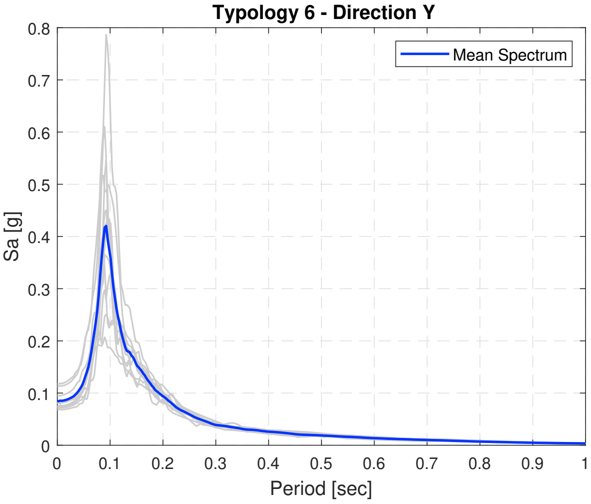
Typology 6 - Direction Y

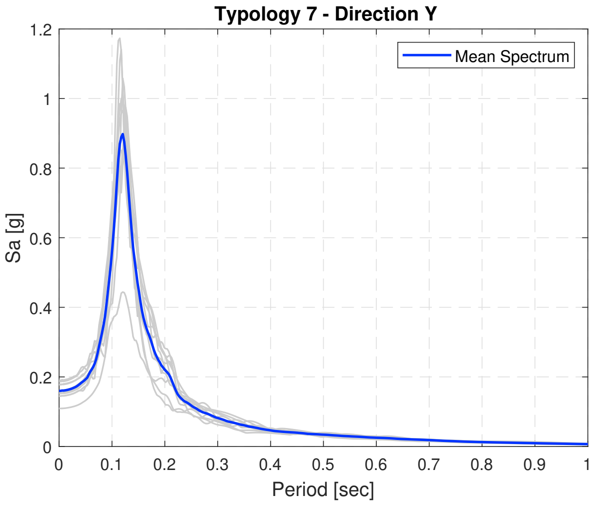

A.2 Groningen

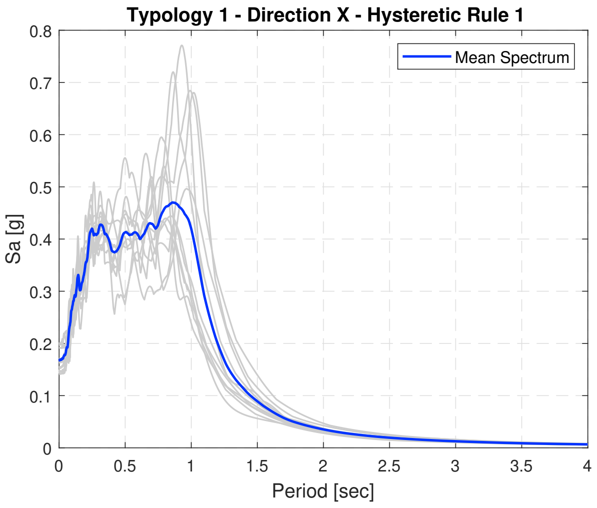

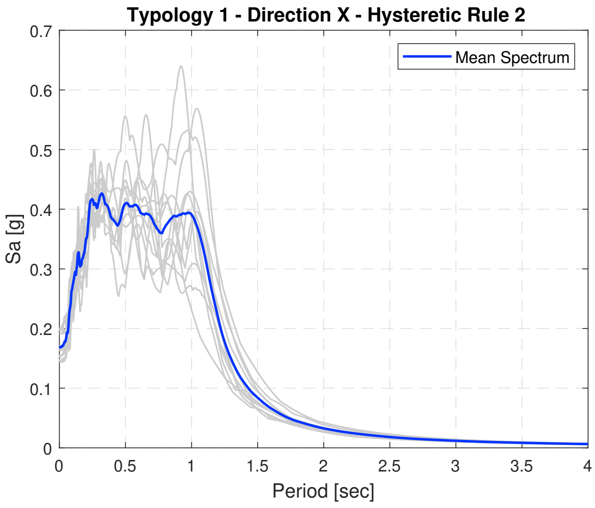

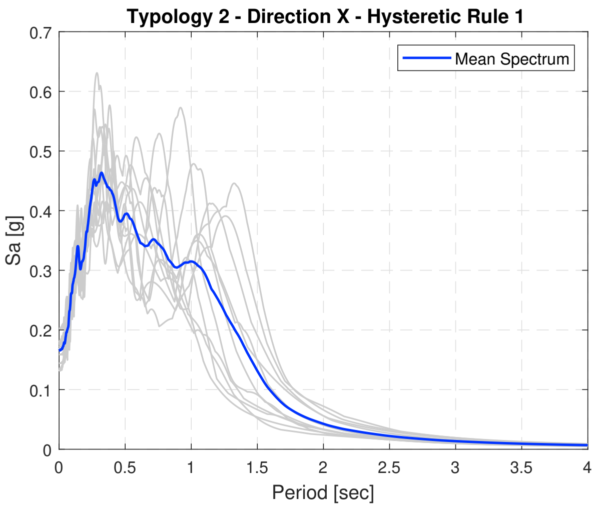

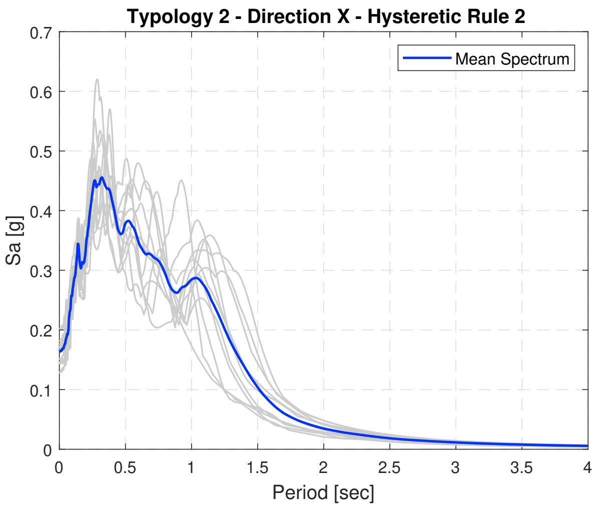

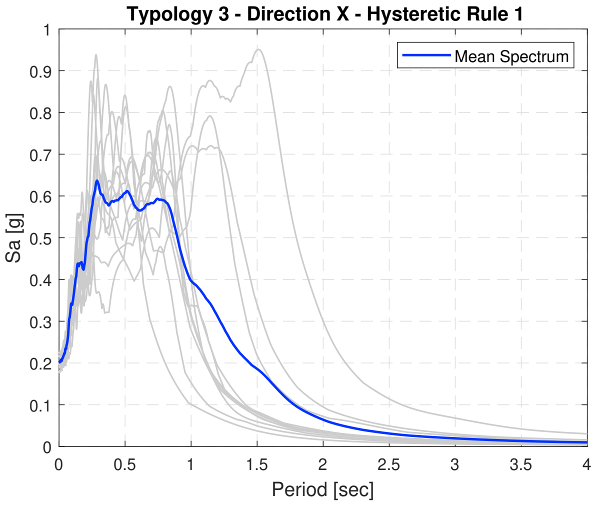
Typology 3 - Direction X - Hysteretic Rule 1
Mean Spectrum
Sa [g]
Period [sec]
0
0.1
0.2
0.3
0.4
0.5
0.6
0.7
0.8
0.9
1
0
0.5
1
1.5
2
2.5
3
3.5
4

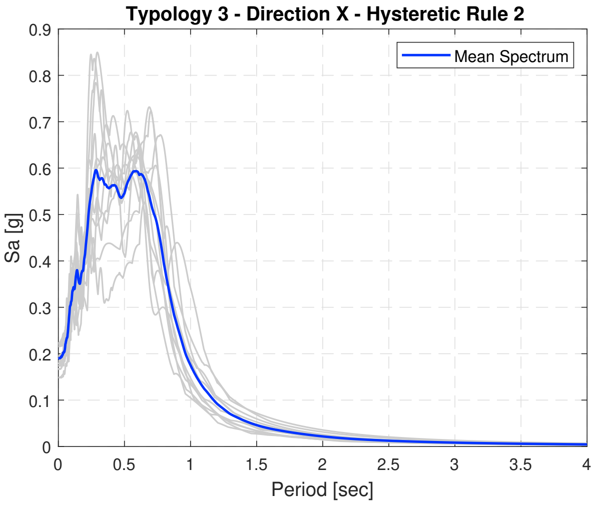
Typology 3 - Direction X - Hysteretic Rule 2
Mean Spectrum
Sa [g]
Period [sec]
0
0.1
0.2
0.3
0.4
0.5
0.6
0.7
0.8
0.9
0
0.5
1
1.5
2
2.5
3
3.5
4

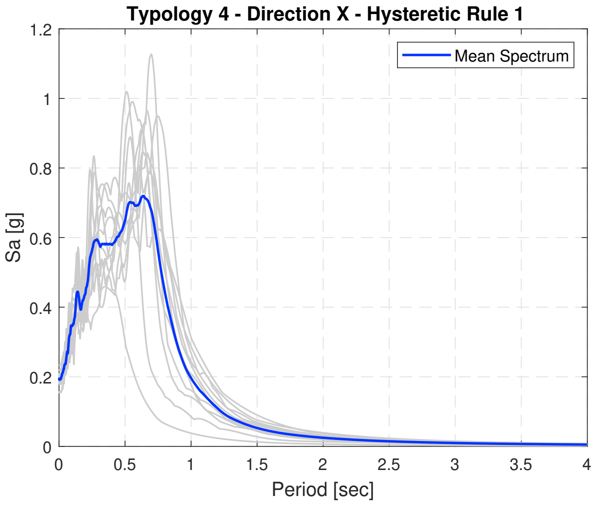
Typology 4 - Direction X - Hysteretic Rule 1
Mean Spectrum
Sa [g]
Period [sec]
0
0.2
0.4
0.6
0.8
1
1.2
0
0.5
1
1.5
2
2.5
3
3.5
4

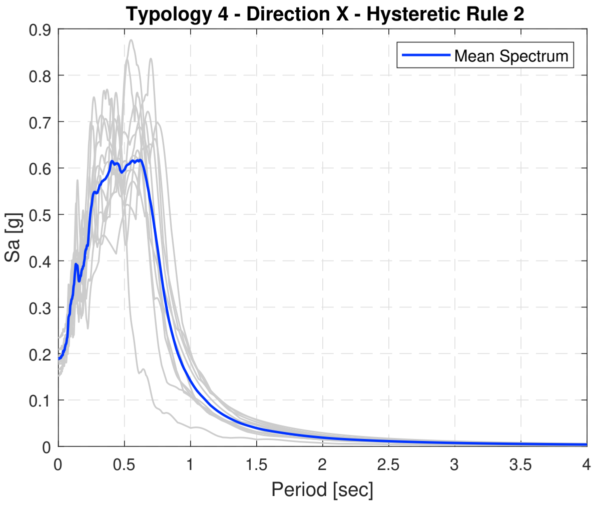
Typology 4 - Direction X - Hysteretic Rule 2
Mean Spectrum
Sa [g]
Period [sec]
0
0.1
0.2
0.3
0.4
0.5
0.6
0.7
0.8
0.9
0
0.5
1
1.5
2
2.5
3
3.5
4

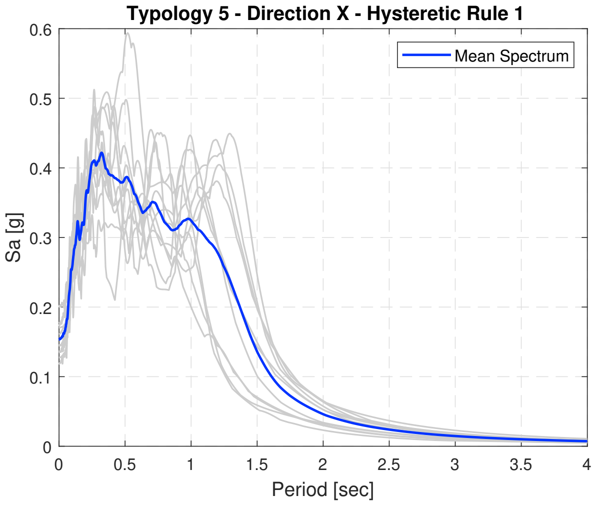
Typology 5 - Direction X - Hysteretic Rule 1
Mean Spectrum
Sa [g]
Period [sec]
0
0.1
0.2
0.3
0.4
0.5
0.6
0.5
1
1.5
2
2.5
3
3.5
4

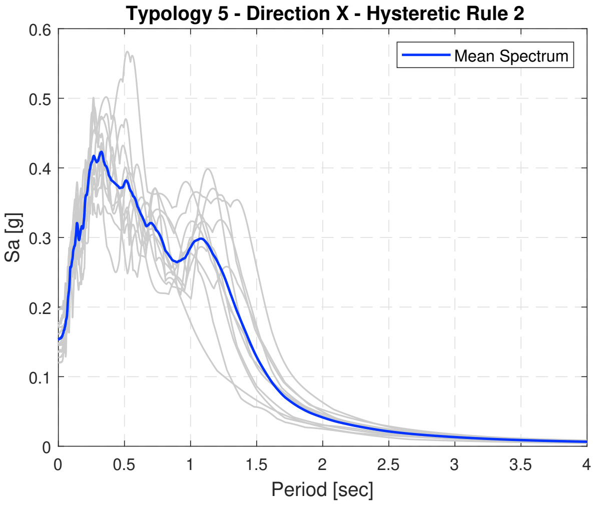
Typology 5 - Direction X - Hysteretic Rule 2
Mean Spectrum
Sa [g]
Period [sec]
0
0.1
0.2
0.3
0.4
0.5
0.6
0
0.5
1
1.5
2
2.5
3
3.5
4

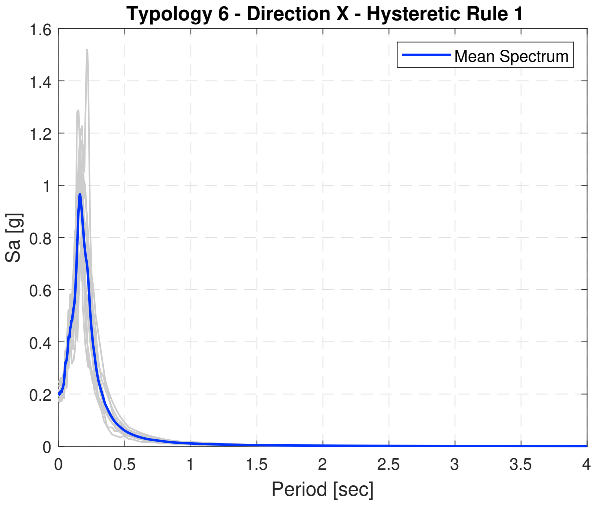
Typology 6 - Direction X - Hysteretic Rule 1

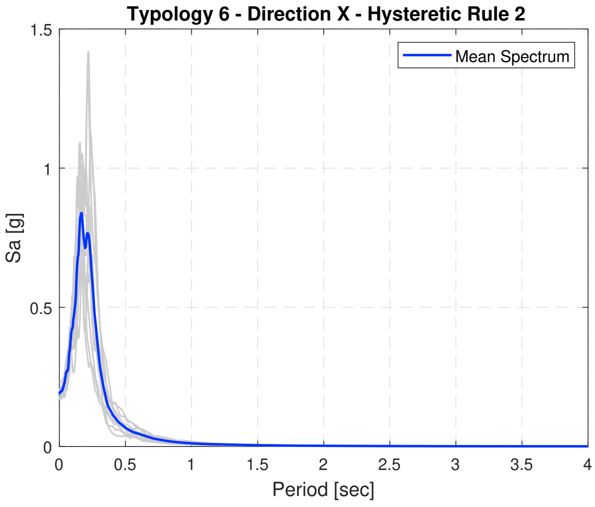
Typology 6 - Direction X - Hysteretic Rule 2

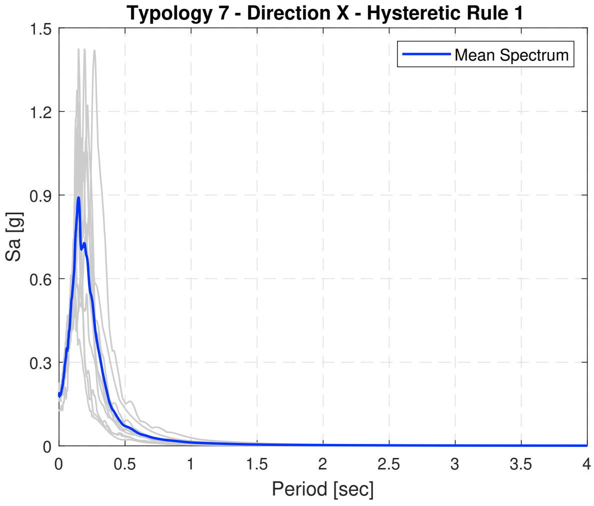
Typology 7 - Direction X - Hysteretic Rule 1

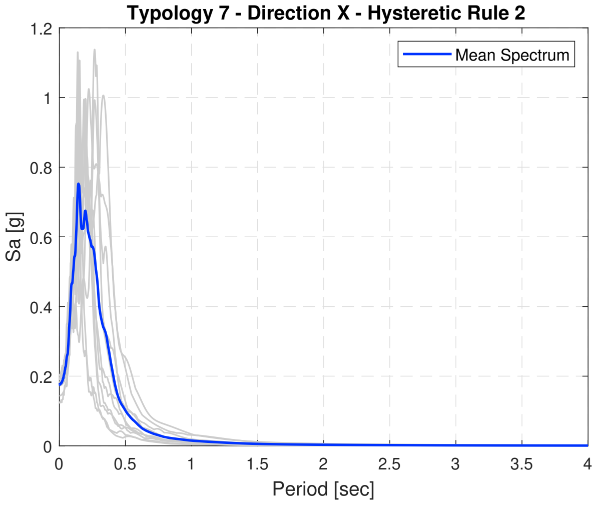
Typology 7 - Direction X - Hysteretic Rule 2

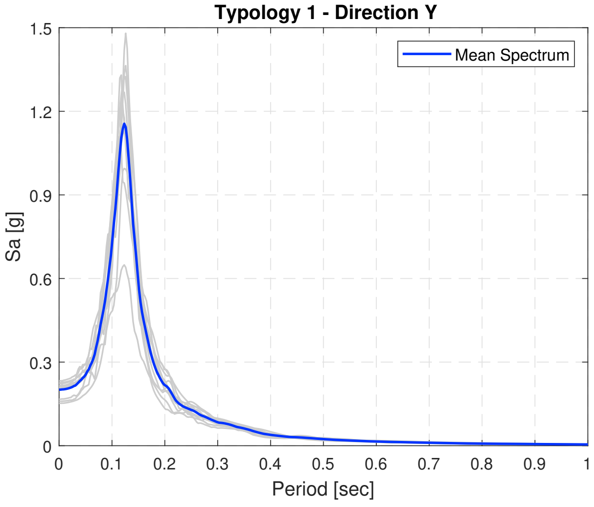
Typology 1 - Direction Y

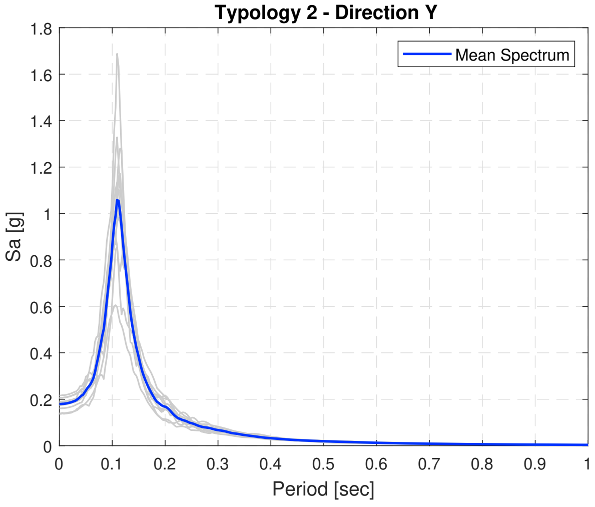
Typology 2 - Direction Y

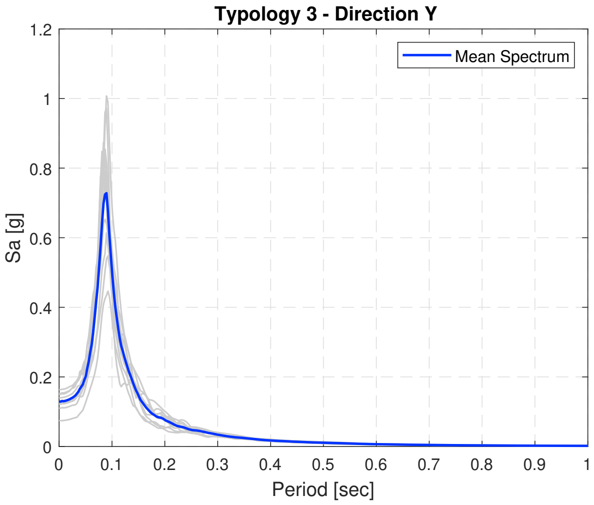
Typology 3 - Direction Y
Mean Spectrum
Sa [g]
Period [sec]
0
0.2
0.4
0.6
0.8
1
1.2
0
0.1
0.2
0.3
0.4
0.5
0.6
0.7
0.8
0.9
1

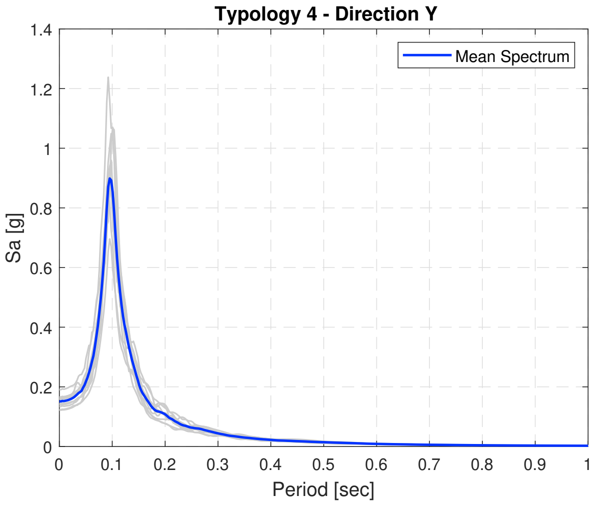
Typology 4 - Direction Y
Mean Spectrum
Sa [g]
Period [sec]
0
0.2
0.4
0.6
0.8
1
1.2
1.4
0
0.1
0.2
0.3
0.4
0.5
0.6
0.7
0.8
0.9
1

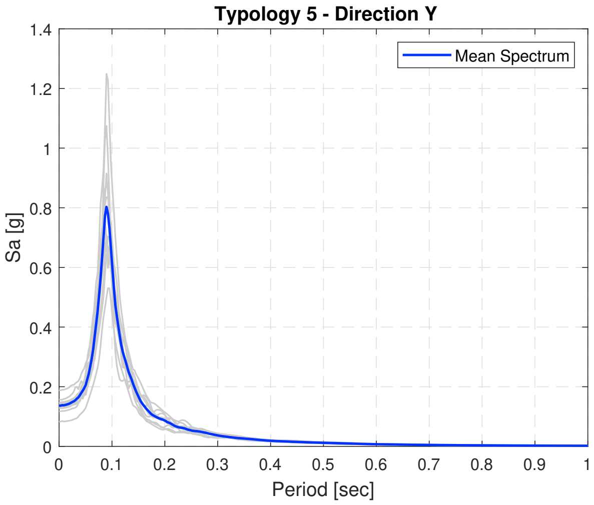
Typology 5 - Direction Y
Mean Spectrum
Sa [g]
Period [sec]
0
0.2
0.4
0.6
0.8
1
1.2
1.4
0
0.1
0.2
0.3
0.4
0.5
0.6
0.7
0.8
0.9
1

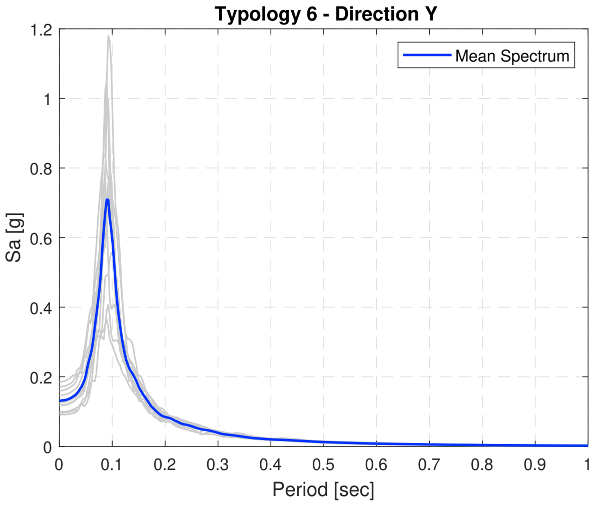
Typology 6 - Direction Y
Mean Spectrum
Sa [g]
Period [sec]
0
0.2
0.4
0.6
0.8
1
1.2
0
0.1
0.2
0.3
0.4
0.5
0.6
0.7
0.8
0.9
1

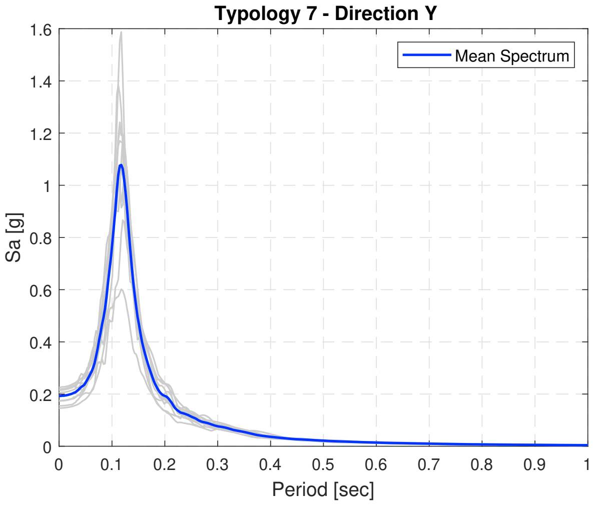
Typology 7 - Direction Y
Mean Spectrum
Sa [g]
Period [sec]
0
0.2
0.4
0.6
0.8
1
1.2
1.4
1.6
0
0.1
0.2
0.3
0.4
0.5
0.6
0.7
0.8
0.9
1

A.3 Hoogezand

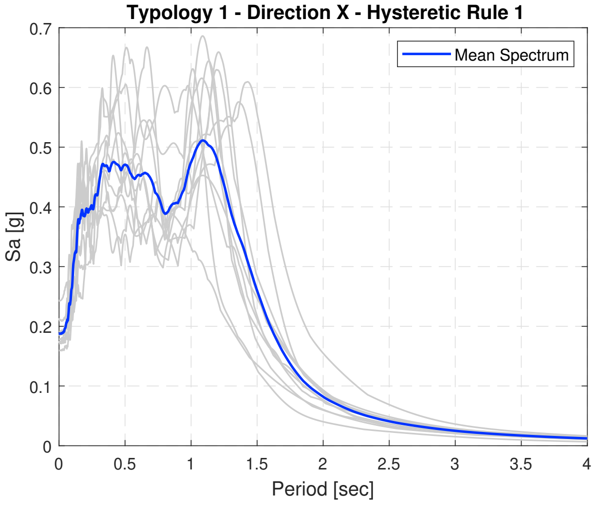
Typology 1 - Direction X - Hysteretic Rule 1

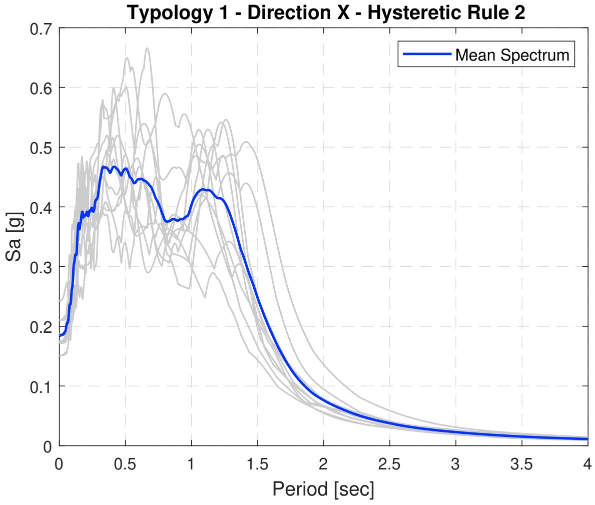
Typology 1 - Direction X - Hysteretic Rule 2

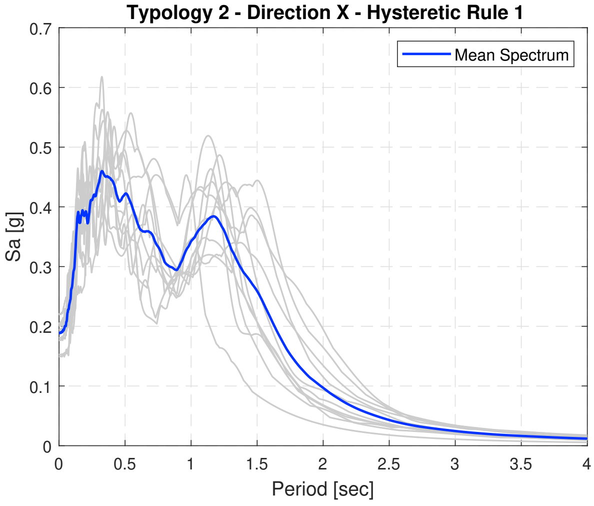
Typology 2 - Direction X - Hysteretic Rule 1

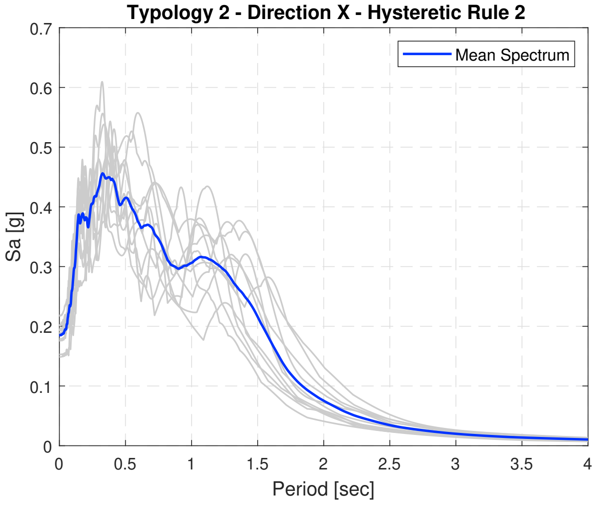
Typology 2 - Direction X - Hysteretic Rule 2

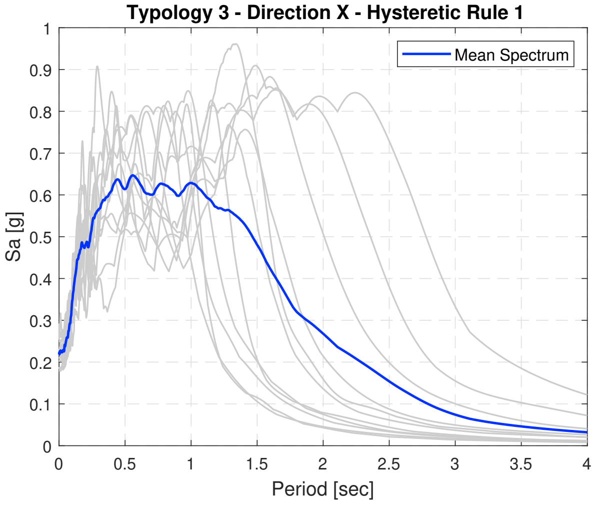
Typology 3 - Direction X - Hysteretic Rule 1

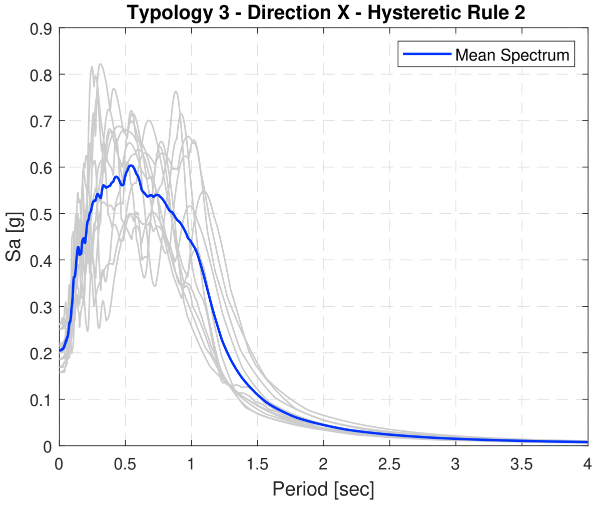
Typology 3 - Direction X - Hysteretic Rule 2

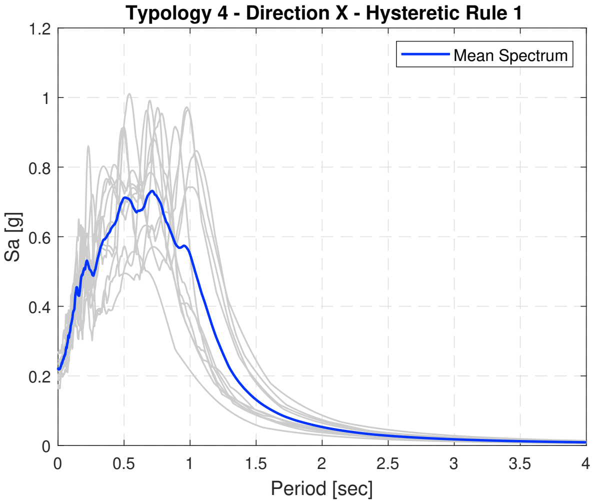
Typology 4 - Direction X - Hysteretic Rule 1

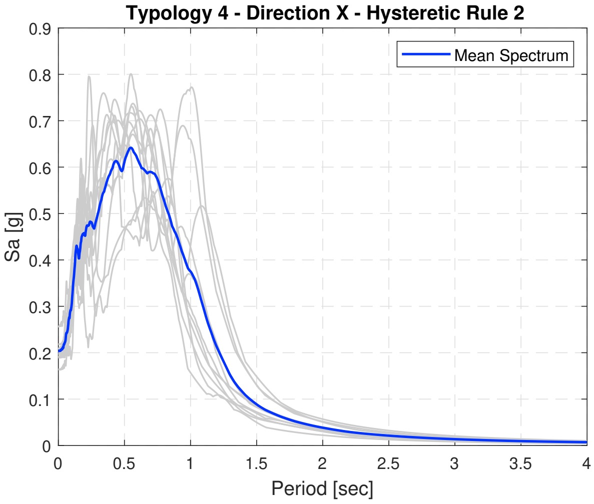
Typology 4 - Direction X - Hysteretic Rule 2

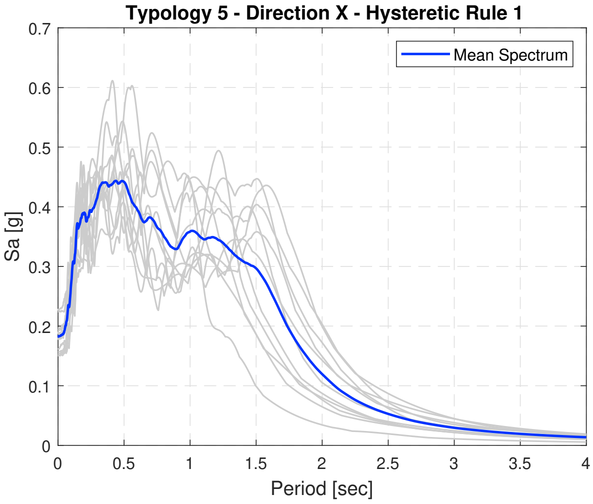
Typology 5 - Direction X - Hysteretic Rule 1

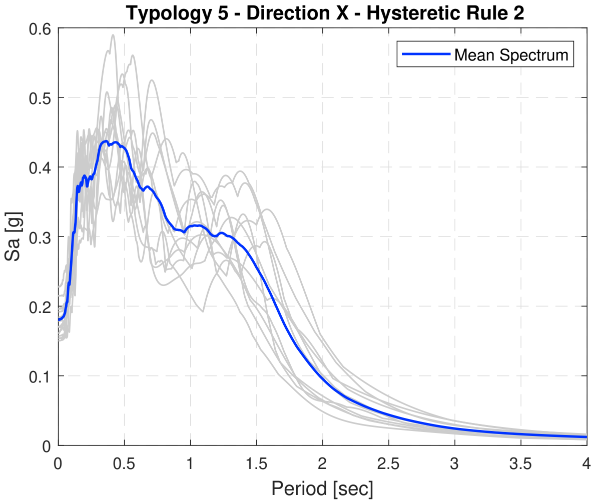
Typology 5 - Direction X - Hysteretic Rule 2

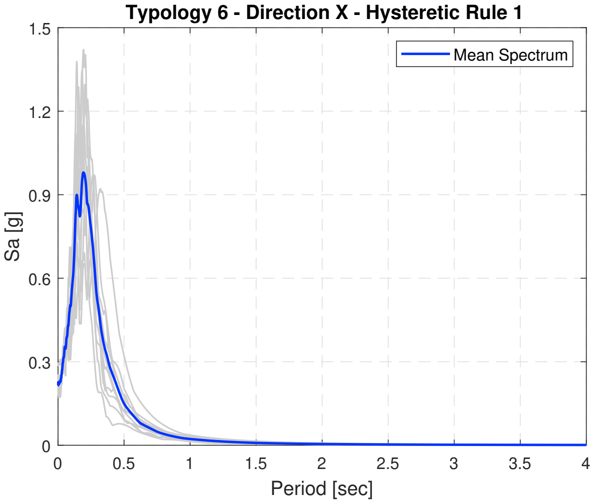
Typology 6 - Direction X - Hysteretic Rule 1

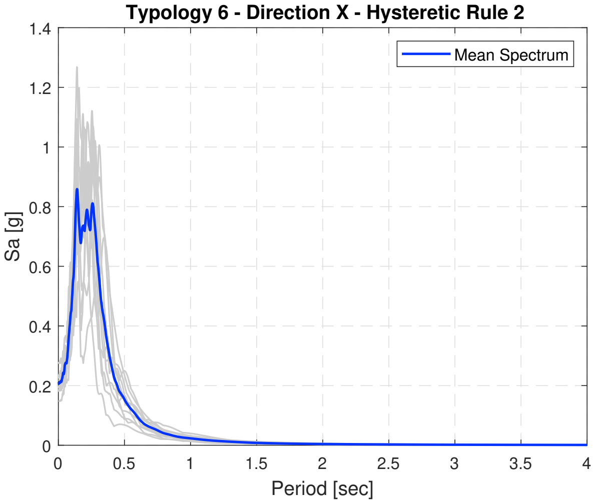
Typology 6 - Direction X - Hysteretic Rule 2

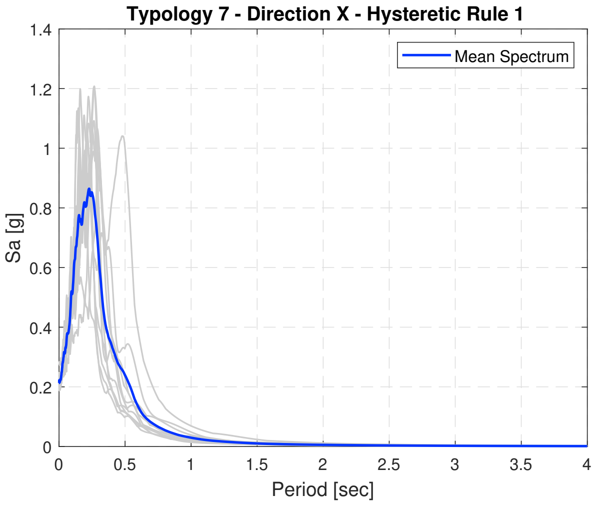
Typology 7 - Direction X - Hysteretic Rule 1

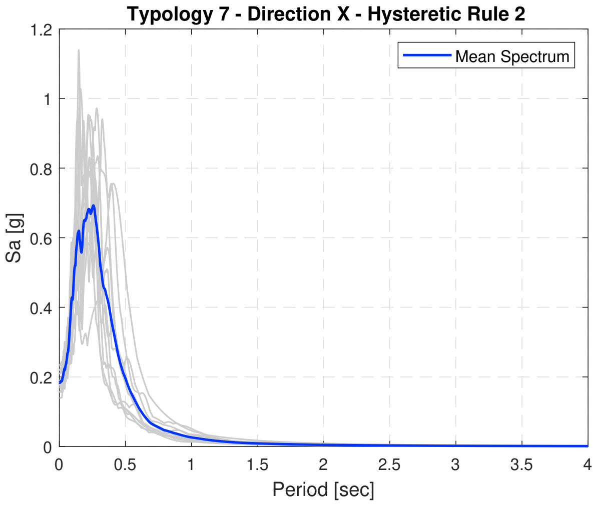
Typology 7 - Direction X - Hysteretic Rule 2

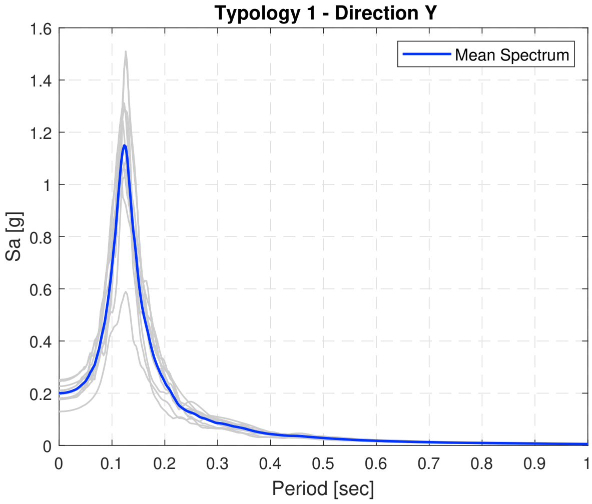
Typology 1 - Direction Y

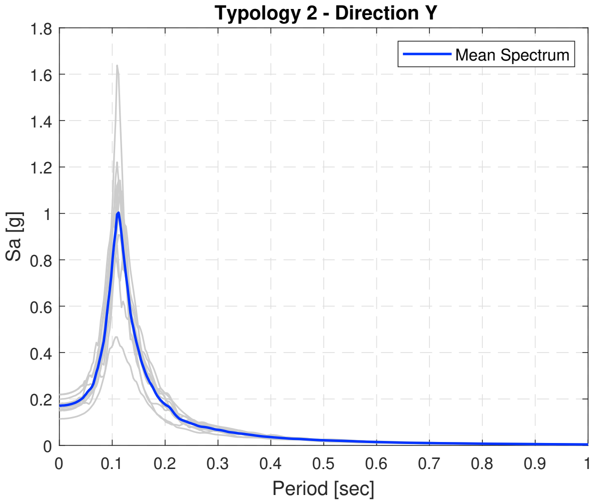
Typology 2 - Direction Y

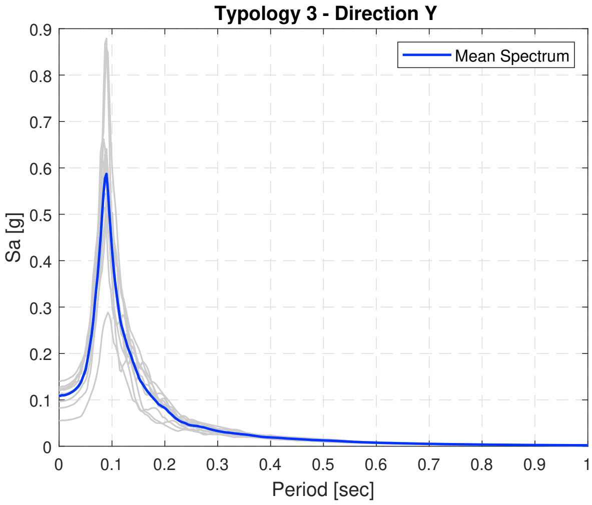
Typology 3 - Direction Y

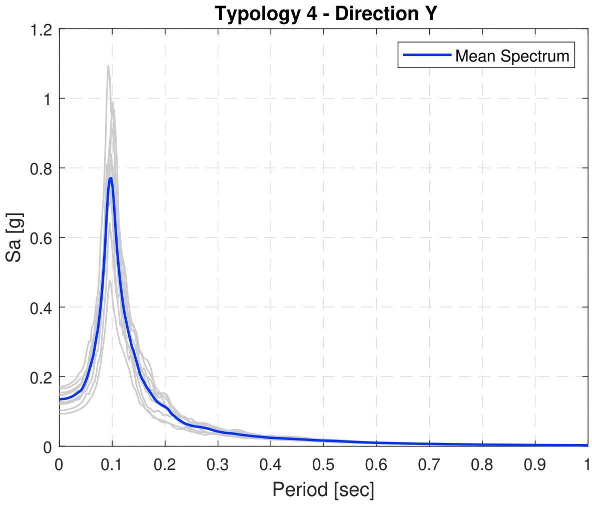
Typology 4 - Direction Y

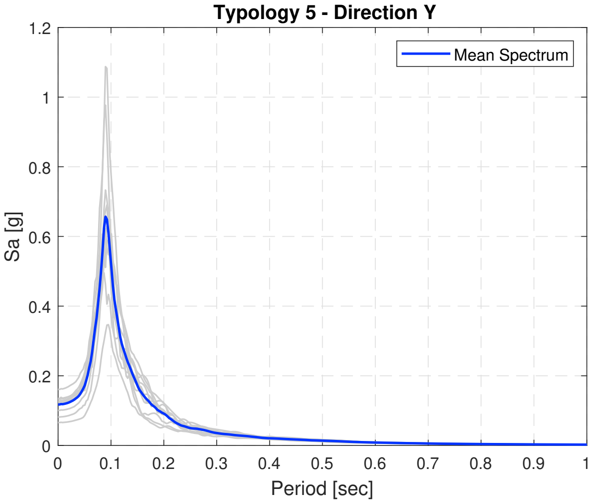

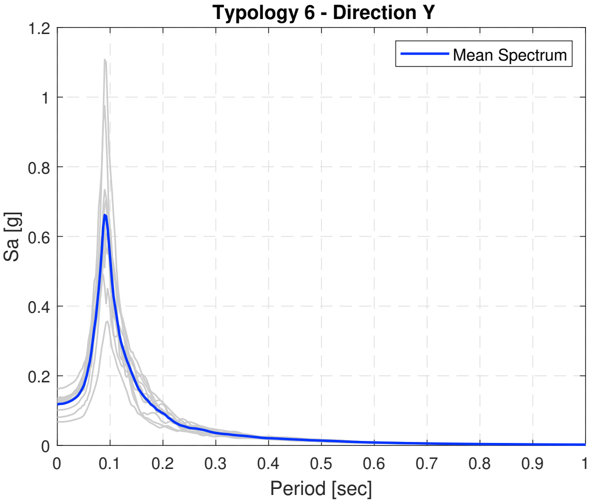

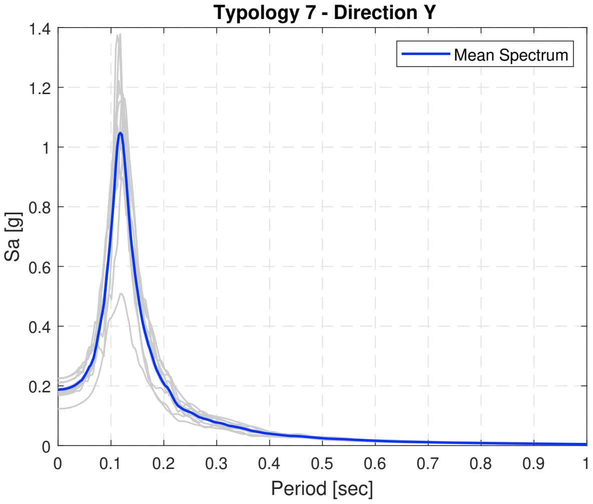

A.4 Loppersum

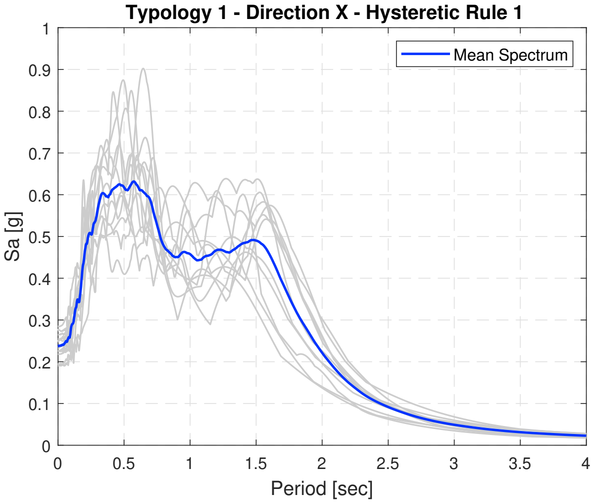

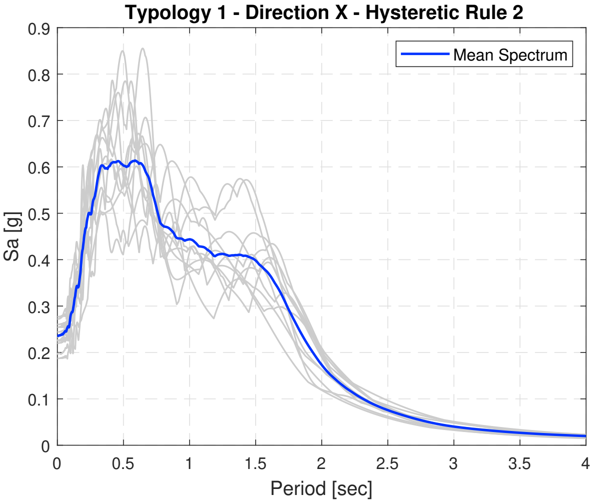

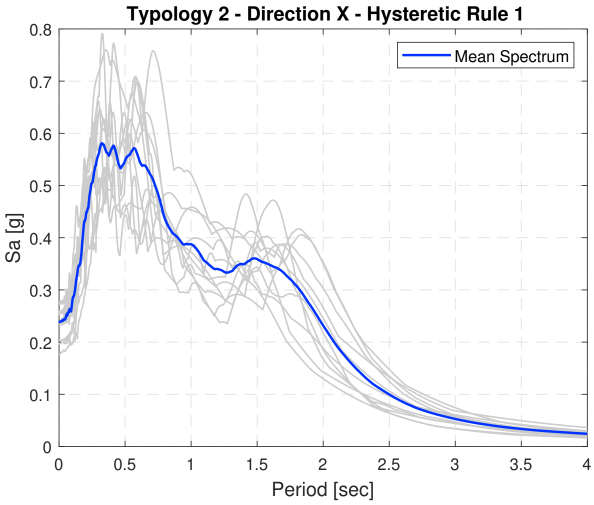
Typology 2 - Direction X - Hysteretic Rule 1

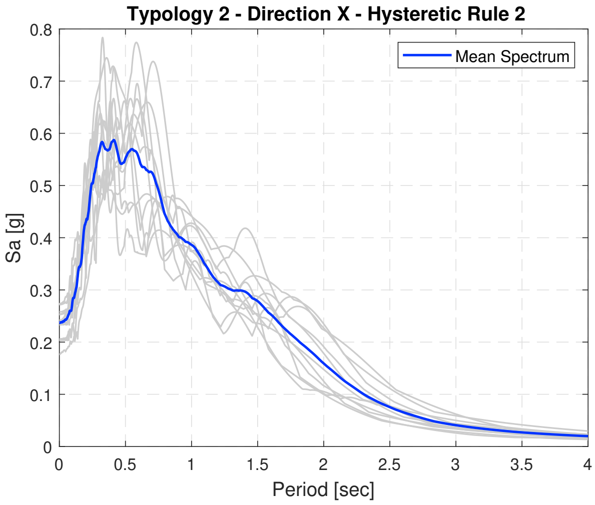
Typology 2 - Direction X - Hysteretic Rule 2

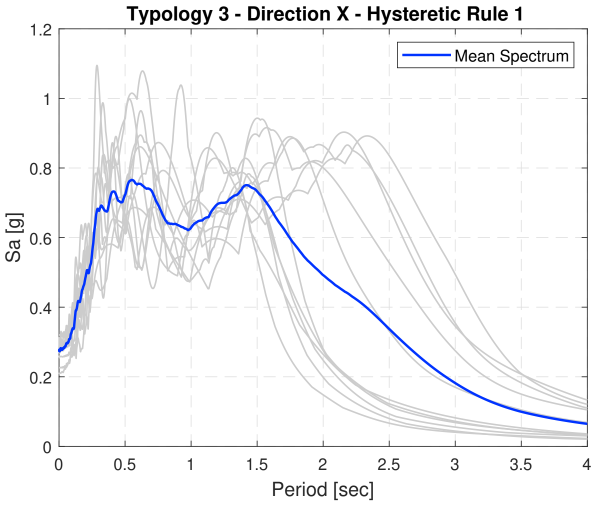
Typology 3 - Direction X - Hysteretic Rule 1

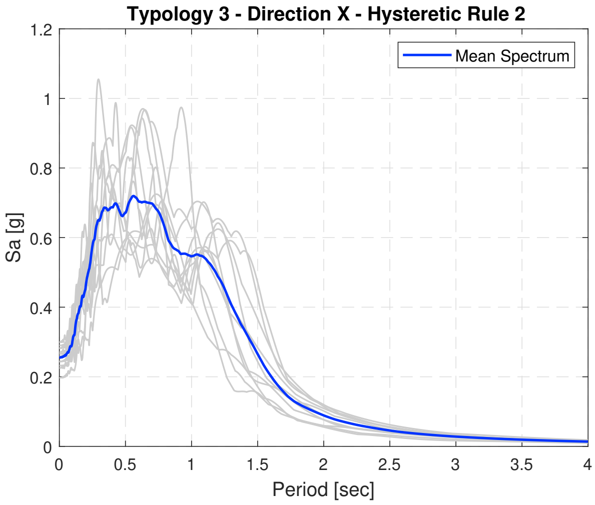
Typology 3 - Direction X - Hysteretic Rule 2

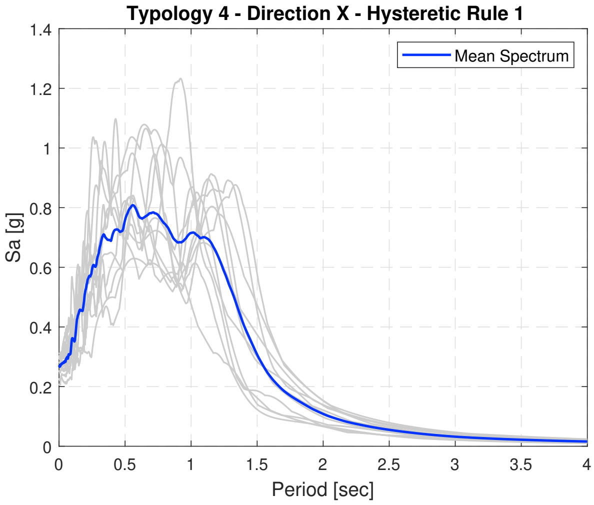
Typology 4 - Direction X - Hysteretic Rule 1

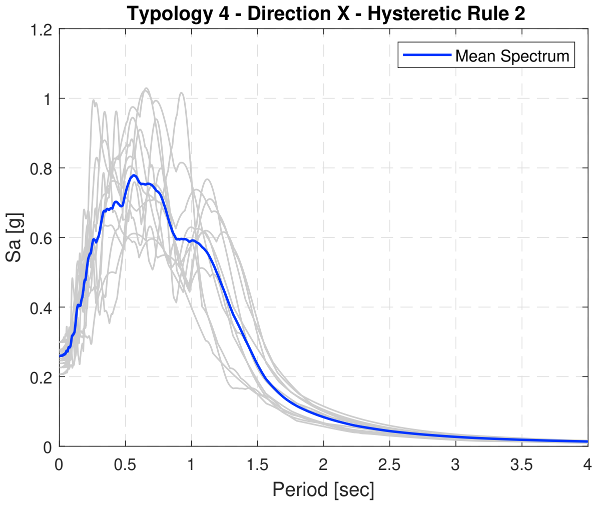
Typology 4 - Direction X - Hysteretic Rule 2

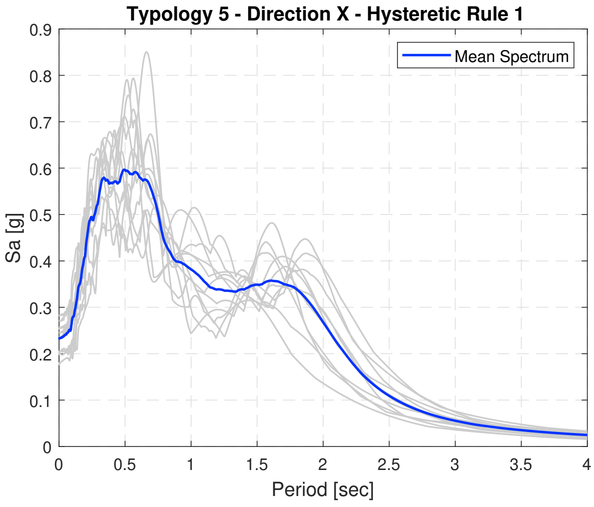
Typology 5 - Direction X - Hysteretic Rule 1
Mean Spectrum
Sa [g]
Period [sec]
0 0.1 0.2 0.3 0.4 0.5 0.6 0.7 0.8 0.9
0 0.5 1 1.5 2 2.5 3 3.5 4

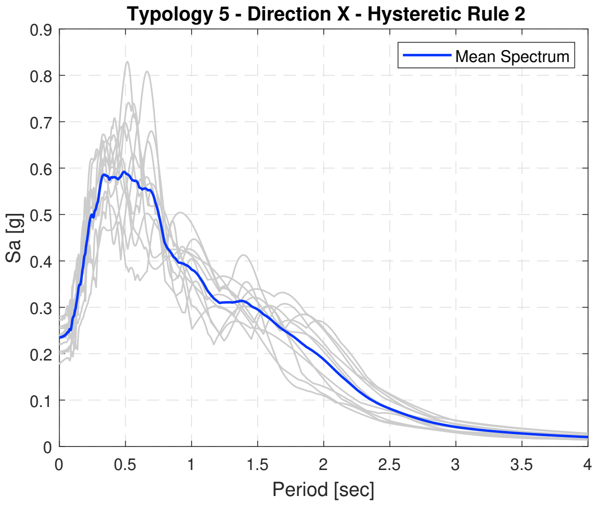
Typology 5 - Direction X - Hysteretic Rule 2
Mean Spectrum
Sa [g]
Period [sec]
0 0.1 0.2 0.3 0.4 0.5 0.6 0.7 0.8 0.9
0 0.5 1 1.5 2 2.5 3 3.5 4

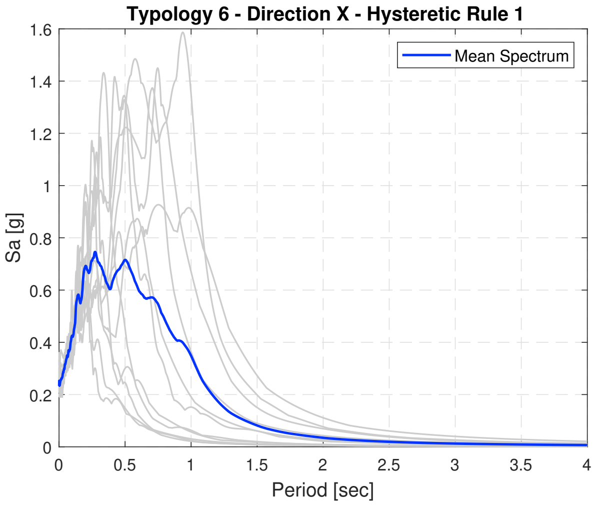
Typology 6 - Direction X - Hysteretic Rule 1
Mean Spectrum
Sa [g]
Period [sec]
0 0.2 0.4 0.6 0.8 1 1.2 1.4 1.6
0 0.5 1 1.5 2 2.5 3 3.5 4

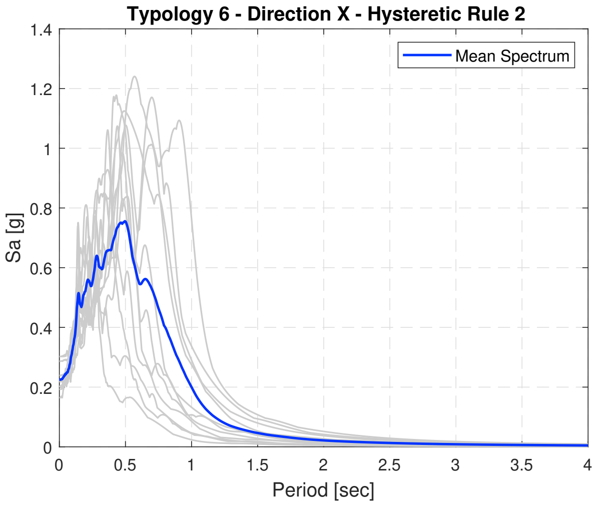
Typology 6 - Direction X - Hysteretic Rule 2
Mean Spectrum
Sa [g]
Period [sec]
0 0.2 0.4 0.6 0.8 1 1.2 1.4
0 0.5 1 1.5 2 2.5 3 3.5 4

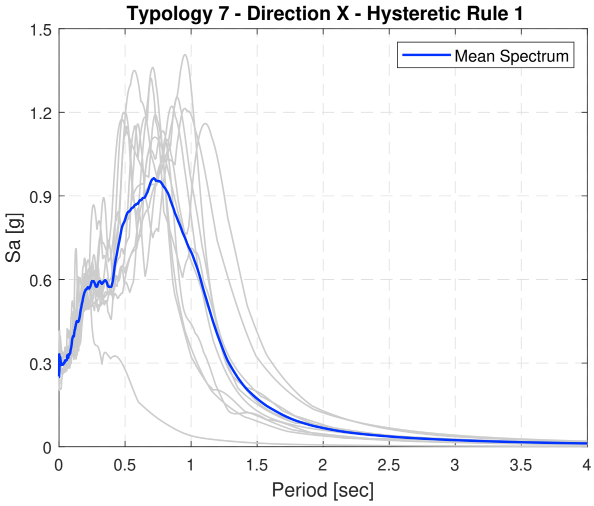
Typology 7 - Direction X - Hysteretic Rule 1
Mean Spectrum
Sa [g]
Period [sec]
0 0.3 0.6 0.9 1.2 1.5
0 0.5 1 1.5 2 2.5 3 3.5 4

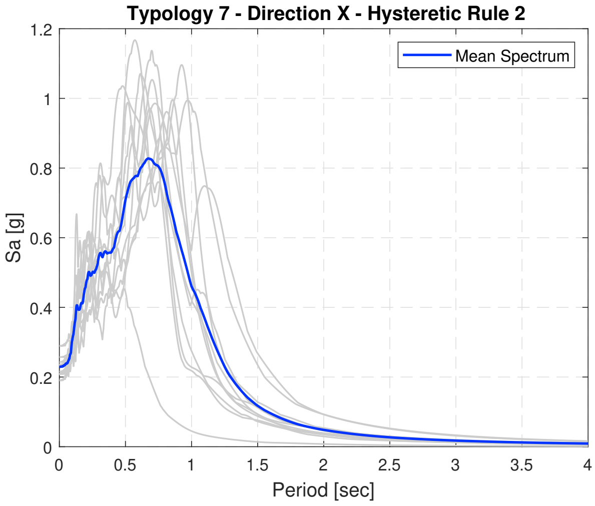
Typology 7 - Direction X - Hysteretic Rule 2
Mean Spectrum
Sa [g]
Period [sec]
0 0.2 0.4 0.6 0.8 1 1.2
0 0.5 1 1.5 2 2.5 3 3.5 4

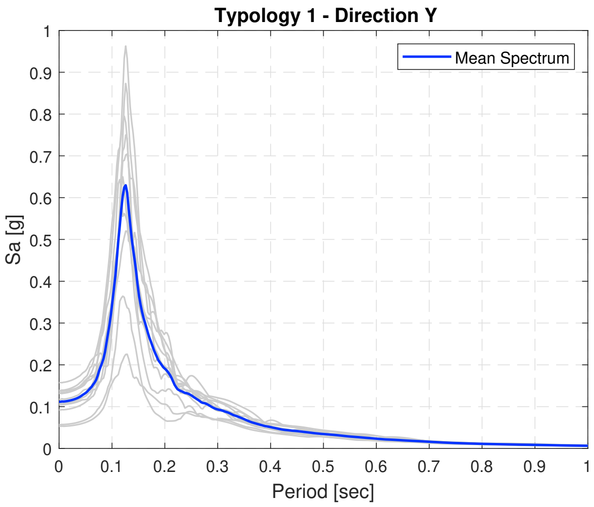
Typology 1 - Direction Y
Mean Spectrum
Sa [g]
0
0.1
0.2
0.3
0.4
0.5
0.6
0.7
0.8
0.9
1
Period [sec]
0
0.1
0.2
0.3
0.4
0.5
0.6
0.7
0.8
0.9
1

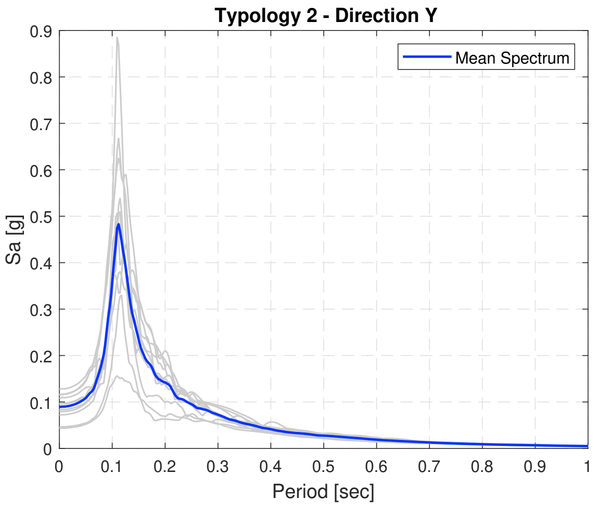
Typology 2 - Direction Y
Mean Spectrum
Sa [g]
0
0.1
0.2
0.3
0.4
0.5
0.6
0.7
0.8
0.9
Period [sec]
0
0.1
0.2
0.3
0.4
0.5
0.6
0.7
0.8
0.9
1

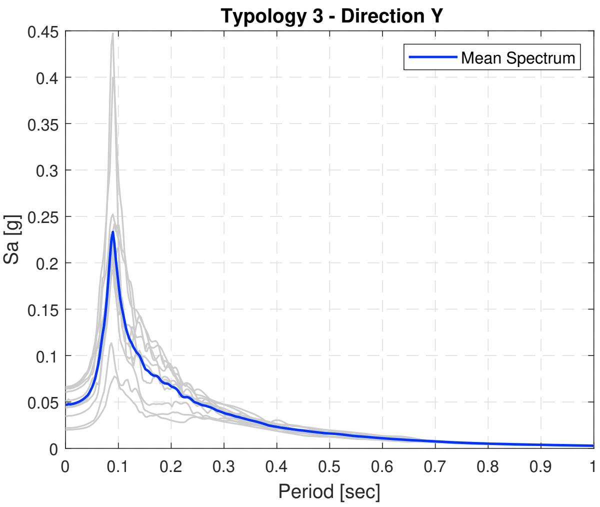
Typology 3 - Direction Y
Mean Spectrum
Sa [g]
0
0.05
0.1
0.15
0.2
0.25
0.3
0.35
0.4
0.45
Period [sec]
0
0.1
0.2
0.3
0.4
0.5
0.6
0.7
0.8
0.9
1

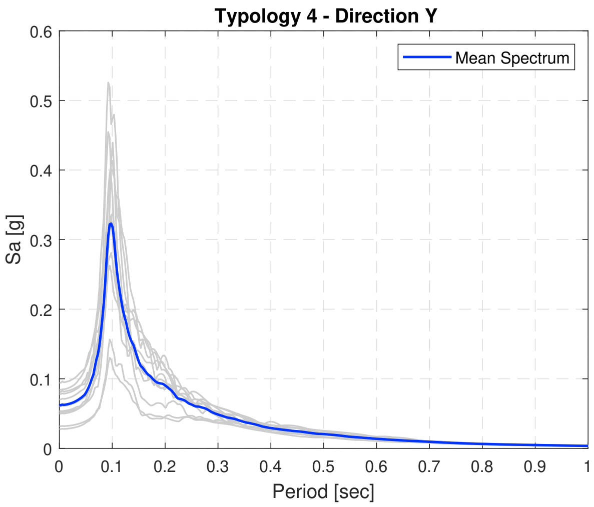
Typology 4 - Direction Y
Mean Spectrum
Sa [g]
0
0.1
0.2
0.3
0.4
0.5
0.6
Period [sec]
0
0.1
0.2
0.3
0.4
0.5
0.6
0.7
0.8
0.9
1

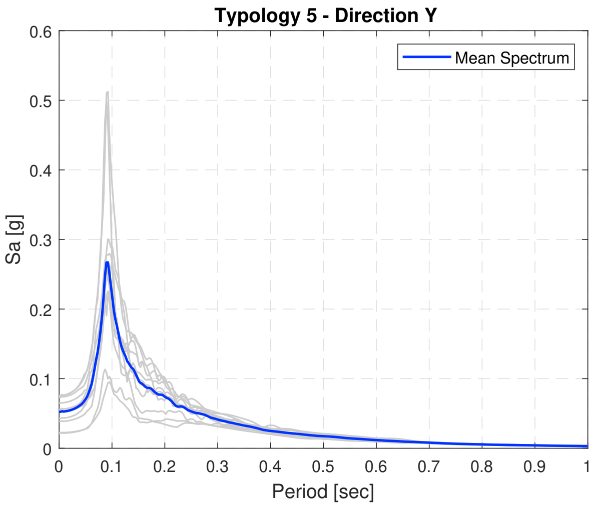
Typology 5 - Direction Y
Mean Spectrum
Sa [g]
0
0.1
0.2
0.3
0.4
0.5
0.6
Period [sec]
0
0.1
0.2
0.3
0.4
0.5
0.6
0.7
0.8
0.9
1

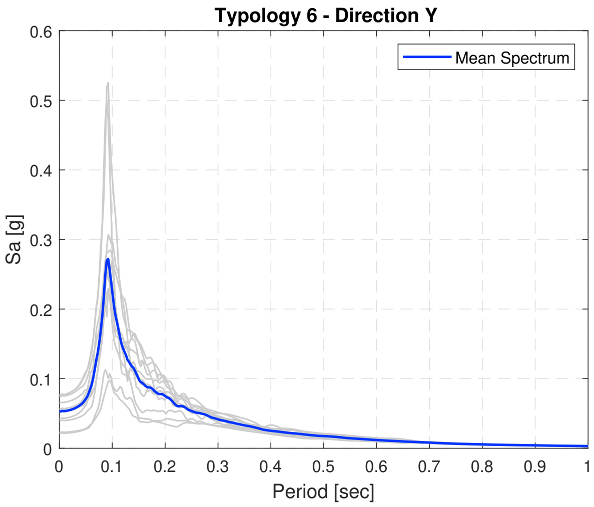
Typology 6 - Direction Y
Mean Spectrum
Sa [g]
0
0.1
0.2
0.3
0.4
0.5
0.6
Period [sec]
0
0.1
0.2
0.3
0.4
0.5
0.6
0.7
0.8
0.9
1

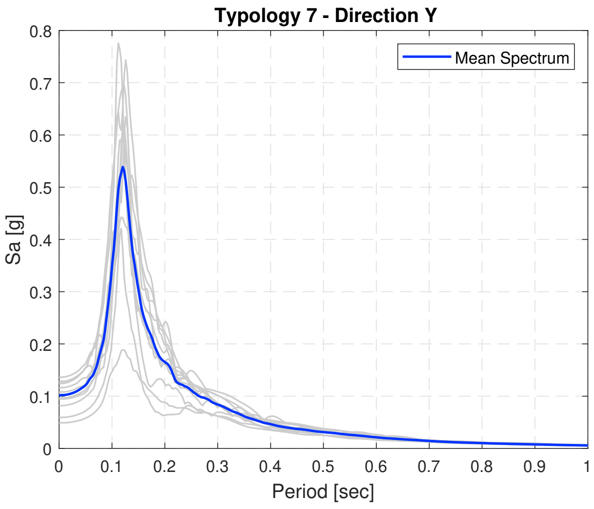
Typology 7 - Direction Y

A.5 Overschild

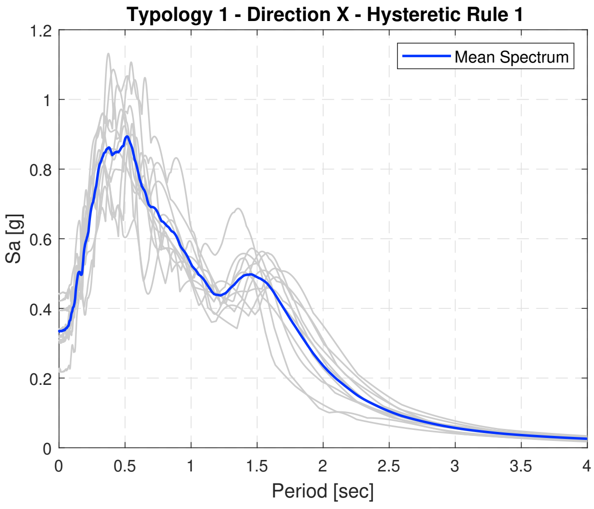
Typology 1 - Direction X - Hysteretic Rule 1

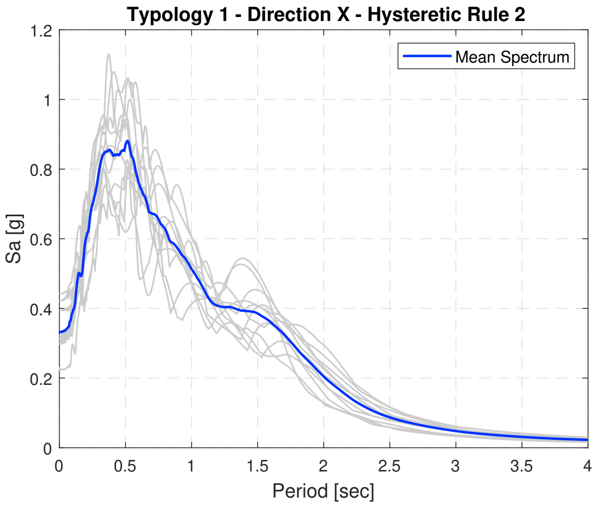
Typology 1 - Direction X - Hysteretic Rule 2

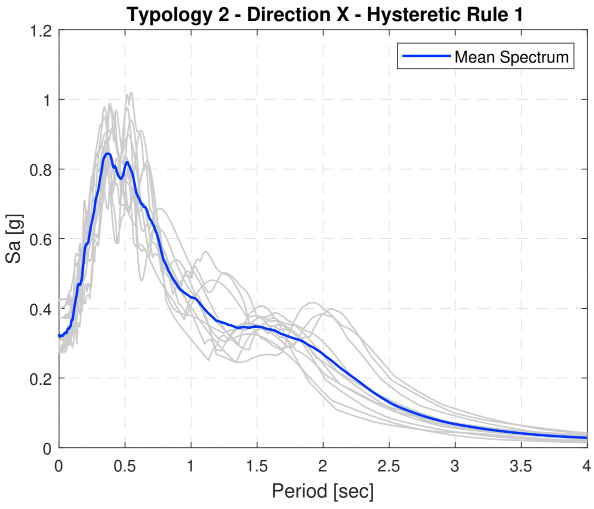
Typology 2 - Direction X - Hysteretic Rule 1

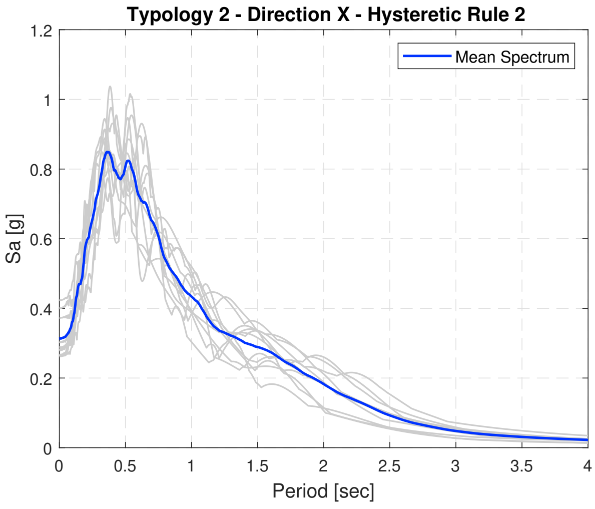
Typology 2 - Direction X - Hysteretic Rule 2

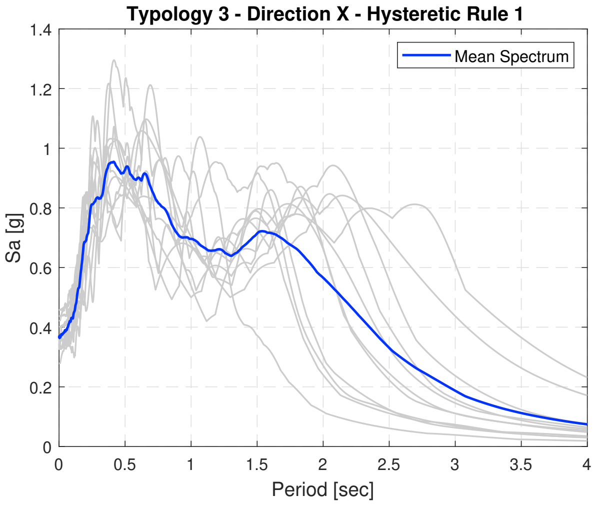
Typology 3 - Direction X - Hysteretic Rule 1

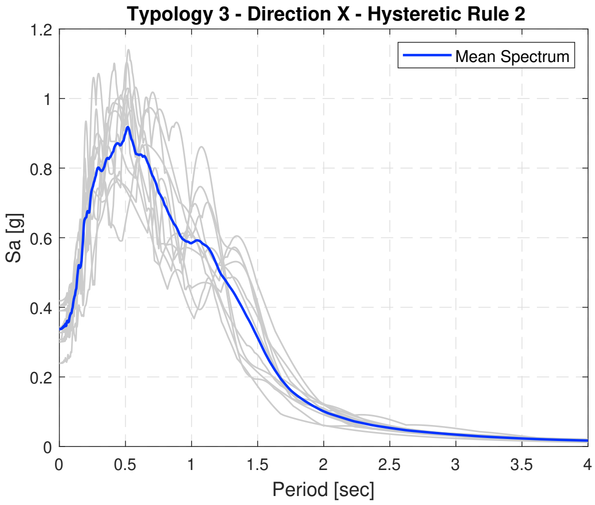
Typology 3 - Direction X - Hysteretic Rule 2

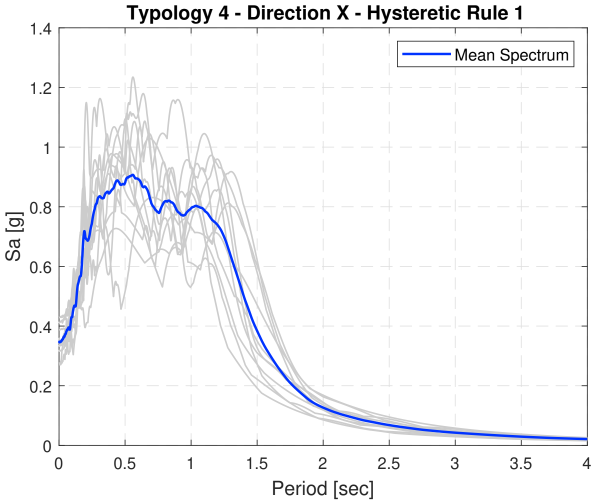
Typology 4 - Direction X - Hysteretic Rule 1

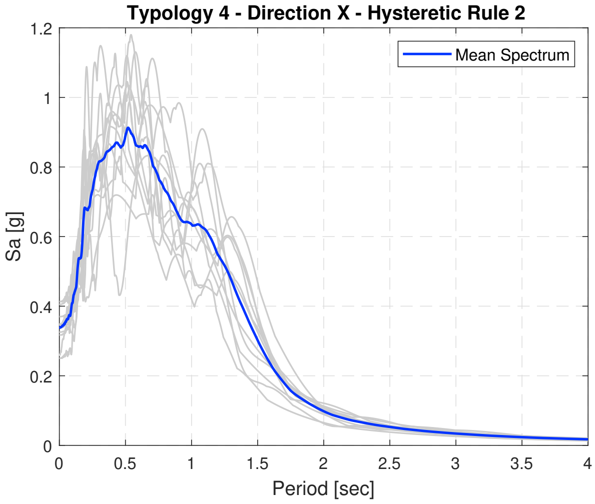
Typology 4 - Direction X - Hysteretic Rule 2

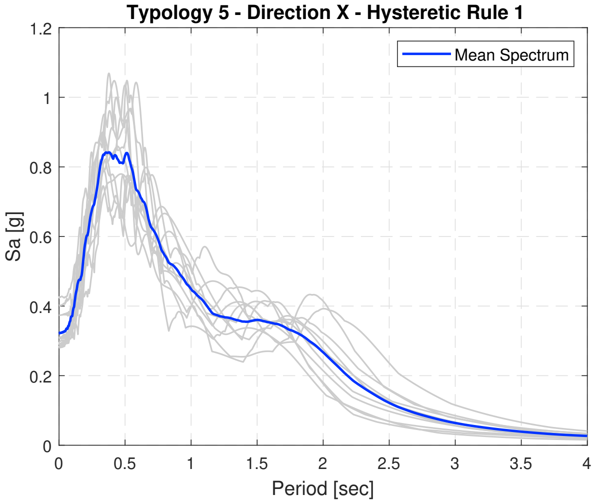
Typology 5 - Direction X - Hysteretic Rule 1

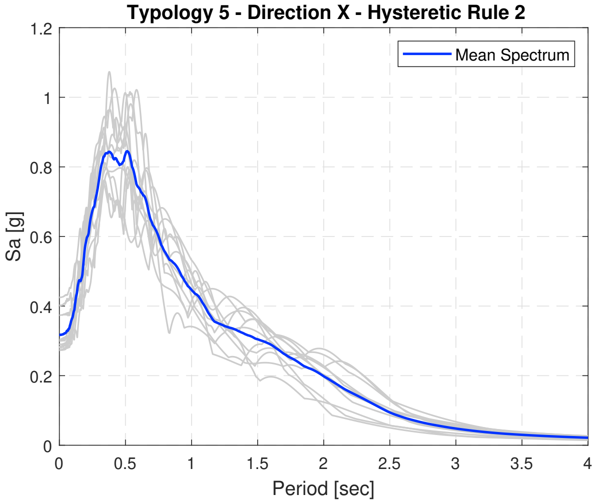
Typology 5 - Direction X - Hysteretic Rule 2

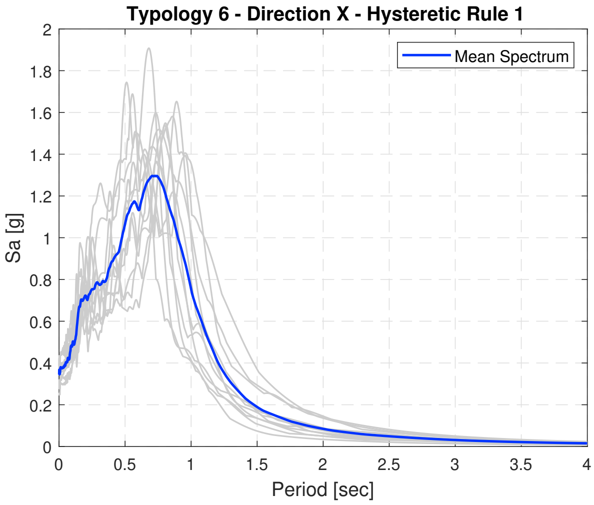
Typology 6 - Direction X - Hysteretic Rule 1
Mean Spectrum
Sa [g]
Period [sec]
0
0.2
0.4
0.6
0.8
1
1.2
1.4
1.6
1.8
2
0
0.5
1
1.5
2
2.5
3
3.5
4

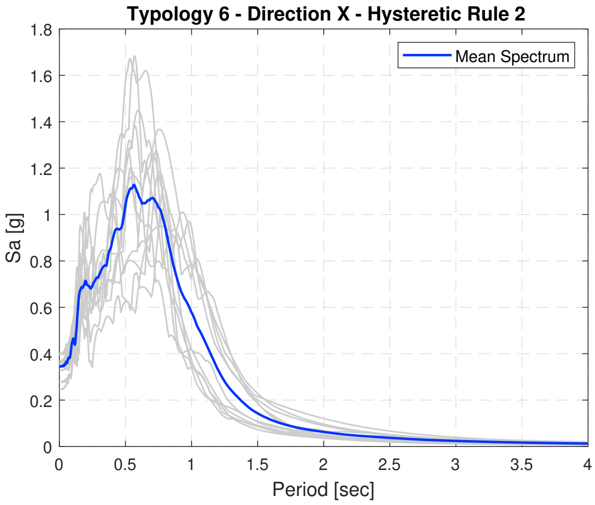
Typology 6 - Direction X - Hysteretic Rule 2
Mean Spectrum
Sa [g]
Period [sec]
0
0.2
0.4
0.6
0.8
1
1.2
1.4
1.6
1.8
0
0.5
1
1.5
2
2.5
3
3.5
4

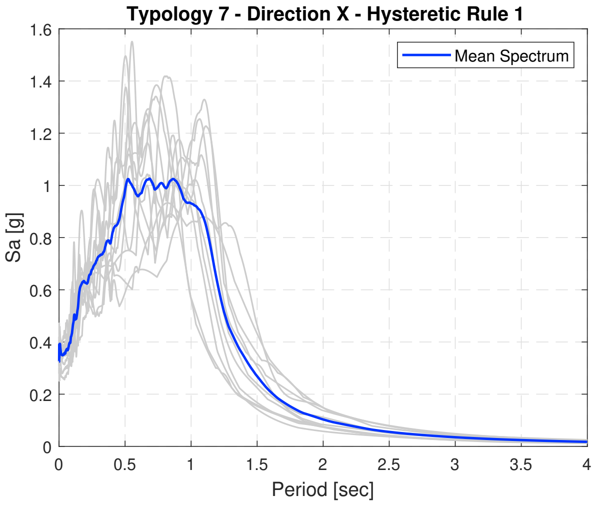
Typology 7 - Direction X - Hysteretic Rule 1
Mean Spectrum
Sa [g]
Period [sec]
0
0.2
0.4
0.6
0.8
1
1.2
1.4
1.6
0
0.5
1
1.5
2
2.5
3
3.5
4

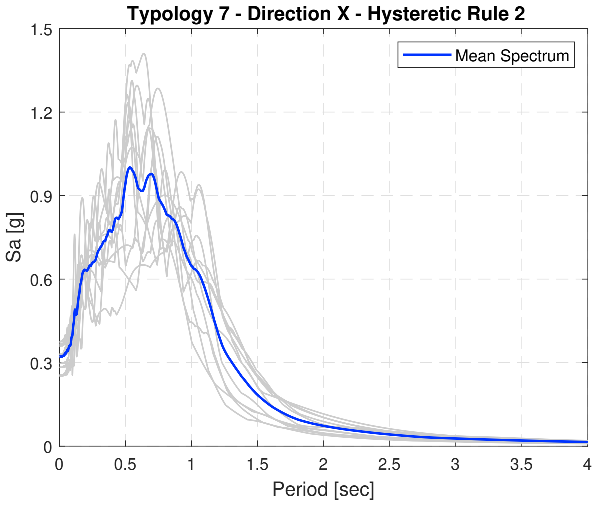
Typology 7 - Direction X - Hysteretic Rule 2
Mean Spectrum
Sa [g]
Period [sec]
0
0.3
0.6
0.9
1.2
1.5
0
0.5
1
1.5
2
2.5
3
3.5
4

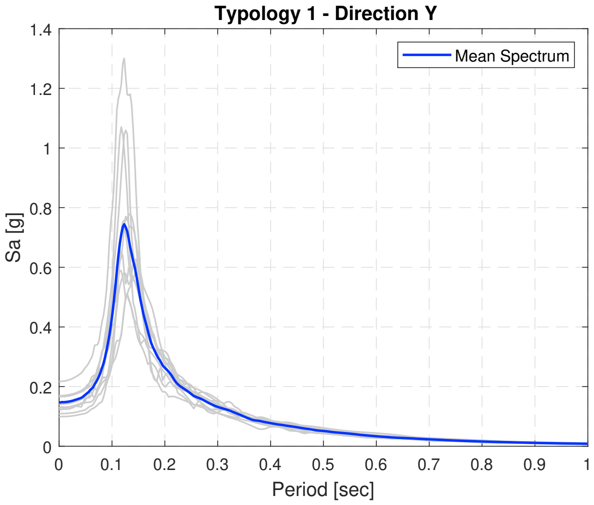
Typology 1 - Direction Y
Mean Spectrum
Sa [g]
Period [sec]
0
0.2
0.4
0.6
0.8
1
1.2
1.4
0
0.1
0.2
0.3
0.4
0.5
0.6
0.7
0.8
0.9
1

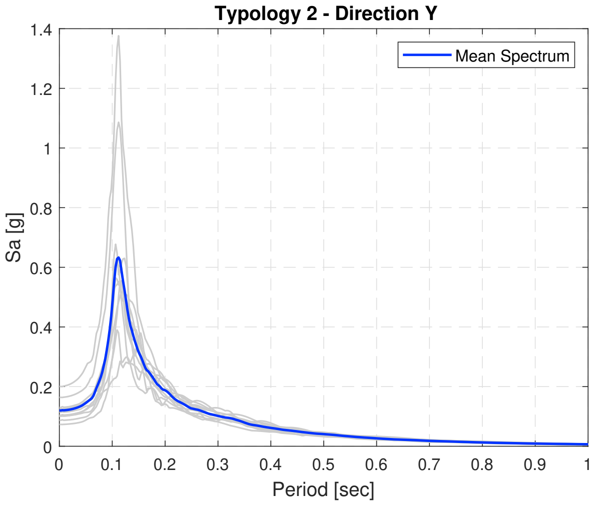
Typology 2 - Direction Y
Mean Spectrum
Sa [g]
Period [sec]
0
0.2
0.4
0.6
0.8
1
1.2
1.4
0
0.1
0.2
0.3
0.4
0.5
0.6
0.7
0.8
0.9
1

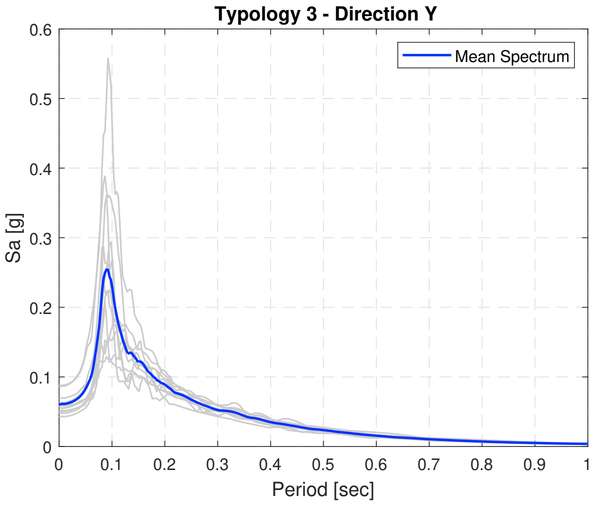
Typology 3 - Direction Y
Mean Spectrum
Sa [g]
0
0.1
0.2
0.3
0.4
0.5
0.6
Period [sec]
0
0.1
0.2
0.3
0.4
0.5
0.6
0.7
0.8
0.9
1

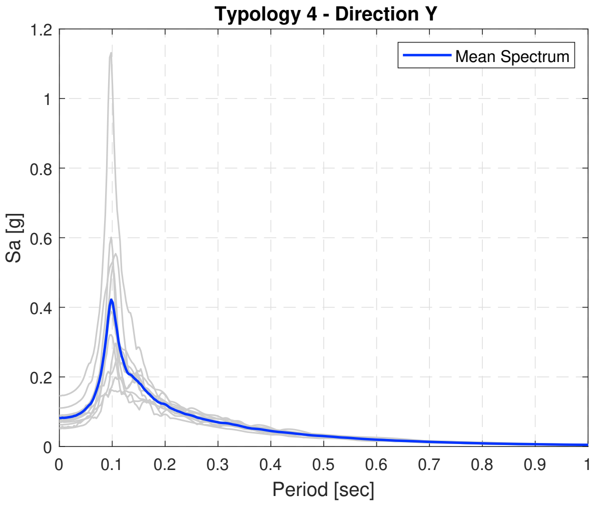
Typology 4 - Direction Y
Mean Spectrum
Sa [g]
0
0.2
0.4
0.6
0.8
1
1.2
Period [sec]
0
0.1
0.2
0.3
0.4
0.5
0.6
0.7
0.8
0.9
1

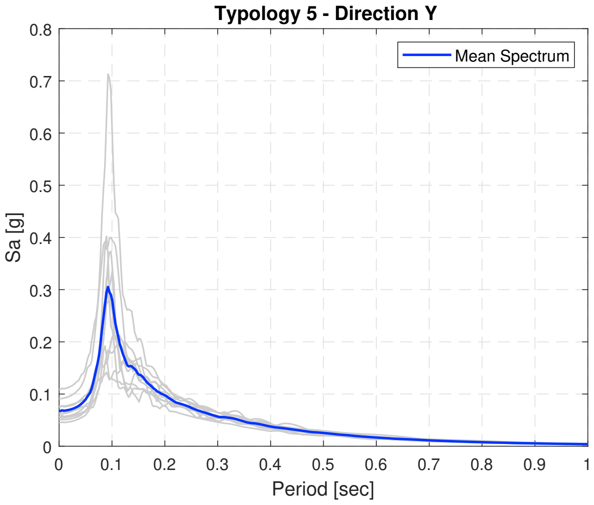
Typology 5 - Direction Y
Mean Spectrum
Sa [g]
0
0.1
0.2
0.3
0.4
0.5
0.6
0.7
0.8
Period [sec]
0
0.1
0.2
0.3
0.4
0.5
0.6
0.7
0.8
0.9
1

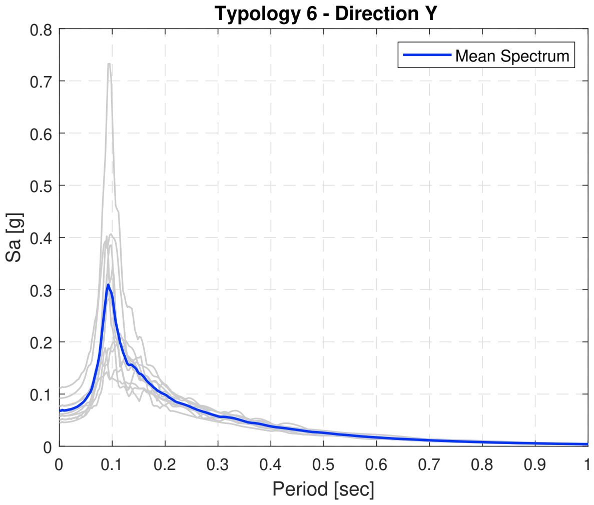
Typology 6 - Direction Y
Mean Spectrum
Sa [g]
0
0.1
0.2
0.3
0.4
0.5
0.6
0.7
0.8
Period [sec]
0
0.1
0.2
0.3
0.4
0.5
0.6
0.7
0.8
0.9
1

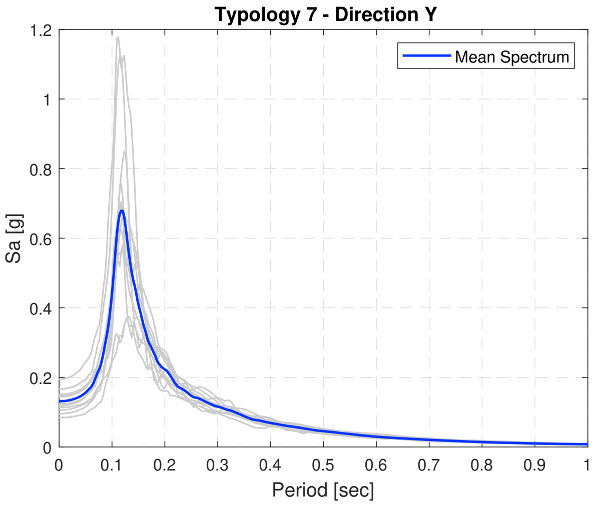
Typology 7 - Direction Y
Mean Spectrum
Sa [g]
0
0.2
0.4
0.6
0.8
1
1.2
Period [sec]
0
0.1
0.2
0.3
0.4
0.5
0.6
0.7
0.8
0.9
1

Appendix B

Design Floor Accelaration Spectra Results

B.1 Appingedam

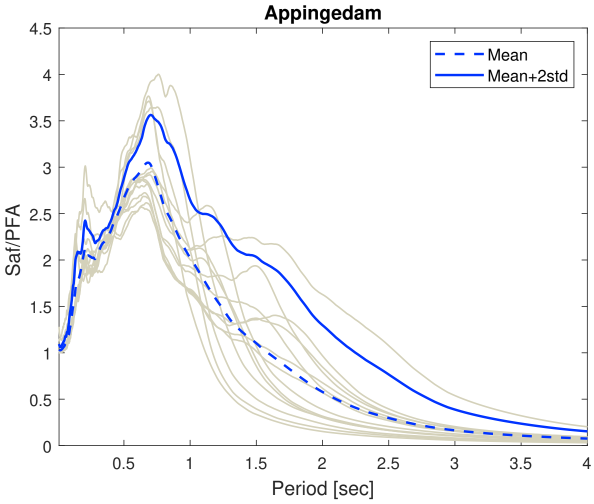

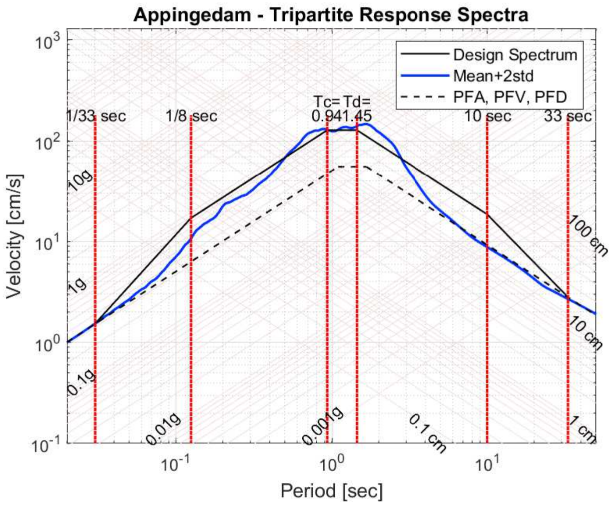

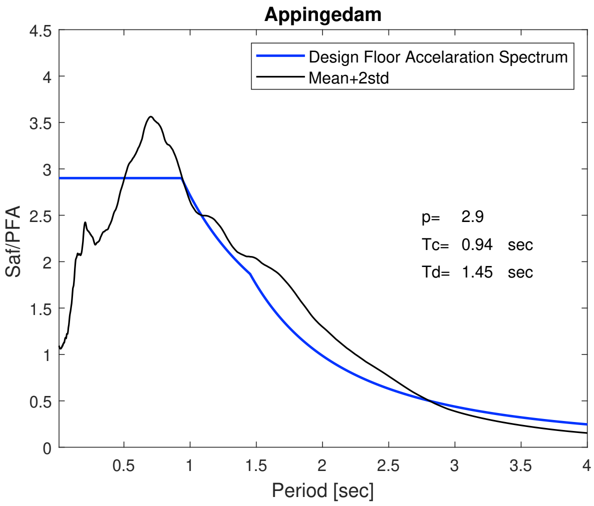

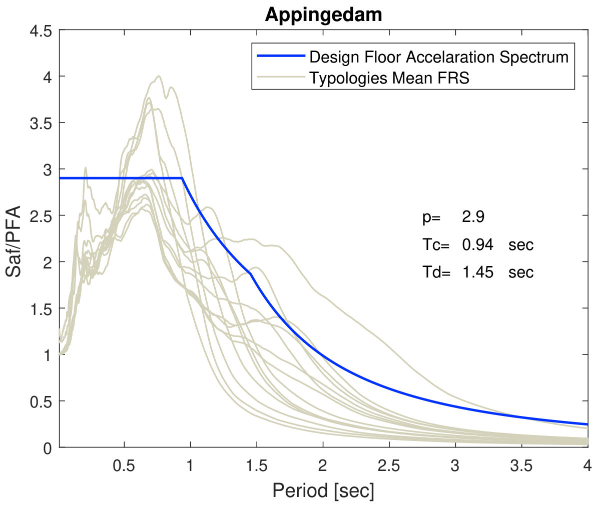

B.2 Groningen

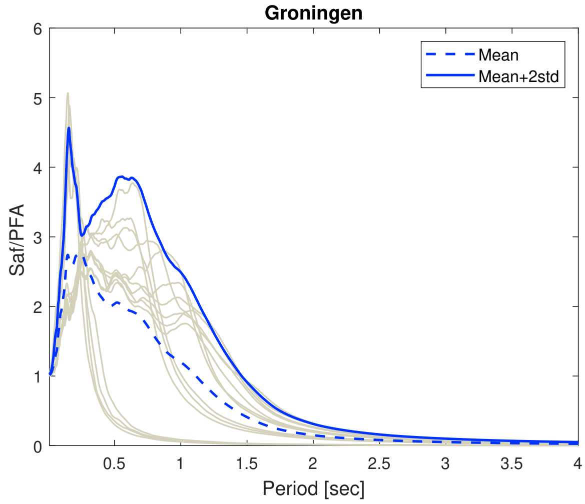

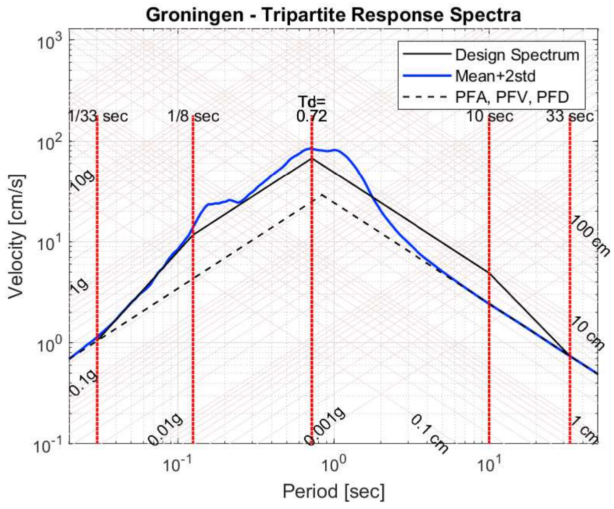

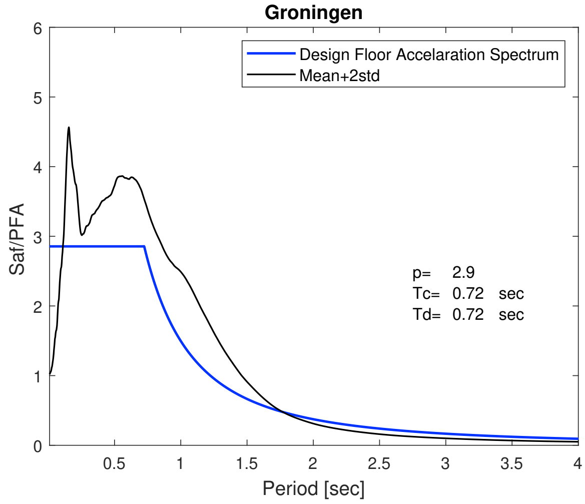

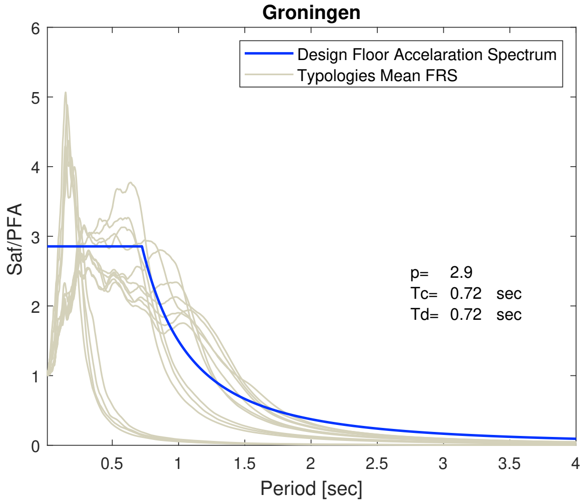

B.3 Hoogezand

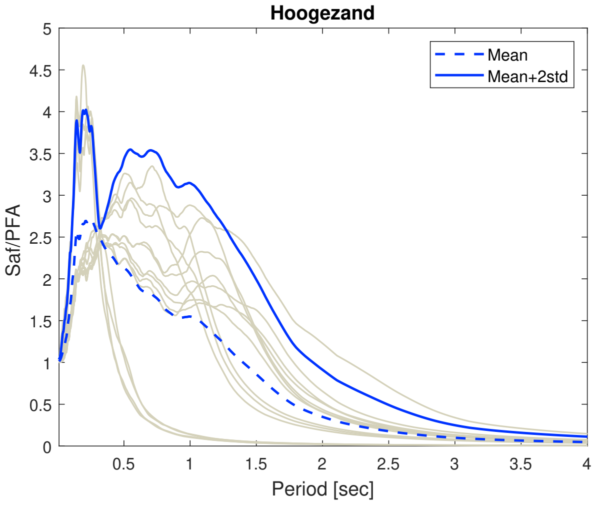

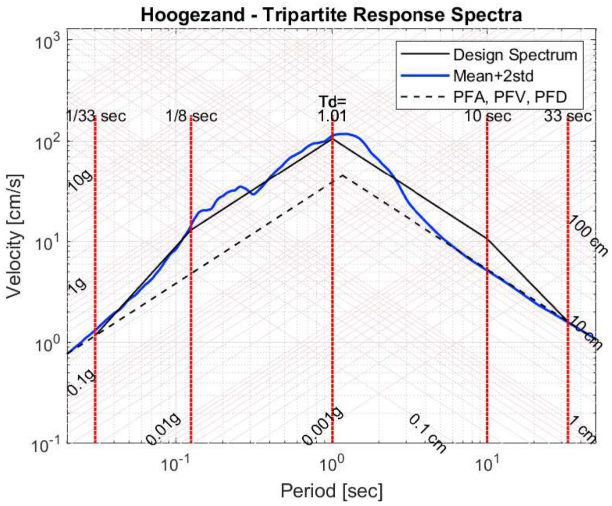

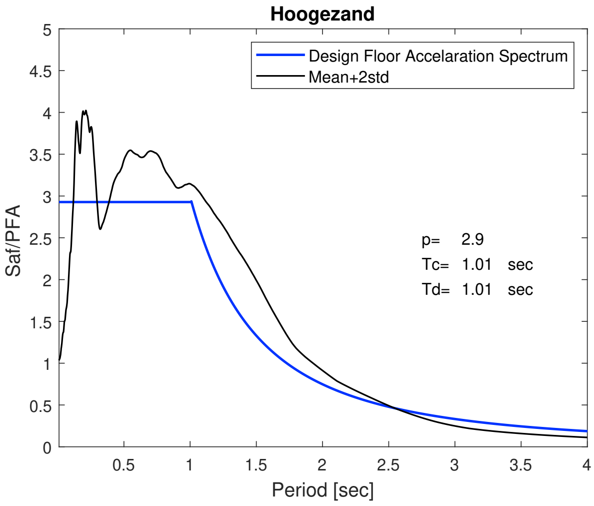

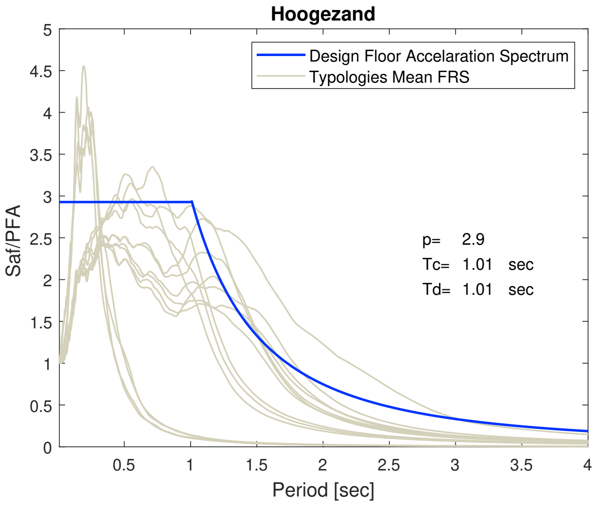

B.4 Loppersum

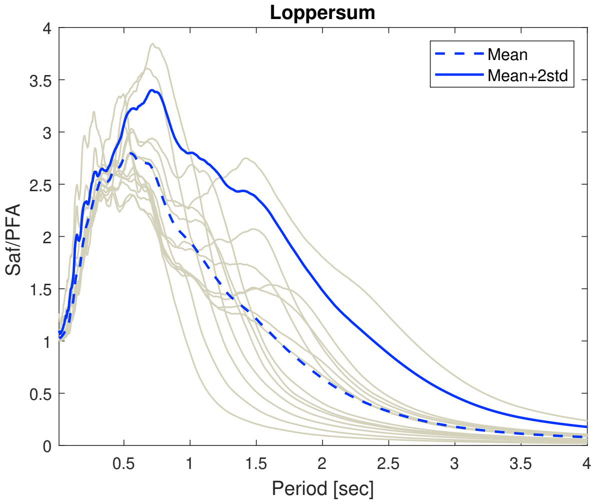

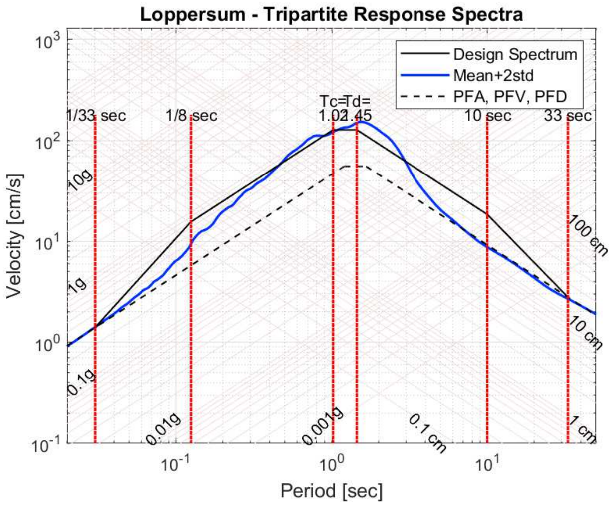

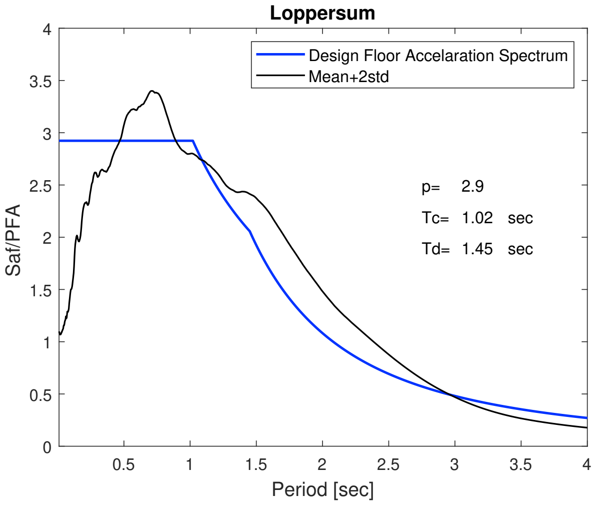

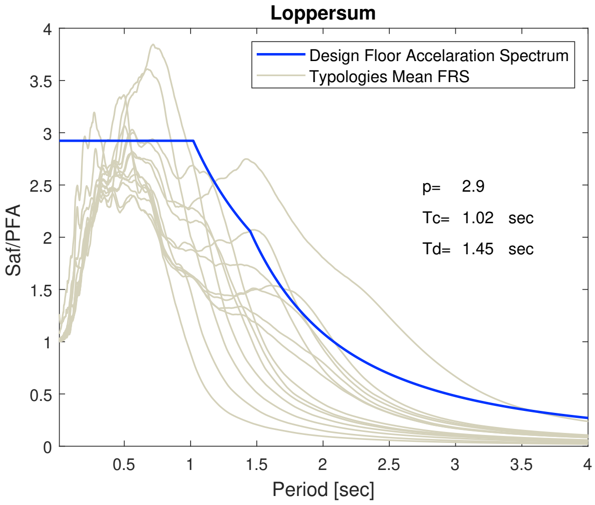

B.5 Overschild

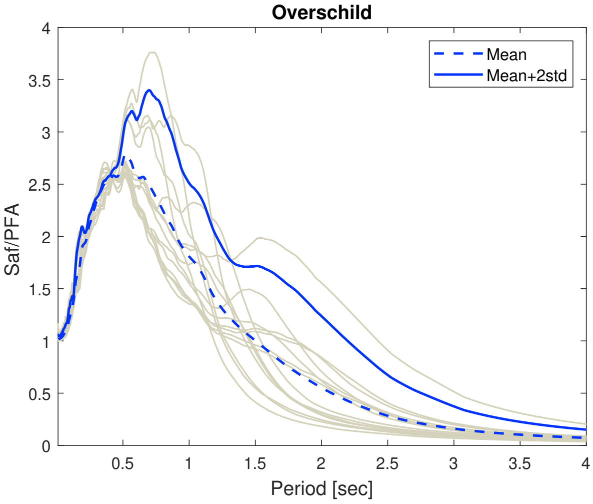

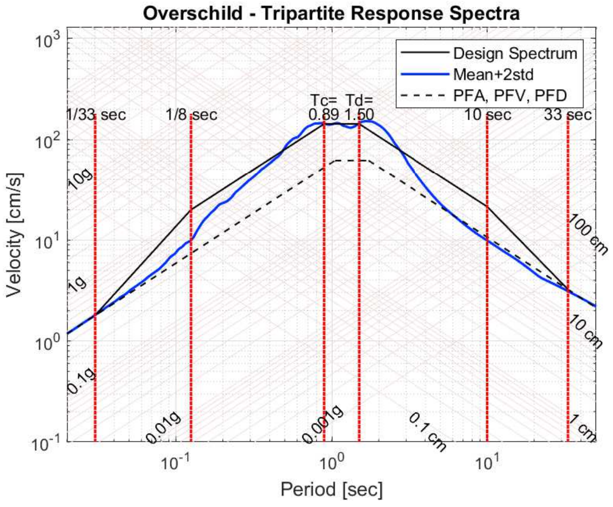

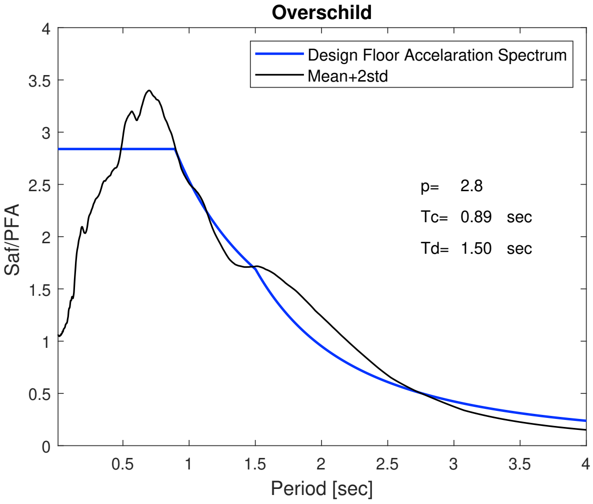

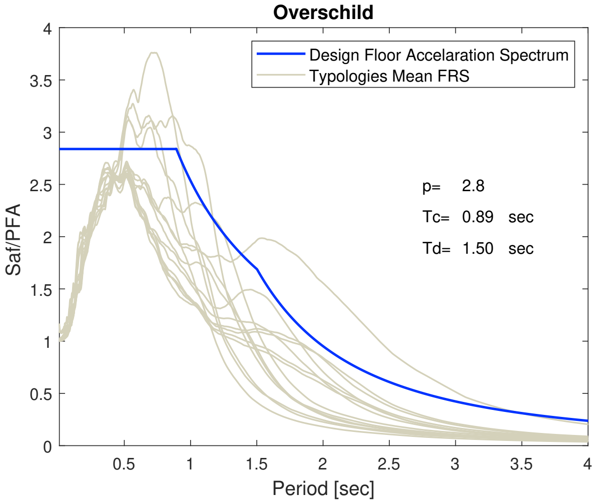

Appendix C

OOP walls in ANSR-II and NLKA method

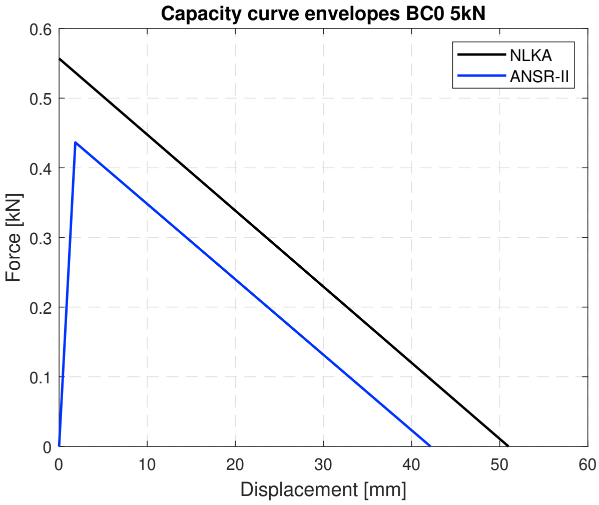
Capacity curve envelopes BC0 5kN

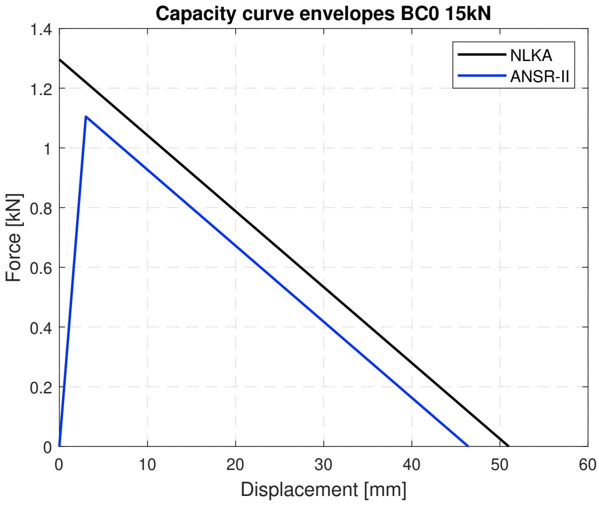
Capacity curve envelopes BC0 15kN

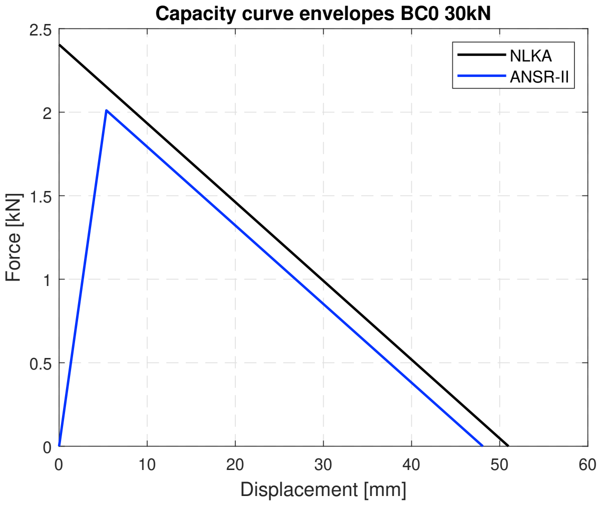
Capacity curve envelopes BC0 30kN

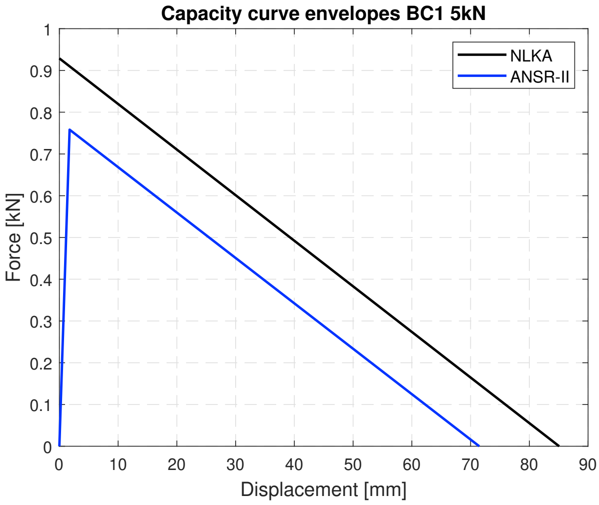
Capacity curve envelopes BC1 5kN

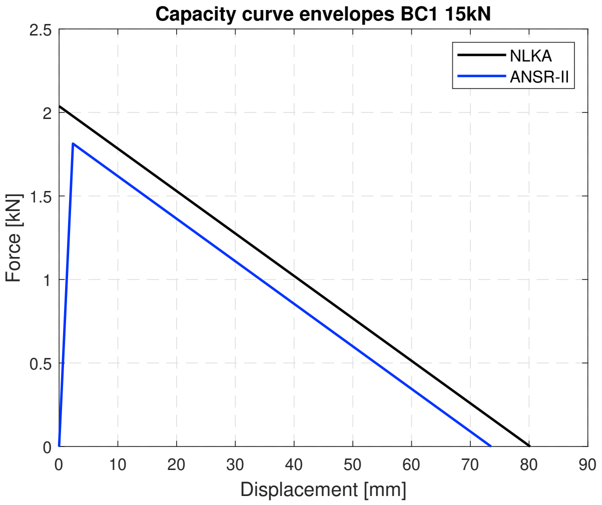
Capacity curve envelopes BC1 15kN
NLKA
ANSR-II
Force [kN]
Displacement [mm]
0
0.5
1
1.5
2
2.5
0
10
20
30
40
50
60
70
80
90

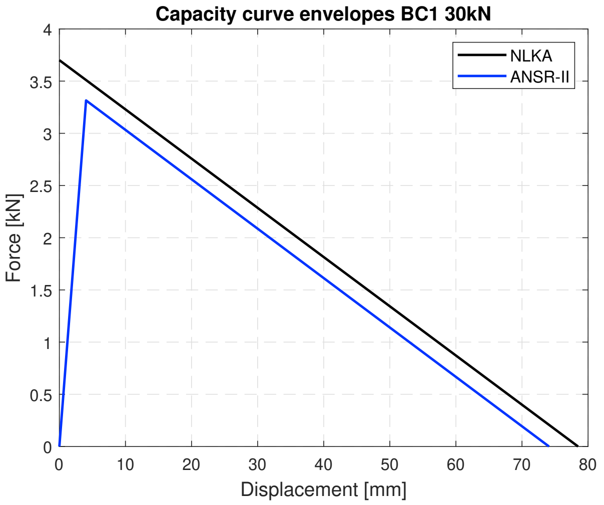
Capacity curve envelopes BC1 30kN
NLKA
ANSR-II
Force [kN]
Displacement [mm]
0
0.5
1
1.5
2
2.5
3
3.5
4
0
10
20
30
40
50
60
70
80

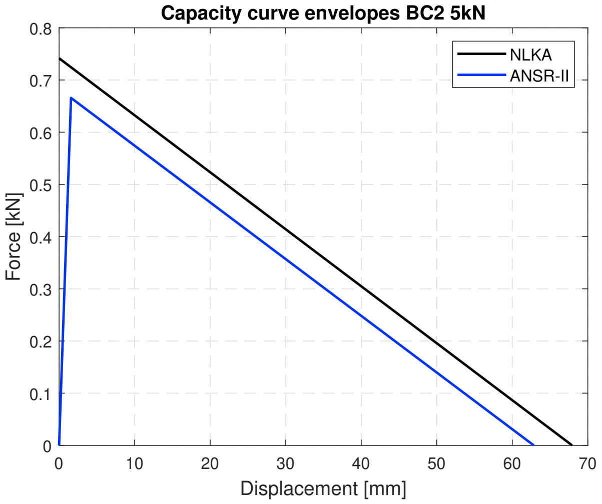
Capacity curve envelopes BC2 5kN
NLKA
ANSR-II
Force [kN]
Displacement [mm]
0
0.1
0.2
0.3
0.4
0.5
0.6
0.7
0.8
0
10
20
30
40
50
60
70

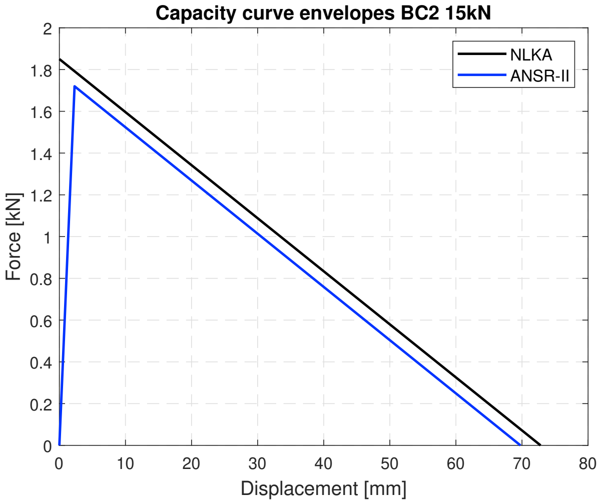
Capacity curve envelopes BC2 15kN
NLKA
ANSR-II
Force [kN]
Displacement [mm]
0
0.2
0.4
0.6
0.8
1
1.2
1.4
1.6
1.8
2
0
10
20
30
40
50
60
70
80

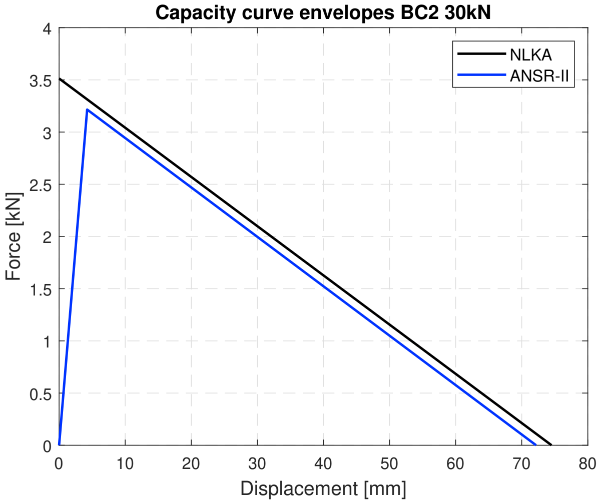
Capacity curve envelopes BC2 30kN
NLKA
ANSR-II
Force [kN]
Displacement [mm]
0
0.5
1
1.5
2
2.5
3
3.5
4
0
10
20
30
40
50
60
70
80

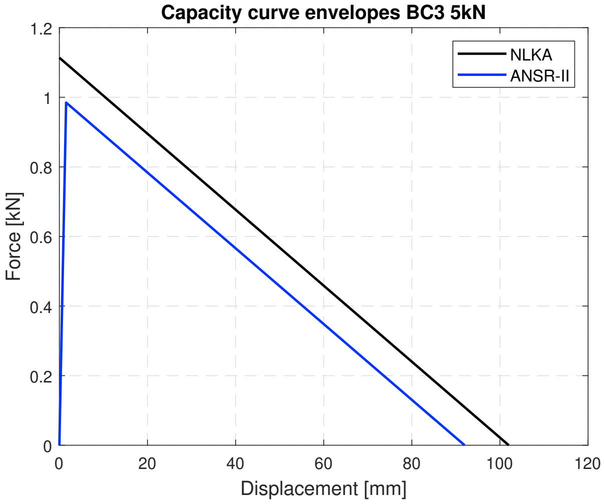
Capacity curve envelopes BC3 5kN
NLKA
ANSR-II
Force [kN]
Displacement [mm]
0
0.2
0.4
0.6
0.8
1
1.2
0
20
40
60
80
100
120

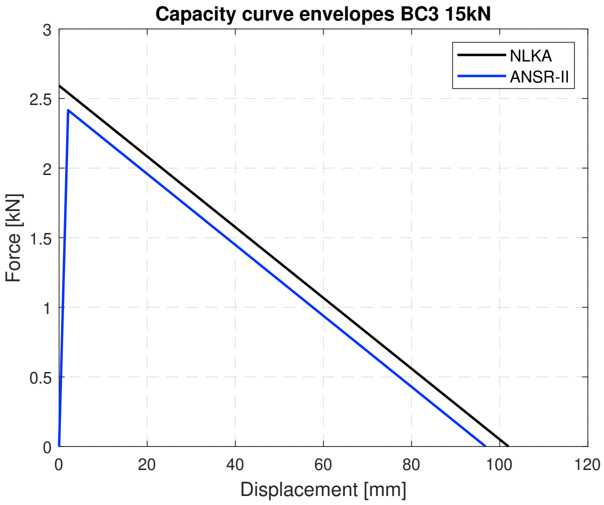
Capacity curve envelopes BC3 15kN
NLKA
ANSR-II
Force [kN]
Displacement [mm]
0
0.5
1
1.5
2
2.5
3
0
20
40
60
80
100
120

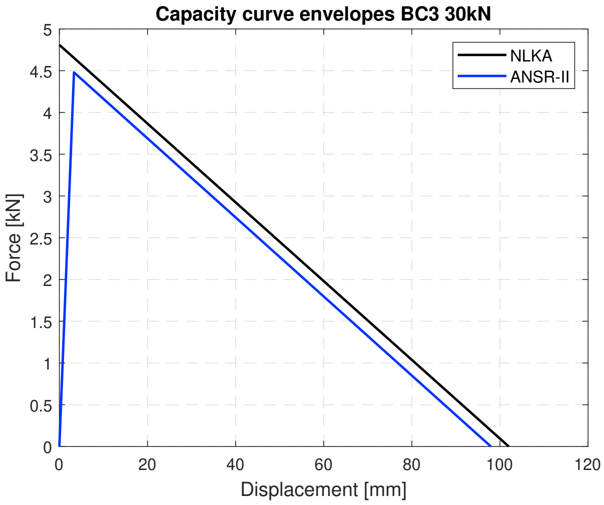
Capacity curve envelopes BC3 30kN
NLKA
ANSR-II
Force [kN]
Displacement [mm]
0
0.5
1
1.5
2
2.5
3
3.5
4
4.5
5
0
20
40
60
80
100
120

Appendix D

Damage state of the 3D Model

In this Appendix, the damage state of the 3D Model is presented for one record per area. The colours in the damaged elements are related to the acceptance criteria in accordance with the table G.5 of Draft NPR 9998:2017 [12].

Damage	Colour
<DL	NONE
<SD	🟩
<NC	🟦
>NC	🟥

D.1 Appingedam

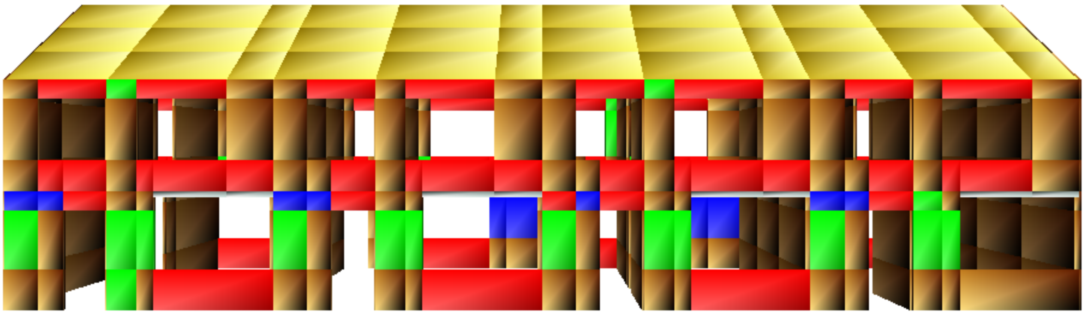

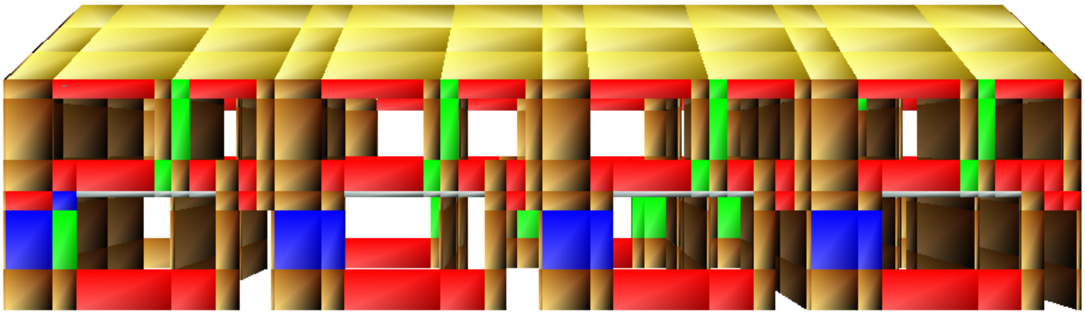

D.2 Groningen

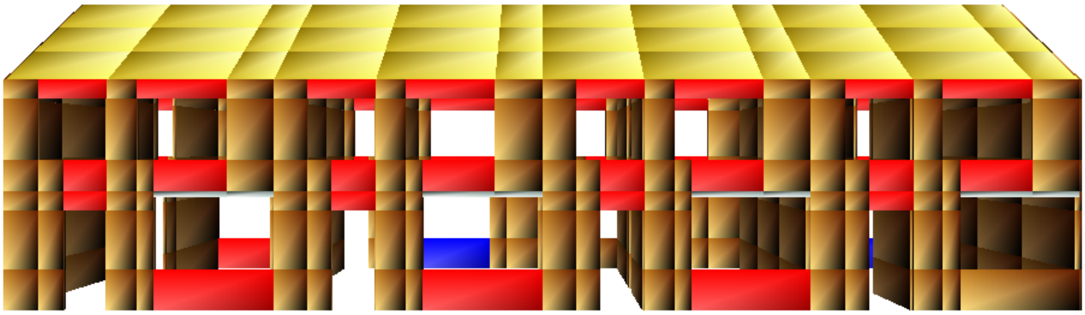

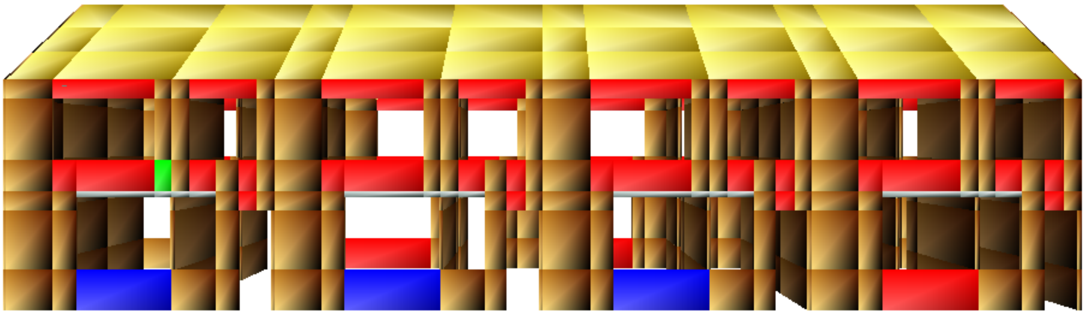

D.3 Hoogezand

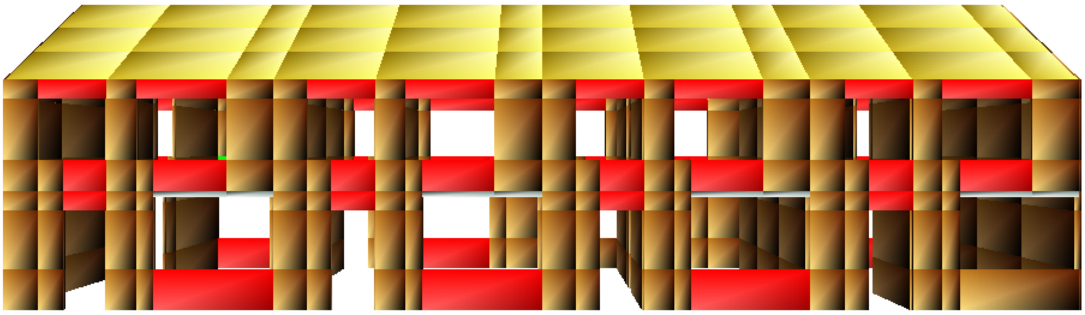

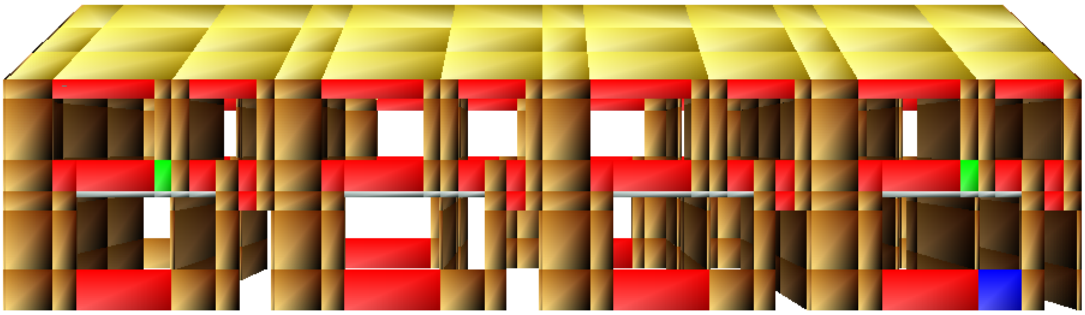

D.4 Loppersum

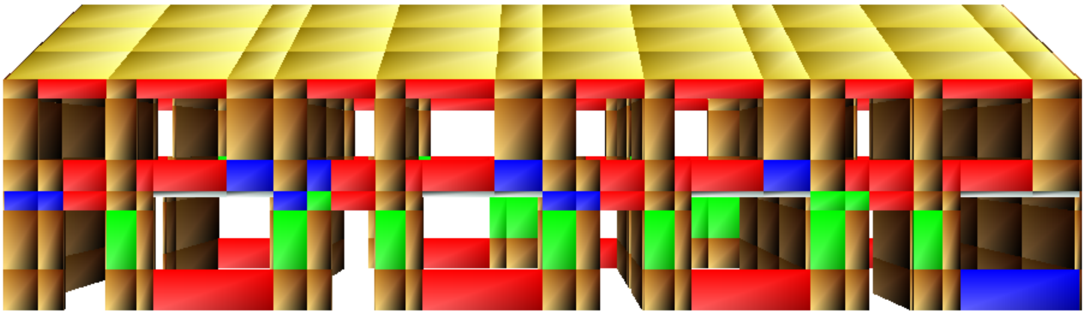

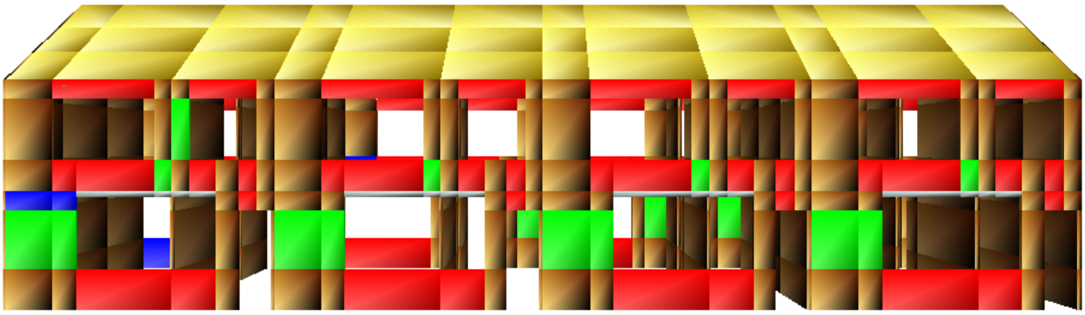

D.5 Overschild

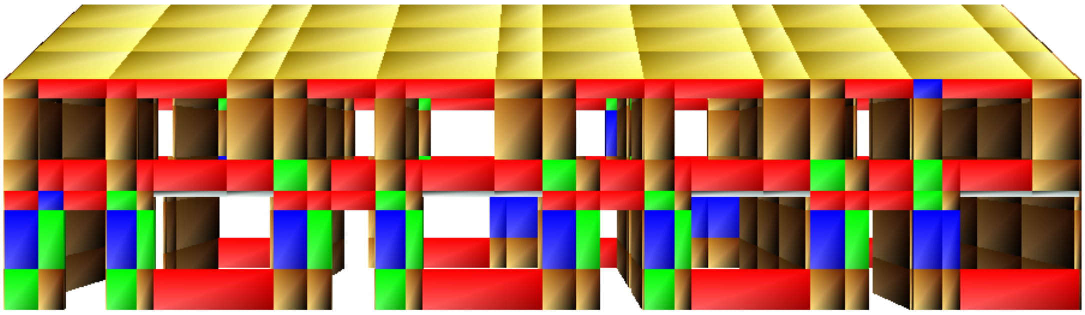

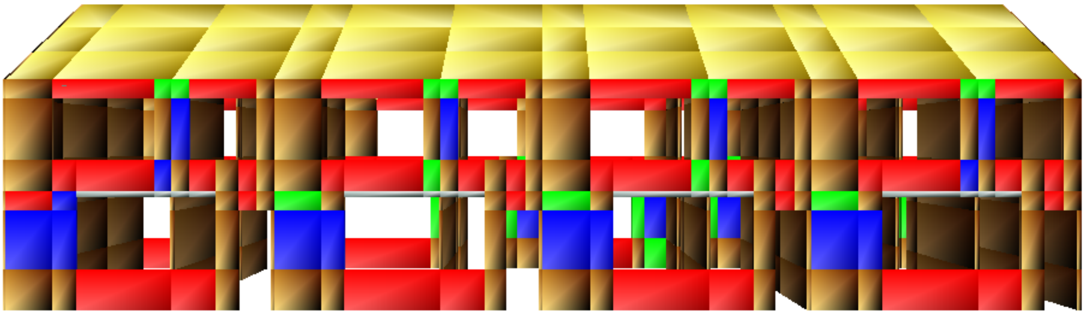

Appendix E

3D Model FRS Results

E.1 Appingedam

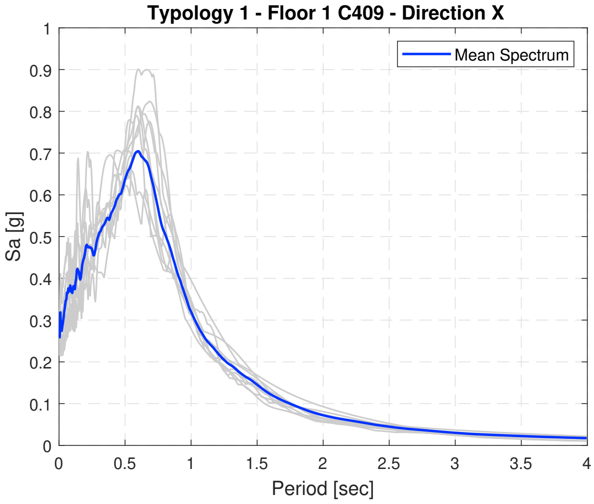

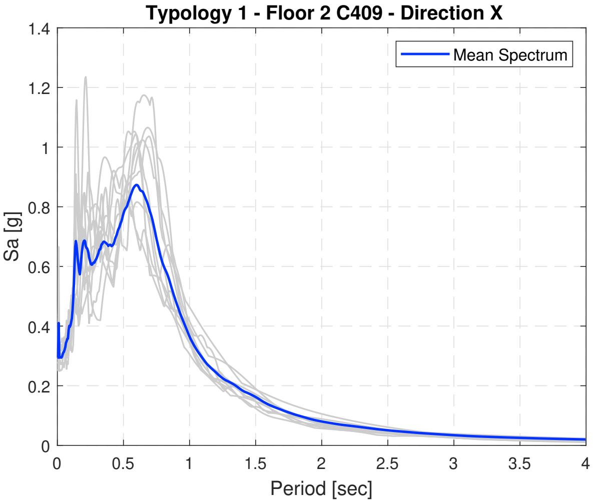

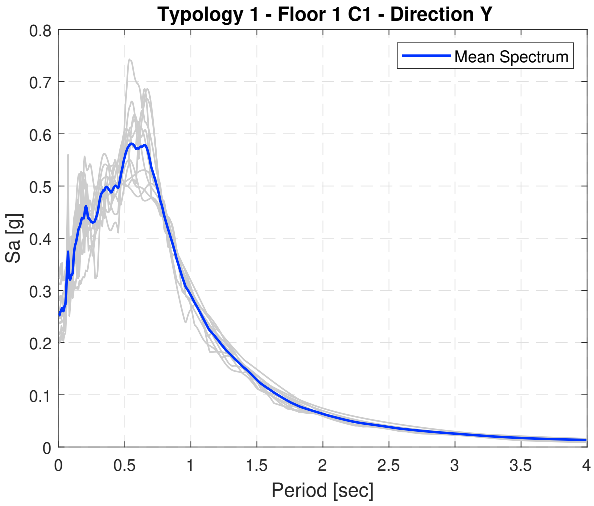

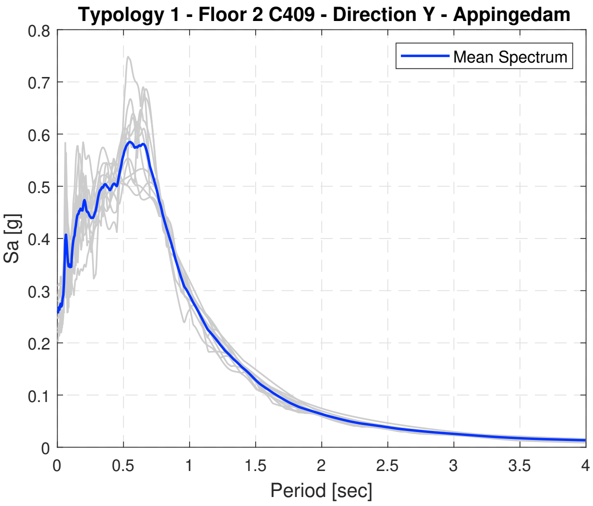

E.2 Groningen

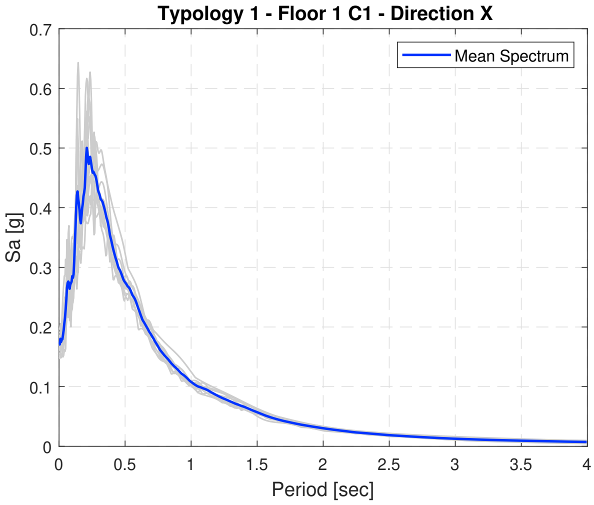

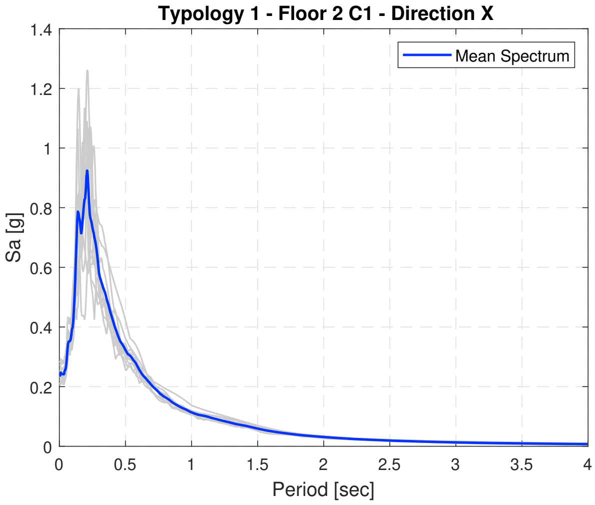

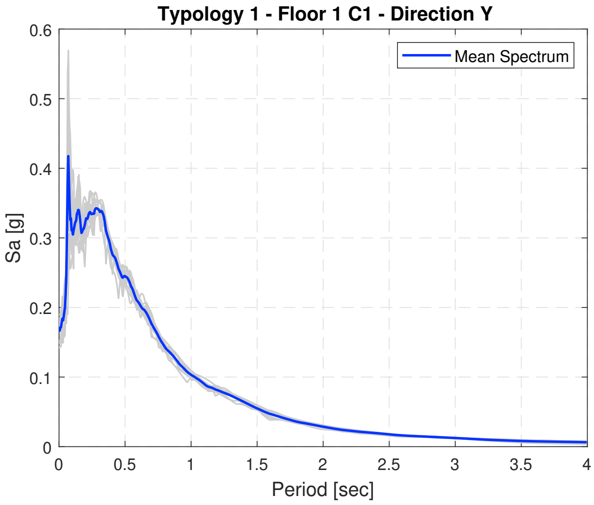

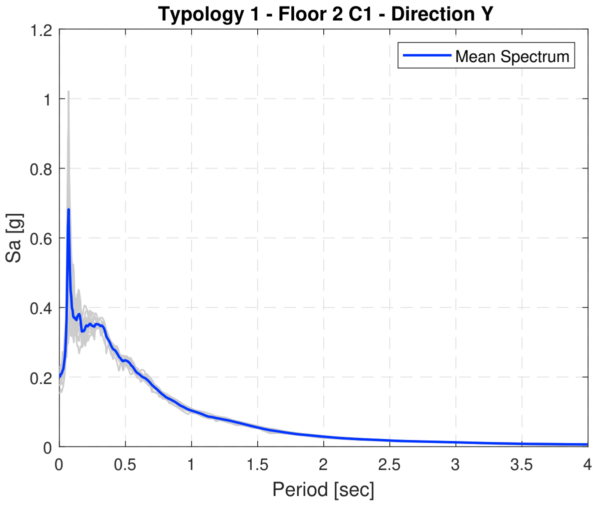

E.3 Hoogezand

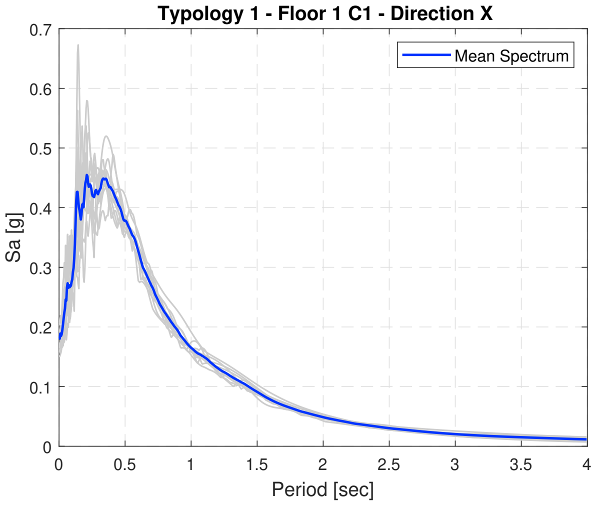

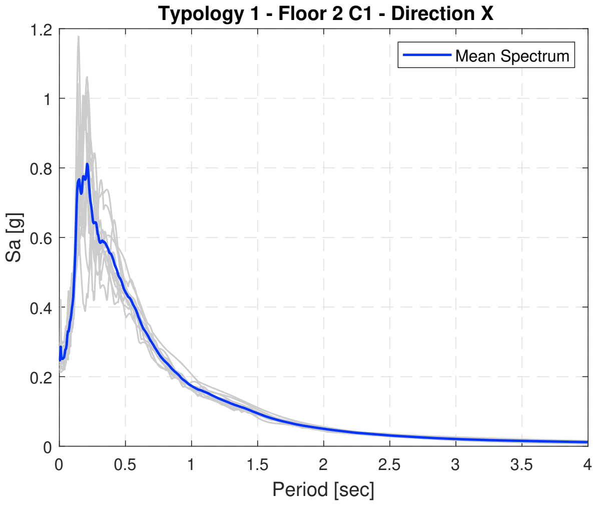

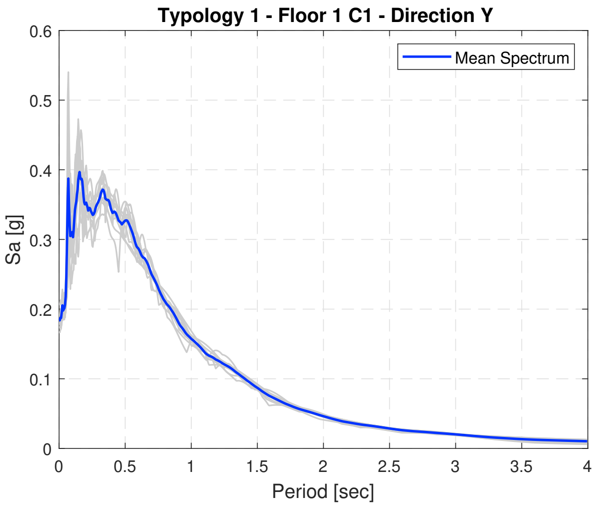

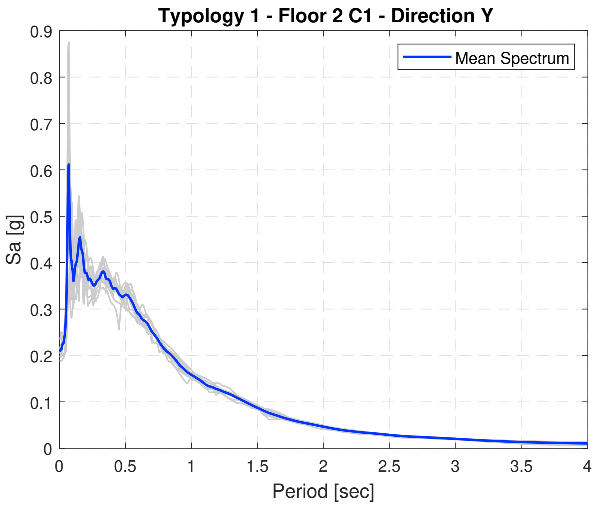

E.4 Loppersum

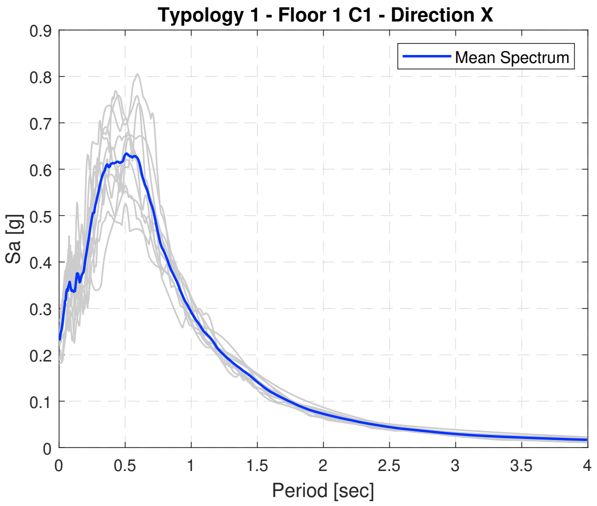

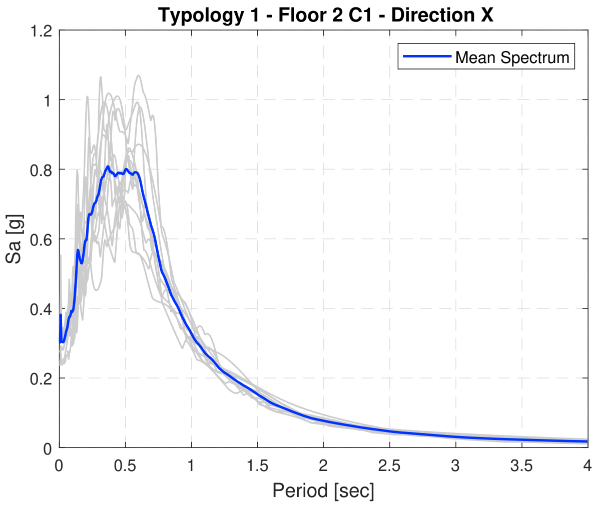

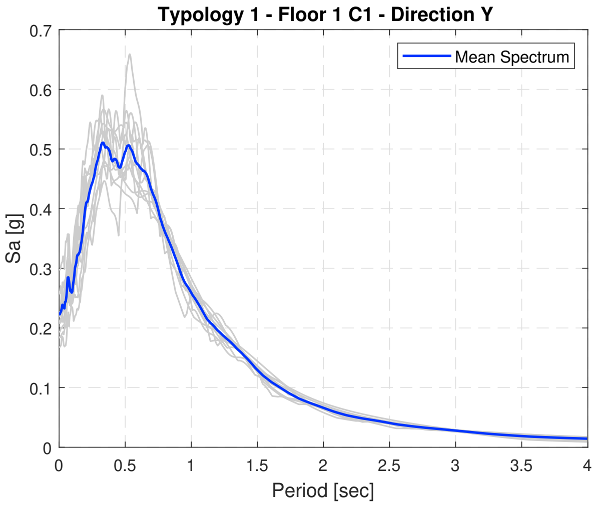

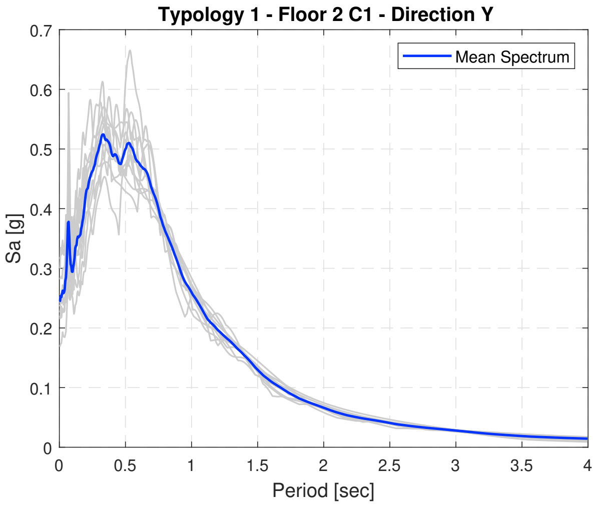

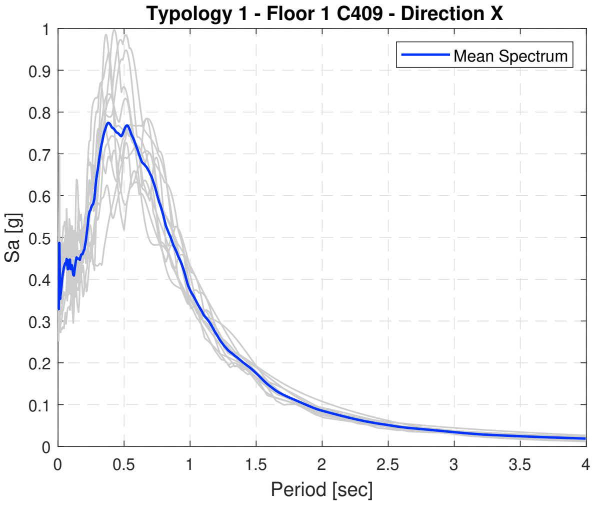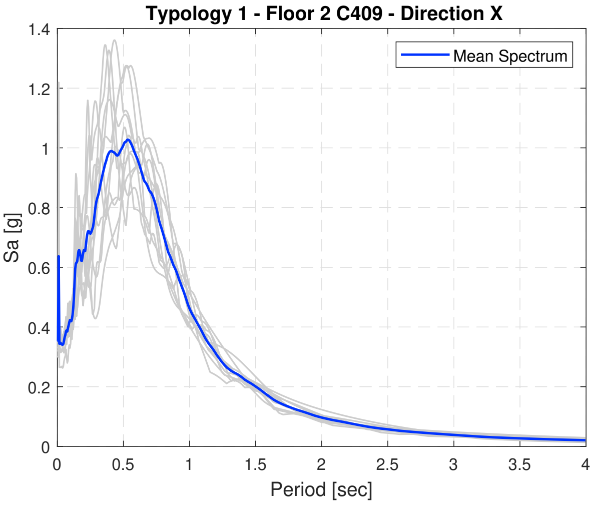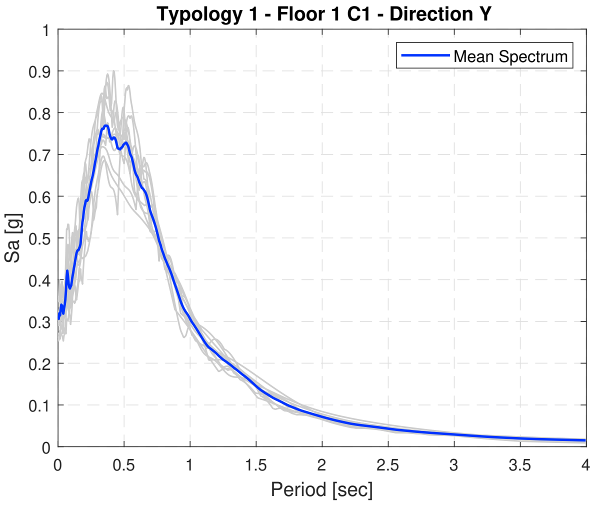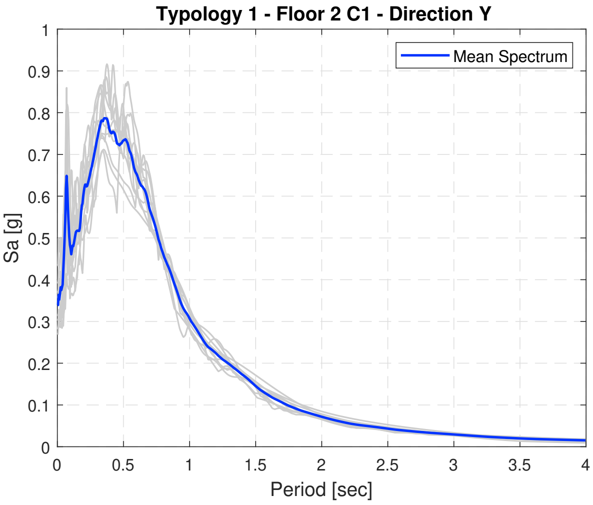E.5 Overschild